APPLICATION OF ~~THE SCANNING~~ AN ELECTRON MICROSCOPE

CONDUCTIVE MODE OF OPERATION FOR THE STUDY OF

OPTOELECTRONIC DEVICES

Ph.D., thesis submitted by M.P. Lesniak,

Imperial College of Science and Technology,

Department of Metallurgy and Materials Science,

London SW7 2BP.

September, 1985

CONTENTS

Page No.

ABSTRACT I

NOTATIONS III

ABBREVIATIONS VI

1. INTRODUCTION 1

2. LITERATURE SURVEY 5

2.1. Physics and Phenomenology 5

2.2. Types of Conductive Mode Signals. 14

2.3. EBIC Line Scans Across Devices. 20

2.4. Application of the SEM EBIC Method for Plan View Image Analysis. 25

2.5. The Electrical Behaviour of Dislocations in Silicon 27

2.6. Detection of Electrical Effects of Dislocations using the SEM EBIC Technique. 29

2.7. Effect of Impurities and Core Structure on EBIC Contrast from Dislocations. 33

2.8. The Temperature Dependence of EBIC Contrast on Defects 38

2.9. Resolution Limits for the SEM EBIC Method 40

2.10. Microplasma Instability in Silicon. 43

2.11. Identification of Microplasma Sites in Silicon. 46

2.12. Diffusion Induced Imperfections in Silicon. 48

2.13. Dislocation Retarded Phosphorus Diffusion Effect 52

CONTENTS (Cont'd/....)

Page No.

3. EXPERIMENTAL METHODS 54

3.1. The Conductive Mode Detection System. 54

3.1.1. Design Requirements. 55

3.1.2. The Mark I Conductive Mode Detection System 59

3.1.3. The Mark II CMDS 63

3.1.4. The Mark II Head Amplifier 66

3.1.5. Specimen Mounting. 83

3.1.6. Measurement of the Electron Beam Current. 84

3.2. Description of "Hot" and "Cold" Specimen Stages for the SEM Charge Collection Mode. 87

3.3. A.C. Biasing using the Mark II CMDS 94

3.4. Preparation of Large Area Electron Transparent Silicon Devices 98

3.5. Introduction of the Experimental Quantities and Error Analysis for the EBIC Measurements on Dislocations in RTAPDs. 105

4. RESULTS 110

4.1. Electrical Characterisation using the SEM Charge Collection Mode 110

4.1.1. Evaluation of the Resistivity using the Specimen Current 110

4.1.2. Electrically Active Defects in Small Si Photodiode Arrays. 114

4.1.3. Short Observation on Polycrystalline Si Solar Cell 120

4.1.4. Discussion 123

CONTENTS (Cont'd/....)

Page No.

4.2. Characterisation of Microplasma Sites in Silicon N^+P Reach-Through Avalanche Photodiodes 128

4.2.1. Preliminary Observations 132

4.2.2. Correlation between RTAPD I-V Characteristics and SEM Charge Collection Contrast. 137

4.2.3. The SEM Contrast Mechanisms of line Defects. 165

4.2.4. The Nature of the Dark Line Defects and Microplasma Sites. 174

4.2.5. Measurement of the Depth of the Misfit Dislocations using the EBIC Technique. 186

4.2.6. SEM EBIC Contrast and depth resolution on Misfit Dislocations 210

4.2.7. Observations of the EBIC Temperature Dependent Contrast on Misfit Dislocations 231

4.2.8 Discussion 244

5. CONCLUSIONS 251

6. APPENDIX 257

7. BIBLIOGRAPHY 260

ACKNOWLEDGEMENTS 273

ABSTRACT

A modular detection system for conductive mode, charge collection microscopy and electrical microcharacterisation in a scanning electron microscope is reported. It makes possible the recording of both the short-circuit current (EBIC) and the open circuit voltage (EBIV) generated by the barrier or the bulk electron voltaic effect. The constant current β-conductivity voltage signal and the constant voltage β-conductivity current signal, can also both be recorded. The design of the system emphasises noise minimisation, a wider range of operating characteristics, quantitative monitoring and simple signal processing.

This work demonstrates the capabilities of the detection system as applied to the Silicon optoelectronic devices. Electrically active defects in photodiode arrays, polysilicon solar cells and reach-through avalanche photodiodes (RTAPDs) have been studied. Defects investigated include phosphorus-diffusion pipes, precipitates and dislocations.

When the EBIC signal was collected from the RTAPD's, n^+p junction diffusion induced misfit dislocation networks, giving black contrast, was observed. After applying high bias voltage, bright stripe contrast appeared, flanking most of the dislocation lines. It is shown that this contrast is caused by irregularities in the junction resulting from a local retardation of the phosphorus

diffusion at points where dislocations occur. The junction irregularities appear to be responsible for the microplasma noise.

Conclusions on the electrical activity of dislocations in the recombination of charge carriers are given. The results indicate that the strength of recombination of dislocations at different depths depends strongly on the solute phosphorus concentration. Only those dislocations associated with the highest possible P-concentrations are shown to act as recombination centres for the injected carriers and only those were effective as far as retardation is concerned. Model calculations carried out for various primary electron energies give the possibility to determine the depth location of dislocations. The defects may be imaged with a spatial resolution w exclusively determined by the electron range R_e and the defect depth Z_o i.e., $w = R_e + Z_o$. The defects were examined in the charge collection mode at temperatures from 77 to 500 K. The results indicate that the interpretation of the EBIC temperature dependent contrast on dislocations must refer to the effect of the electron excitation level.

NOTATIONS

C	-	Normalised contrast on dislocations (%)
C_i	-	Concentration of the solute atoms within the Cottrell altmosphere (cm^{-3})
C_o	-	Average concentration of solute atoms (cm^{-3})
d	-	Electron beam diameter (µm)
D, D_e, D_h	-	Diffusion constant (D) for electrons (D_e) and holes (D_h) (cm^2/s)
e_i	-	Carrier pair creation energy (eV)
E	-	Interaction energy between solute atoms and dislocation [eV]
E_b	-	Electron beam energy (KeV)
f	-	Z/R_e
g(Z)	-	Generation rate at the depth Z (electron/hole pairs per sec per µm)
G	-	Generation factor
I	-	Electric current (A)
I_a	-	Actual maximum of the charge collection (A)
I_{cc}	-	Charge collection current (A)
I_D	-	I_{cc} current measured with the electron beam located at the defect (A)
I_b	-	Electron beam current (A)
I_B	-	Background current (undefected area) (A)
I_g	-	Maximum beam generated current (A)
I_j	-	Junction current (A)
I_m	-	Theoretical maximum collection current (A)
I_o	-	Saturation reverse bias current (A)
I_s	-	Specimen current (A)

I_{sc}	-	Short circuit current (A)
k	-	Boltzman constant
L, L_e, L_h	-	Diffusion length (L) for electrons and holes (μm)
n	-	Ideality factor
n_{cc}	-	Charge collection efficiency
N_d	-	Doping density (cm^{-3})
N_t	-	Carrier trap density (cm^{-3})
P_o	-	Equilibrium hole density (cm^{-3})
q	-	Electronic charge
R	-	Recombination rate
R_e	-	Electron range (μm)
S	-	Surface recombination velocity (cm/s)
T	-	Temperature (K)
V_b	-	Electron beam potential (kV)
V_{br}	-	Breakdown voltage (V)
V_{oc}	-	Open circuit voltage (V)
V_{th}	-	Carriers thermal velocity (cm/s)
W	-	Depletion region width (μm)
w	-	EBIC image spatial resolution (μm)
X, Y, Z	-	Orydinates
Z_o	-	Defect depth location (μm)
γ	-	Line recombination velocity of a dislocation
ΔI_β, ΔV_β	-	β-conductivity component signal current (ΔI_β) voltage (ΔV_β)
ΔI_D	-	Dislocatioon absorbed current (A)
Δn, Δp	-	Excess electron, hole density (cm^{-3})

$\Delta\hat{n}$, $\Delta\bar{n}$	-	Maximum and mean carrier density within energy dissipation volume (cm^{-3})
σ	-	Capture cross section (cm^2)
ρ	-	Resistivity (Ω cm)
χ	-	Energy fraction of the incident electron beam that is reflected from the sample surface
$\lambda(f)$	-	Normalised electron energy depth-dose function
τ, τ_e, τ_h	-	Lifetime (τ) for electron (τ_e) and holes (τ_h) (sec)
τ, τ_{nr}, τ_{ns}	-	Carrier lifetime for radiative (τ_r) and nonradiative recombination (τ_{nr}), at the specimen surface (τ_{ns})

ABBREVIATIONS

BEVE	Barrier Electron Voltaic Effect
CC	Charge Collection
CM	Conductive Mode
CMDS	Conductive Mode Detection System
EBIC	Electron Beam Induced Current
EBIV	Electron Beam Induced Voltage
HA	Head Amplifier
HVEM	High Voltage Electron Microscope
RTAPD	Reach Through Avalanche Photodiode
SEM	Scanning Electron Microscope
TEM	Transmission Electron Microscope

1. INTRODUCTION

The utilisation of scanning electron microscopy is increasing within the semiconductor and electronic industry. The ever decreasing size and increasing compexity of modern semiconductor devices usually makes it necessary to use some form of microscopic inspection. At times during the development, production and testing of micro-circuits, problems occur and the SEM is capable of rapidly giving information that can aid in solving these problems. The SEM with its wide magnification range, large depth of field and high resolution ability, is ideal for this purpose. Its utility is enhanced by the numerous modes of operation available. Each of them provides information on a different group of chemical or physical properties of materials.

The oldest of these, the emissive and X-ray modes, already have an established position in laboratories and are useful research aids. The emissive mode voltage contrast for instance, presents a unique method for the inspection of large scale integrated circuits. However, not much information can be acquired as regards semiconductor material parameters, when using the above two techniques. The SEM conductive mode and cathodoluminescence (CL), are now mainly responsible for the growing interest in scanning electron microscopy. The main reason for this is that the addition of conductive mode or CL detection system to the SEM, can transform the instrument into a high resolution semiconductor material analyser. Many of the most important parameters of the semiconductor can be measured with the aid of these techniques.

They have an advantage over the more usual techniques employed in industry, in that high spatial resolution, better than 1 μm, can be achieved. High resolution characterisation techniques are essential where the sample or device is very small or inhomogenous on a micron scale.

In the case of the conductive mode detection, such parameters, for example, as carrier diffusion length and lifetime or sample resistivity variation can be assessed. This technique is also vital to monitor production for process induced defects. It can be used in conjunction with other techniques, for example, transmission electron microscopy, to define which of the defects present is electrically active and potentially ruinous for the device operation. Recently, a new field for the application of the conductive mode techniques has been introduced. The involvement of both time and temperature as experimental variables offers the possibility that still more detailed information concerning the electronic properties of defects may be obtained.

The information that can be obtained in any mode of the SEM is dependent on the instrumental characterisation of the detection system employed. This is recognised in relation to the emissive, X-Ray (microanalysis), cathodoluminescence and transmissive (STEM) modes of the SEM. However, while the conductive mode has been widely used for the study of semiconducting materials and devices (Schick 1981; Bresse 1982; Leamy 1982), little effort has been devoted to suitable detection systems (Holt 1981). It is only recently that the importance of such dedicated conductive mode

detection systems has been recognised and the first such systems developed (Unvala et al. 1981; Wilshaw et al. 1983, Lesniak et al. 1984).

The SEM conductive mode uses currents or voltages arising in electron bombarded specimens as signals. The important signals are those that arise through "charge collection" (CC), that is the separation of electron bombardment generated holes and electrons. The collected carriers constitute a signal which can be fed to the SEM display unit through "some form" of a current or voltage sensing amplifier. "Some form" of the CC signals can be accessed relatively easily since the specimen itself acts as a detector or "collector" of the electronic charge that makes up the video signal. The electron beam induced signals are usually strong under most commonly employed experimental conditions.

In order to obtain well defined signals to which analytical expressions can be applied, special detection systems are needed. This is primarily because the input characteristics of the detector must meet the particular requirements for that type of signal. It must have a very low input impedance compared to the specimen to detect short circuit current I_{sc}. It must have a very large input impedance in order to obtain the open-circuit voltage due to a bulk or barrier electron voltaic effect. It must provide either constant-current biasing or constant-voltage biasing to the specimen to obtain quantitatively interpretable β-conductivity signals. In addition the detection system must be able to deal with currents, voltages, frequency bandwidths and noise levels of the magnitude

encountered in practice. Biasing, backoff, electronic signal processing and monitoring facilities and a computer interface are desirable features of such a detection system.

The main objectives of this work were:-

1. To develop a conductive mode detection system according to specific design requirements.

2. To test the equipment's performance through experiments.

2. LITERATURE SURVEY

2.1. Physics and Phenomenology

The SEM beam contains monochromatic electrons focused $\sim$ 100 Å. As these electrons penetrate the sample, they lose energy and direction. Large angle elastic scattering by the atomic nuclei is responsible for spreading the beam as it penetrates into the specimen. This occurs to a greater extent in high atomic number specimens in which the stronger angular scattering leads to many more electrons being scattered back out of the target and reduces the mean penetration depth of electrons. The fraction of incident beam energy being back scattered in the case of silicon is very small, $\mathcal{X} = 0.08$ and is energy independent (Sternglass 1954; Bishop 1965).

Between large angle scattering events, the high energy primary electrons undergo a number of inelastic electron-electron collisions. This results in the creation of electron-hole pairs in the semiconducting material. Electrons are raised from filled states in the valence band to empty states in the conduction band.

Electron bombardment of typical semiconductor materials results in rather enormous charge carrier generation. This is because the incident electrons have typically tens of keV energy while the average formation energy of an electron-hole pair e_i, is about three times the forbidden band gap energy. For example, in silicon $e_i = 3.65$ (Holt 1974). The generated carriers constitute an "injected" current given by:

(1) $$I_g = G\ I_b$$

where I_b is the electron beam current, G is the generation factor i.e., the number of electron-hole pairs produced for each incident electron. It can be defined as:

(2) $$G = E_b\ (1 - \chi\ )/e_i$$

where E_b is the electron beam energy.

Electron hole pairs are created in the target through the energy dissipation volume. This is a small volume beneath the focused beam spot. The excitation volume is characterised by the range of electrons R_e which is essentially the depth at which an average primary electron becomes thermalised. An empirical expression for R_e obtained for silicon is:

(3) $$R_e = 0.0171\ E_b\ ^{1.75}$$

where E_b is in kiloelectronvolts and R_e in μm. The expression itself is due to Everhart and Hoff (1971). It is accurate for $5 \leqslant E_b \leqslant 25$ keV. The simple model assumes uniform energy dissipation through a spherical volume. However, evidence for scaling of the energy loss distribution with distance beneath the surface in solids, comes from observations of electron beam exposed resists by Shimizu et al. (1975). Everhart and Hoff (1971) have experimentally determined a function describing the energy deposition versus penetration depth. The function is:

$$(4) \qquad \lambda(f) = \begin{cases} 0.6 + 6.21f - 12.4f^2 + 5.69f^3 & 0 < f \leq 1.1 \\ 0 & f > 1.1 \end{cases}$$

where $f = Z/R_e$, Z being the distance from the surface. Estimates of the generation distribution in lateral direction can be derived from the results of Shea et al. (1978). Shea et al., have shown that the generation distribution is one of the exponentials, each valid over a certain range. The Gaussian form was also found to provide a satisfactory fit (Davidson and Dimitriadis 1980; Oelgart et al. 1981).

In semiconductor materials, the electron-hole pair formation will only result in a transient effect. In the absence of an electric field, charge carriers generated within the sample diffuse randomly down the gradient of carrier concentration away from the source at a rate that is governed by the diffusion coefficient D. During diffusion, recombination of the oppositely charged carriers occurs generally via an intermediate stage in which one of the carriers becomes trapped at a specific point in the crystal. Before being trapped the carrier moves freely for a time τ :

$$(5) \qquad \tau = \frac{1}{\sigma \; N_t \; V_{th}} \qquad \text{(Sze 1969)}$$

where N_t is the trap density and σ the trap capture cross section, V_{th} is the carriers thermal velocity.

The charge carrier recombination process has two main effects: radiative and non-radiative processes. Radiative and non-radiative processes usually occur simultaneously in parallel and can be related to τ as follows (Thornton 1968):

$$\frac{1}{\tau} = \frac{1}{\tau_r} + \frac{1}{\tau_{nr}} \tag{6}$$

τ_r can be regarded as the carrier lifetime which would exist in the specimen under the same conditions if the non-radiative process occurred so slowly as to be insignificant. Similarly τ_{nr} can be regarded as the limiting value of τ in the absence of radiative recombination. The ratio τ/τ_r is a measure of the radiative efficiency. When recombination radiation is excited by electron bombardment the resultant luminescence is called cathodoluminescence. The collection and display of this light as a video signal forms a useful SEM technique.

The mutual effect of the diffusion and recombination processes of charge carriers is most often expressed through the mean carrier diffusion length L. This is a parameter describing the average distance between the point of creation of a carrier and the point of its annihilation. L is related to both the carrier diffusion coefficient and "free lifetime":

$$L = (D\ \tau)^{\frac{1}{2}} \qquad \text{(Sze 1969)} \tag{7}$$

If the majority carrier density greatly exceeds the minority carrier density as is usually the case (n- or p-doped materials), the lifetime of carrier pairs is determined by the minority carrier free lifetime τ_h (τ_e), because so many majority carriers are available to recombine with a trapped minority carrier. For small Δn (representing the excess minority electron concentration in p-type material) the recombination rate R is just $\Delta n/\tau_n$. In a specimen that contains a homogenous distribution of carrier traps, excess carriers are constantly being removed via recombination at a rate proportional to the local carrier density. The linearity assumption is not valid however, unless $\Delta n \ll P_o$ (P_o is carrier concentration in thermal equilibrium). According to the Schockley-Read-Hall theory, the lifetime will increase from a low level value, determined by the minority carrier capture cross section of the dominant recombination centre, to a high level value determined by the majority carrier capture cross section. The essential idea is that if the injected carrier density Δn becomes larger than the equilibrium density P_o, the recombination statistics may alter e.g., the recombination centres may become saturated so that effective recombination time τ would increase, (Cornu et al. 1974). From relation (7) it can be expected that the carriers diffusion length will also increase with increasing injection level since the diffusion constant only varies slowly with carrier density (Smith 1964; Davidson et al. 1981).

In addition the carrier lifetime or diffusion length was shown to alter with the doping dose itself. This was investigated experimentally in diffused layers of silicon for solar cell

applications (Hovel 1975). It appears that the lifetime decreases with increasing doping. Within the doping range 10^{13} - $10^{17}cm^{-3}$, an inverse power low of the following form appears to apply:

$$\tau \propto N_D^{-1/m} \tag{8}$$

Where, N_D is the doping and m lies between 1.3 and 3. The practical meaning of the dependence of the carrier lifetime on doping and injection levels, is that the same electron beam will tend to result in smaller densities of injected carriers in the material of a higher doping level.

Yet another effect which can alter the density of injected carriers, is the variation of carrier lifetime or the diffusion length with temperature. Although low temperature examination of semiconductor materials can lead to an increase in carrier mobility, (Sze 1969), carrier lifetime is found to be reduced, due to increased trapping effects (Dumke 1970). In addition, the recombination on crystallographic defects is also found to increase with decreasing temperature, (Kimerling et al. 1977 a; Lesniak et al. 1983).

When the diffusion length is significantly larger than the electron range R_e, most of the carriers will diffuse well away from the generation region before recombining. Surface recombination becomes in this case an important factor limiting the excess minority carrier density because the carriers will mostly be generated within a diffusion length from the surface. Analogously to the bulk-recombination process, the surface recombination rate

is given by:

(9) $S = \ell / \tau_{ns}$ (Sze 1969)

ℓ is the thickness of the surface recombination region,

τ_{ns} is a minority carrier lifetime on the specimen surface. S has dimensions of cm/sec and is consequently known as the surface or boundary recombination velocity. The effect of surface recombination is not only to decrease Δn near the surface but also to reduce the extent of the energy dissipation volume (Van Opdorp 1977; Watanabe et al. 1977).

To calculate the excess carrier distribution, the generation function must be put into the continuity equation which then should be solved satisfying the appropriate boundary conditions. For the general case, this is difficult but is simplified somewhat if the surface recombination velocity can be assumed to be either zero or infinity. In addition an accurate calculation of Δn based upon the experimental $\lambda(f)$ are not available. Berz and Kuiken (1976), discussed this topic on the basis of the uniform generation approximation. They conclude that for silicon $\Delta n \leqslant p_o$ for most of the experimentally accessible conditions. For GaAs, Leamy and Kimerling et al. (1977 b), have demonstrated that high injection conditions may easily be obtained. The injected carrier density clearly varies over many orders of magnitude with distance from the source, making it impossible to define a precise injection level. Davidson and Dimitriadis (1980), introduced useful expressions allowing to assess a mean injection level $\Delta\bar{n}$ and maximum carrier density $\Delta\hat{n}$ within the generation distribution. This is for two

cases of surface recombination, S = 0 and S = ∞ . The mean injection level $\Delta\bar{n}$ was defined to represent a situation where half of the generated carriers recombine at densities higher than this and half at lower. For S = ∞ , $\Delta\bar{n}$ and $\Delta\hat{n}$ are given by:

$$(10) \quad \Delta\bar{n} = \frac{Ga}{25DL^2} \qquad (11) \quad \Delta\hat{n} = \frac{G}{16Da}$$

and for S = 0:

$$(12) \quad \Delta\bar{n} = \frac{G}{50DL} \qquad (13) \quad \Delta\hat{n} = \frac{G}{5Da}$$

The parameter a is related to the electron range by $a \simeq R_e/2$. These expressions should be adequate to determine whether the injection level is predominantly high or low with respect to the doping density. Expressions from (10) to (13) were derived assuming the Gaussian form of carrier density distribution (Davidson and Dimitriadis 1980).

The presence of the electric field E, constitutes yet another factor strongly influencing the distribution of injected carriers. In the presence of an electric field, the generated charge carriers are influenced to depart from purely diffusive motion, they are "collected" by an electric field to constitute a current that may be detected in an external circuit. Mobile charge carriers, electrons and holes are swept in opposite directions by the field until a steady state is established. If such drift motion occurs the resultant current or voltage may be used as a video signal of the SEM and this is known as the charge collection mode or more generally conductive mode of operation of the SEM.

A distinguishable feature of this mode of image formation is that the specimen itself acts as the detector or "collector" of the electronic charge that makes up the video signal.

The charge collection can also be properly called the barrier electron voltaic effect (BEVE) by analogy with the familiar barrier photovoltaic effect (Ehrenberg 1951). The first observation of charge collection phenomena, referred to by Leamy (1982), was done by Everhart (1958).

2.2. Types of Conductive Mode Signals

The conductive mode signals in general, rely on the ability of the SEM electron probe to inject excess carriers into the specimen. One can distinguish two basic types of conductive mode signal i.e.:

1. Specimen current, I_s

2. Charge collection effect signals

The specimen current I_s is the leakage current from the beam via the specimen to the ground. The signal is complementary to the total emissive current. The electrons emitted from the surface of the specimen into the vacuum chamber I_e plus specimen current I_s, must equal the beam current I_b. I_s can be recorded in the absence of any internal electric field inside the specimen. The specimen current technique has found an application in displaying the compositional (Z-number) variations across the specimen surface (Holt 1974).

Charge collection (CC) signals arise due to the separation of charge pairs by an internal "built-in" field or by an externally applied bias.

There are six forms of CC signals that can be quantitatively analysed. They are listed in Table 1.

TABLE 1

QUANTITATIVELY INTERPRETABLE TYPES OF CC SIGNAL

MECHANISM	FORMS OF SIGNAL		INTERPRETIVE REFERENCES
Barrier electron voltaic effect	I_{sc} (EBIC)	V_{oc} (EBIV)	Czaja (1966), Holt (1974), Balk et al. (1975), Huang et al. (1983).
Bulk electron voltaic effect	I_{sc} (EBIC)	V_{oc} (EBIV)	Munakata (1966, 1967 a, 1967 b), Holt (1974).
β-conductivity	ΔI_{β} (ΔV_{cc} = const.)	ΔV_{β} (ΔI_{cc} = const.)	Munkata (1968 a, 1968 b, 1969, Gopinath (1970), Gopinath and De Monts De Savasse (1971), Holt (1974).

The electric field required for charge collection may be produced by means of a p-n junction, a Schottky barrier, a heterojunction or by non uniform dopant distribution inside the specimen. The generated carriers move under the influence of the field and induce a compensating motion in the external circuit. The current that results is called the charge collection current I_{cc}. The methods by which this is achieved in practice are illustrated in Fig. 1.

The excess minority carriers generated at a certain distance from the space charge region (Fig. 1(a)) diffuse down the gradient of carrier concentration away from the source. The number of minority carriers that "meander" into the depletion region depends in general on: the diffusion coefficient D_e (D_h), lifetime τ_e (τ_h), surface activity S and the distance from the depletion region X. When the carriers are injected directly into the depletion region, the collection is maximum (provided low injection level conditions are ensured):

$$I_{cc} = n_{cc}\, I_g \tag{14}$$

Where, n_{cc} is the charge collection efficiency of the barrier for the particular experimental geometry employed (Fig. 1).

If the specimen is short circuited the maximum possible external current flows. In SEM terminology this is called (BEVE) barrier electron voltaic effect short circuit current I_{sc}. This refers to the situation when the input impedance of the detecting amplifier is negligible compared to that of the specimen. The net externally

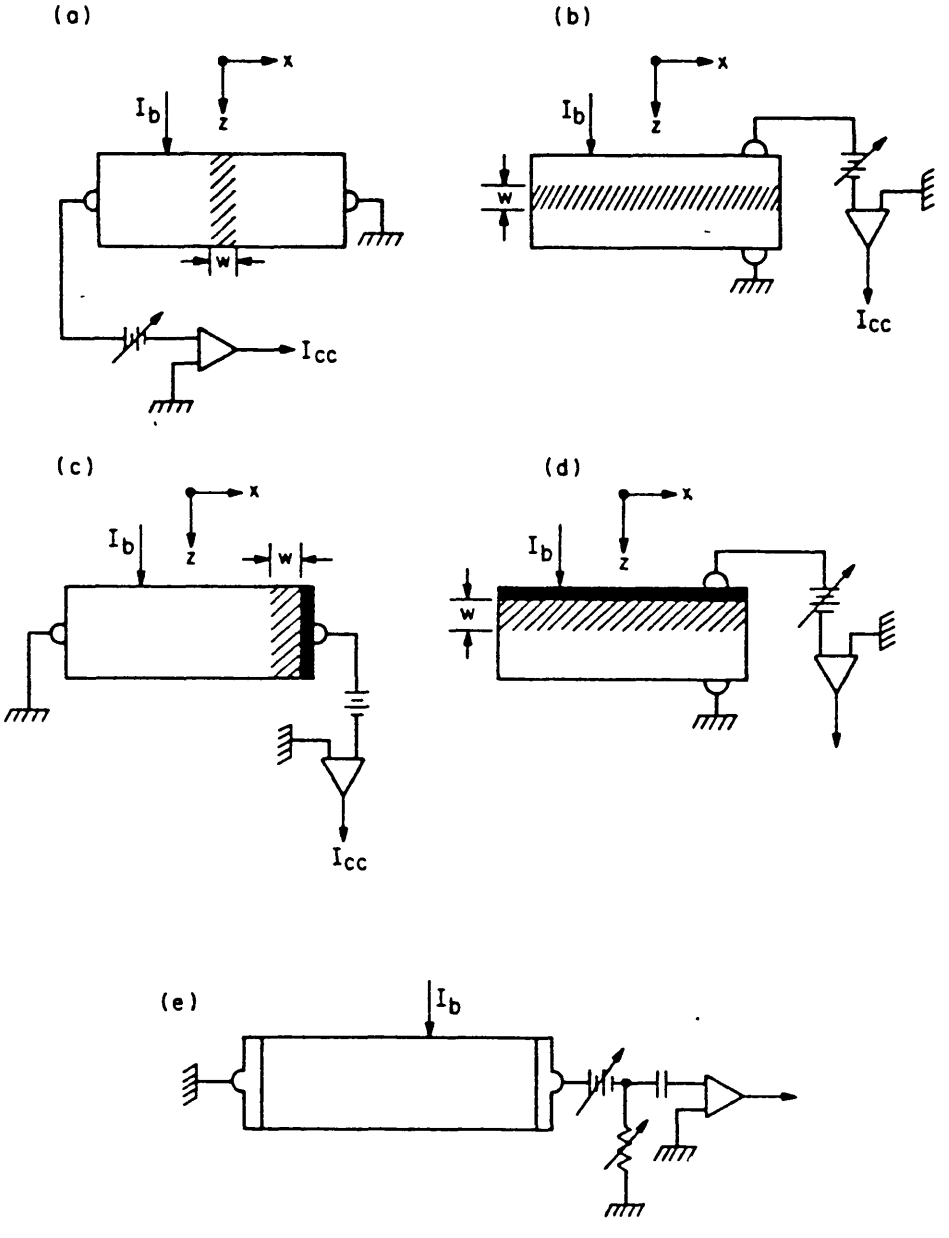


Fig. 1 - Schematic illustration of charge collection geometries a) and b) illustrate perpendicular and planar p-n junction geometries in which the space charge region is denoted with cross hatching; c) and d) are equivalent Schottky barrier geometries; e) shows the specimen configuration for β-conductivity technique.

observable I_{sc} is a result of two constituents:

$$I_{sc} = I_{cc} - I_j \tag{15}$$

The I_j is a junction current given by:

$$I_j = I_o \, (\exp \, (qV/nkT) - 1) \tag{16}$$

where I_o is a saturation reverse bias current, V is the diode voltage, n is an ideality factor, T is temperature, q - electron charge and k - Boltzman constant. Since the junction is short circuited the situation represented in eq. (15) implies: $I_j = I_o$.

I_{cc} is given by equation (14) and in SEM terminology is known as the electron beam induced current (EBIC).

When the specimen is effectively open circuited, there is no external current flow and the maximum possible voltage BEVE V_{oc} can be measured. Rearrangement of equation (15) with $I_{sc} = 0$ provides true open circuit voltage V_{oc} (Balk et al. 1975):

$$V_{oc} = (nkT/q) \quad \ln(1 + I_{cc}/I_o) \tag{17}$$

The BEVE V_{oc} is also known as electron beam induced voltage (EBIV) technique (Balk et al. 1975; Huang et al. 1982). It was shown by Balk et al., that the information obtainable from I_{sc} and V_{oc} is quite different. The bulk electron voltaic effect is similar to the BEVE but arises in regions of changing doping density not at barriers such as p-n junctions (Holt 1974).

"β-conductivity" is the analogue of photoconductivity arising from an electron ("β-Ray"). β-conductivity is a phenomenon occurring when dc - biasing is applied across the specimen and can be observed in the absence of any electron barrier voltaic effects. The electron beam changes locally the conductivity of the specimen in the bombarded region. This can be detected in the external circuit as changes in the measured current if a constant biasing voltage is applied, (Gopinath 1970; Gopinath and de Monts de Savasse 1971). Constant current biasing results in a voltage variation, the β-conductivity component of which can be shown to be proportional to the square of the resistivity (Munakata 1968 a, b, 1969). Here ΔV_{cc} represents the total voltage variation signal and ΔV_{β} represents the component due to β-conductivity.

The theories for the interpretation of the SEM conductive mode signals and adequate terminology were reviewed by Holt (1974).

2.3. EBIC Line Scans Across Devices

Minority carrier diffusion length is the most widely measured semiconductor parameter using the SEM EBIC technique and a vast majority of papers in the conductive mode field are dedicated to this topic. This fact emphasises both the importance of this parameter in a device design and the attractiveness of the SEM EBIC technique in its determination.

Wittry and Kyser (1965), showed that if surface recombination effects were neglected (S = 0) and the carrier generation was assumed to be spherically symmetric, the variation of the charge collection current I_{sc} with X, the distance from the junction (Fig. 1(a)), should have the form:

$$I_{cc}(X) = I_m \exp(-X/L) \tag{18}$$

where L is the minority carrier diffusion length in the material on that side of the junction and I_m is the theoretical maximum collection current, n_{cc} = 1 (eq. 14), corresponding to the electron beam, positioned within the space charge region (X = 0). They pointed out that the diffusion length can be obtained from the slope of log ($I_{cc}(X)$) vs X plot. By extrapolating back to the junction from straight line portions of the curves in log ($I_{cc}(X)$) vs X plots, the value of I_m can be found. The value of the charge collection efficiency of the junction is given by (Bresse 1971):

$$n_{cc} = I_a / I_m \tag{19}$$

where I_a is the actual maximum value of the charge collection, I_{cc} current for X = 0, i.e., junction position.

A more detailed form of the EBIC variation with distance from the junction including the influence of surface activity has been calculated by a number of authors (Van Roosbroeck 1955; Bresse and Lafeuille 1971; Berz and Kuiken 1976), the most thorough treatment being that of Berz and Kuiken (1976).

The effect of finite source size was approximated as a sphere of uniform generation rate. The method considered I_{cc} (X) as a function of S and L in a calculable and correctable way.

It was shown that non-exponential behaviour of I_{cc} (X) plot is due to surface recombination, but the slope of the EBIC characteristic still tends to the diffusion length under most circumstances, (Berz and Kuiken (1976). The effect of S was shown to be reduced with an increasing penetration depth of the electron beam.

Both upper and lower limits exist to the values of the diffusion length which can be measured using the SEM. The upper limit is usually set by the dimensions of the sample (Zimmerman 1972). The smallest measurable value of L is determined by the generation distribution and hence the beam voltage. Shea et al. (1978), have shown that diffusion lengths down to $R_e/4$ can be measured.

The analytical solutions obtained by Berz and Kuiken (1976), are valid for electron beam excitation outside of the space charge

region within the homogenous semiconductor. It was assumed that the diffusion length is constant through the sample and independent of carrier injection density.

Recently, Davidson et al. (1981), studied doping profiles with (p^+nn^+) and (n^+pp^+) junctions using EBIC and photocurrent (PC) techniques. The EBIC linescans across these profiles were found to be sensitively dependent on the beam power. In order to account quantitatively for these variations they had to extend the existing theory (Berz and Kuiken 1976), to incorporate a minority carrier lifetime which varies with the position, doping and injection level. The variation in the shape of the EBIC line scans with the increasing beam power was said to have arisen due to the injection level dependent surface recombination velocity. In poorly doped p- and n- regions it was necessary to consider the injection dependent effects both in the bulk and at the surface to explain observed characteristics.

Most recently, Marten and Hildebrand (1983), have applied a different method of analysis of the EBIC line scans across p-n junctions. Contrary to the conventional model with a limited extension of the field region, they postulated that a non-zero electric field exists through the crystal. Their computed $I_{cc}(X)$ curves mimic experimental results and imply that the EBIC line scans depend on asymmetries in all: doping, carrier lifetimes and the mobilities between minority carriers on both sides of a p-n junction. They postulated that major changes in the EBIC line scans at increased injection levels occurred because of the redistribution

of the electric field caused by higher generation rates. Their theoretical and experimental results were in good agreement for InP and p+pn- junctions. They claimed that the maximum of the EBIC signal is not located at the crystallographic p-n junction if the minority carrier lifetimes or mobilities are different or doping profiles are asymmetric.

The depletion layer width W can also be determined from EBIC line scans using the experimental arrangement of Fig. 1(a) and 1(b). If $W \gtrsim R_e$ then W (W - width of the depletion region) will appear in $I_{cc}(X)$ as a region of relatively constant I_{cc} (MacDonald and Everhart 1965). The edges of the depletion zone are not often obvious because the resolution of the method is limited by R_e.

The transition from the drift to the diffusion controlled EBIC, resulting from a variation of the point of excitation, produces a point of inflection in junction $I_{cc}(X)$. Balk, Kubalek and Menzel (1975), used the phase sensitive detection method to produce $dI_{cc}(X)/dx$ and accurately determine the extent of the depletion region. The edge of the depletion region corresponds to the point where $dI_{cc}(X)/dx = 0$. The method has been extended by Schick (1981), for sectioned device analysis. He claimed a precision of approximately 300 Å of measured channel length in an FET transistor.

Although the geometry arrangements shown in Fig. 1(a) and 1(c) are most frequently employed for the evaluation of parameters such as L, S, or junction depth, it is equally possible to use the plan view geometries Fig. 1(b) and 1(d) for this purpose. (Wu and Wittry

1978; Possin and Kirkpatrick 1979 a, b; Chi and Gatos 1977).

More complete treatments of quantitative applications of EBIC methods were discussed by Holt (1974); Bresse (1977); Davidson (1977); Davidson and Dimitriadis (1980), and Leamy (1982).

2.4. Application of the SEM EBIC Method for Plan View Image Analysis

Charge collection images are produced by recording I_{cc} during a two-dimensional scan of a specimen in any of the geometries presented in Fig. 1. The major advantage of the CC mode is that it is sensitive specifically to the electrically active defects and depletion regions such as p-n junctions or Schottky barriers. Application of the EBIC technique to the microelectronic devices allows for visual display of location and form of the depletion regions in a device structure. Defects such as mishapen or misplaced junctions, short or open circuit metalization faults are readily detectable. The high resolution and magnification range obtainable in the SEM, together with the unique sensitivity of the CC mode to the electrical structure, dictates the potential application of the technique for the inspection and failure analysis of integrated circuits. Everhart et al. (1964), was the first to apply the technique to visualise junctions in a device. Although straightforward for interpretation in the case of simple microelectronic devices, the charge collection images of complex integrated circuits require careful analysis if they are to be properly interpreted, (Thornton 1968). Such analysis of complex CC contrast usually requires the device geometry to be understood in detail. The scale of integration i.e., the number of component elements per silicon circuit has doubled each year since integrated circuits were first produced in 1960. VLSI (verylarge scale integrated) circuits are now appearing. The number of features in a junction array is so large that complete examination of a circuit by

direct visual inspection (Galloway 1976), at required magnifications is a formidable task. An approach to this problem was proposed by Holt, Lesniak and Luther (1983). Since SEM micrographs of periodic silicon integrated circuits (such as memories or photodiode arrays) are regular two-dimensional patterns, their Fourier transforms should be analogous to the transmission electron diffraction patterns of thin crystals. A He-Ne laser optical bench has been used (Holt et al. 1983), to produce a spatial frequency spectrum of an EBIC image from an integrated circuit. By filtering out specific frequency components of the image corresponding to the regular array period, an image of random defects has been extracted.

During the last years the investigation of the electrical activity of individual crystal defects in semiconductors has gained increasing importance in semiconductor physics and technology (Heydenreich 1981; Holt 1983). Crystallographic defects such as dislocations, stacking faults and precipitates usually reduce the lifetime of carriers in their vicinity. In CC micrographs, therefore, they appear as features of reduced I_{cc}.

The method is now in widespread use. Planar geometry p-n junctions and Schottky barriers are usually employed as means for charge collection. The advantages of this technique were first recognised by such workers as Lander et al. (1963); Czaja and Wheatley (1964) and later, de Kock et al. (1975); Kawado et al. (1975).

2.5. The Electrical Behaviour of Dislocations in Silicon

Dislocations in silicon are known to produce two essential effects that can have important influences on the electrical properties of the crystal. The first effect is concerned with an elastic stress associated with dislocations that can stretch to considerable distances. A second effect is that due to the presence of dangling bonds at the dislocation. Read (1954) put forward the fundamental idea of edge dislocations behaving as lines of acceptors in n-type semiconductors with diamond structure. The acceptor behaviour was presumed to result from the dangling bonds associated with the atoms at the dislocation core. In order to preserve space change neutrality the negatively charged dislocation repels electrons from the donor atoms around it to form a positive charge cylinder. The result is the creation of a potential barrier for electrons and potential well for holes (in n-type material) extending out to the edge of the space charge cylinder.

Although the intrinsic properties of individual dislocations are governed by the presence of the space charge cylinder, the usual electrical behaviour of dislocations is through the presence of impurities in association with the defects. Impurity decoration of dislocations occurs readily due to the presence of elastic stress associated with dislocation.

The impurity segregation along dislocation lines can result in the formation of the Cottrell atmosphere. The Cottrell model is known to be applicable in the case of Si (Kaiser et al. 1956).

Concentration of the solute atoms within the Cottrell atmosphere can be expressed as (after Ciszewski 1972):

$$C_i = C_o \exp (E/kT) \quad (20)$$

Where C_o is an average concentration of solute atoms, E is the interaction energy between a solute atom and a dislocation.

Calculations for common impurities such as Fe, Ni and Cu show that the interaction energy between the atoms of these metals and a dislocation in silicon are fairly large such that the formation of impurity atmospheres and impurity percipitates at dislocations should be considered as a rule rather than the exception (Kurtz et al. 1956).

2.6. Detection of Electrical Effects of Dislocations using the SEM EBIC Technique

The unique value of the charge collection contrast is that it provides information about electrical activity of defects and their distribution. The charge collection contrast has to be correlated with the use of other imaging techniques so that it can be determined which of the defects present is electrically active and so that its character and crystallography can be identified.

Dark dislocation contrast in EBIC images is interpreted as due to enhanced recombination at or near the dislocation (Czaja 1966). The contrast is defined to be:

$$C = (I_B - I_D)/I_B \tag{21}$$

where I_B and I_D are the EBIC values for the bulk material i.e., for the beam incident far from any defect and at the dislocation respectively (Fig. 2(b)).

Lander et al. (1963), and Czaja et al. (1964, 1965, 1966 a), used a well developed preferential etching technique, followed by optical microscope observations. This was done to ensure the coherency between EBIC contrast and the identification of dislocations studied. Later, Holt and Ogden (1976) used X-ray topography in direct one to one correlation with EBIC image of dislocations in Si phototransistors. Transmission electron microscope techniques are uniquely important in the task of finding correlation between the

structure of crystal defects and their electrical properties. The major advantage of using TEM imaging methods is associated with the high resolution obtainable. The first to use conventional diffraction contrast EM in conjunction with EBIC imaging were Ravi et al. (1973) and Varker and Ravi (1974), in the study on oxidation induced stacking faults in silicon. More recently the use of the high voltage transmission electron microscope (HVEM) allowed the investigation of identical defects (stacking faults and dislocations) by the use of both methods, for example, Blumtritt and Gleichmann 1977, Heydenreich et al. 1979, Blumtritt et al. 1979. Two other TEM techniques proved to offer further possibilities in the fields of correlated images. The high-resolving weak-beam technique demonstrated its superiority over conventional diffraction EM in providing much more detailed information about dislocation morphology and the extent of its decoration, (Ourmazd and Booker, 1979, Ourmazd et al. 1983). On the other hand the use of scanning transmission electron microscopy (STEM) provides the possibility of simultaneous application of both imaging techniques and secures the interpretation of the observed contrast features, (Petroff et al. 1978, 1980; Fathy et al. 1980). Combined SEM(EBIC)/TEM or STEBIC investigations are capable of providing information about the electrical activity of individual defects, i.e., recombination efficiency for minority carriers. However, no direct information about the mechanism of such activity can be gained from these techniques. At present the specific interest of research dedicated to defects in semiconductros can be related to such problems as: assessment of the defect capture coefficient for charge carriers, the relation between electronic states of dislocation and both its

core structure and state of decoration. The answers to these questions can possibly be provided by the use of additional correlating techniques such as the electron beam based DLTS (deep level transient spectroscopy) method, (Lang 1974), especially the scanning - DLTS, (Petroff and Lang 1977; Breitenstein 1982; Breitenstein and Heydenreich 1983), or from observations of the temperature dependent EBIC contrast (Kimerling et al. 1977, Ourmazd et al. 1983). A more thorough survey of the combined uses of the EBIC method with other SEM and TEM based techniques was carried out by Heydenreich et al. (1981).

The progress in the EBIC technique was also accompanied by the development of microscopic theories of recombination through dislocations. Recently, such completely theoretical models were proposed by Donolato (1978, 1979 a, 1979 b), for charge collecting Schottky barriers and Pasemann (1981, 1982), for the p-n junction case. Donolato's theory considers dislocations as line sinks for minority carriers. Their effect is represented by introducing a cylinder of radius r, round the dislocation line in which the minority carrier lifetime has a value $\tau' < \tau$, the bulk value. Computer simulation was used (e.g., Donolato and Klann 1980), to predict the contrast due to a dislocation on oxidation induced standing fault loops intersecting the surface and a tetrahedral stacking fault, for various values of the incident beam, etc. The results were in good quantitative agreement with microscopic observations. The theory was extended to the case of EBIC contrast profiles in STEM conditions by Donolato (1981). Quantitative measurements carried out by Toth (1981) on dislocations in Si

Schottky barriers were all in good agreement with Donolato's theory. Both theories interpret the EBIC contrast as combination of electrical properties of defect alone and influence of several "extrinsic" factors. The latter relate to the location of the defect in respect to a specimen surface and charge collecting junction, geometry of electron excitation volume, material parameters i.e., minority carrier diffusion length and surface recombination velocity. The result of the Donolato theory can be summarised in the form, (After Ourmazd et al. 1983):

$$C = \gamma \cdot F\,(L, Z_o, R_e) \tag{22}$$

where L is the bulk diffusion length, Z_o the defect depth and R_e the electron range. The factor γ then represents the recombination activity of the defect (line recombination velocity). The contrast expression (22) represents the so called first order approximation, since it implicitly involved only the equilibrium value P_o of minority carrier density (Donolato 1983). Higher order approximations concerning the use of the actual electron beam injected minority carrier density, have found consideration in Pasemann's theory, leading to better quantitative agreement with the experiment (Pasemann 1981).

2.7. Effect of Impurities and Core Structure on EBIC Contrast from Dislocations

The line recombination velocity (eq. (22)), is directly related to the line density of recombination centres N' (Kittler and Seifert 1981; Donolato 1983):

$$\gamma = N' \cdot \sigma \cdot V_{th} \tag{23}$$

where V_{th} is the carrier thermal velocity, σ represents the defect capture cross-section. Kittler and Seifert (1981) introduced a method for obtaining γ from experimental data. Since V_{th} is known, the experimental value of γ yields the value of the product $N' \cdot \sigma$. This allows the value of N' to be assessed provided some information about the nature of the recombination centres is available (σ). Equation (23) has been used by Kittler and Seifert (1981), to estimate the EBIC "detectability" limits for dislocations. They calculated that the minimum EBIC contrast usually observable ($\simeq$0.5%) corresponds to $\gamma/D = 0.03$, where D is the minority carrier diffusion coefficient. Assuming that recombination is through impurity states with $\sigma = 10^{-14}cm^2$ they obtained $N'_{min} = 200\ \mu m^{-1}$ which means that a dislocation needs at least one impurity recombination centre every 50Å to be observable in EBIC. If the recombination is only due to recombination centres at a clean dislocation with $\sigma = 10^{-16}cm^2$, the minimum line density becomes $N' = 2 \times 10^4\ \mu m^{-1}$. Since this value appeared to be too high, they concluded that really clean dislocations should be hardly detectable in usual EBIC practice.

This statement appears to be in agreement with many experimental observations. Marcus et al. (1977) and Kittler and Seifert (1981) have found some stacking fault tetrahedra in epitaxial layers which could not be detected by EBIC. The defects revealed different activities depending on the cleanness of the epitaxial process. In some cases originally inactive defects become visible after a short thermal treatment (Kittler and Seifert 1981). Henniger et al. (1980) have shown that from among grown-in dislocations usually considered as very clean ones, only specially produced dislocations in floating-zone silicon have no detectable EBIC contrast at room temperature which is altered even after a very short treatment at 600°C.

The evidence of impurity segregation on dislocations comes from direct observations. Marcus et al. (1977) found nickel in precipitates at stair-rod dislocations of stacking fault tetrahedra by X-ray analysis. Kawado (1980) observed precipitates at Frank partial dislocations in oxidation induced stacking faults. Dushman et al. (1979) investigated the effect of stacking faults on the electrical behaviour of CMOS integrated circuits in Si. Correlation of SEM EBIC and TEM observations showed that stacking faults intersecting p-n junctions were electrically active when they were impurity decorated. Heydenreich (1979) investigated a variety of Si device type specimens using the SEM EBIC and the TEM strong beam method to determine the nature of defects present. Examination of the same defects by the two methods showed that those segments of dislocations decorated with observable impurity particles gave EBIC contrast of 10 - 20% typically at room temperature. Those segments

not decorated gave no detectable contrast. All these observations suggest that dislocation activity may result from impurity segregation on dislocations rather than from the dislocation itself.

Blumtritt et al. (1979), provided evidence to show that impurity segregation, core structure and the type of dislocation are all important in determining the magnitude of the EBIC contrast. The observations were based on direct comparisons between usual diffraction contrast EM images of dislocations and corresponding EBIC micrographs taken from the same area. Defects were diffusion induced misfit dislocations produced by boron diffusion into phosphorus doped silicon substrates ((001) - orientated). It was shown that the "dark" contrast associated with 90° dislocation was accompanied by bright regions flanking it from both sides.

The presence of the bright contrast surrounding the dislocation was claimed to result from the gettering effect of the dislocation, so that in their neighbourhood, zones denuded of impurity atoms were formed. In relation to the fact that point defects (impurities) reduce the lifetime of minority carriers (and therefore the EBIC signal too), it was concluded that a denuded zone has a higher EBIC signal (bright zone). So that higher gettering efficiency of the 90° dislocation (higher decoration effect) was claimed to explain strong EBIC contrast on this type of dislocation.

Observations reported by Heydenreich (1981), were obtained from a sample comparable to that of Blumtritt (1979). Two types of dislocations were examined. Some of then were identified as screw

dislocations and revealed very weak contrast just above the limit of detectability (0.3 - 0.5%). The other type involved 60° dislocations identical to those observed in the previous reference. Two groups of 60° dislocations were recognised in respect of the strength of the EBIC signal produced; some with medium contrast 1 - 3% and the others with strong contrast 5 - 10%. All of the mentioned dislocations were found to be located at the same level below the sample surface.

Ourmazd and Booker (1979), studied the electrical behaviour of dislocations using the SEM EBIC method. The electrical activity of individual defects was related to the structure of the same individual defects as determined by the weak beam technique of TEM. The defects studied consist of edge dislocations, Frank partial dislocations and stacking faults present in the phosphorus - doped ($10^{19}cm^{-3}$) emitter region of a bipolar transistor. Comparison between SEM EBIC and weak-beam TEM images of the a/2 ⟨110⟩ edge dislocations showed that the EBIC contrast was always enhanced when the dislocations were dissociated indicating that increased electrical recombination efficiency is associated with the dissociated dislocations. The maximum contrast observed varied from 0.6% for dissociated segments of edge dislocation down to detection limit of 0.1% for undissociated parts. A narrow ribbon of intrinsic stacking faults separating the partial dislocations was found electrically inactive. For the Frank dislocations associated with the stacking fault defect the electrical recombination was increased when the dislocation direction changed from ⟨2 1 1⟩ to ⟨1 1 0⟩, even though the Burgers vector character of the dislocations was

maintained the same. The contrast changed from 0.15% to 0.5% at room temperature.

For all defects studied by weak-beam TEM, no evidence for impurity decoration was observed directly (down to 20 Å level). The changes in contrast have been attributed mainly to changes in the core structure of the dislocations.

2.8. The Temperature Dependence of EBIC Contrast on Defects

If the influence of geometry on EBIC contrast can be ignored (eq. (22) - factor F), then the EBIC contrast can be considered as a function of the defect capture cross-section (eq. (23)). The capture cross-section is in turn determined by the charge state of the defect i.e., the position of the defect energy level E_o with respect to the Fermi energy E_f and temperature: $C = C(E_o, E_f, T)$ or alternatively, $C = C(E_o, N_d, T)$ where N_d is the dopant concentration (Ourmazd et al. 1982). It is therefore possible in principle to deduce the position of the energy level associated with an individual defect by monitoring the variation of EBIC as a function of temperature and dopant concentration (Ourmazd et al. 1981, 1983).

Kimerling et al. (1977) have demonstrated that as the temperature is reduced from 278 to 82 K, stacking faults in silicon become more efficient recombination centres. At high temperature, only the bounding partial was still found to function as a region of recombination. From an analysis of the temperature dependence of the EBIC contrast it is possible to assign an energy level in the band gap to the various defects. The faults were estimated to introduce levels in the upper half of the gap about 0.1 eV below the edge of the conduction band, whereas partial dislocations were calculated to introduce levels lower than 0.3 eV below the edge of the conduction band. In addition, precipitates such as SiO_2 were observed to function as microplasma sites at temperatures below room temperature.

Ourmazd and Booker (1979), and Ourmazd et al. (1981, 1983), studied experimentally and theoretically EBIC contrast on dislocations as a function of the dislocation type and the specimen temperature. They were able to observe a difference in the temperature dependence of the EBIC contrast for dissociated and for undissociated dislocations indicating different recombination mechanisms for these two cases. Such differences were found for both edge and screw (Ourmazd et al. 1983 a, b) type dislocations. It was found that the standard theories are unable to describe correctly the temperature dependence of the EBIC contrast. The assumption that the bulk minority carrier diffusion length is constant thoughout the sample was suggested to be the possible reason causing the dissagreement between the theory and the measurements.

2.9. Resolution Limits for the SEM EBIC Method

For the SEM EBIC investigations the planar junction geometries are usually employed. This involves both p-n junctions (Fig. 1(b)) and Schottky barriers (Fig. 1(d)). When the image of a defect is represented by a dark spot or line the resolution w is usually taken equal to half of its maximum width (Donolato 1979; Blumtritt and Gleichmann 1977). EBIC scan lines like those represented in Fig. 2(a), are used for the assessment of w.

The spatial resolution achievable depends on several factors, i.e. spot size d, generation volume represented by R_e, charge carrier diffusion length L, location of the defect in respect to the specimen surface and the charge collecting junction (Fig. 2(b)).

The SEM can always be operated so that the spot size is very small thereby not limiting the resolution.

The influence of R_e and L on EBIC contrast and resolution has been determined theoretically by Donolato (1978, 1979 a, b). Donolato's model applies mainly to Schottky barriers and shallow p-n junctions but in its basic lines can be applied to other collection geometries. Donolato's results for a dislocation perpendicular to the surface (1979 a, b) show that the image width of the defect decreases with R_e and that w can be well approximated by the value of R_e itself. This is in agreement with the experimental finding by Leamy et al. (1976). Contrary to the intuitive notion, the influence of L appeared to be small. The computed image width

revealed only slight degradation with an increase in L. Donolato (1978) has computed contrast for a point defect located at distance Z_o below the sample surface. In this case the resolution was shown to be approximately Z_o for $R_e < Z_o$ and approximately R_e for $R_e > Z_o$. In addition, the contrast found was to reach its maximum value at $R \simeq Z_o$.

The influence of drift field E on the EBIC resolution was demonstrated by Leamy (1982). These results have basically verified the fact that the image resolution can be directly expressed by R_e, even in the presence of electric field. In accordance with expectation the contrast C was shown to be most sensitively dependent on E being reduced drastically with increase in E.

Since factor w depends most strongly on R_e, the resolution can often be significantly improved when the beam voltage is reduced. Depending on the experimental arrangement employed, resolutions of the order of 0.1 um are commonly reported (Varker and Ravi 1977; Schick 1981).

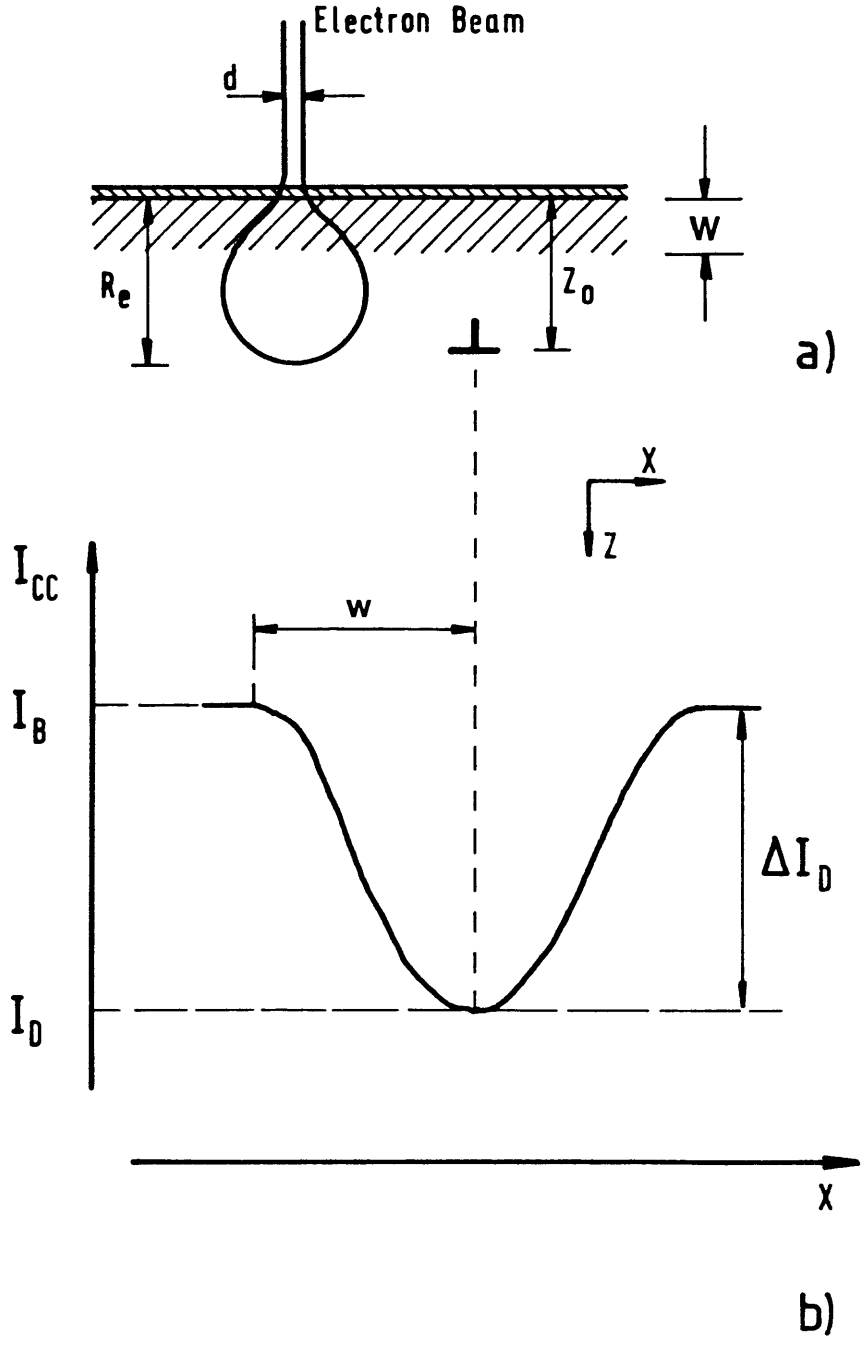


Fig. 2 - Schematic representation of EBIC contrast ΔI_D and resolution w as observed in Schottky barrier geometry shown in Fig. 1(d).

2.10. Microplasma Instability in Silicon

Carrier multiplication by impact ionization is now known to be one of the principal mechanisms causing electrical breakdown in reverse biased semiconductor p-n junctions. Since the early work by McKay (1954), the avalanche breakdown by impact ionization in high electric fields has been studied extensively and its main characteristics are well understood (for review see H. Kressel (1967)). The avalanche breakdown in silicon diodes can be associated with two different situations. Firstly, it can occur through very small defective areas of reduced breakdown voltage. The mechanism of formation of these local breakdown spots has been considered by Rose (1957), who gave them the name of microplasmas. The second kind of breakdown occurs in the absence of microplasmas and is distributed uniformly over the whole junction area and was first observed by Batdorf et al. (1960). The most characteristic symptoms of non uniform p-n junction breakdown are:

(1) "Soft" reverse bias I-V characteristics of the form of $I \alpha V^m$ whose n is a constant, $3 \leqslant m \leqslant 7$ typically (Goetzberger and Schockley, 1960).

(2) Light emission in discrete spots.

(3) Large amplitude fluctuations of the current in the breakdown region.

The soft I-V characteristics are usually associated with metallic precipitates in p-n junctions.

If the junction is sufficiently close to the crystal surface, the microplasmas can be seen as a pattern of light emitting spots. The subject of light emission from back-biased junctions is closely related to the general area of electroluminescence in semiconductors (reviewed by H.K. Henisch 1962). It was shown by Chynoweth and Pearson (1958), that as the avalanche current increases, the number of light spots increases in proportion, while their individual intensities were essentially unaltered. It was found that the spotty emission observed could be correlated with dislocations although only a small fraction of the dislocation sites emitted light. The distinguishing feature of this light emission in silicon is its broad spectrum with maximum at about 1.1 eV and the extensive tail reaching 3 eV (Chynoweth and McKay 1957). The presence of the high energy tail was explained in terms of the recombination of hot electrons and holes having energies up to the ionization energy.

When the reverse bias applied to a p-n junction approaches the onset of avalanche breakdown, the current passing through the junction often exhibits a characteristic form of noise arising from the fact that the current is rapidly switching back and forth in a random manner between two distinct levels. The average "on" and "off" times depend on the net current through the junction. The first sign of microplasma noise is a few narrow rectangular pulses of current of amplitude of 25-100 μA, randomly distributed in time. As the average current is increased these pulses become both longer and more numerous until the point is reached where the microplasma current is on as much as it is off. Further increase in the current

achieves the situation where the microplasma current is on for a greater fraction of the time than it is off, the "off periods" becoming steadily fewer and widely separated. Eventually, the current becomes essentially quiet again, corresponding to the condition where the microplasma remains "on" indefinitely. Further increase in the avalanche current causes a steady rise in the current carried by the microplasma that is limited by an effective resistance arising from mobile space-charge effects spreading resistance and microplasma heating (McIntire 1961). The observation of such imcroplasma cycles can be repeated as another microplasma is formed. Often the sets of noise for different microplasmas show considerable overlap.

2.11. Identification of Microplasma Sites in Silicon

The existence of microplasmas has been attributed to several causes. Evidently, the ionization rate is higher at the microplasma site than elsewhere in the junction. Two reasons for this have been suggested. Firstly, the electric field may be increased locally by the presence of impurities or as the result of junction curvature, and secondly, the threshold energy required for ionization may be reduced by crystal imperfections (Chynoweth and Pearson 1958).

It has been conjectured by Shockley (1961), that the sites of localised electrical breakdown in reverse bias junctions originate from the field enhancement caused by electrical precipitates such as SiO_2. He calculated the field concentrating effect of small precipitates. Shockley (1961), suggested that the effects were due to precipitates that occurred at some dislocations but not others. Microplasmas have indeed been found on dislocations by a number of authors, for example, Chynoweth and Pearson (1958), Goetzberger and Stephens (1961), Queisser and Goetzberger (1963). The practical problem was essentially solved by Goetzberger and Shockley (1960). It was shown that the slices of Si contaminated with Cu, Fe, Mn or Au and processed into p-n diodes gave devices most of which have soft reverse characteristics. It was shown that these harmful effects could be prevented or removed by "gettering". It was suggested that the harmful effect of the metal contamination was due to precipitates threading the junction and the gettering eliminated the precipitates. Only much later was TEM used to confirm directly the correctness of the interpretation (Cullis and Katz 1974).

Combined SEM and TEM studies showed that the precipitates could also form at the partial dislocations, bounding the oxidation and diffusion induced stacking faults (Ravi et al. 1973; Varker and Ravi 1974; Heydenreich et al. 1981).

The existence of high field sites was also related to extended precipitates acting alone, Augustus et al. (1980), observed $FeSi_2$ precipitates which were responsible for the electrical degradation of p-n junctions in bipolar transistors. Donolato et al. (1977), observed dopant impurities (SiP) in connection with local dislocation networks in n^+p silicon avlanche photodiodes.

Resistivity variations or striations in crystals have been shown to cause localised breakdown in Zener diodes (Varker 1971).

Junction non-uniformities caused by diffusion voids were also revealed to cause pronounced avalanche sites, (Gaylor 1966; Varker 1971).

From the data available it can be concluded that microplasmas are most often found to coincide with regions of crystal damage but evidently because those sites also act as nucleation centres for impurities. Dislocations or stacking faults as long as they are not decorated seem never to generate high field effects (Heydenreich et al. 1981; Ravi 1981).

2.12. Diffusion Induced Imperfections in Silicon

Among four common dopants (P, As, Sb, B), the effect of phosphorus and boron have been studied extensively in view of their widespread use as n- and p- type dopants in silicon. Phosphorus is most commonly used to form shallow n^+p junctions with a high surface concentration of the dopant. The high solute concentration imposed by shallow diffusion causes the generation of dislocations and precipitates in silicon. These are particularly undesirable in view of electrical parameters of devices based on shallow junctions.

The fundamental characteristics of diffusion induced dislocations were widely studied in the mid-sixties. The investigation techniques involved: X-ray topography (Schwutte and Queisser 1962; Rupprecht and Schwuttke 1966; Ghezzi and Servidori 1974), chemical etching, (Joshi and Wilhelm 1965), transmission electron microscopy, (Washburn et al. 1964; Jaccodine 1964; Joshi and Wilhelm 1965; Joshi 1965) and the SEM charge collection mode (Lander et al. 1963; Czaja and Patel 1965; Czaja 1966 a). The general characteristics of diffusion induced dislocations can be briefly described as follows:

The dislocations form as a network that is essentially planar and parallel to the diffusion front and hence crystal surface. These dislocations are generally of edge character with Burgers vector of the type a/2 <110>. A unique feature of these dislocations is that a majority of them are confined to a planar region within the crystal. It is typically observed that the network occupies a

position roughly one third to two thirds of the distance of the p-n junction from the surface (Levine et al. 1967). The dislocations induced in the course of the diffusion process move in and interact to produce networks of forms consistent with the symmetry of the Si slice. That is, rectangular crossed grides are formed in (001) sliced wafers (Washburn et al. 1964) and triangular (Ghezzi and Servidori 1974) or hexagonal mesh networks in (111) oriented slices (Joshi and Wilhelm 1965; Ashburn et al. 1977; Ravi 1981).

The generation of dislocations in the crystal as a result of diffusion can result from several causes. The general phenomena can be divided into homogenous and inhomogenous factors.

Attention was mainly devoted to the homogenous nucleation process. In this case lattice parameter variations accompanying gradients in the solute concentration cause internal stress in the crystal; if this exceeds the yield stress then plastic relaxation introduces a network of dislocations (Czaja 1966 b; Prussin 1961). The stress generated by the diffusing atoms has been postulated to generate dislocations and move them from the surface to a distance within the crystal at which point the diffusional stresses are reduced to zero. The integrated excess concentration of the dopant required to exceed the yield stress of silicon has been derived by Czaja (1966) and for phosphorus in silicon was found to be about $4 \times 10^{20} cm^{-3}$, assuming a complementary error function impurity profile. The experimental value was found to be about half of this (Czaja 1966). The importance of the degree of atomic misfit was explored by Joshi and Wilhelm (1965). They studied the structural differences between

arsenic and phosphorous diffused silicon. On the basis of atomic radii P and B atoms are undersized in silicon whereas As is almost the same size. In both cases of doping, high surface impurity concentrations were used ($\sim 5 \times 10^{20} cm^{-3}$). The TEM investigations gave evidence of the presence of dislocations and percipitates in P - diffused samples. The As - diffused specimens revealed an absence of any significant amount of dislocations.

Among diffusion induced imperfections solute precipitates are the most important besides dislocations. When the concentration of the diffusant in the solid exceeds the solid solubility limit at the diffusion temperature, the excess diffusant precipitates in the form of the element or a compound with silicon. Since the concentration of the diffusant is generally highest at the silicon surface, precipitation effects are confined to the surface and the near surface regions of the wafer. The precipitation of phosphorus in the form of silicon phosphide has been studied in detail (Servidori and Armigliato 1975). A direct indication of the occurence of precipitation is the observation that the amount of electrically active phosphorus is less than the total phosphorus content of the diffused layer. At concentrations above 10^{20} atoms/cm^3 the excess phosphorus is in the form of precipitate and is electrically inactive (Tannenbaum 1961). The precipitates form as fine needle shaped features of base-centred orthorombic structure and are elongated along ⟨110⟩ directions (Servidori and Armigliato 1975). The heterogenous factors governing the generation of diffusion induced imperfections in silicon involve the effects of pre-existing defects. These are the effects of concentration of stress localised

at surface inhomogenities like precipitates, scratches and cracks. In this case, the correlation between the dopant concentration and the presence of dislocation lines is not significant. The influence of the heterogenous factors on the diffusion process was widely discussed by Ravi (1981).

2.13. Dislocation Retarded Phosphorus Diffusion Effect

The first microscopic observation of the retardations caused by the diffusion induced dislocations was reported by Duffy et al. (1968). It was found that the diffusion of phosphorus is enhanced when the surface concentration of phosphorus is not high and a small number of dislocations were induced. However, when a very high concentration of phosphorus diffused into Si was involved and a large number of dislocations was induced then the letter reports that the diffusion was retarded at the sites where diffusion induced dislocations exist. In practical terms reduced junction penetrations were produced and the junctions were then not flat but "ragged".

The possible mechanisms explaining retardation phemomenon were discussed. It was suggested that the diffusion induced dislocation may modify a strain enhanced diffusion mechanism which is still operative below the ragged junction regions. An alternative suggestion was that the diffusion induced dislocation and precipitates may reduce the effective mobility of the diffusing atoms by providing precipitation sites for some phosphorus atoms. The retardation phenomenon was studied on bevelled and etched sections of P-diffused Si transistors.

Similarly prepared cross sections of transistor type structures were studied by Yoshida and Kanomari (1970). The retardation effect was observed under changing doses of boron and phosphorus diffused during subsequent fabrication stages to produce base and emitter

regions respectively. They found that the junction was not ragged when the diffusion induced dislocation does not reach the junction.

Ashburn and Bull (1979) studied Si transistors using the SEM EBIC technique. They observed bright contrast lines which they attributed to irregularities in the emitter base junction formed at 1.8 μm below the surface. These irregularities were ascribed to local retardation of the phosphorus diffusion at the points where the diffusion induced dislocations occurred.

3. EXPERIMENTAL METHODS

3.1. The Conductive Mode Detection System

There are two systems involved in this work and these are described as "Mark I" and "Mark II".

The Mark I was developed earlier in this laboratory. It provided BEVE I_{sc} and V_{oc} detection. On the basis of the experience gained with this CMDS an improved Mark II CMDS was designed and built as a major part of this research. It extends the capabilities of the previous system in several ways. For example, it has much lower noise levels, is more versatile, convenient and quantitative in operation. This is the system which was mainly used in this work.

A brief account of the Mark I design, the design principles of the Mark II detection system and its calibration factors will be presented in the following pages.

3.1.1. Design Requirements

The design principles of the versatile, quantitative detection system required for the CM work can be defined as follows:

There are several forms of signal obtainable from semiconductors in the conductive mode that can be quantitatively analysed. In order to detect each of these signals an appropriate circuit of the experimental set up must be ensured. This includes the provision of low and high input impedance amplifiers to detect BEVE I_{sc} and V_{oc} signals and the provision of facilities for detecting a β-conductivity voltage signal. A flexible system which would detect all forms of the CM signal is needed. In addition a fast method of switching the system in order to extract a desirable form of signal must be ensured.

Operation in the CM always involves a compromise between the signal-to-noise ratio and spatial resolution i.e., the resolution is often significantly improved when the beam voltage is reduced, the limit then being set by the minimum signal detectable. The prerequisite for this kind of work is a precision amplifier, capable of sensing low level current and voltage signals. The essential parameter determining the performance of this amplifier is the noise arising within the circuit which can be minimised by the special design of the detector. Basically, there are two

different types of noise in the circuit. Inherent noise is a function of a particular amplifier and can be influenced by the choice of appropriate circuit components. Reduction in interference noise can be achieved by locating the "sensing" amplifier inside the SEM vacuum chamber, adjacent to the specimen stage. Signal amplification thus occurs initially before noise pick up in the cable to the external modules.

The CM signals obtainable from various materials and devices differ over several orders of magnitude. A set of calibrated gains is needed in order to cover all desirable sensitivity ranges.

For the purposes of micrography, quantitative work or visual examination, it is necessary to use a wide range of the electron beam scanning speeds. Thus, an accurately linear amplification of the CM signals in as wide a frequency range as possible is required. In other words, wide bandwidth, high slew rate detection equipment is needed in order to avoid signal distortions at any scanning speed applied. In contrast to this, Fig. 3 presents one of the CM detectors frequently used in the past. The battery increases the charge collection efficiency of the reverse biased junction. The a.c. - coupling is applied so the d.c. current from the biased sample does not overload the amplifier. This simple detector, however, has a disadvantage in that the low frequency components of the

signal are attenuated due to the filtering action of the passive components attached to the amplifier input. This arrangement proved useful for micrography in defect studies (Varker and Ravi 1974; Holt and Ogden 1976), however, it can not be used for quantitative analysis. Within the limitations imposed by the response characteristic of the amplifier itself, the main improvement can be made by applying direct coupling of an amplifier to a specimen. Discrete components interfacing the specimen either to the amplifier or to "earth" should be avoided. In this case the sample biasing can be accomplished directly through the amplifier circuitry either by applying voltage to the non-inverting input (Mark I) or by the use of "floating" power supplies (Mark II). The last method enables one to work with a very wide range of bias voltages (up to to several hundred volts). A d.c.- signal suppression can be provided by means of the back off current technique.

For micrography, some signal processing functions such as differentiation can be very useful. This is mainly for contrast enhancement.

It is essential for the quantitative work to have the CM system interfaced to the computer so that the data can be conveniently recorded and quickly processed.

The various functions and facilities of the system should be provided by different units and modules. Such a design

makes it possible to modify any constituent unit without changing the others. Thus, the system can be developed in response to experience and to take advantage of new integrated circuits and other components as they become available.

Suitably designed equipment is needed to meet the above requirements.

3.1.2. The Mark I Conductive Mode Detection System

The system consists of several interconnected modules represented in Fig. 5. The head amplifier is mounted inside the specimen chamber of the JEOL - 35 SEM close to the specimen stage as shown in Fig. 4. The rest of the modules are in an external rack mounted unit; the head amplifier and the rack mounted unit are electrically connected by means of a single multicore shielded coaxial cable via a port in the SEM specimen chamber. The head amplifier can be used as a current-to-voltage converter with low input impedance, or in 'voltage mode' as a unity gain voltage amplifier with very high input impedance. This is selected by a toggle switch on the top of the head amplifier. Two rotary switches vary respectively the back off current range and the feedback resistor and hence the amplifier gain in the current mode. The circuit diagram of the low noise head amplifier is shown in Fig. 6. The functions of the interface module are to provide the necessary supplies to the head amplifier and to connect the signal from the head amplifier to the intermediate amplifier and metering module. The back off current is injected into the inverting input of the head amplifier working in the current mode of operation and offsets a selected d.c. component of the current from the biased electron bombarded specimen. The display on the metering unit makes it possible to adjust to zero net current from the specimens. The intermediate amplifier is provided in

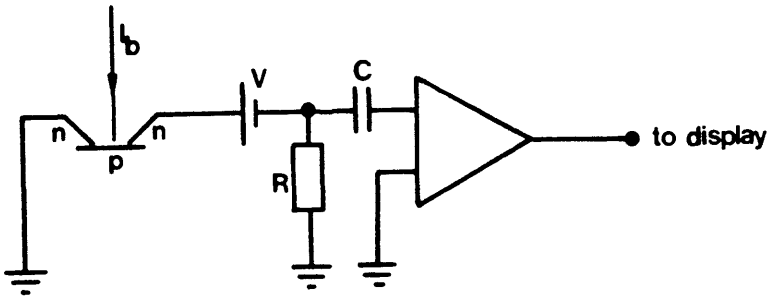


Fig. 3

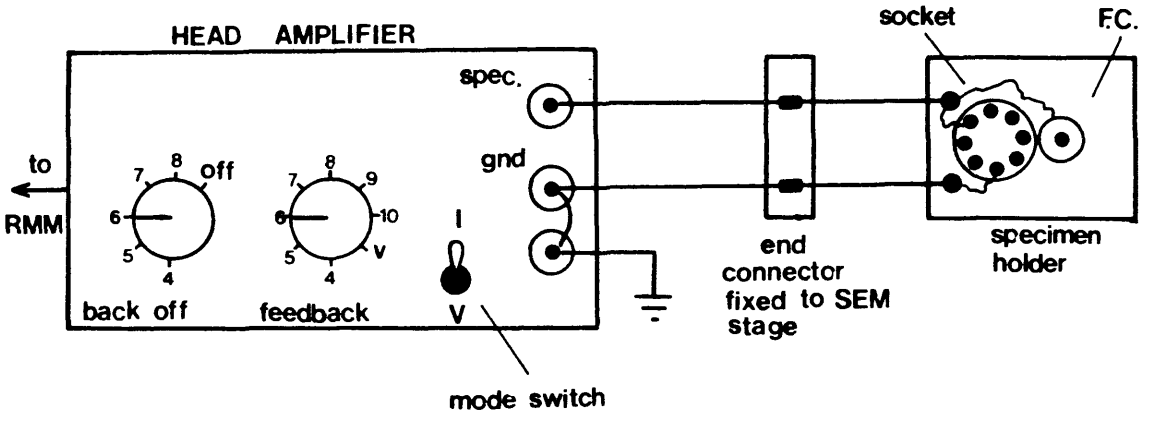


Fig. 4

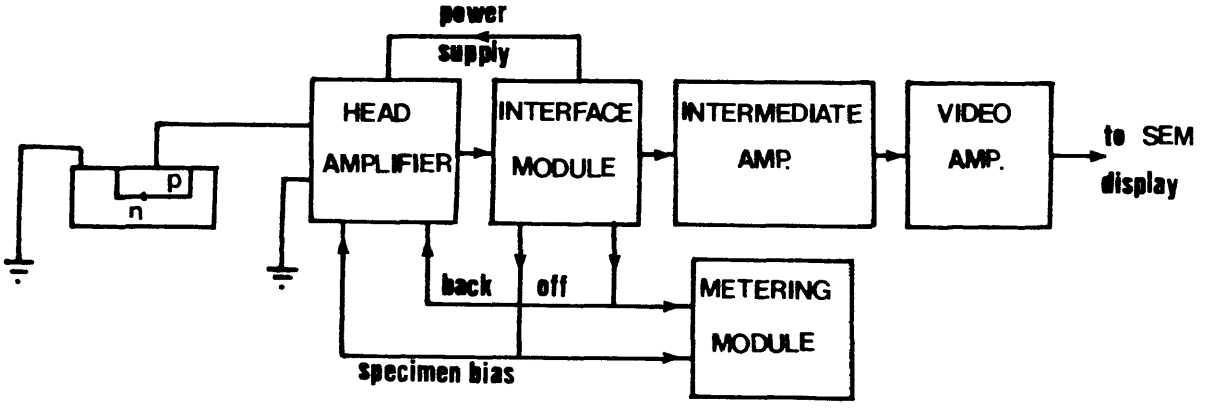


Fig. 5

order to select the optimum signal strength and contrast conditions for micrography. The minor voltages arising in the electronics of the rack mounted unit can be balanced out by means of the offset control provided in this unit. The intermediate amplifier also contains an inverting amplifier to invert the contrast on the picture and a low-pass filter with changeable bandwidth. The low-pass filter can be used to improve picture quality when there is excessive high frequency noise. The video amplifier can provide the final linear gain control or it can work as a differentiator with a changeable time constant. Differentiating the signal enhances the contrast of the micrograph and is used only for certain pictorial applications, e.g., to locate low contrast features prior to linear signal optimisation. The metering module provides a digital read-out of the specimen current or its logarithm or the open cicuit voltage from the specimen. The bias voltage and back off current can be read by selecting the appropriate switch position.

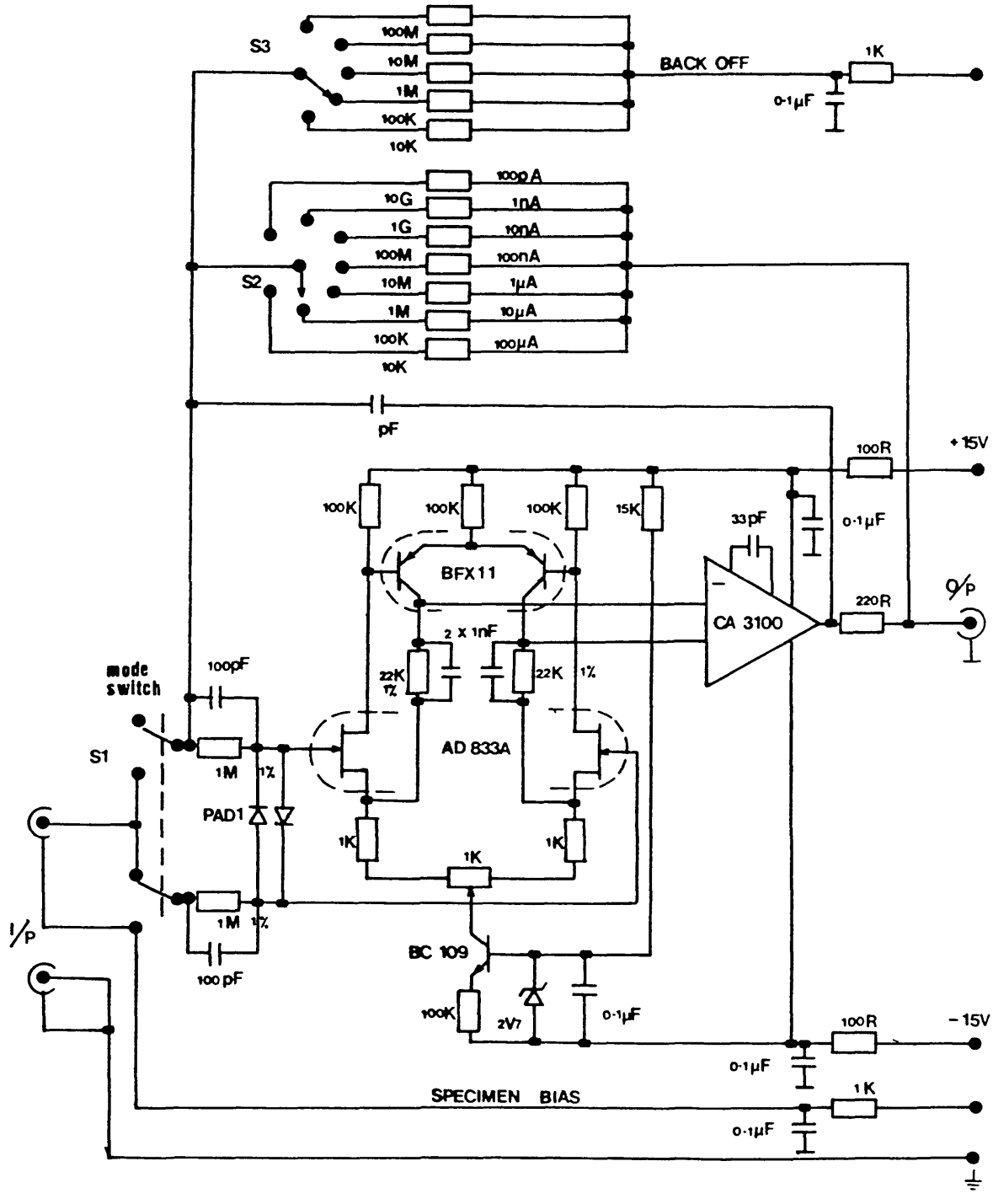


Fig. 6 - Circuit of the Mark I Head Amplifier.

3.1.3. The Mark II CMDS

The modular structure of the detection system is shown in Fig. 7.

The system consists of four modules. There is a head amplifier unit mounted through a port inside the specimen chamber of the SEM. It contains a current amplifier to detect either the BEVE or bulk EVE short-circuit current I_{sc}, or β-conductivity ΔV_{cc} signal. The voltage amplifier is used to detect BEVE or bulk open-circuit votages V_{oc}. The port mounted module includes other units attached to the outside of the specimen chamber port. These provide power to the head amplifiers and facilities to switch the current amplifier between its I_{sc} and its β-conductivity operational configuration and to switch from the current to the voltage amplifier. It also contains interface amplifiers, current back off and gain-switching facilities. The remaining active units are contained in a rack-mounted module. These are a signal processing unit and a metering and computer interfacing unit. The signal-processing unit can be switched to select linear amplification for most quantitative work or differentiating amplification with frequency filtering to enhance contrast and minimise noise for micrograph observations. Logarithmic and square root amplification can also be selected to obtain certain types of signal in immediately quantitatively interpretable forms. The

metering unit contains a digital multimeter to display the quantitative values of I_{sc} or V_{oc}, the back off current or the bias voltage. It also contains the interface which synchronises the work of the A-D converter at the digital multimeter with the external computer and the SEM scanning sequence.

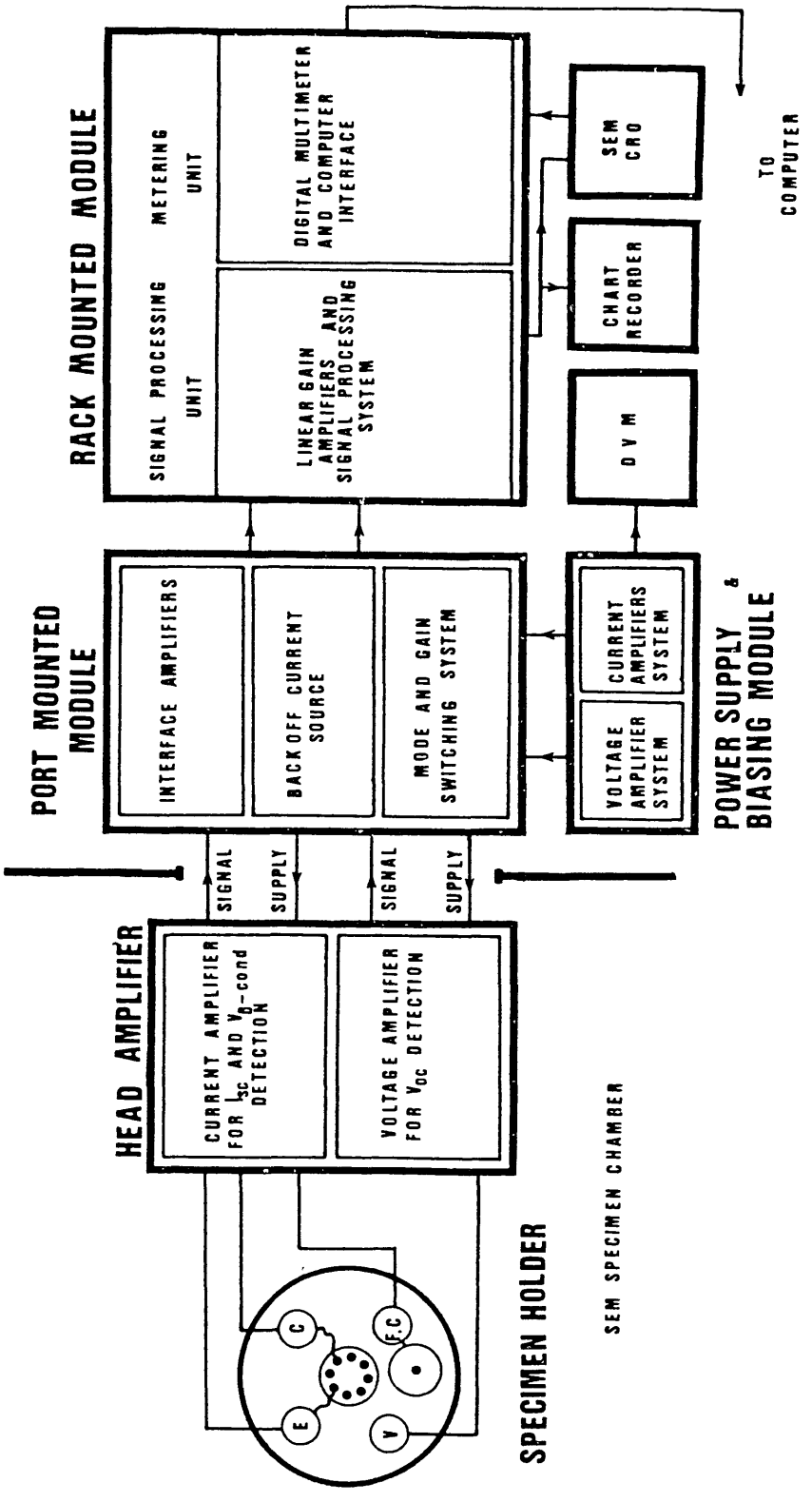


Fig. 7 - Block diagram of the Mark II conductive mode detection system. The specimen mounted on a TO5 header is inserted in the socket in the centre of the specimen holder. Appropriate contacts to the specimen material or device are connected via the socket to two of the terminals marked C, V and E to detect the chosen type of signal. For some purposes terminal E is earthed. The connections shown are those for detecting the short-circuit current or the β-conductivity voltage signal. The terminal FC is connected to a Faraday cage adjacent to the socket.

3.1.4. The Mark II Head Amplifier

This is the unit which ultimately limits the performance of the system. Fig. 8 is the circuit diagram of the head amplifier. This design is based on precision FET (field effect transistor) input, operational amplifiers of the AD515K and AD528K types which are the best for this application that are available at present. In particular, they provide very low bias currents (150 fA max in the case of the AD515K), have low input offset voltages, low drift and an excellent noise figure combined with a relatively high bandwidth (10 MHz in the case of the AD528K).

The head amplifier (H.A.) consists of three subunits. The first is used for open-circuit voltage detection. This is a very high input impedance non-inverting amplifier, marked A1 in Fig. 8, which involves the AD515K. This unit can work as a voltage follower (unity gain) or with a gain of 100 by means of relay S2. The protection of the input against the application of excessive voltages is necessary to avoid damage. Large input voltages can arise by the accidental positioning of the SEM electron beam on the input contact of this amplifier. The necessary protection is provided by the segment of the amplification circuitry that incorporates a 100 K resistor and a pair of low leakage diodes. These are of PAD1 type with a 1pA leakage current.

The other two subunits are the current amplifiers. One of

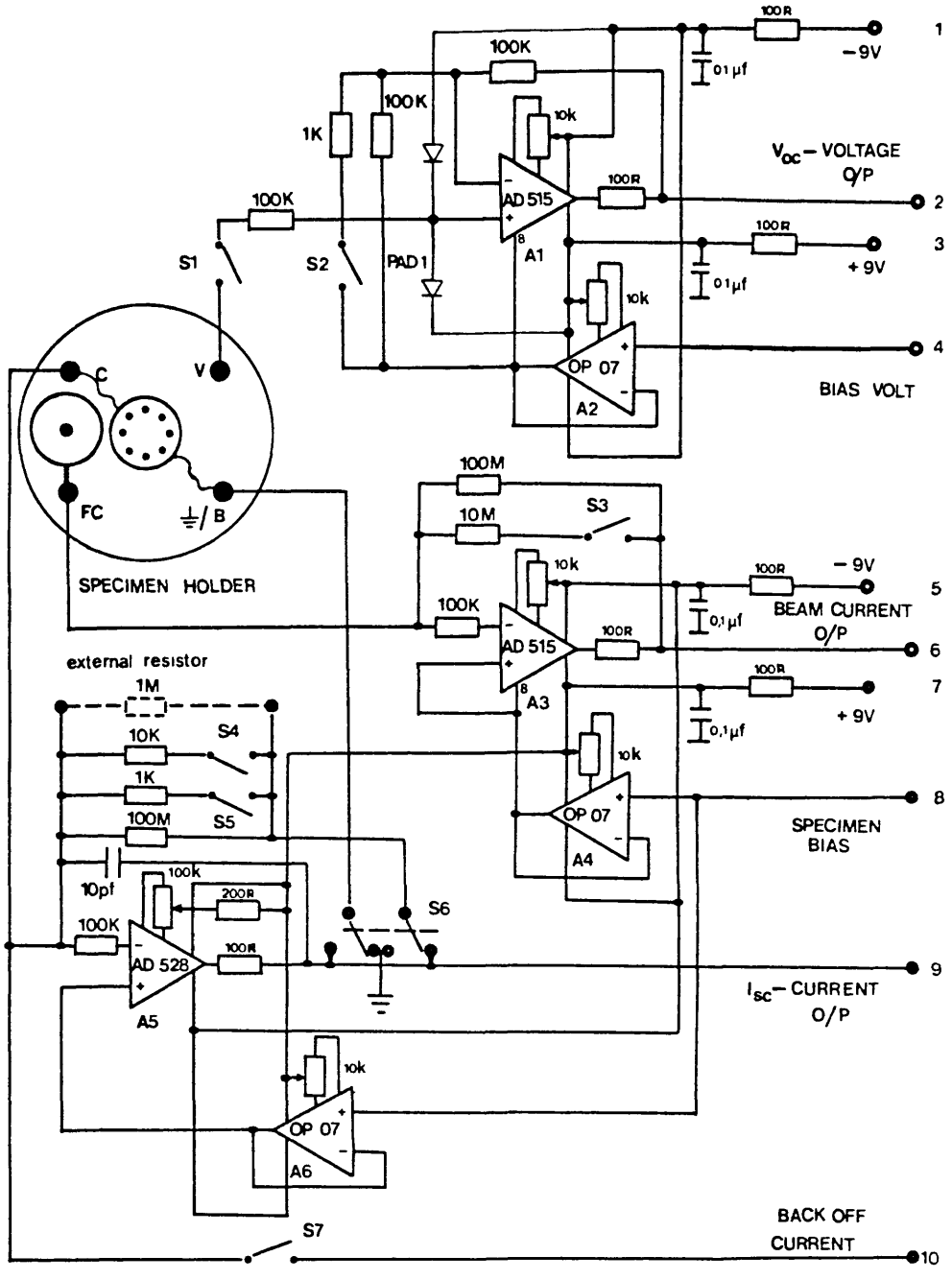
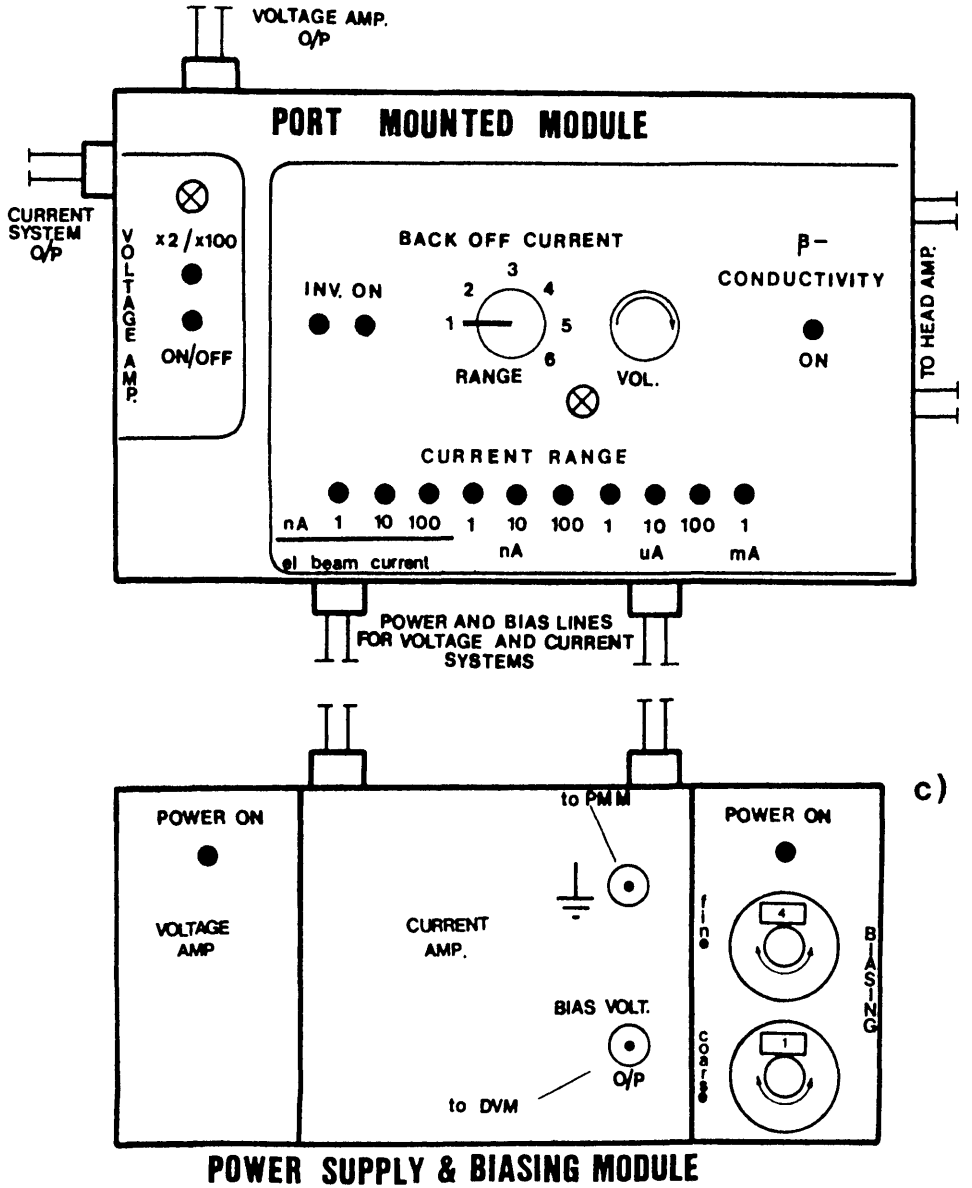


Fig. 8 - The head amplifier circuitry. The operation of portions of this circuit to detect the various forms of CC signal is described in the text and, schematically, in Fig. 11.

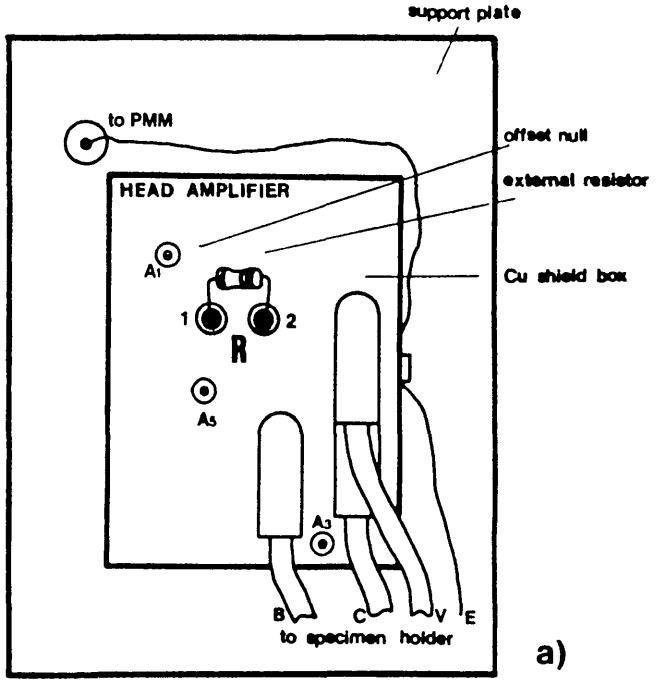
them, marked A3 in Fig. 8, is assigned mainly to the measurement of the electron beam current. The input to this unit is connected to a Faraday cage mounted on the specimen holder (Fig. 12). The sensitivity of this unit is set by the 10 M and 100 M resistors. It suffices for the most widely used range of electron beam currents which have a maximum value of 100 nA for the JEOL JSM-35 SEM.

The second current amplifier, marked A5 in Fig. 8, works in the range of nanoamperes up to 1 mA. It involves the fast AD528K op amp. The role of this unit is twofold. Firstly, it can work as a current amplifier to detect short-circuit current signals. The feedback resistor Rf can be selected from a set with the values of 1 K, 10 K, 1 M, and 100 M. These values suffice to enable the amplifier to cover all the current sensitivity ranges that have been found to be important. The 1 K, 10 K and 1 M resistors can be selected by means of relays S4 and S5. The 1 M resistor is fixed externally (Fig. 9(a)) at the special contacts provided at the front of the metal shield of the H.A. This external resistor works always in parallel to the 100 M one. In order to extend the sensitivity range to 10 nA or 1 nA the 1 M resistor must be removed. From the experience gained in using the Mark I detection system, it was found that only five current ranges were often used in the detection of short-circuit current from Si devices namely: 0 - 1 mA, 0 - 100 μA, 0 - 10 μA, 0 - 1 μA, and 0 - 100 nA. This applies in part because of the limited electron beam


VOLTAGE AMP. O/P
PORT MOUNTED MODULE
CURRENT SYSTEM O/P
VOLTAGE AMP.
x2 / x100
ON/OFF
BACK OFF CURRENT
INV. ON
RANGE
VOL.
β− CONDUCTIVITY
ON
TO HEAD AMP.
CURRENT RANGE
nA 1 10 100 1 10 100 1 10 100 1
el beam current
nA
uA
mA
POWER AND BIAS LINES FOR VOLTAGE AND CURRENT SYSTEMS
POWER ON
VOLTAGE AMP
CURRENT AMP.
to PMM
BIAS VOLT.
O/P
to DVM
POWER ON
FINE
COARSE
BIASING
POWER SUPPLY & BIASING MODULE

b)

c)


support plate
to PMM
offset null
external resistor
HEAD AMPLIFIER
Cu shield box
R
to specimen holder

a)

d)

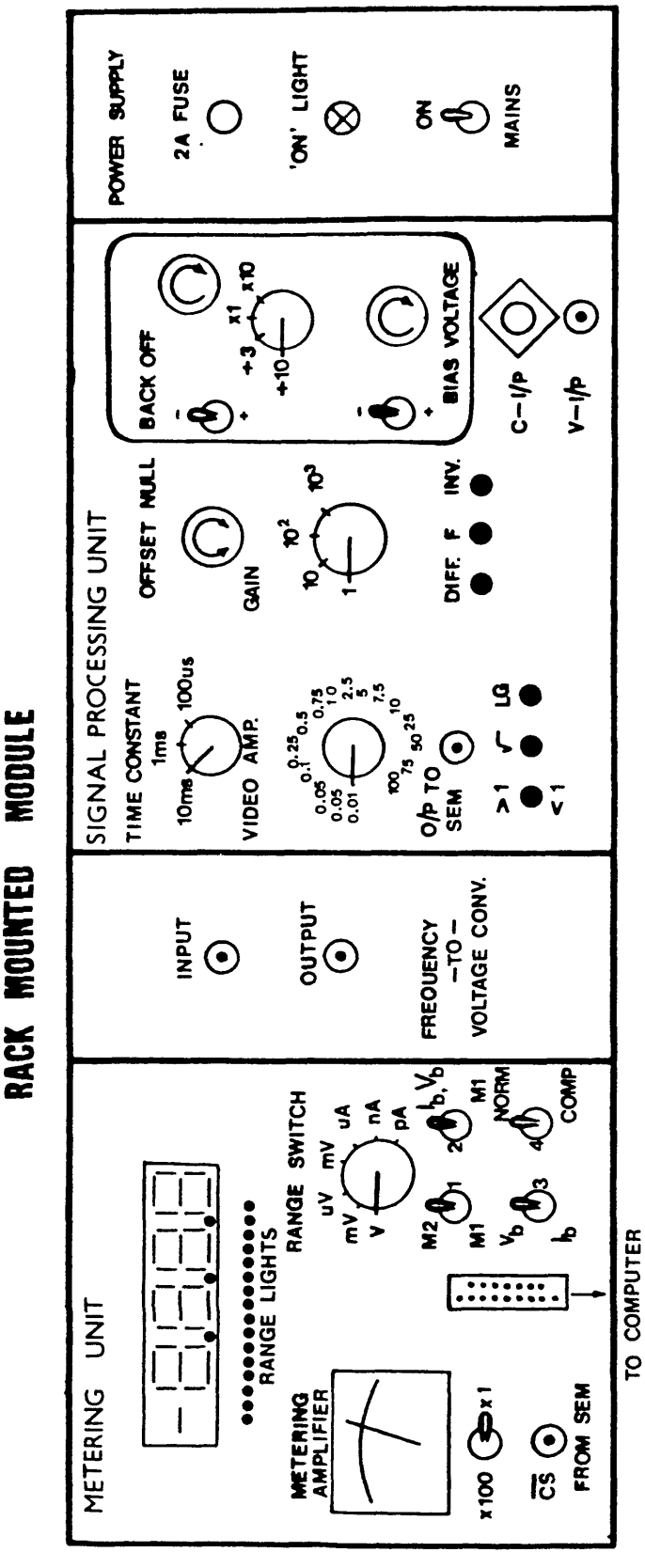


Fig. 9 - Panel controls: Head amplifier (a), port mounted module (b), power supply module (c), rack mounted module (d).

current of 100 nA max available on the JSM - 35. For this reason the 1 M resistor is normally attached to the external contacts of the H.A. (See Table 2).

Further amplification of the signal from the H.A. is provided by the even-value range amplifier (EVRA) in the port-mounted module, Fig. 10. This was designed to work with both the current amplifiers in order to provide a uniform output level for the current input signals corresponding to different current ranges.

Separate supplies were provided for the voltage and the current amplifiers of Fig. 8. An essential feature of this detection system is the application of the floating power supplies. The floating power supplies provide a convenient means for specimen biasing (current amplifier A5) and zeroing adjustment (current amplifier A3). Specimen biasing in the current mode of operation can be accomplished by the biasing circuit provided in the power supply module (Fig. 10). A d.c. bias voltage can range from -8 to +8 V. The input terminals of the amplifier remain at the potential of the power supply common so that common errors do not arise. Higher bias voltages can be used by applying a suitable voltage source externally to the terminal provided at the power supply module (Fig. 9(c)). The circuitry of the H.A., P.M.M. and power supply module were specially insulated to enable safe biasing up to 700 V. The final null setting of the current amplifier

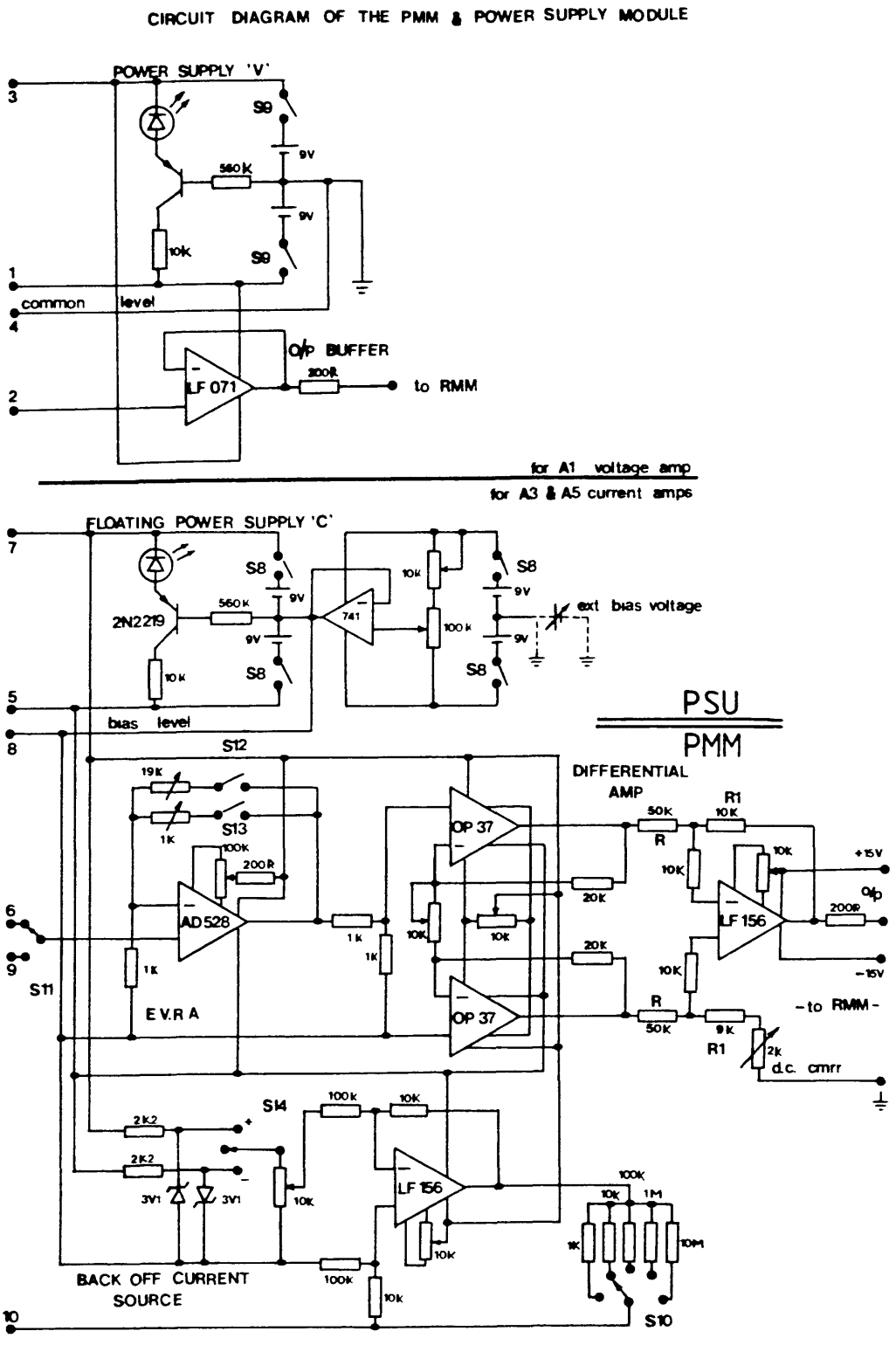


Fig. 10 - The port mounted module and power supply module circuitry.

A5 can be obtained by the selection of the appropriate back off current level. The back off current source and suitable current level and polarisation controls are provided in the port-mounted module (Fig. 9(b)).

The current amplifier A5 (Fig. 8) can alternatively be switched to work in "voltage" configuration in Fig. 11(d). This arrangement was designed mainly for the detection of β-conductivity voltage signals ΔV_{cc}, observable with constant current polarisation of the sample. The specimen provides the feedback R_s when the amplifier A5 operates in this configuration and R_f is switched to be the input resistor. The conversion from "current" to "voltage" arrangement of the A5 amplifier is completed by the relay S6 (Fig. 8). The detector provides a gain of unity and this is not affected by the ratio R_f/R_s as contrasted to the "current" configuration. Amplification of the signal is provided by the P.M.M. and R.M.M. modules. The R_f can be a value different from any of those given in the set in Table 2. It has to be matched to the actual feedback resistor R_s (sample) in order to ensure stability of the A5 operational amplifier, in general the condition $R_f \gg R_s$ must be fulfilled. The selected R_f replaced the externally attached 1 M resistor (Fig. 8, Table 2). The constant current biasing, essential for β-conductivity detection can be provided in two ways. Firstly, the floating power supplies of the A5 amplifier can be used to control the biasing current level (I_{B1} in Fig. 11(d)) within the

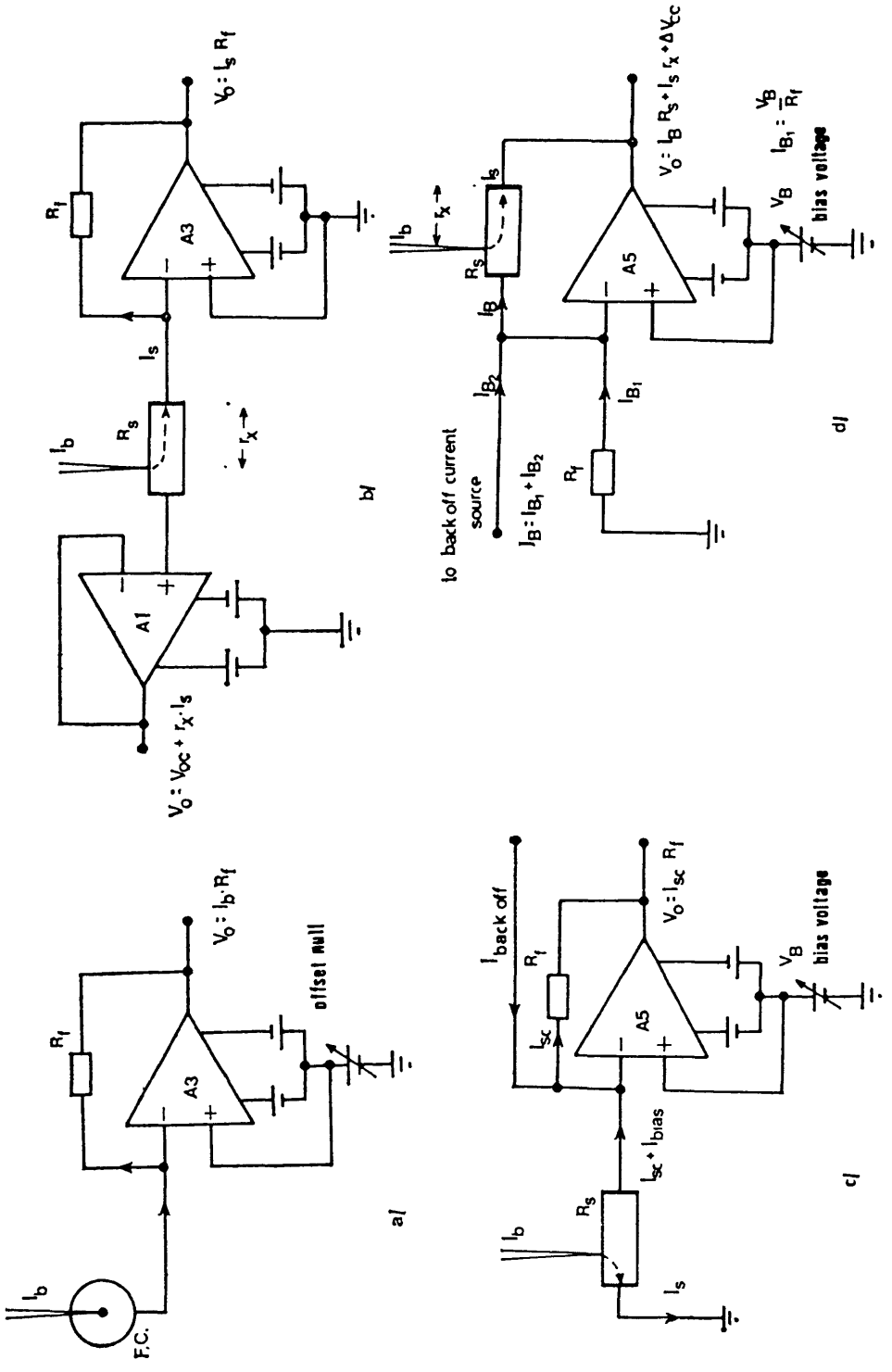


Fig. 11 - The principles of the operation of portions of the circuitry of Fig. 2 to measure (a) the beam current, I_b using the Faraday cage, (b) the open-circuit voltage, V_{oc}, (c) the short-circuit current, I_{sc} and (d) the β-conductivity ΔV_{cc}. I_s is the specimen, or absorbed electron, current to earth via a portion of the specimen. Either the back-off current, I_{B2}, or the current due to a bias voltage, I_{B1}, but not both, will generally be supplied. Hence I_B, the constant specimen bias current, will be determined by one or the other.

limit set by the resistor R_f i.e., $I_{B1} = V_B/R_f$. Alternatively, the back off current source can be used for specimen biasing (I_{B2} in Fig. 11(d)) and the appropriate current range and polarisation can be selected by means of suitable controls (Fig. 9(b), 10) provided at the P.M.M. In both cases the constant current forced through the sample can be quantitatively controlled. Although this detector has been assigned mainly for the observation of β-conductivity ΔV_{cc} signals, the same arrangement can also be used for the detection of bulk and barrier e.v.e. V_{oc}.

The voltage amplifier A1 measures V_{oc} together with the ohmic voltage due to the specimen current I_s, i.e., the current due to the electrons absorbed by the specimen from the beam, flowing to earth through a part of the sample marked r_x in the diagram. At the same time the current amplifier A3 measures the specimen current. The measured value of I_s can be used for correction of the observed value of V_{oc}.

The configuration used for detecting the short-circuit current I_{sc} and β-conductivity current signal ΔI_{cc}, is shown in Fig. 11(c). In this case the effect of the specimen current can be neglected since I_{sc} is generally $\gtrsim I_b$, the electron beam current.

The arrangement used for detection of β-conductivity voltage signals ΔV_{cc} is represented in Fig. 11(d). Two alternative ways of specimen biasing are indicated. The output voltage observed consists of three subcomponents.

TABLE 2. HEAD AMPLIFIER PARAMETERS

HEAD AMPLIFIER			PORT MOUNTED MODULE	
CURRENT AMPLIFIER	CURRENT RANGE	FEEDBACK RESISTOR	GAIN OF THE EVRA	OUTPUT VOLTAGE FROM THE PMM
	0 - 1 mA	10^3	1	1V
	100 µA	10^4	1	1
	10 µA	10^4	10	1
A5	1 µA	10^6	1	1
	100 nA	10^6	10	1
	10 nA	10^8	1	1
	0 - 100 nA	10^7	1	1
A3	10 nA	10^7	10	1
	1 nA	10^8	1	1

The β-conductivity voltage variations ΔV_{cc} are superimposed on a d.c. signal, the product of bias current I_b and sample resistance R_s, together with the ohmic drop due to the absorbed specimen current I_s, flowing through a part of the sample marked r_x in the diagram.

The operational amplifiers employed within the head amplifier (H.A.) circuits are devices which have a minimal initial offset requirement. However, all of them can be expected to exhibit temperature drift due to the vacuum environment of the H.A. box in the specimen chamber of the SEM. This of course eliminates conduction and convection by the atmosphere which would otherwise minimise electrical heating effects. Consequently, compensation required the measurement of the drift at the output of each operational amplifier in the circuitry, after the attainment of the equilibrium temperature reached in vacuum. These drift currents were balanced out using the potentiometers provided with all the operational amplifiers in the H.A. circuitry. There then remains only a slow drift that occurs over a long time due to small changes in the battery power supply voltage level. This can be reduced to zero by the adjustment of the back off current source provided in the port-mounted module.

The frequency response of each module was measured using a signal generator (Kröhn-Hite Model 2000) and a double probe oscilloscope (Telequipment Model D61A). The input and

output signals for the module under test were measured directly from the oscilloscope traces. The frequency response for each module is represented by the value of the break frequency. The frequency response for the H.A. working in the current mode i.e., so as to detect the short circuit current from the specimen, is expressed by its value of the unity gain cut-off frequency. This is the value for the A5 current amplifier. Amplifier A3 is used only for measurements of the electron beam current and so works in approximately constant current conditions. The results are collected in Table. 3.

The noise generated by the H.A. was measured for both current and voltage mode operation. Two sets of noise measurements are usually made. These are low-frequency noise for the range from 0.1 to 10 Hz, and wide band noise in the range from 5 Hz to 50 kHz. The noise measurement bandwidth was set by connecting a sharp cut-off bandpass filter to the output of the amplifier under test. The wide band noise is given by its r.m.s. value and was measured by connecting a true r.m.s. reading voltmeter after the filter. The results for both the current and voltage amplifiers are listed in Table. 4.

The observed results are in fair agreement with the values to be expected for the low noise operational amplifiers employed in the H.A. circuits. The measured low frequency noise corresponds precisely to the average values of the

peak noise given in the data sheets for both the AD515K and AD528K operational amplifiers. The measured wide band noise includes the calculated resistance generated noise which is caused by the passive components of these amplifiers, the resistive component of the sample impedance attached to the H.A. and the feedback resistor R_f. The actual bandwidth of the H.A. also has a direct influence on the noise performance. (Resistance noise E r.m.s = $4kTR\Delta f$ where f - represents actual bandwidth).

The calibration procedure involved also an evaluation of the corrections for the display and the metering module. The aim of this was to find the corrections necessary for the digital read-out of the metering module against known d.c. - currents and voltages supplied to the H.A. The corrections were required because of the combination of small gain errors caused by the amplifiers involved in linear signal processing in the head amplifier, port-mounted module and rack-mounted module. Each signal detection configuration of the H.A. required a separate set of corrections. The current mode of operation revealed the largest tolerances before correction. This was 1 - 5%. The use of correction factors determined in the calibration procedure provides measurement accuracy within the range 0.5%. This is for all modes and ranges of operation. A d.c. current calibrator type 609S made by Time Electronics Limited, was used for the calibration of the CMDS in the current mode configuration. The current range

TABLE 3. FREQUENCY RESPONSE RANGES OF THE MODULES OF THE MARK II C.M.D.S

MODULE		GAIN	BREAK FREQ	UNIT LIMITING THE BANDWIDTH
Head amp.				
current amp.	A5	1	3 MHz	
Voltage amp.	A3	2	460 KHz	
"	A3	100	10 KHz	
Port mounted module		1	3 MHz	Even - value range amplifier
		10	140 KHz	
Rack mounted module		1	5 MHz	input differential amplifier

TABLE 4. NOISE LEVELS IN THE HEAD AMPLIFIER UNITS

CURRENT AMP.	GAIN	INVERTING INPUT RESISTOR	LOW FREQ	HIGH FREQ	
			µV p-p	Observed µVrms	Calculated µVrms
A5	6.7	1.5 K	5.0	1.18	1.0
A3	10	100 K	4.0	13.7	12.9
A1	2	1 K	4.0	1.38	1.3

selected was first checked against a Keithley digital electrometer type 615. The source current was then fed to the current input terminal of the H.A. switched to its short circuit current detecting configuration.

This procedure was carried out for different ranges of sensitivity of the CMDS. For each range a number of measurements were made for different input currents. The corresponding read-outs from the metering module and the Keithley digital electrometer were used to determine the correction factor average for the particular current range. The calibration procedure for the system working in voltage mode employed a constant voltage source applied to the voltage terminal of the H.A. The voltage displayed by the metering module was compared to the value of the applied voltage measured with the Keithley digital multimeter. The constant voltage source used was a simple resistive voltage divider supplied from 1.5 V battery. The resistors were selected in order to match the output voltage to the required sensitivity range.

The difference between the β-conductivity voltage observed at the output from the head amplifier and the voltage displayed by the metering module arises from a combination of small gain errors in the units following the head amplifier. The calibration procedure involved the measurement of known voltages applied to the input of the even value range amplifier (EVRA). The read out from the

metering module was recorded. This was then compared to the accurate value displayed on the Keithley digital meter for the same input voltage.

The performance of the head amplifier in the β-conductivity configuration depends on the impedance of the actual sample and on the input resistor R_f. The H.A. should be calibrated after the external components are selected. This should include:

(i) Determination of the frequency response. This is done in order to estimate the maximum scanning frequency for the electron probe for which the β-conductivity signal will not be distorted. This can be important for samples having larger impedances.

(ii) Measurement of the resistance R_f. The accuracy of the nominal value of this resistor determines the error of the bias current since $I_b = V_b/R_f$. The β-conductivity signal observed at the output from the H.A. is directly proportional to the value of I_b.

3.1.5. Specimen Mounting

The specimen is mounted on a TO5 or a DIL mount and plugs into an appropriate socket in the specimen holder. This is shown for the specific case of TO5 mounted specimens in Fig. 12. Short, shielded cables are used to connect the head amplifiers to the contacts at the specimen holder.

3.1.6. Measurement of the Electron Beam Current

A Faraday cage with a cleaved silicon edge is exposed at the top of the specimen holder. This enables one to measure the beam current and beam diameter by the method of Joy (1976). The Faraday cage is shown in Fig. 13.

Fig. 14, presents an experimental profile taken over a Si edge for the most frequently used level of the electron beam current in JEOL - 35 SEMs i.e., 0.50 nA (this is for the CM work). The electron beam diameter was assumed to be the distance between 10% and 90% total signal points on the profile (approximately linear portion of the profile). The horizontal axis was calibrated by determining the magnification. The measured value of the beam diameter was 360Å (100 nm aperture was used).

A different approach was adopted for the situation when "hot" or "cold" stages were used. Due to the lack of space required for the Faraday cage to be fitted, the electron beam current was measured by means of a small copper wire covered with a coat of carbon and attached to one of the three terminals of the TO-5 header as illustrated in Fig. 15.

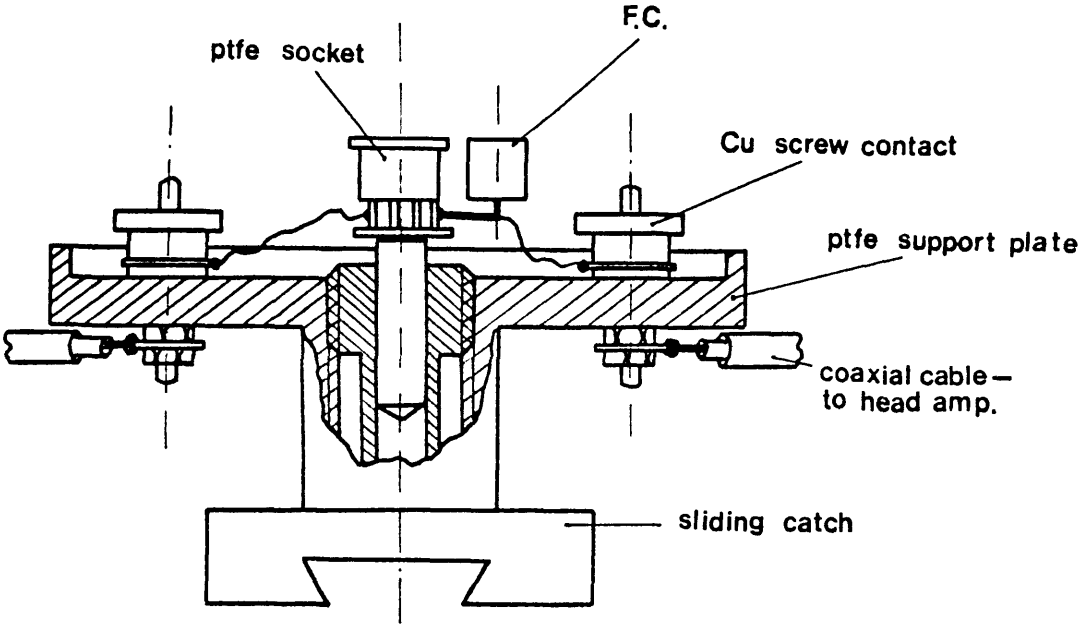


Fig. 12 - The SEM Conductive Mode specimen stage.

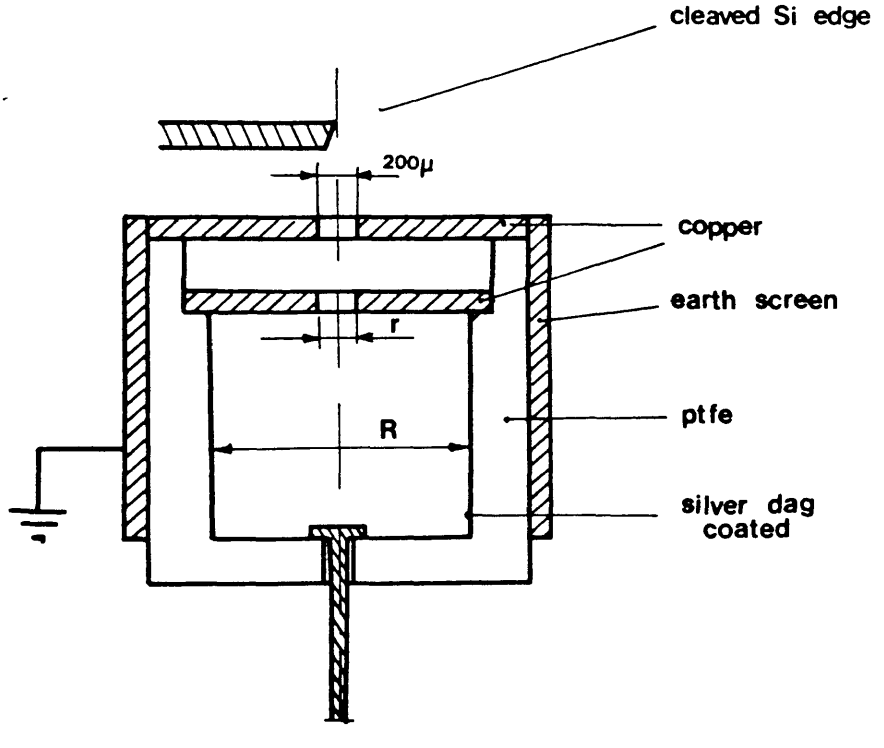


Fig. 13 - Schematic representation of the Faraday Cage.

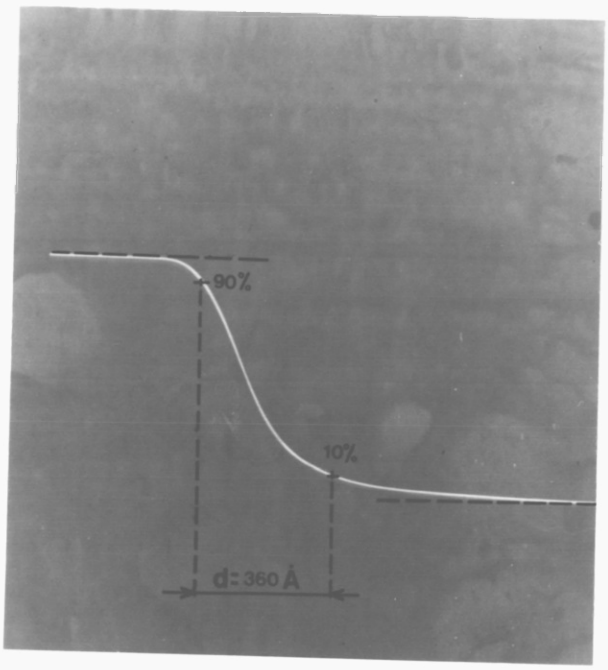


Fig. 14 - Electron beam scan line as recorded using the Faraday Cage.

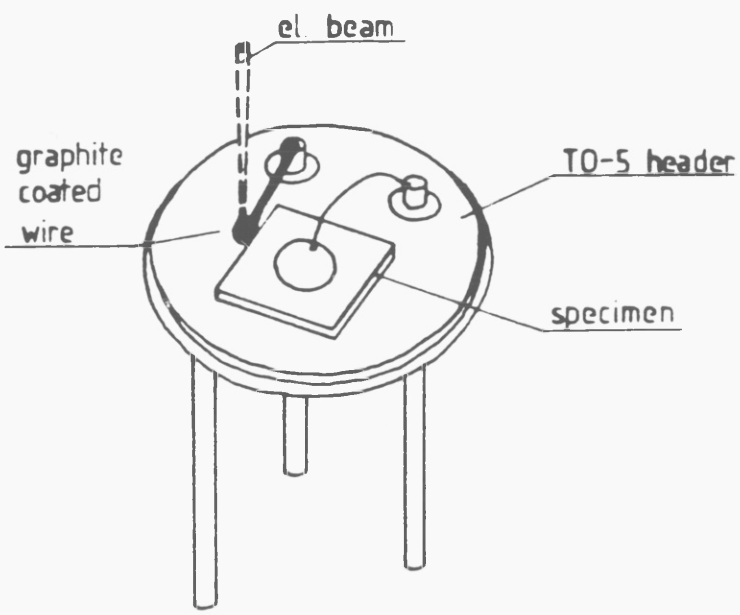


Fig. 15 - The arrangement used for electron beam current measurements adopted for "hot" and "cold" stages.

3.2. Discription of "Hot" and "Cold" Specimen stages for the SEM Charge Collection Mode

Both "hot" and "cold" stages described in this paragraph constitute a part of the Mark II CMDS design. They were constructed to facilitate the investigation into the temperature dependence of EBIC contrast of defects in Si avalanche photodiodes.

a) The "hot" stage is shown schematically in Fig. 16. It consists basically of four elements i.e., metal base, thermal insulation, thermal shield, and heater unit. The base (1) is made of duraluminium. It fits the slider catch of the SEM specimen platform (2). The base transits the specimen movement and provides the mechanical support for the heater unit (3). Both the base and the heater are thermally isolated by means of a silica tube (4) and alumina ring firmly attached to the base. The heater itself is a small rectangular plate made of dural. The plate contains a tungsten filament (6), its electrical contacts (7) and a thermocouple (8). A sample (9) is mounted upon the three terminal TO-5 header (10). The header fits into a shallow cavity at the centre of the heater plate. There are two miniature screws (11) provided to hold the TO-5 header in position and secure good thermal contact between the header and the heater. The heater rests on the top of the silica tube with the TO-5 plugged into a teflon socket (12) being attached to the alumina ring (5). The electrical connections to the sample, heater and thermocouple are provided by means of edge connectors, one being attached to the base

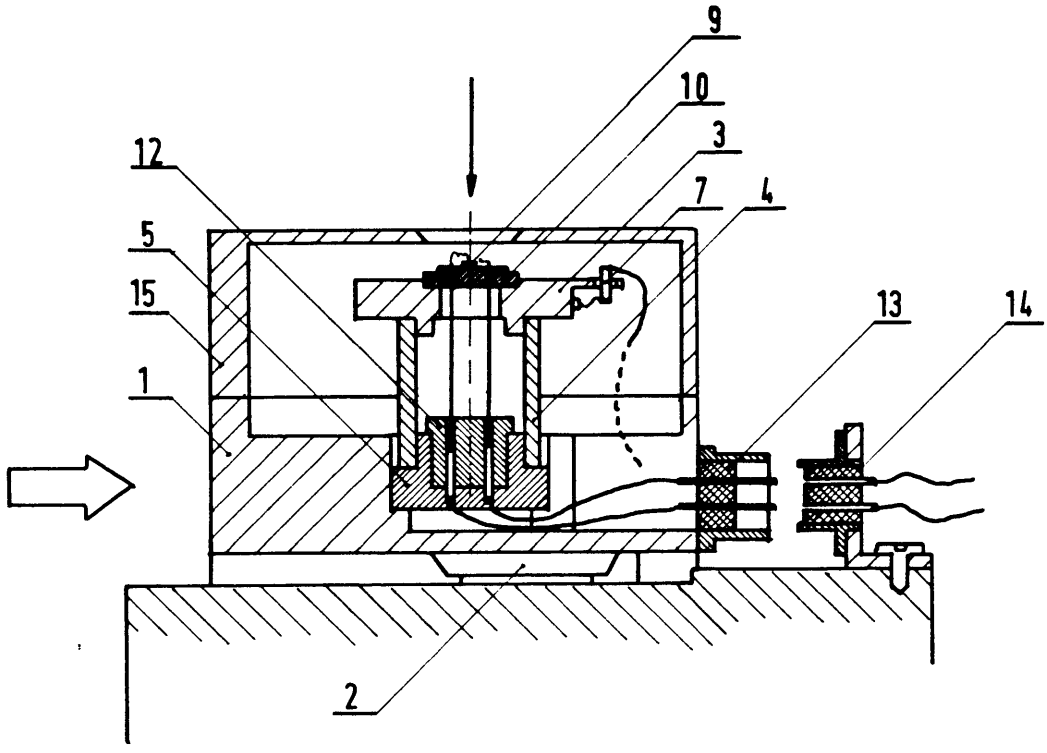


Fig. 16(a) - Cross Section of the "hot" specimen stage.

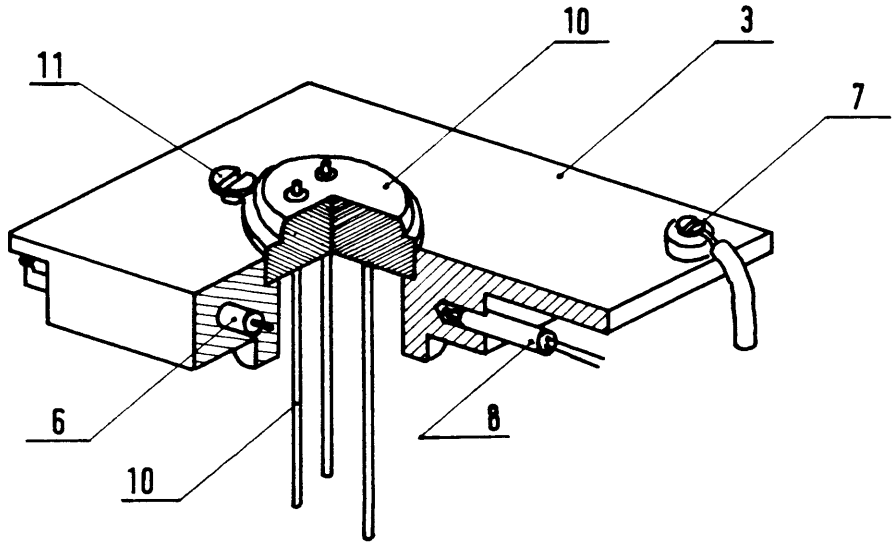


Fig. 16(b) - The Heater.

(13) and the other to the SEM specimen platform (14). The heater is operated from a variable high output current ($\sim$ 2 Amp) d.c. power supply. Power to the heater is provided through a feedthrough at the SEM port. The stage works up to 300°C without the need of cooling the base and the thermal shield (15).

b) The "cold" stage involves two separate units. Firstly, there is a liquid helium cooling assembly, originally used for the CL mode of operation (Holt 1981) and described briefly in point c) below. The other part is a special specimen stub-holder designed for the purpose of this work. The CC mode specimen stub-holder illustrated in Fig. 17, has a high thermal impedance and couples onto the cooling arm by pushing the specimen stub into a sliding block (1) which is thermally connected to the arm by sliding contacts. The holder itself consists of a metal base (2), (similar to that of the hot stage), metal rings (3,4), two PTFE sockets (5,6), PTFE spacer (7) and copper cup (8). The copper cup fits into the opening at the sliding block (1) and provides thermal contact between the sliding block and a TO-5 header (11) nesting a specimen (12). In addition, the cup protects the specimen against any mechanical damage (for example, when pushed up cautiously against the sliding block). To make the structure reasonably rigid and thermally well isolated, the PTFE socket (5) with TO-5 header and the base (2) are coupled together by means of two fitted silica tubes (16), arranged as illustrated in Fig. 18. The temperature is measured by thermocouple (13) placed

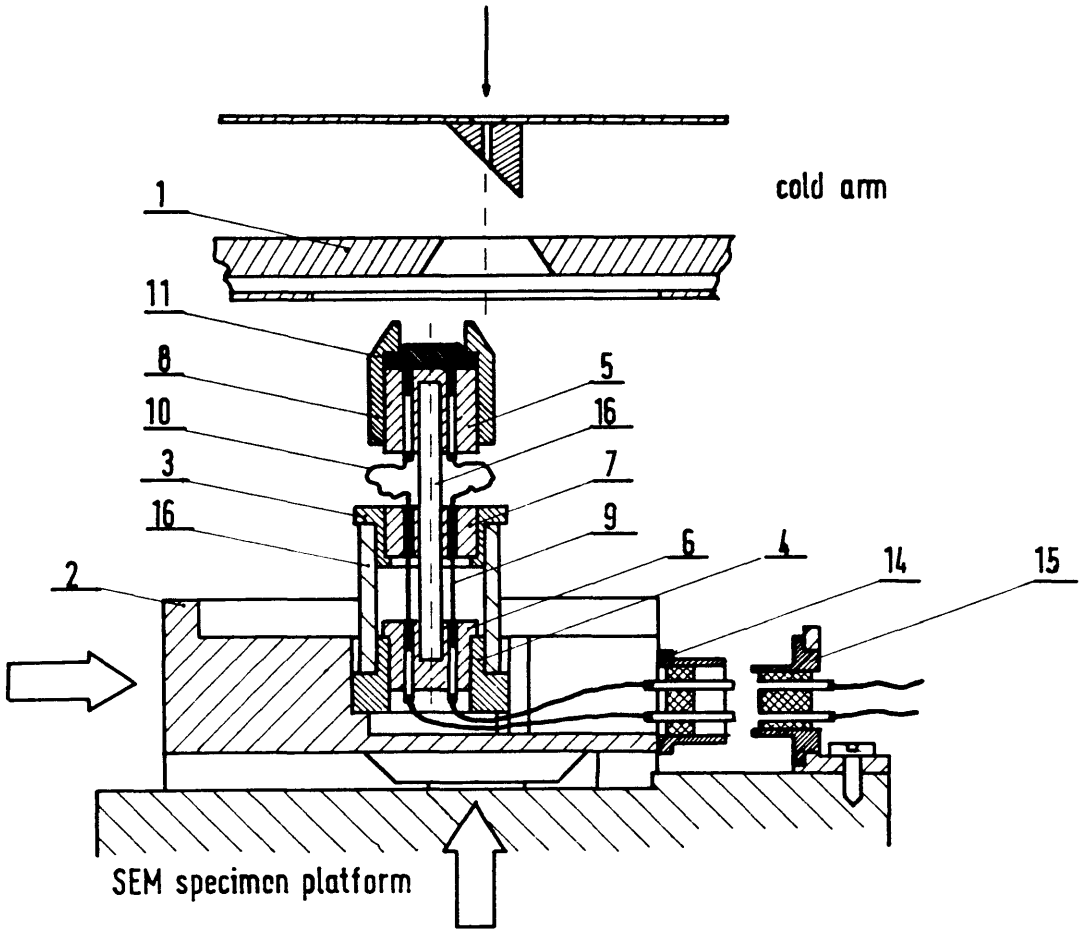


Fig. 17(a) - Cross section of the "cold" specimen stage.

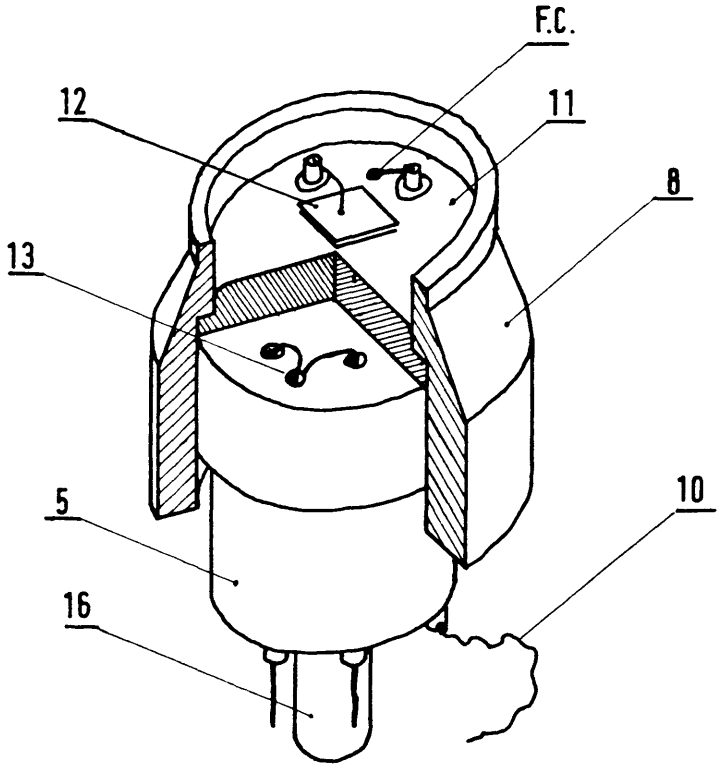


Fig. 17(b) - The Head Exchanger.

directly beneath the TO-5 header. The terminals of the PTFE socket (4) are connected to the base socket (5) by means of short copper rods (9) and very thin gold wires (10). The thermocouple and the base socket (6) are connected to the edge connector (14) provided at one end of the base (2), which then plugs to the matching connector fixed to the SEM specimen platform (15). The holder can be removed or inserted through the SEM airlock without the necessity of exposing the specimen chamber. Using this stage and liquid nitrogen as a coolant, instead of liquid helium, temperatures within the range from 77 K to 300 K were obtained when measured directly at the TO-5 header.

c) For low temperature CC observations a liquid helium stage was used. The stage was recently completed in our laboratory. It is based on an Oxford Instruments continuous flow crystat (CFC) system, shown in Fig. 18. The operation principle of the CFC system is based on the continuous transfer of a coolant (liquid helium) from a storage vesel to a vacuum insulated radiation shielded sample space. The pressure difference necessary to produce coolant flow arises due to the gas flow pump mounted in series to the storage vessel and the CFC. By controlling the flow of the coolant the sample temperature can be chosen within the range of the CFC, and held more accurately by controlling the electrical heater attached to the heat exchanger (at the very end of the crysostat). The flow and pressure in the helium return line are monitored on the flow controller. The temperature at which the system finally

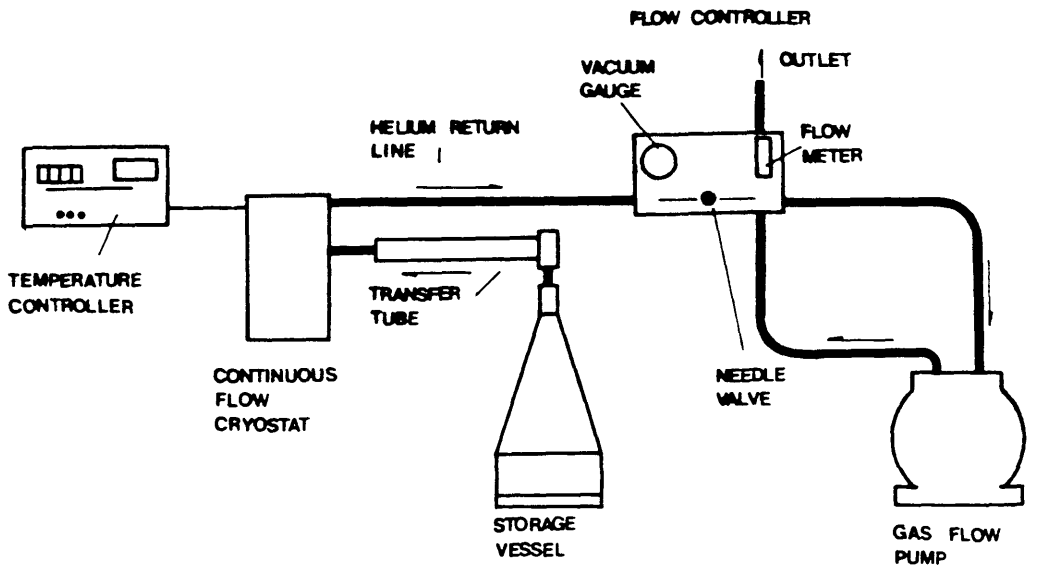


Fig. 18 - The Oxford Instruments temperature controlled, continuous flow liquid helium crystat.

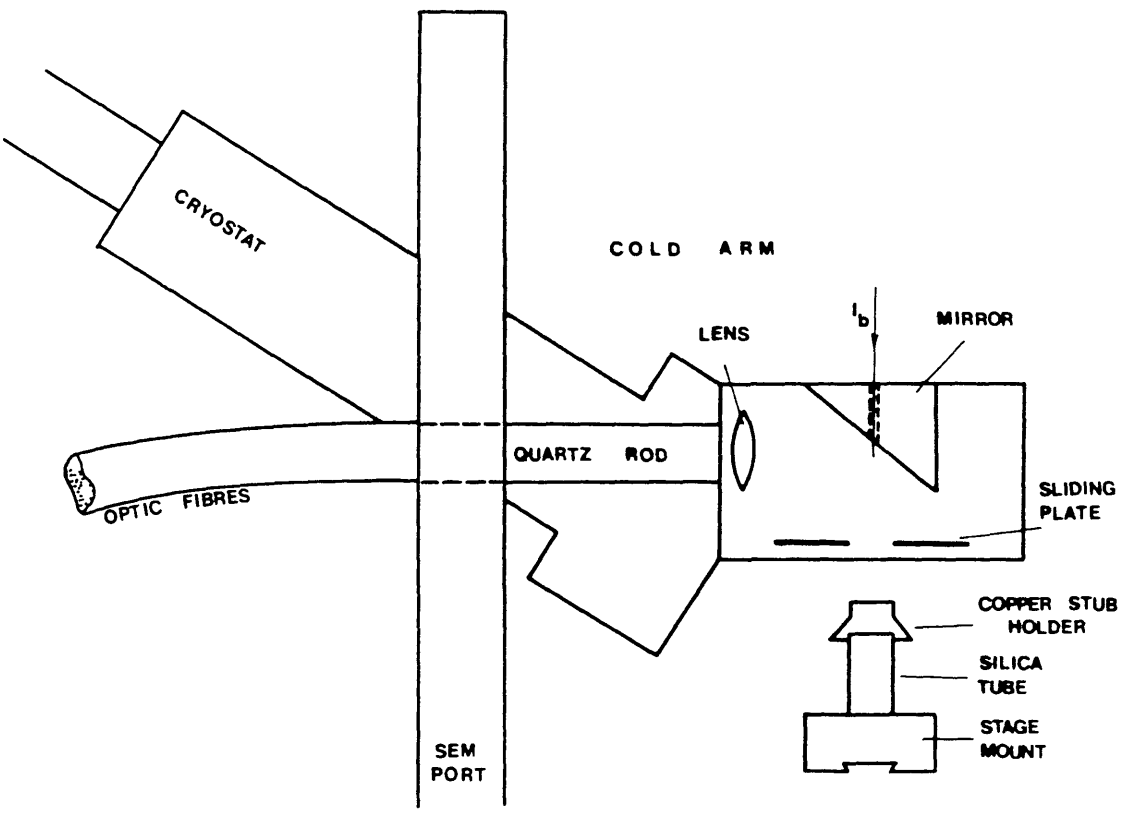


Fig. 19 - Schematic diagram of the liquid helium stage for SEM CL observations.

settles is displayed on the temperature controller and is measured by a temperature sensor (resistance thermometer).

The liquid helium stage is illustrated in Fig. 19. It is mounted on a side port of the SEM. The cold arm of the stage includes the specimen shielding box, a light collecting and transmitting device and contact plate. The specimen stub-holder has high thermal impedance and couples onto the cooling arm by pushing the specimen stub into a sliding plate which is thermally connected to the cold arm by a sliding contact.

The stage retains specimen movement in the horizontal plane and provides the ability to change specimens easily through the airlock provided at the SEM chamber.

3.3. A.C. Biasing Using the Mark II CMDS

The arrangement shown in Fig. 20 was designed to allow the study of the characteristics of the localised electrical breakdown in avalanche photodiodes APDs. The investigation was concerned mainly with measurements of the delay time which occurs between the application of an overvoltage (voltage above the diode breakdown level) and the actual starting of the avalanche discharge. When a waveform of sufficiently high voltage pulses is applied to the APD, the delay time can be obtained when both voltage and corresponding avalanche current waveforms are recorded and displayed simultaneously.

The Mark II CMDS is the central part of the experimental set up presented in Fig 20. It allowed small bias voltage pulses to be superimposed upon a high offset voltage (several hundred volts). Thus, the amplitude of the voltage pulses necessary to exceed the breakdown level of the APD was reduced to a minimum. In addition, the current back-off facilities available in the CMDS were readily used to subtract any d.c. component of the diode current, so that the avalanche current pulses could be separately amplified and displayed. The arrangement enabled the experiment to be performed inside the SEM specimen chamber. Hence the results could be immediately correlated with EBIC observations.

The d.c. bias was obtained from a stabilised supply. The voltage could be varied up to 500 V. This was stable to within 1%. The d.c. bias was applied to the diode through the vacuum feedthrough at

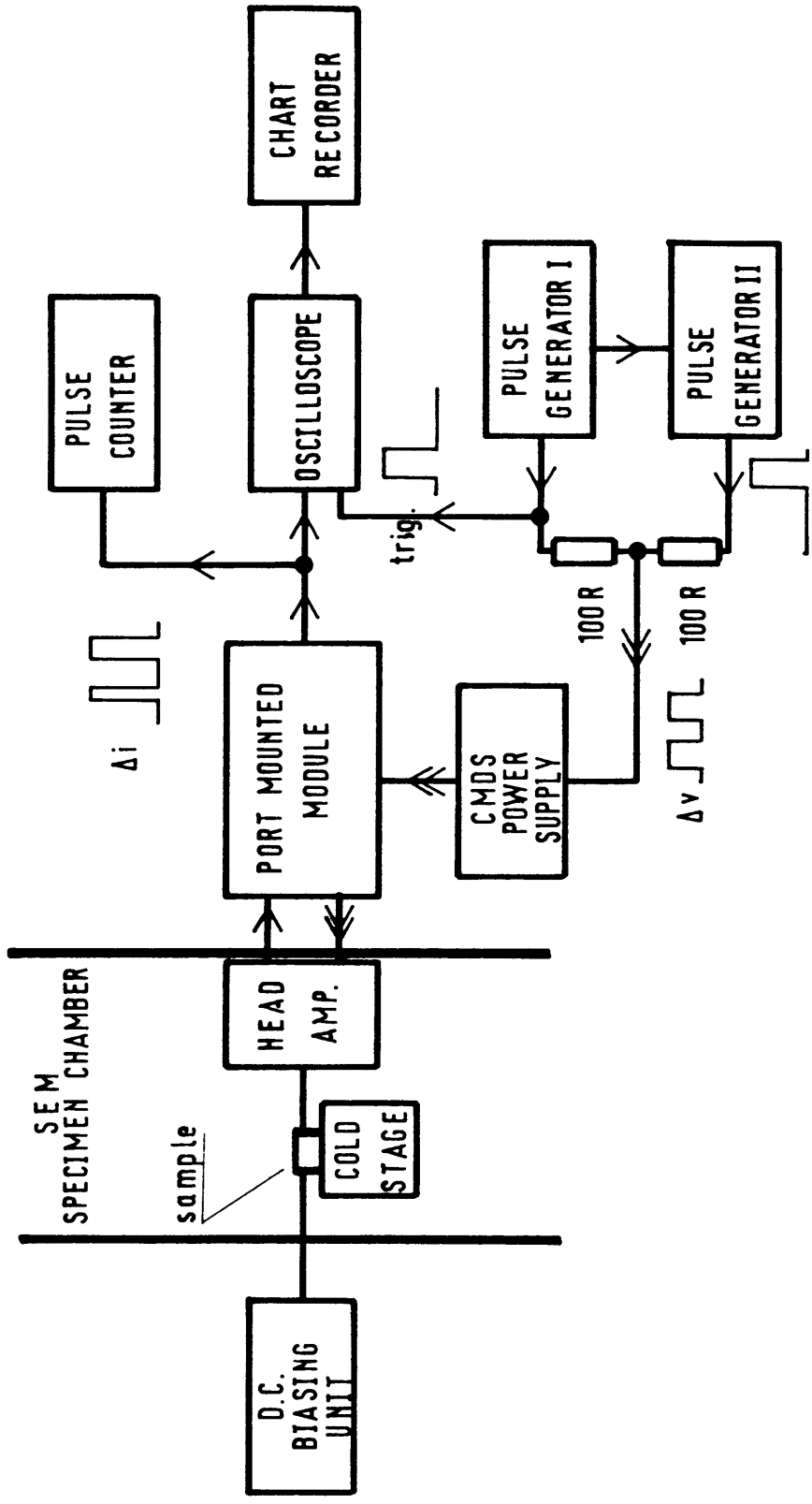


Fig. 20 - Diagram of circuit used for pulse application and delay time measurement.

the microscope port. For the work with single pulses, the Gould PG58A signal generator was used. The a.c. waveform was applied to the common point of the CMDS (floating) power supply (Fig. 10). The same voltage waveform was then induced at the inverting input of the current amplifier A3 (Fig. 8), connected directly to the sample. The generator gave pulses with rise time less than 10 ns. The pulse width could be varied up to 0.1 μs. A double voltage pulse waveform (represented in Fig. 21), was obtained by cascading two similar Gould signal generators. The voltage pulses were always of the same amplitude. The time intervals t_1, t_s, t_2 (Fig. 21) could be varied independently. The time delay between the two pulses was adjustable within the range from 0.1 μs to 1 s. Both voltage and current waveforms, could be simultaneously displayed on the double channel oscilloscope, or measured when recorded in a digital memory storage oscilloscope (IWATSU DMS-6430) and next the chart recorder.

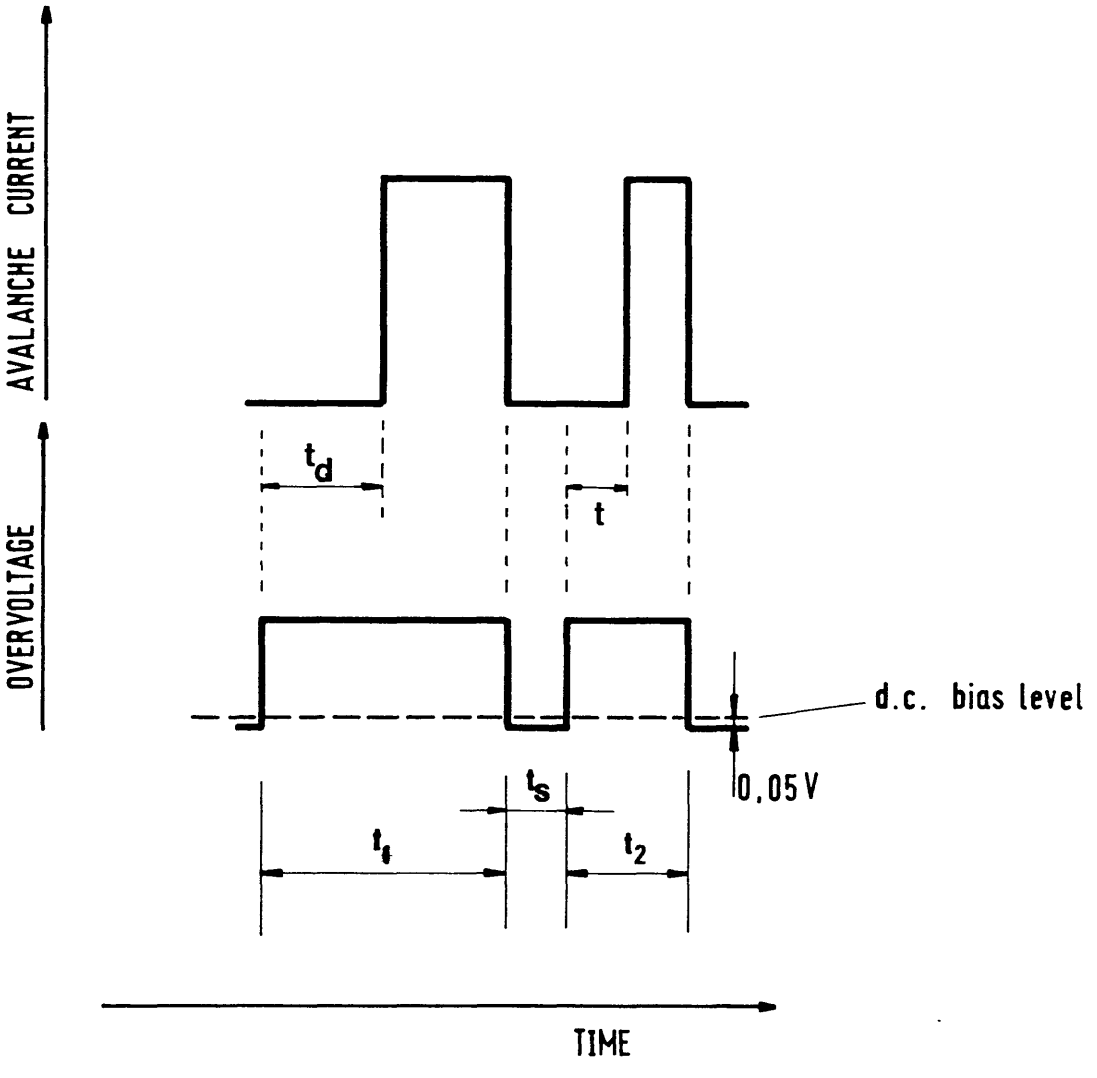


Fig. 21 - Diagram representing single (a) and double (b) pulse over-voltage cycles together with corresponding avalanche current waveforms.

3.4. Preparation of Large Area Electron Transparent Silicon Devices

In silicon devices today, the active structures are situated in the top, thin layer of the chip. The devices have lateral dimensions of the order of a milimeter. To examine these structures in a transmission electron microscope, it is necessary to remove the substrate material uniformly and completely. It is often required also to take off a part of the top active region in order to ensure satisfactory conditions for microscopy. For example, 5 μm thick silicon can easily be examined using a 1 MeV electron microscope. However, with lower voltage microscopy, further thinning of the sample is necessary. In some cases, silicon devices have a very low density of defects. It was therefore desirable to obtain a method for preparing large electron transparent areas of silicon samples.

Preparation of semiconductor samples for electron microscopy is usually accomplished either by chemical thinning or by ion beam polishing. The electrochemical polishing method so far has been less used in this application. Several modifications of chemical thinning have been developed in the past. These techniques involve generally jet-etching the bottom side of the sample directly under the area of interest (Das and O'Neil 1974). For the preparation of large electron-transparent areas from silicon wafers, samples are immersed and rotated in a polishing solution (Kolbsen et al. 1975; Mahar von Staszewski 1978).

Initially, chemical thinning in an HNO_3 - HF mixture was used for sample preparation. However, several diffulties were encountered.

These included imprecise control of the area thinned and the obtainable electron transparent area was non-uniform and small in size (less than 10 μm in diameter). A convenient and reliable means of mounting the specimens while jetting was not found due to the small size of the device to be processed (about 3 mm in diameter).

Ion beam polishing permits large, uniform areas to be prepared (Pettie and Booker 1971). However, it has a disadvantage in comparison to the chemical method. It is very slow (1-3 μm/h for silicon). For this reason ion beam polishing is most economical when applied in the finishing stage of the specimen thinning.

There are already reports of large area thinning for silicon devices by means of electro-chemical polishing. An electrochemical bath polishing represents one possibility. It was used for thinning and separation of individual transistors by anodic dissolution of the substrate and isolation areas (the p-regions are etched preferentially), (Smith et al. 1974). However, the technique was based on the specific configuration of the device and cannot be easily extended to others. An electrochemical jet method represents another possibility. It has been developed for the polishing of large wafers (Booker and Sticker 1962). Its application in the preparation of uniformly thin areas on small silicon discs remained unexploited because of associated electrical contact problems. A new jet-electropolishing technique for transmission electron microscopy samples was developed for the work reported in this thesis. It was found that in spite of the task of making electrical contacts the preparation of samples by means of this method, as

contrasted to chemical means, presents the advantages of cleanliness and much improved smoothness of the final surface, large electron transparent areas (more than 500 μm) and flexible control of the process.

The polishing apparatus is presented in Fig. 22. The equipment consists of a polyethylene container with a screw on suport for a perspex syringe. There is a stainless steel nozzle mounted at the end of the syringe. The nozzle works as a cathode in this system. The sample (3 mm disc) is fastened centrally on a rotatable anode mount. The electrolite is gravity fed at a rate controlled by the screw valve. It falls from a polyethylene resevoir through a flexible tubing and syringe, to form a jet stream at the end of the nozzle. The electrolite is caught below the container in the drip pan and can be recycled. The system involves also a light source located in front of the anode mount. The light from the halogen lamp (300 W) can be focused at the centre of the specimen disc by means of the colliminating lenses. A flask through which cooling water could be circulated is mounted between the lamp and the anode. This is to remove a large portion of the heat from the projected beam of light. The halogen light offered an effective means of carrier injection for silicon samples. The electropolishing process occurs uniformly and preferentially over the illuminated region. Thus, a saucer shaped area of controllable size can be formed by thinning. The process is stopped before perforation by visually monitoring the colour of transmitted light, which varies with the thickness as in Table 5 (Pankove 1962).

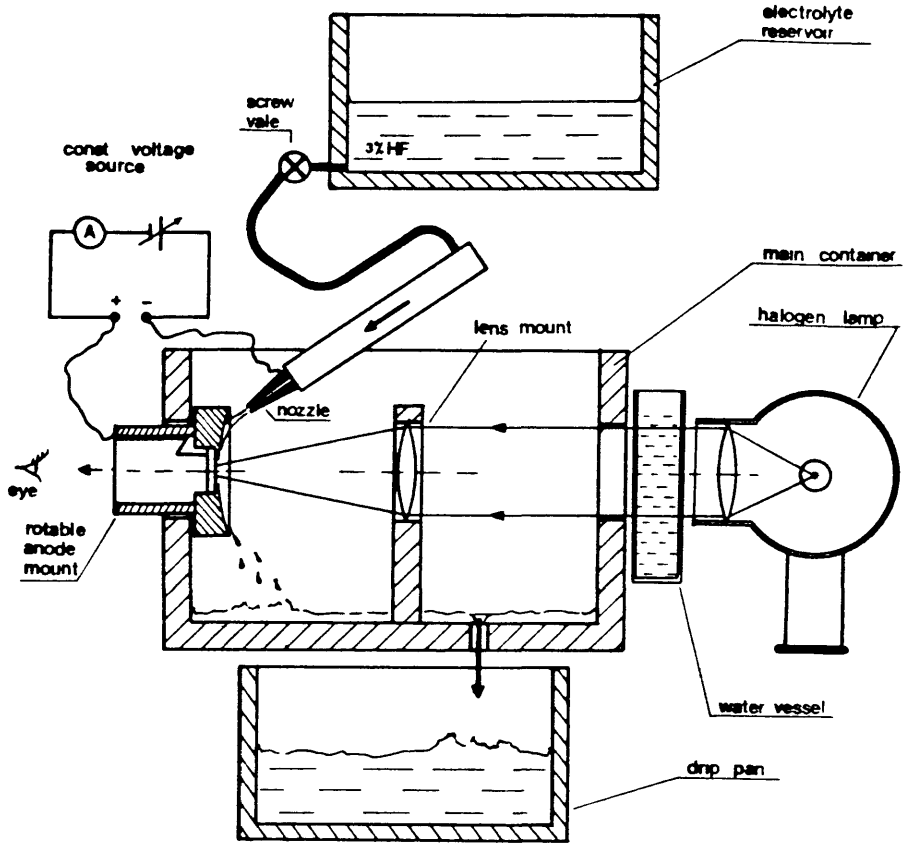


Fig. 22 - Schematic diagram showing the photo-electropolishing column.

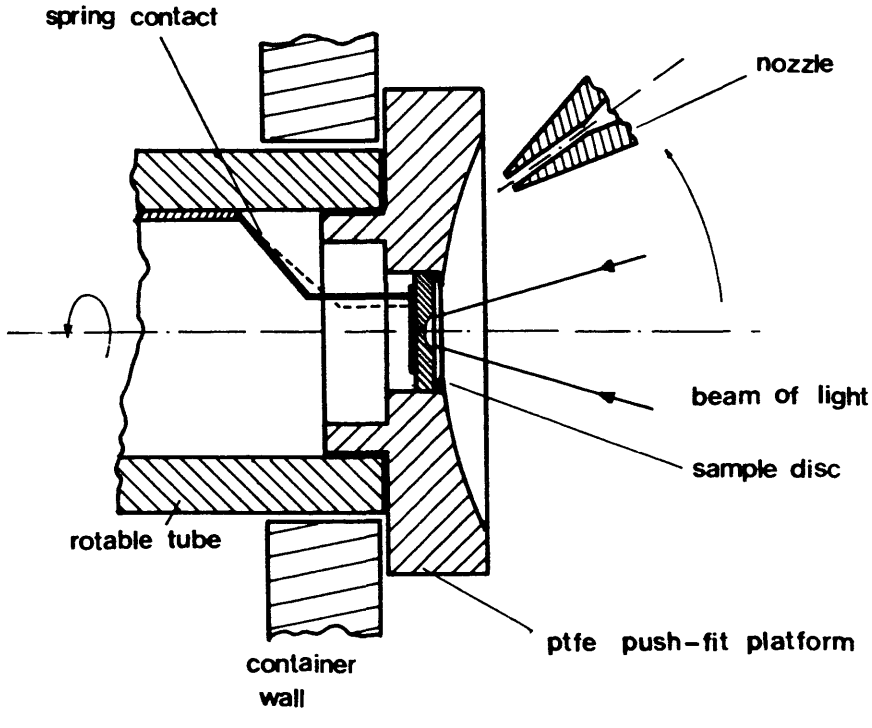


Fig. 23 - Specimen holder.

The sample, 3.18 mm in diameter and 200 μm thick is placed in the circular cavity at the centre of the PTFE pushfit platform (Fig. 23). The area of the disc specimen exposed to the electrolite is a circle with a diameter of 2 mm. The sample is secured inside the cavity with a clear varnish and a miniature spring connector. The application of the clear varnish prevented leakage of the polishing solution around the sample. The teflon holder was fitted onto a rotable polyethylene tube which also supported the spring connector to the specimen.

Table 5 - Colour of Light Transmitted by Silicon as a Function of Silicon Thickness

Red	15 - 9 μm
Orange	9 - 5 μm
Yellow	5 - 2.5 μm
White	2.5 μm

The syringe with the jet nozzle can be fixed in two positions. Firstly, it can work horizontally to project a jet stream which is perpendicular to the specimen surface. This configuration can be applied for polishing of p-type substrates. The syringe can also be tilted above the sample holder in order to provide a laminar flow of the electrolite over the surface to be polished. The syringe when suspended over the sample holder, clears the space in front of the sample and permits the illumination system to be applied. This arrangement was used for thinning of π (lightly doped p-type)

substrates, where intense illumination of the sample was found to be important in order to sustain a uniform and pitting-free eletropolishing process. (The polishing process is not essentially affected by illumination in the case of p^+ and p-type silicon (Meek 1971; Arita and Sunochara 1977)).

The electropolishing column (Fig. 22), has been assembled mainly for the preparation of the reach through avalanche photodiode (RTAPD) samples for TEM examination. The structure of the RTAPD is represented in Fig. 34. Each diode to be examined in TEM has been "photoelectropolished" through the π type substrate. The positive potential has been applied through a point contact to the rear n^+ layer of the sample. The essential process parameters governing the quality of the thinned area were: the bias voltage applied between the sample (anode) and jet nozzle (cathode); the concentration of the HF in the water solution, and the intensity of illumination applied. The best results were obtained when using electrolites containing small concentrations of HF (2 - 3% wt), at the lower end of the practical range of concentration for electropolishing silicon (1 - 10% wt), (Turner 1962). The voltage applied across the cell was from 15 - 20 V. The intensity of illumination was adjusted to ensure a current density of the order of 200 mA/cm^2. Corresponding material removal rates ranged from 4 - 8 μm/min.

Preparation of the avalanche photodiode samples for TEM examination involved essentially the three following steps:

(a) Mechanical polishing of the 3.18 mm device disc from the

substrate side (π -type material). This was performed to reduce the thickness of the disc to about 100 μm. A special Gatan jig was used.

(b) Electropolishing of the substrate side until the light transmitted through becomes yellowish (indicating about 5 um in thickness of the remaining n^+ film).

(c) Ion beam polishing of the thin surface film to remove an additional 1 μm thick silicon layer from both sides.

3.5. Introduction of the Experimental Quantities and Error Analysis for the EBIC Measurements on Dislocations in RTAPDs

Application of the SEM EBIC method for the quantitative study of RTAPDs involved direct measurements of the following experimental parameters:

1. Electron beam current I_b,
2. Background current I_B,
3. Dislocation "absorbed" current ΔI_D,
4. EBIC image resolution on dislocations w,
5. Temperature T.

Values of I_B are the intensities of the background short circuit current I_{sc}, representing undefected areas of the n^+p junction.

The ΔI_D current is a measure of the electrical recombination efficiency of a dislocation. It represents the amount of dark contrast associated with a defect when observed on EBIC micrographs or line scans. ΔI_D values were determined by scanning a single line across a dislocation and using the amplified signal to give a waveform image. Such line scans were recorded in the digital memory storage oscilloscope (IWATSU DSM-6439) and subsequently, on the chart recorder. ΔI_D was measured as a difference between a d.c. level, representing undefected areas of the n^+p junction, and the peak of the negative going EBIC response due to dislocations. The CC spatial resolution w of a dislocation was determined as the half width of such line profiles (see Fig. 60).

The error in measuring I_B, ΔI_D and I_b was relatively small as far as the analog tolerances of the CMDS were concerned. In view of the calibration tests accomplished the error was 0.5% of the measured value.

However, the background current I_B was observed to vary for different points within the n^+ region. This was due to the fact that the planar n^+p junctions in the RTAPDs were not exactly uniform. Short distance variations when referred to the average I_B value were ± 1% at the most.

ΔI_D and w were also found to vary along the dislocation line. This was ± 6% and ± 4% for ΔI_D and w respectively, when referred to their average values. The errors were measured from a series of line scans taken at different points along the dislocation line which was parallel to the surface.

Additional measurement errors were caused by shot and thermal noise. The effect of thermal noise was stronger although important only at specimen temperatures above 80°C. It was interesting to observe that the effect of shot noise was not so much dependent on I_b as on E_b. The noise figure was seen to increase markedly for larger E_b levels i.e., when the generation zone of minority carriers was shifted nearer towards the n^+p junction (Fig. 60).

I_B values were practically free from the influence of the error due to noise. The reason for this was that the experimental I_B levels employed were relatively high. On the other hand, accuracy

in measurements of ΔI_D suffered more. The effect of shot noise on ΔI_D was important for E_b values above 25 keV. Thermal noise was significant at elevated temperatures being ± 10% of the measured ΔI_D value at 120°C.

The absolute error in EBIC contrast C on dislocations due to measurement errors was calculated from the relation

$$(24) \quad \left|\Delta C\right| = \left|\frac{\delta C}{\delta I_B}\right| \cdot \left|\Delta I_B\right| + \left|\frac{\delta C}{\delta(\Delta I_D)}\right| \cdot \left|\Delta(\Delta I_D)\right|$$

$$= \left|\frac{\Delta I_D}{I_B{}^2}\right| \cdot \left|\Delta I_B\right| + \left|\frac{\Delta(\Delta I_D)}{I_B}\right|$$

since $C = \Delta I_D / I_B$

Considering the experimental relation C vs T presented in Fig. 76 (sample 1), calculated values of the absolute error $\left|\Delta C\right|$ were I_B dependent, changing from 1.2% at room temperature to 0.5% at 120°C. This is after considering $\left|\Delta(\Delta I_D)\right| = 0.1\left|(\Delta I_D)\right|$ and $\left|\Delta I_B\right| = 0.02\ \left|I_B\right|$ i.e., without any consideration given to the influence of shot and thermal noise. In fact, the effect of shot noise was observed to be negligible at 18 keV electron beam for both ΔI_D and I_B values (Fig. 76). The effect of thermal noise, however, had to be considered for ΔI_D values measured at high temperatures. The ΔC error for ΔI_D at 120°C increased from 0.5% to 1.3% after assuming $\left|\Delta(\Delta I_D)\right| = 0.3\ \left|\Delta I_D\right|$. In result, the absolute error $\left|\Delta C\right|$ in Fig. 76, was assumed for convenience to be 1.3% for the whole experimental range of temperatures.

Experiments described in the following chapters involved a series of measurements of I_B, ΔI_D and w as functions of T and E_b. In order to minimise the influence of the above mentioned errors, the experiments were carried out following certain precautions:-

1. I_B values were always collected at the same reference point, immediately adjacent to the dislocation being examined.

2. ΔI_D and w were measured from line scans being collected from the same point on the dislocation i.e., following the same scanning track.

3. Both ΔI_D and w were evaluated from line scans passed beforehand through a second order low pass filter. High frequency components were eliminated to such an extent that the influence of shot and thermal noise was practically excluded from consideration.

Execution of these precautions resulted in improved accuracy of the experimental data. This can be seen through comparison between C vs T relations given in Fig. 76 (sample 1) and Fig. 77 (sample 2). The latter is characterised by a much smaller dispersion of the experimental points. Residual errors in I_B, ΔI_D and w were related to the fact that both requirements 1 and 2 (above) could not be controlled precisely. A major contribution to this was related to the image drift problem. The collection of data necessary for the completion of each of the C vs T and ΔI_D vs E_b experimental relations was usually spread considerably in time. In addition,

high magnification was employed (x 8000). As a result the images had to be checked and corrected for most of the experimental points within a single series of measurements. The errors in I_B, ΔI_D and w were evaluated from several measurements before and after repositions, referring to the same experimental conditions (I_b = 7 nA, E_b = 25 keV, T = 25°C). Maximum relative errors were: $\Delta I_B = \pm 1\%, \Delta(\Delta I_D) = \pm 4\%$, $W = \pm 2\%$. The calculated absolute error ΔC (eq. 21) was ± 0.2%. The experimental errors specified above were accepted to be the same for all the practical values of I_b, E_b and T employed in this work.

The specimen temperature was measured by a K-type thermocouple (Fig. 16 and 17). The experimental error due to T measurement was estimated as $|\Delta T|$ = 3 deg.

4. RESULTS

4.1. Electrical Characterisation using the SEM Charge Collection Mode

4.1.1. Evaluation of the Resistivity using the Specimen Current Method

The degree of difficulty associated with the use of different SEM conductive mode signals varies widely from one method to another and one material to another, often limiting their general applicability. Without doubt the EBIC technique is the most widely practiced Conductive Mode method due to, in principle, strong and easy to access signals available. In contrast, the specimen current is known from its undesirable current or voltage contributions to the EBIC or EBIV signals rather than as an independent and useful technique.

Here a simple SEM method is described which allows the resistivity of the homogenous semiconductor and its ohmic contacts to be assessed. This is based on the use of the specimen current signal. So far this simple technique has not been yet evaluated.

Fig. 11(b) shows schematically the set up for the measurement. A focused and scanned electron beam hits the target (Fig. 24). Since the Al is a high input impedance

voltage amplifier, all the specimen absorbed current I_s passes through the part of the sample marked as (resistance of that segment) R_x towards the virtual earth point represented by the input terminal to the high sensitivity current amplifier A3. Thereby the amplifier A3 allows the I_s to be accurately measured. On the other hand, the I_s passing through the resistance R_x promotes a voltage drop V_x which can simultaneously be sensed by the A1. If the electron probe is positioned on the ohmic contact being the nearest to the A1, a maximum voltage V_m will be measured and the total resistance of the specimen can be evaluated simply as $R = V_m/I_s$. Under the condition of the specimen being entirely homogenous and in the form of a rectangular bar, a simple linear relation should be observed on the V_x vs distance scan lines. Thereby the specimen resistivity ρ , is given as:-

$$(24) \qquad \rho\ [\Omega\,\mathrm{cm}] = \frac{R\ t\ h}{l} = \frac{V_m/I_s}{1/(t\ h)}$$

where, t, h and l are the geometrical parameters of the specimen bar as indicated in Fig. 24.

The same method should allow the ohmic contacts of the specimen to be assessed. This should be observed as two voltage steps pronounced on both sides of the linear portion of the line scan representing the semiconductor. The resistance of the contact can be evaluated in the experiment as:-

$$(25) \qquad R_C = \frac{V_C}{I_S}$$

where V_C is the voltage drop on one of the ohmic contacts.

In the experiment the specimen was a p-type silicon bar whose thickness t, width h and length l were 0.05, 0.2 and 0.5 cm. Its resistivity was 40 ± 2 cm. The electrical contacts were provided on both sides of the bar simply by means of silver paste. The electron beam current and voltage were 7.9 nA and 20 keV respectively.

Fig. 25 shows the experimental V_X vs X relation observed with the electron beam scanning slowly across the specimen. From this figure the appearance of the linear V_X vs X dependence is evident. The effect of the ohmic contacts, although small, is noticable on both sides of the linear segment. The resistivity of the silicon bar calculated from the measured V_m value of 1.64 mV (see Fig. 25) was ρ = 41.5 cm, providing a satisfactory match to the value of 40 ± 2 cm representing the four point probe method result.

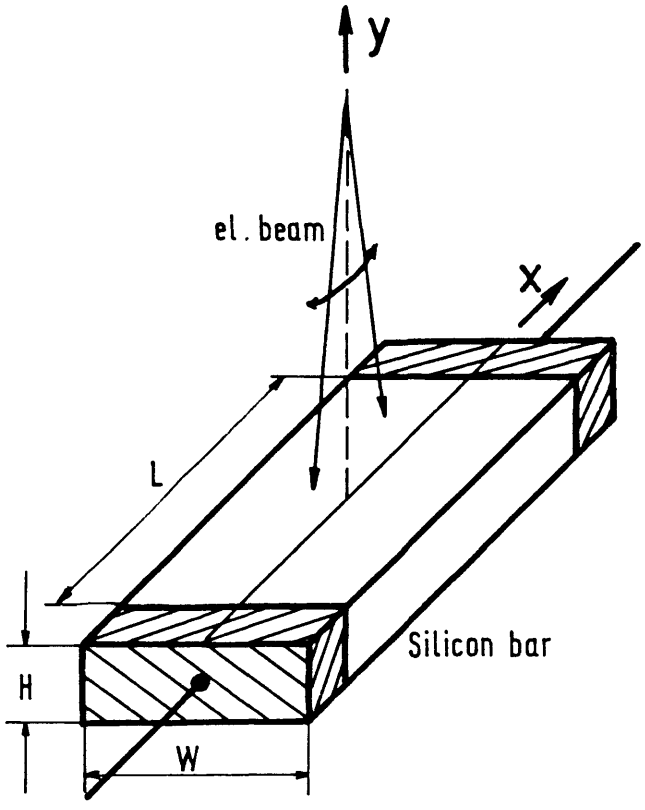


Fig. 24 - The electron beam scanned specimen bar.

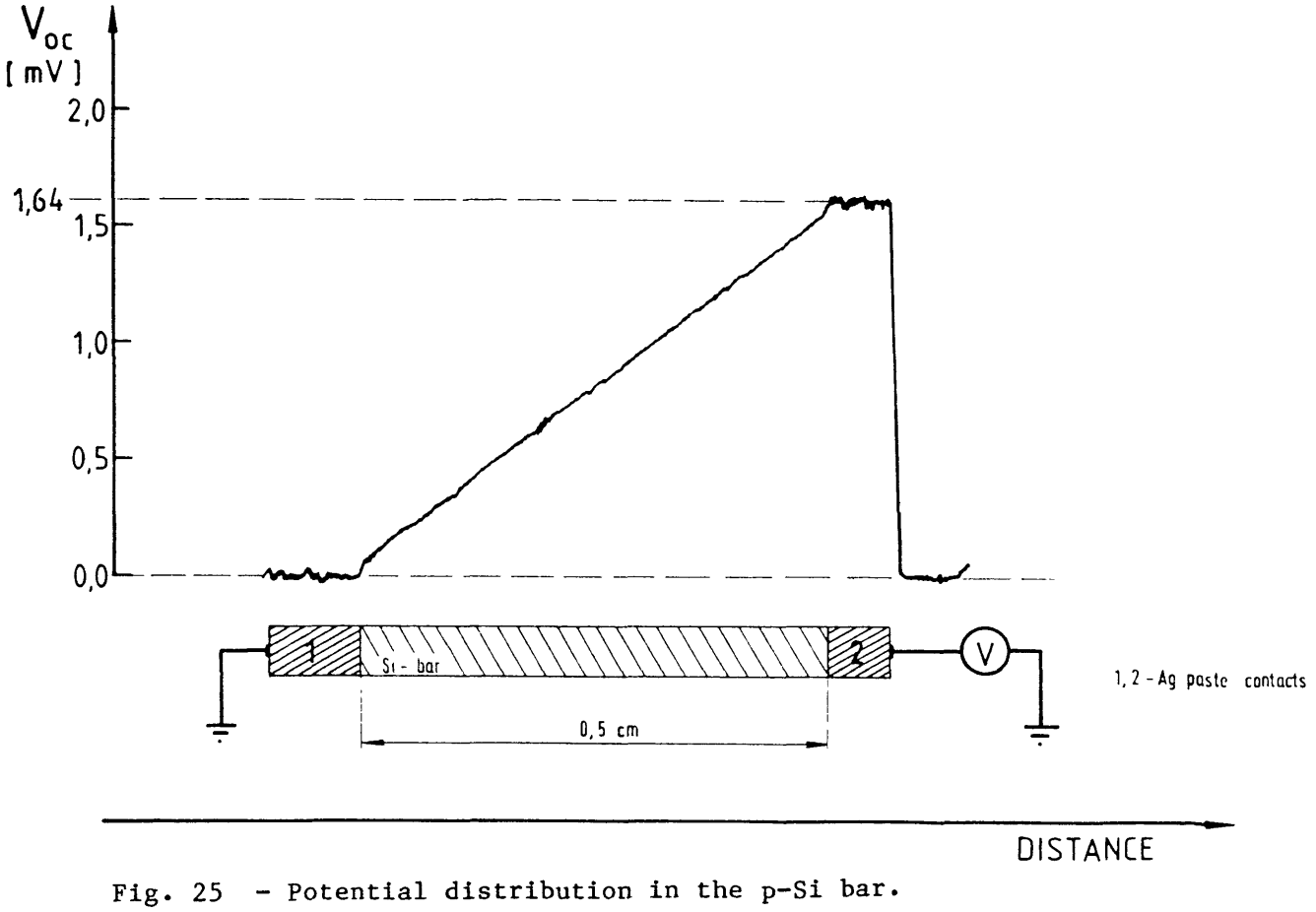


Fig. 25 - Potential distribution in the p-Si bar.

4.1.2. Electrically Active Defects in Small Si Photodiode Arrays

The aim of this investigation was to reveal the mechanism which contributes to the excessive leakage currents in some of the photovoltaic arrays (kindly supplied by Centronics Limited). The photosensitive arrays examined consisted of 16 identical cells processed in a single Si chip. Each cell contained a shallow planar p-n junction with a surface area of 2 mm^2. The form of these diodes is shown schematically in Fig. 26. The p-n junctions were produced by boron diffusion into the n-type Si starting material. The back n^+ contact was fabricated beforehand by phosphorus diffusion.

The devices selected for the examination had been evaluated by measurements of the leakage current for each cell in the arrays separately. The leakage typical of "good" cells was 10 nA at 50 V. The cells showing deviations from these values were selected for further examination. The BEVE short-circuit current (EBIC) was detected using the Mark II detection system. Each cell was connected in such a way that an increased screen brightness was obtained when the p-n junction current increased during the scan. Consequently, the bright areas of the EBIC micrographs correspond to points where larger beam induced junction currents are produced and dark areas represent reduced current collection points.

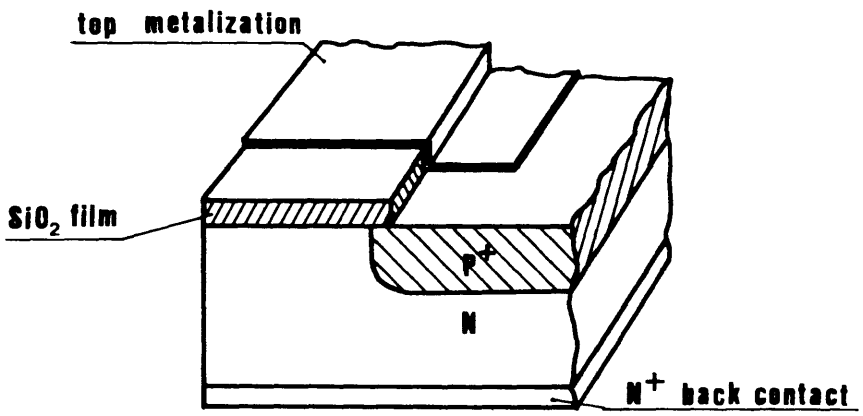


Fig. 26 - Schematic representation of the p-n photodiode.

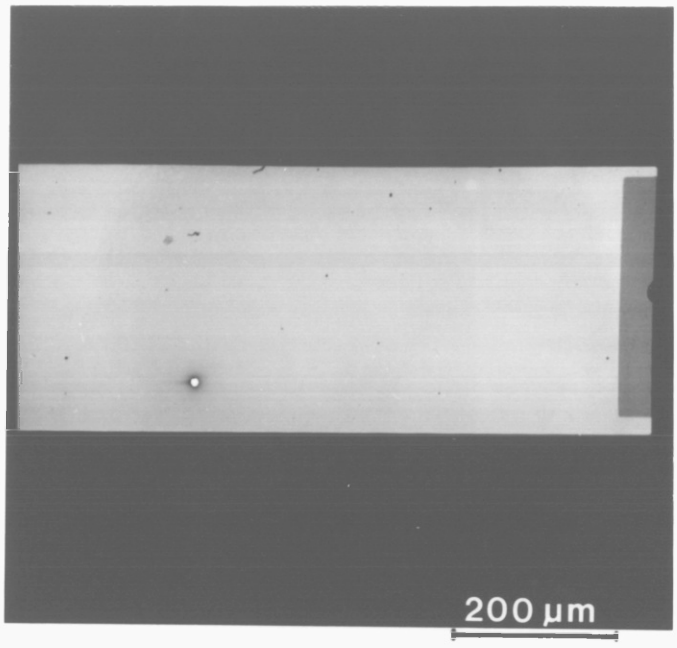


Fig. 27 - Low magnification SEM CC micrographs showing a large defect in the interior of a photodiode at OV bias voltages.

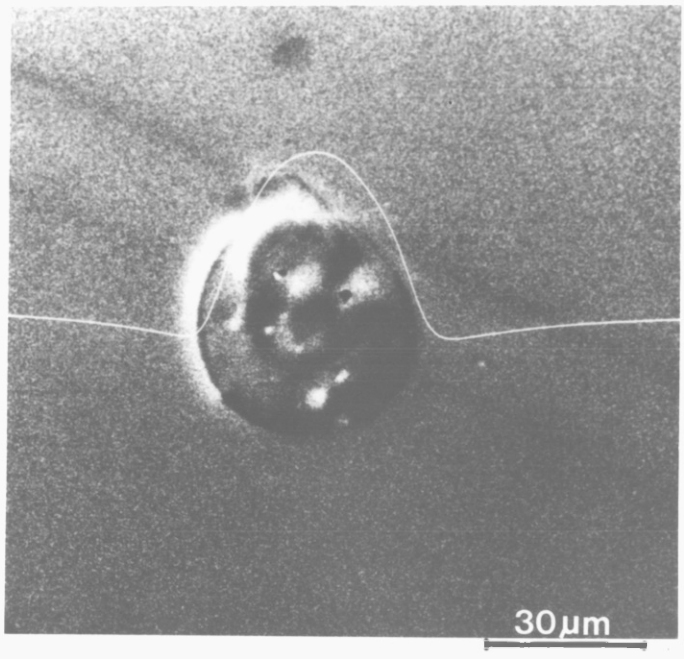


Fig. 28 - The defect of Fig. 27 shown in an emissive mode micrograph with a superimposed I_{sc} scan through the centre point.

Firstly, large defects were seen in the planar areas of many photodiodes as shown in Fig. 27. The contrast was complex and depended on the bias voltage as shown in the series of charge collection (CC) line scans across the defect in Fig. 29. In this case the surface showed topographic contrast as seen in Fig. 28.

Conclusive evidence that these defects were phosphorus-rich, was provided by wavelength dispersive X-ray analysis. The P-peak is shown in Fig. 30.

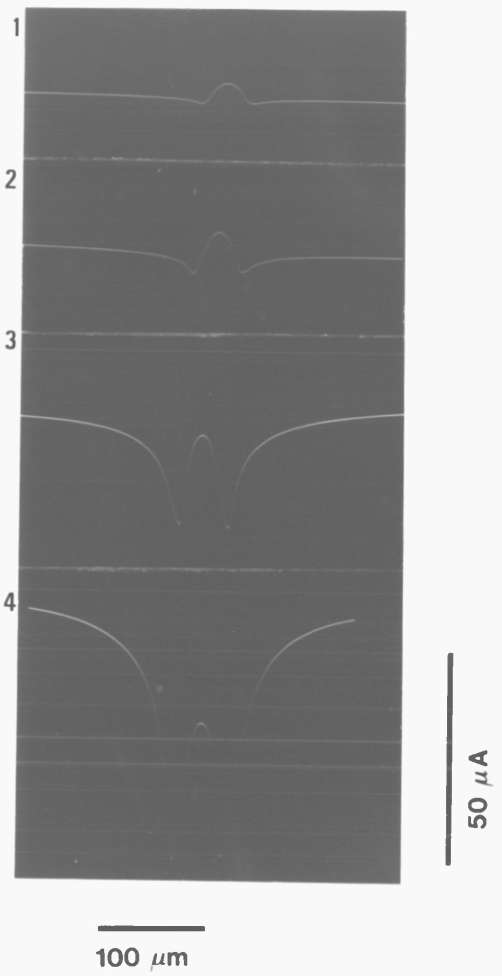


Fig. 29 - I_{sc} line scans across the defect of Fig. 27 for diode reverse biases from 5 to 45V, showing the varying effect on the junction charge collection efficiency.

1. 5V bias
2. 15V
3. 30V
4. 45V

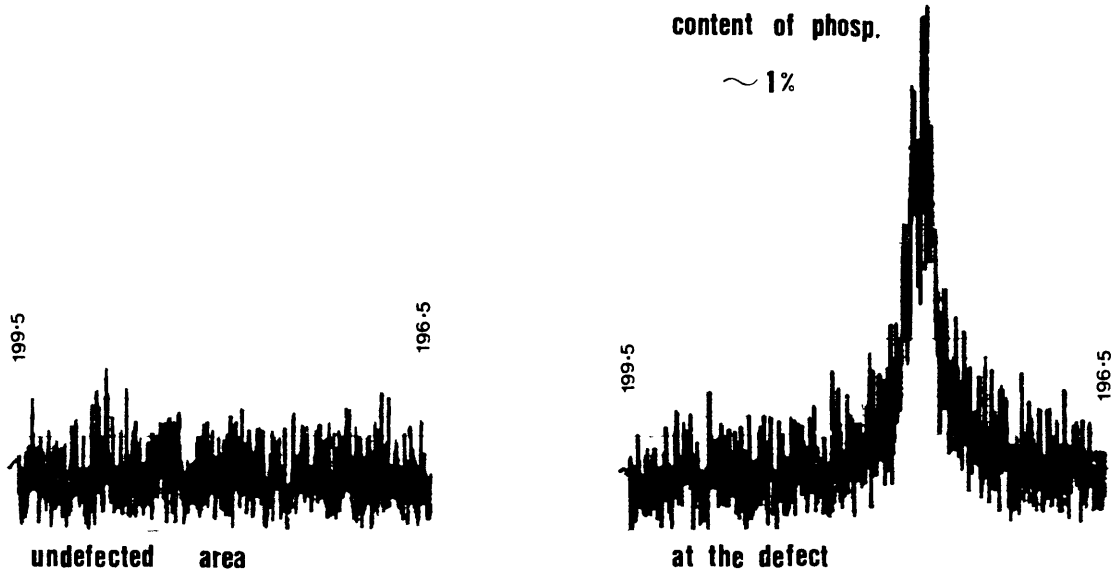


Fig. 30 - Pen charge record of the X-ray count rate showing the phosphorus peak arising from the defect of Fig. 27.

4.1.3. Short Observation on Polycrystalline Si Solar Cell

Use of polycrystaline silicon in the semiconductor solar cell industry is justified allowing relatively low-cost, large area photovoltaic cells for terrestial solar power generation to be fabricated. Most of the processes designed to produce silicon crystals or films at low cost introduce a high density of imperfections in the crystal, which then have a distinct effect on solar cell efficiency (Ravi 1983). In the polycrystaline silicon devices the electrical effect of grain boundaries is one of large concern. With grain boundaries, an essential problem is the role of impurity segregation in modifying the electrical properties of the defect and hence the device performance.

A number of Si photovoltaic polycrystaline solar cells from the European Research Centre in Ispra (Italy) were examined using the SEM EBIC mode of operation. The solar cells examined consisted of a phosphorus doped (about 1 μm thick) window layer and a p-type substrate absorber. A segment of the selected cell was cut from the large area device and mounted on a TO-5 header. The specimen was connected directly to the Mark II H.A. inputs. No bias voltage was applied to the specimen.

An interesting EBIC observation was that the electrical effect of grain boundaries was only pronounced when high electron beam energies were used. This is represented on

the two CC micrographs of Fig. 31. The micrographs were taken at 10 and 30 keV respectively. Grain boundaries are known to act as efficient recombination centres for the minority carriers. This property of the g.b.s. seems to be reflected in the EBIC contrast showing a network of dark zig-zag lines under the 30 keV electron beam. At 10 KeV the electron beam energy dissipation volume was entirely confined within the n-type window layer (R_e = 0.96 µm) and no EBIC contrast from g.b.s. was observed.

Since the g.b.s. run perpendicular to the p-n junction and the surface, it can be expected that they should be pronounced in a similar way on both EBIC micrographs, regardless of the penetration depth of the electron beam.

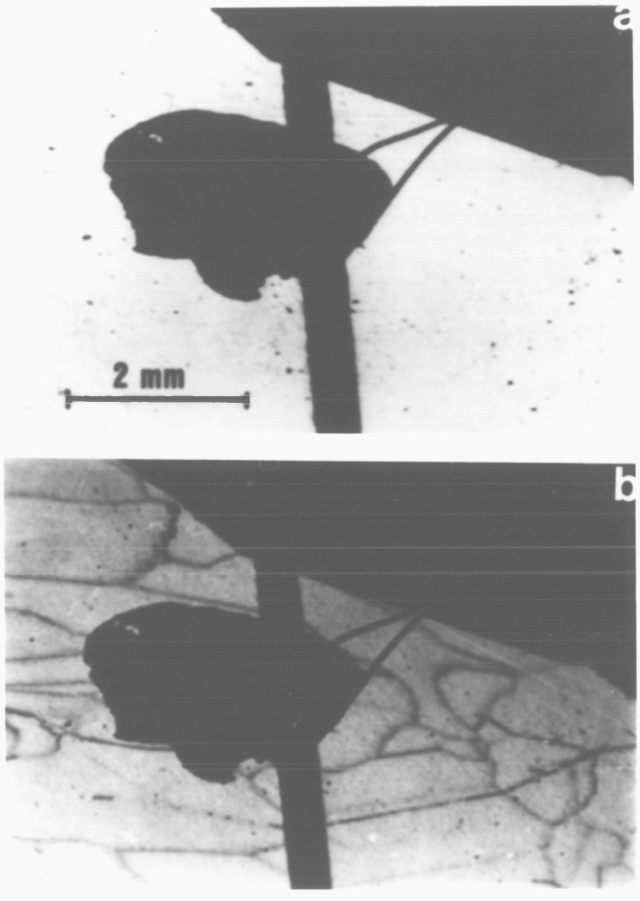


Fig. 31 - EBIC micrographs of a fragment of a broken polycrystalline Si solar cell taken at beam voltages of (a) 10 KeV and (b) 30 KeV. The black bars are surface metalisation on the device and the blob is a silver paint contact.

4.1.4. Discussion

The SEM specimen current technique described in section 4.1.1. provides a simple means for the assessment of the resistivity of an homogenous semiconductor and the resistance of the ohmic contacts. The applicability of the method for low resistivity materials is limited by the sensitivity of the Al high input impedance amplifier i.e., by its noise figure. Assuming that the 10 μV range can be sensed (by good quality commercial operational amplifiers), then using the highest electron beam currents available i.e., I_b = I μA ($\simeq I_s$) a specimen of a total resistance of 10 Ω can be assessed. For high resistivity samples the requirement for voltage sensitivity can be eased considerably. The major drawback associated with this technique is that the geometry of the sample needs to be defined.

The photodiodes used in this investigation exhibited soft I-V characteristics and excessive junction leakage current. The isolated breakdown sites observed within the boron diffused planar areas of the diodes appear to be mainly responsible for these effects. The example of EBIC observation presented in section 4.1.2., seems to reflect the two basic functions of the single, electrically active defect, disclosed within the sample. Firstly, the presence of the excessive bright EBIC contrast area within the centre of the defect (appearing at increased bias

voltages) refers to the defect acting as a preliminary breakdown site. Antecendent breakdown at this site may occur as a result of the small radius of curvature in the junction surrounding the defect. Secondly, it is obvious that the leakage current through the localised channel spreads in the neutral (n-type) part of the device causing a potential drop in the immediate neighbourhood of the defect. This is manifested in the EBIC contrast by the appearance of the dark zone of reduced charge collection efficiency surrounding the defect.

A microprobe analysis of these defects (Fig. 30) indicates that they result from a highly localised concentration of phosphorus. Hence, the sites are phosphorus diffusion pipes formed during n^+ diffusion producing a localised reduction of the breakdown voltage. The formation of such phosphorus sites depends on the quality of the masking oxide prior to n^+ diffusion. The detailed interpretation of the EBIC contrast due to phosphorus pipes is not clear. This is partially because the effect of prior, heavy P-diffusion on the subsequent acceptor p-type diffusion is not known. Further analysis involving TEM examination would be necessary in order to disclose the detailed structure of the defect.

Grain boundaries in silicon crystals and films can have two distinct effects on solar cells. As a consequence of their highly defective nature g.b.s. can function as efficient

recombination centres. They can also act as effective sinks for impurities which in return alter the electrical nature of the boundary.

It appears that both of these g.b.s. properties found reflection in the EBIC observations represented in Fig. 31(a) and (b). The possible electrical effect due to g.b.s. in the examined cell is schematically depicted in Fig. 32. In the n-type window layer, the presence of donor impurities at the grain boundaries can result in a n^+ region surrounding the defect. In such cases the electron beam (or light) generated carriers experience a field in a direction away from the grain boundary, thus preventing recombination at the defect. Consequently, the presence of n^+/n gradients may nullify the effect due to g.b.s. thereby preventing collection losses within the window layer. This situation would be analogous to the case of a back surface field effect, wherein p^+p junction on the reverse side of the absorber layer, serves the purpose of reflecting (light) generated carriers and preventing a back surface recombination effect.

The presence of the n^+n barriers at g.b.s. in the poly-Si solar cells seems to be consistent with the additional observation carried out on polycrystalline GaP samples, dopped with tellurium. The CC micrograph of Fig. 33 was taken simply by applying silver paste (ohmic) contacts on the opposite sides of the GaP sample cut into a bar.

Application of the Schottky barrier technique was not necessary since the g.b.s. involved appeared to act as efficient CC barriers themselves. A segment of the grain boundary in Fig. 33 can be seen distinctly in bright EBIC contrast indicating the presence of the localised band bending required for the barrier formation. This most probably is the consequence of the impurity segregation at the grain boundary, so that it consists of two Schottky barriers back-to-back. A similar conclusion has been reached by Russel et al. (1981) in reference to the EBIC observations on the electrically active g.b.s. in CVD grown ZnSe polycrystalline samples.

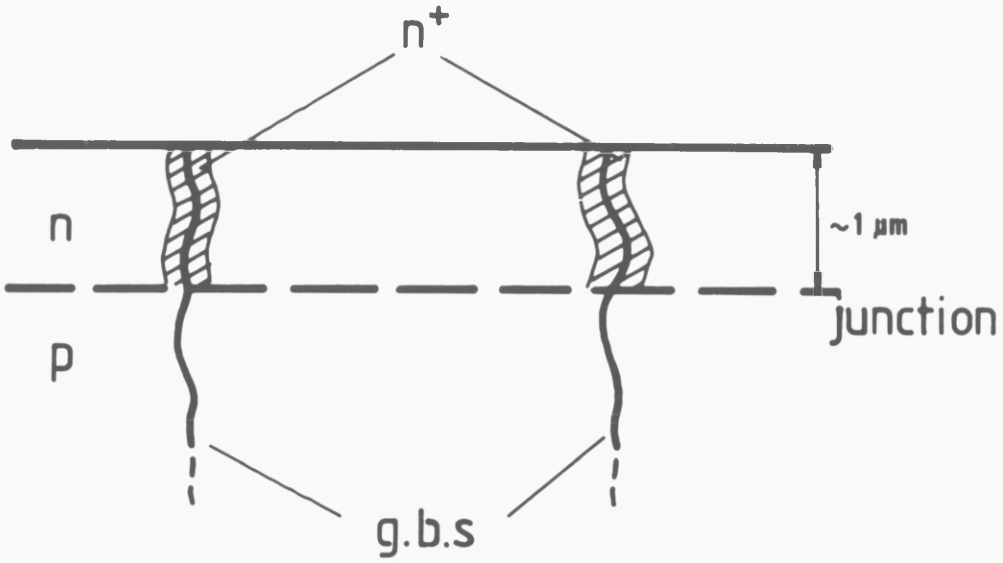


Fig. 32 - Formation of n^+n barriers on grain boundaries.

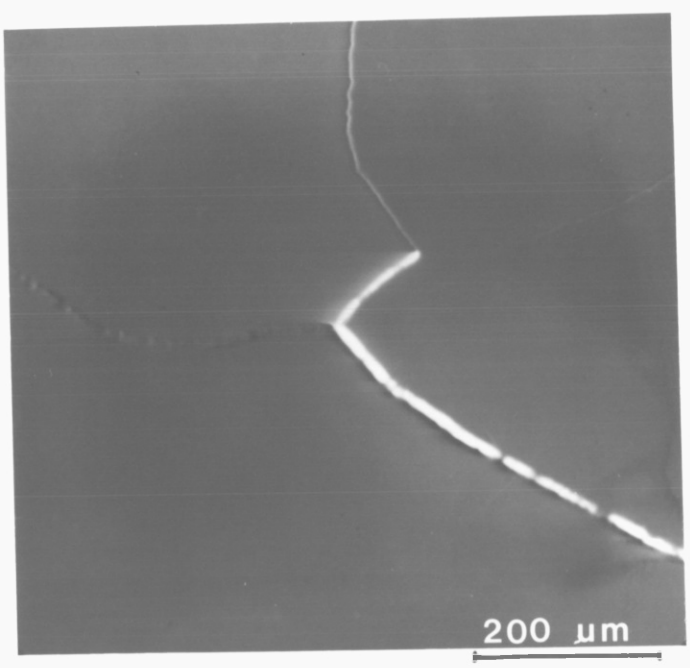


Fig. 33 - EBIC micrograph of grain boundaries observed in polycrystalline GaP.

4.2. Characterisation of Microplasma Sites in Silicon N^+P Reach-Through Avalanche Photodiodes

Reach-through avalanche photodiodes are large discrete Si devices designed to detect near infrared radiation with a considerable gain and they are used in the first generation of fibre optic communication links. The chief problem encountered is that of electrical noise which limits the sensitivity of the device and can be so severe as to render the device useless. RTAPDs are often known to contain defects (Bollen et al. 1976) and are spatially non-uniform to some extent (Mayes 1982). No detailed study of the problem has been published as far as is known.

The object of the investigation presented in this section was to establish the cause and microstructure of defects responsible for the presence of excessive avalanche noise and premature breakdown in diffused n^+p RTAPDs. The samples were kindly provided by Centronics Limited. The investigation involved mainly SEM EBIC studies combined with I-V testing and 1 MeV TEM observations.

The diodes were fabricated by using π ($N_a = 2 \times 10^{12}$ cm^{-3}) type (111)-oriented silicon wafers. The structure of the diode was generally an $n^+p\,\pi\,p^+$ type, described by Kaneda et al. (1976). A cross sectional view of the RTAPD is shown in Fig. 34. The p layer was formed by implantation of boron ions (B^{++}) with a 60 keV accelerating voltage. The implantation was followed by a drive-in

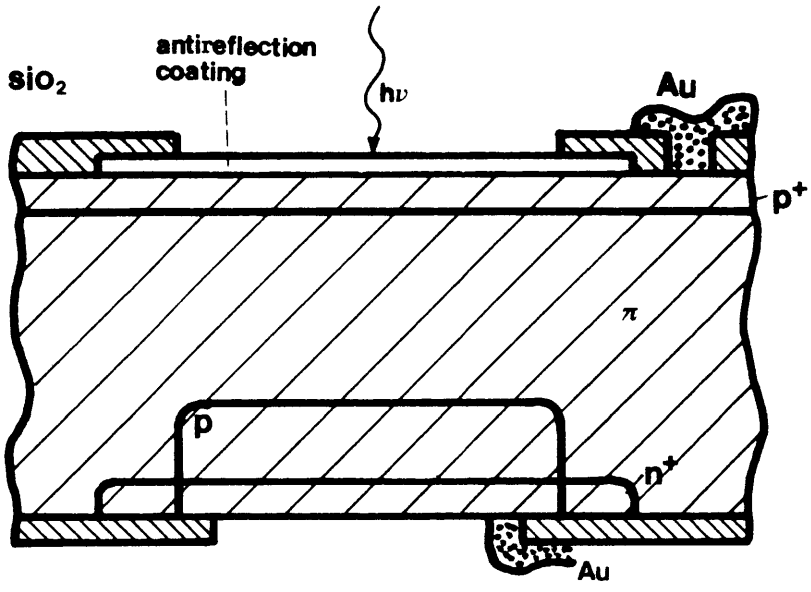


Fig. 34 - Cross Section of Reach-Through Silicon Avalanche Photodiode detector.

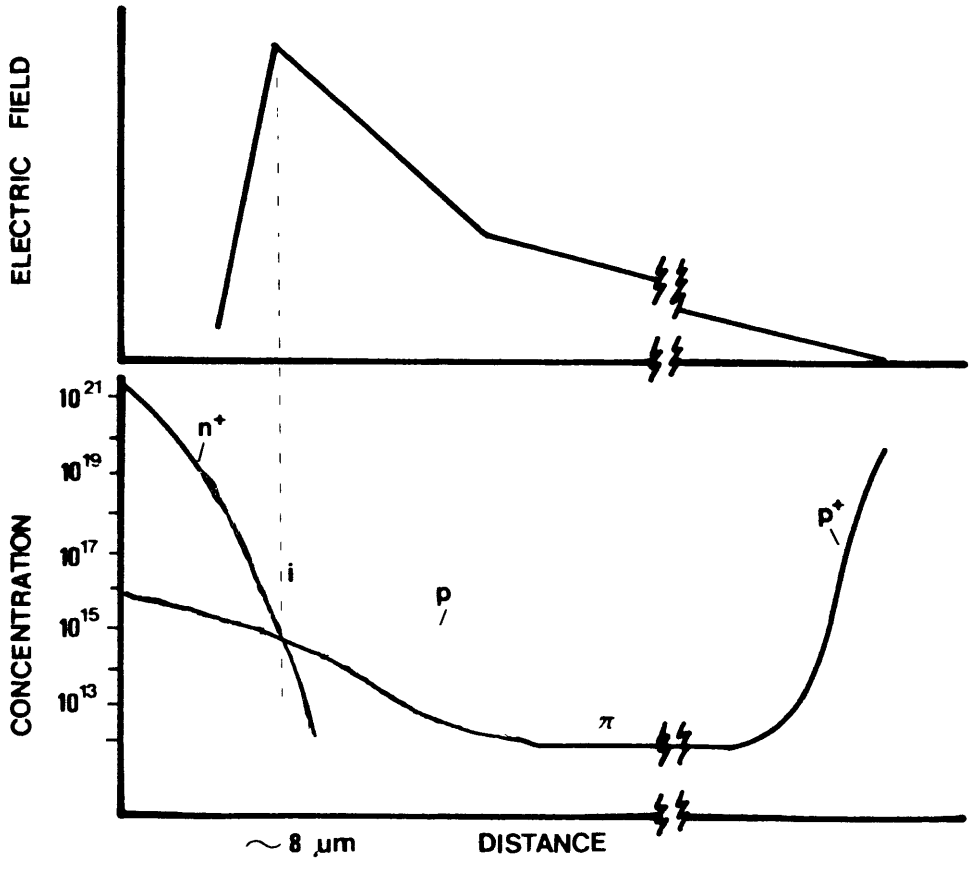


Fig. 35 - Impurity Concentrations and Electric fields in various regions of a reach through device.

process carried out at 1135°C for 160 hours. The implantation dose (1.3×10^{13} boron ions/cm^2) was chosen, as then the breakdown of the diode with a 130 μm depletion layer, occurs at 400 V typically. The depth of the formed p layer was approximately 28 um. The junction was formed by a phosphorus diffusion at about 8 um deep with an integrated P concentration $Q = 6 \times 10^{15}$ cm^{-2}. The diffusion process involved the predeposition of a $POCl_3$ layer (at 920°C) and drive-in at 1075°C for approximately 4 hours. Fig. 35 shows the expected impurity concentrations and electric fields in various regions of RTAPD.

The region between the n^+ and p layer concentration maximum, is assumed to be intrinsic (represented as i in Fig. 35). When the operating voltages are supplied to this structure, the depletion layer extends through the i and π layers. The characteristics of the i region are connected to the key parameters of RTAPDs such as the breakdown voltage V_B, excess noise factor and temperature coefficient of V_B. On the other hand, the π layer becomes the light absorption region in which electron hole pairs produced by an infrared photon are collected.

The field within the i region is so high that the electron (the more mobile carrier) is accelerated to an energy high enough to produce "impact ionization" i.e., to produce a second hole-electron pair. Both electrons will then be accelerated and produce proceeding ionization. In this way gains of up to 100 to 200 can be obtained i.e., pulses of 100 to 200 electrons can be obtained for any single photon absorbed.

The diodes were mounted onto TO-5 headers after being cut out from the device wafers. Each diode was cemented to the TO-5 header using coloidal silver paste. The contact to the top layer was made with a thin Au wire using a thermocompression wedge bonder.

The SEM EBIC technique was used as the main method of examination. The incident electron beam generates electron-hole pairs which are collected through the volume of the device in which there is an electric field. The resultant current was used as a video signal to produce micrographs or line scans. Because this phenomenon is so closely analogous to the barrier photovoltaic effect on which the device actually operates the observations are directly relevant to the operation of the device.

Most of the observations were carried out under high bias voltage applied to the sample, in order to simulate the usual working conditions for the diode. The high bias voltage was applied through the CMDS power supply. The use of the "hot" and "cold" specimen stages (described before) enabled the temperature dependent observations to be performed within a wide range of temperatures.

4.2.1. Preliminary Observations

A number of noisy RTAPDs were examined. Preliminary SEM observations in the emissive and CC modes revealed nothing wrong at the top, light entry surface. The CC images produced by recording I_{cc} during a two dimensional scan of the specimen vertical cross-section, confirmed the geometry of the n^+p junction as can be seen in Fig. 36.

The EBIC line scan over the RTAPD cross-section, confirmed the depth of the n^+p junction to be 8.3 μm. Fig. 37(a) presents an EBIC line scan $I_{cc}(X)$ through half the thickness of the APD. The junction location is ascribed here to the maximum of the $I_{cc}(X)$ response.

Fig. 37(b) presents the same $I_{cc}(X)$ scan line recorded as a log current plot. Quantitative analysis of such scans showed the material in general to have the required $n^+p\,\pi$ properties. The straight line segments of the log (I_{cc}) trace follow the equation (18), and the relevant values of the minority carrier diffusion length were obtained for various regions within the device.

Only when the devices were inverted so the n^+p junction was exposed to the electron beam, the defect contrast was observed in CC mode micrographs as shown in Fig. 38. Good, noise free RTAPDs showed no such contrast in the central

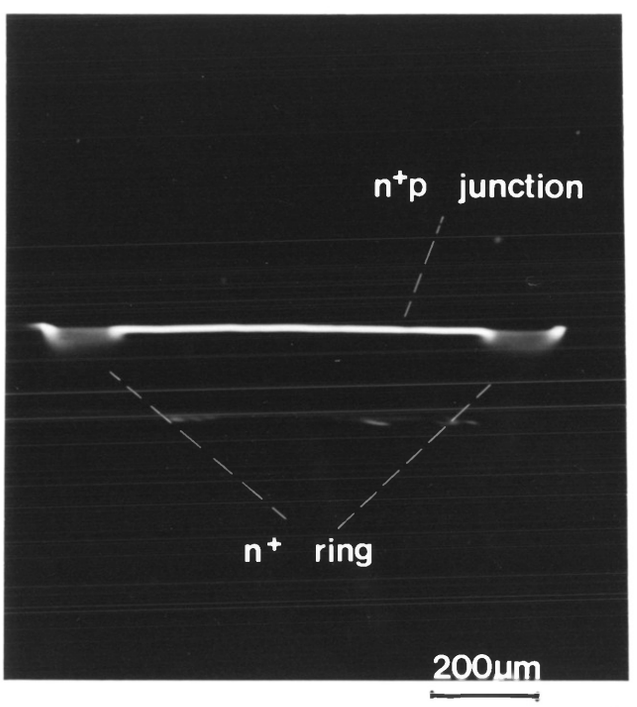


Fig. 36 - Charge collection image of the cleaved edge of the RTAPD.

active n^+p junction area as that shown in this device. Thus, the small depth of penetration of the electron beam showed that the defect structure was confined to the shallow, heavily diffused n^+ layer.

The plot of Fig. 37(b), obtained directly from the logarithmic amplification facility, immediately demonstrated that the signal variation had the exponential form over considerable distances, so reliable values for L could be obtained in the two exponential regions on the p (left hand) side. Thus, two values for L are obtained. The linear region with the steeper slope adjacent to the n^+p junction gives the value for the p material. The region with the lower value of the slope gives that for the π material. The log (I_{SC}) vs x relation within the n^+ layer was considerably bowed and the straight line portion was only found far from the junction.

It is important that the CMDS can secure accuracy down to at least 1% (within a single H.A. sensitivity range) so that accurate values could be obtained for the small currents at the tail of the I_{SC} vs x response (π - region, see Fig. 37(b).

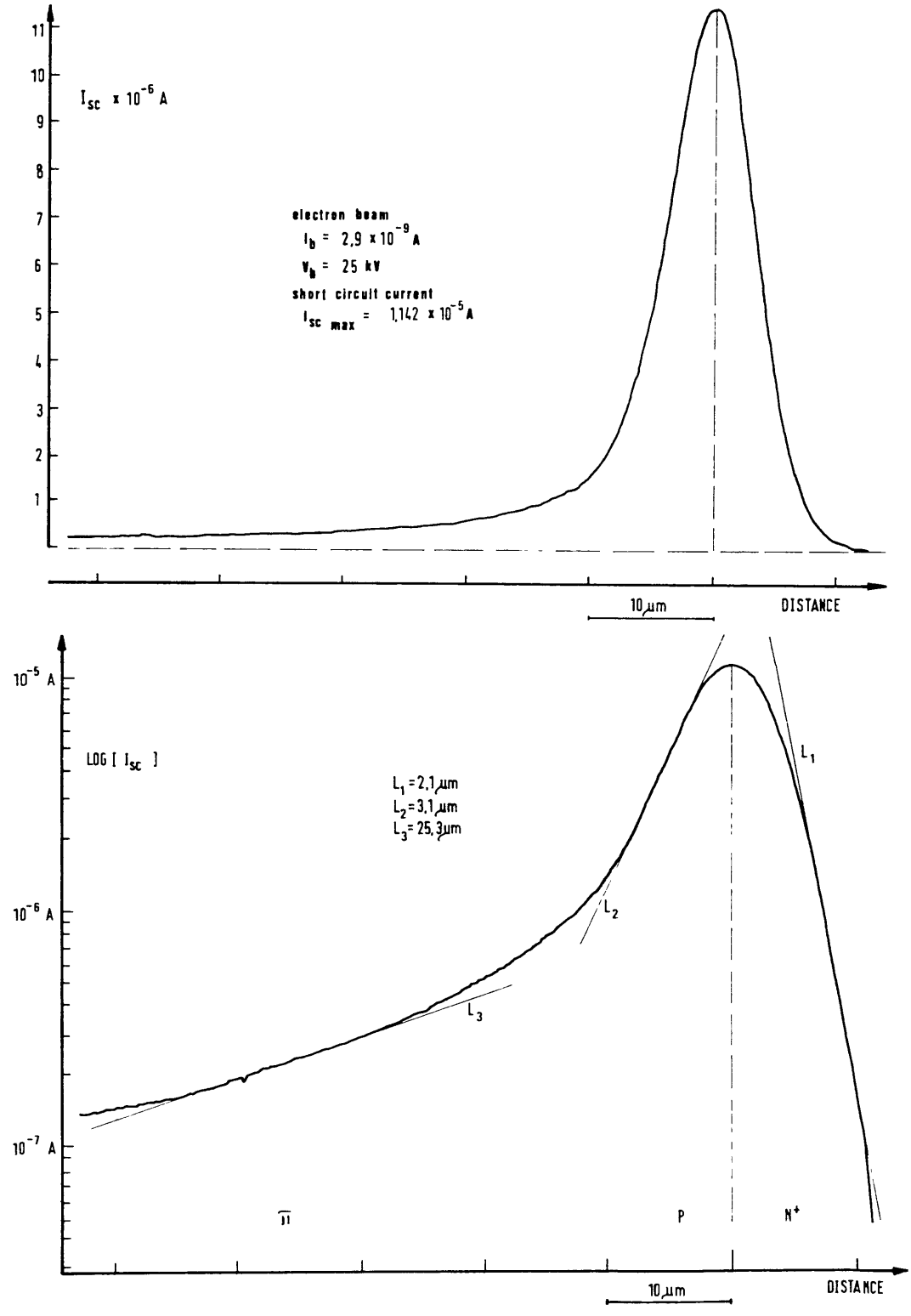


Fig. 37 - True EBIC line scans over a cross-section of an APD from the π material at the left through the p-type material to the n-type material at the right. (a) I_{sc} versus distance and (b) the logarithm of the short-circuit BEVE current versus distance.

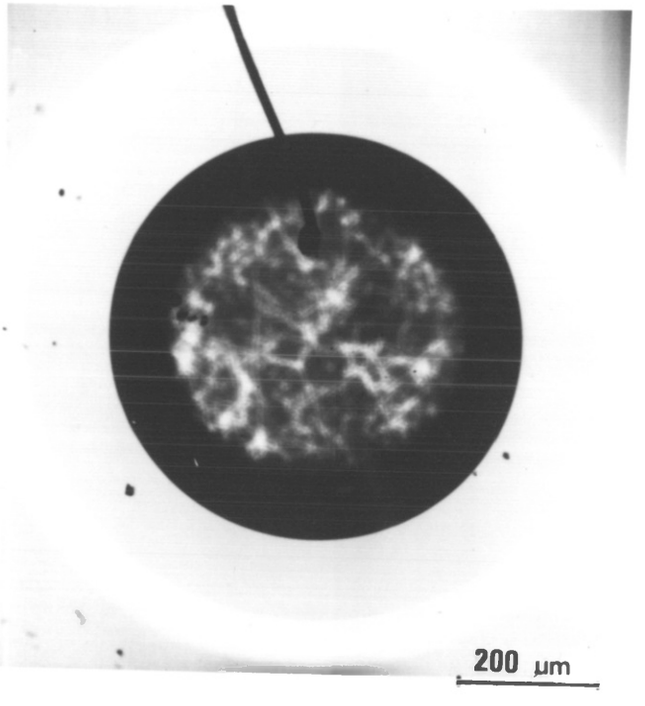


Fig. 38 - EBIC micrograph of the whole of the RTAPD. The central P-N junction can be seen to be electrically non-uniform.

4.2.2. Correlation between RTAPD I-V Characteristics and SEM Charge Collection Contrast

(a) First, the APD device wafers were examined on a Tektronix Type 576 curve tracer to check up on the electrical effects of the defects involved. The devices having abnormal reverse I-V characteristics were then cut out of the wafers and mounted on the TO-5 headers. Forty defective APD's were selected. It was found that the diodes could be classified in three distinct groups in respect of degree of departure from correct current voltage characteristics.

The diode which was selected to represent the first group of the defective APDs (referred to as D1 below), produced "stepped" and noisy breakdown reverse characteristics shown in Fig. 39(a). The avalanche current discontinuities observed, are representative of the microplasma switching effect. In addition the operating range of the diode was prematurely terminated by the breakdown of a microplasma at 360 V. The second I-V curve disclosed in Fig. 39(a) was taken under bright light illumination. This reveals a relatively short region of avalanche multiplication, followed by a sudden transition into avalanche breakdown. This indicates that the devices cannot sustain high gains (Melchior 1966). Similar behaviour was typical for 70% of APDs which were examined.

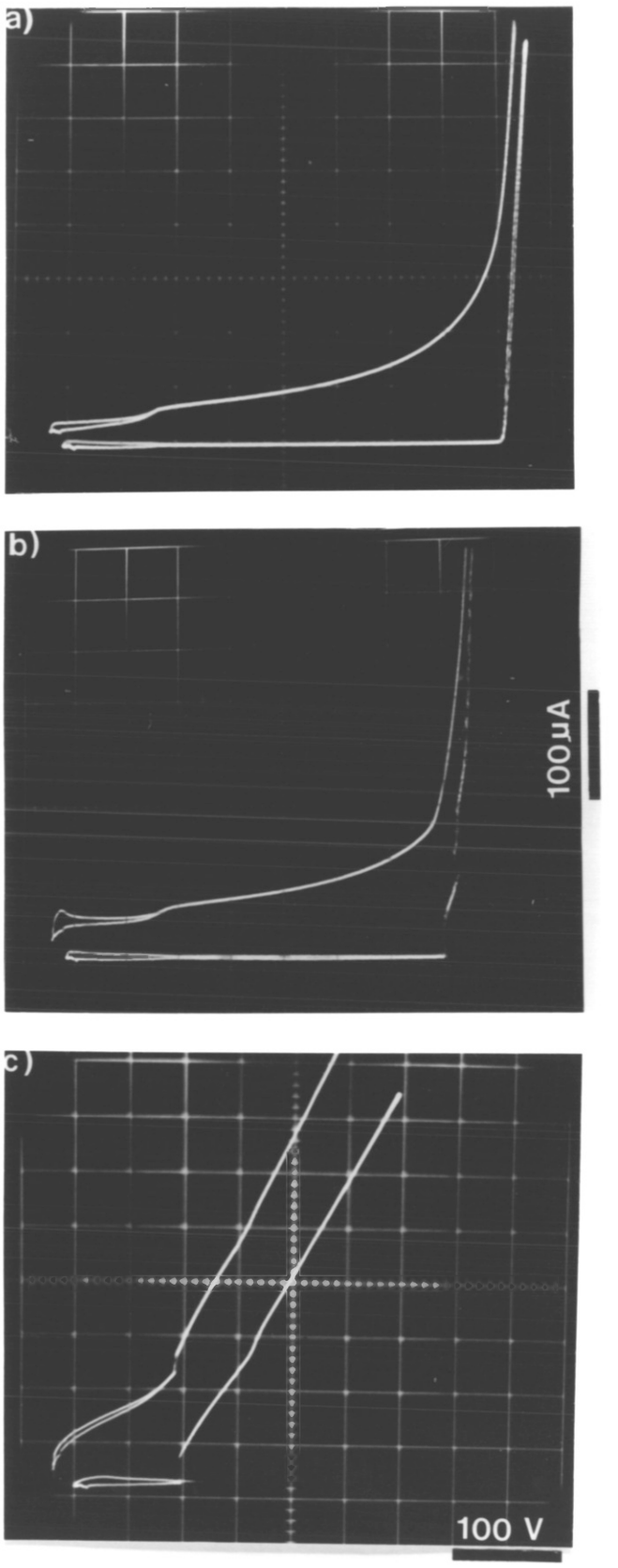


Fig. 39 - Reverse current voltage characteristics of three RTAPDs exhibiting (a) a hard form, (b) a soft, "stepped" and (c) very soft with a single step form. In each case the upper curve is the reverse characteristic representing the device under illumination.

The reverse characteristic shown in Fig. 39(b) represents the second group of defective APDs. It is nearly ideal. That is, it exhibited a low reverse current up to a sharp breakdown at about 400 V bias. When illuminated, it exhibited correct, smoothly changing current versus voltage characteristics, indicating a microplasma free device (represented as D2). However the avalanche breakdown region revealed the presence of excessive noise, traces of which are visible in the I-V characteristic, in Fig. 39(b). The amplitude of this noise was increasing rapidly with increasing avalanche current. Such a diode suffers from a poor signal to noise ratio, hence has a low sensitivity. Similar characteristics were representative for approximately 25% of examined APDs.

Finally, the biggest departure from the ideal I-V characteristic was observed in several diodes classified into the third group. These devices exhibited considerably reduced breakdown voltages (approximately 200 V). The reverse I-V characteristics were of a very "soft" form with typically a single avalanche current discontinuity at the breakdown "knee". This is represented in Fig. 39(c). The diode is referred to as D3.

In the following stage the diodes were examined in the SEM using the charge collection mode of operation. This employed the b.e.v.e. short circuit current as a video signal. All defective diodes examined, revealed direct

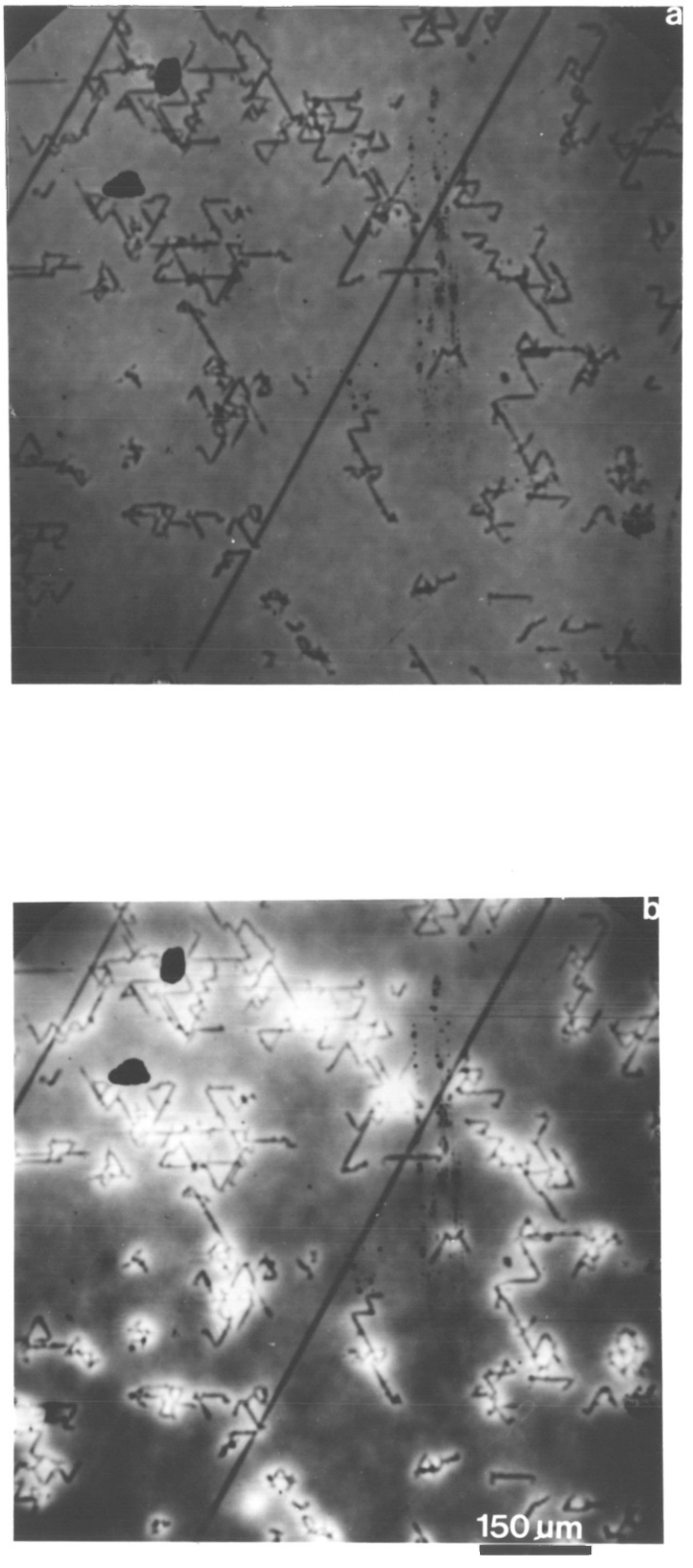


Fig. 40 - SEM CC micrographs of the n^+p junction area of a device with a low density of line defects at biases of (a) OV and (b) 250V. (Diode D1)

correspondence between the types of reverse current-voltage characteristics and types of EBIC contrast observed. Again the same diodes D1, D2 and D3 were used to illustrate this correspondence.

Figures 40(a) and (b) are b.e.v.e. short circuit current micrographs of D1 taken under different bias conditions. A network of dark lines can be seen in (a) corresponding to 0V bias. The dark lines represent a locally enhanced recombination rate of the injected minority carriers and correspond to the presumed network of diffusion induced misfit dislocations. A number of current enhancement sites appear in bright contrast in micrograph 40(b), recorded at a reverse bias just below the turn-on voltage. These are microplasma sites corresponding to the locally enhanced current multiplication.

Micrographs 40(a) and (b) were recorded at different ranges of sensitivity set at the H.A. The level of the short circuit current detected, corresponding to the reverse biased sample, was on average an order of magnitude higher than that obtainable from the unbiased sample.

It is evident that the network of dark lines stretches through the entire n^+ region. The lines can also be seen within the n^+ ring surrounding the central n^+p junction area (Fig. 41).

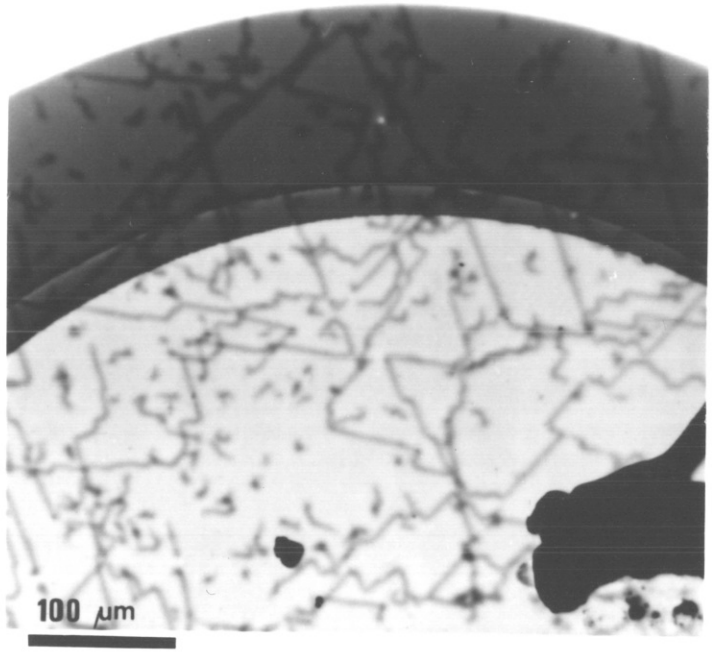


Fig. 41 - EBIC micrograph showing a part of the diffused n^+ region outside of the implanted p region.

Diode D2 producd much higher densities of dark lines when examined in the SEM and this is shown in Fig. 42(a) and (b). The dense pattern of lines consists of three sets of parallel lines crossing each other at an angle of 60^{o}. A large number of microplasma sites appear in micrograph 42(b) recorded at 312 V bias. The breakdown voltage of this device was 405 V when measured at room temperature. The microplasma sites are much smaller compared to the previous case and many of these were found to be in the "on" state simultaneously at the onset of the avalanche breakdown, distributing the total avalanche current over many channels.

The third group represented by diode D3 revealed a different type of microplasma. The micrographs of Fig. 43(a) and (b) reveal a single microplasma site at different states of activation dependent on the reverse bias voltage level. The distinguishing feature of this channel is its regular circular shape and the fact that it is not associated with dislocation network nodes.

No clear correlation between $n^{+}p$ junction leakage current and EBIC contrast was discovered. The reverse bias current measured, varied from device to device (for a single device wafer) within the wide range from 11 nA to 250 nA.

(b) Fig. 44 shows the I-V characteristic of another diode which revealed the microplasma switching effect appearing at the

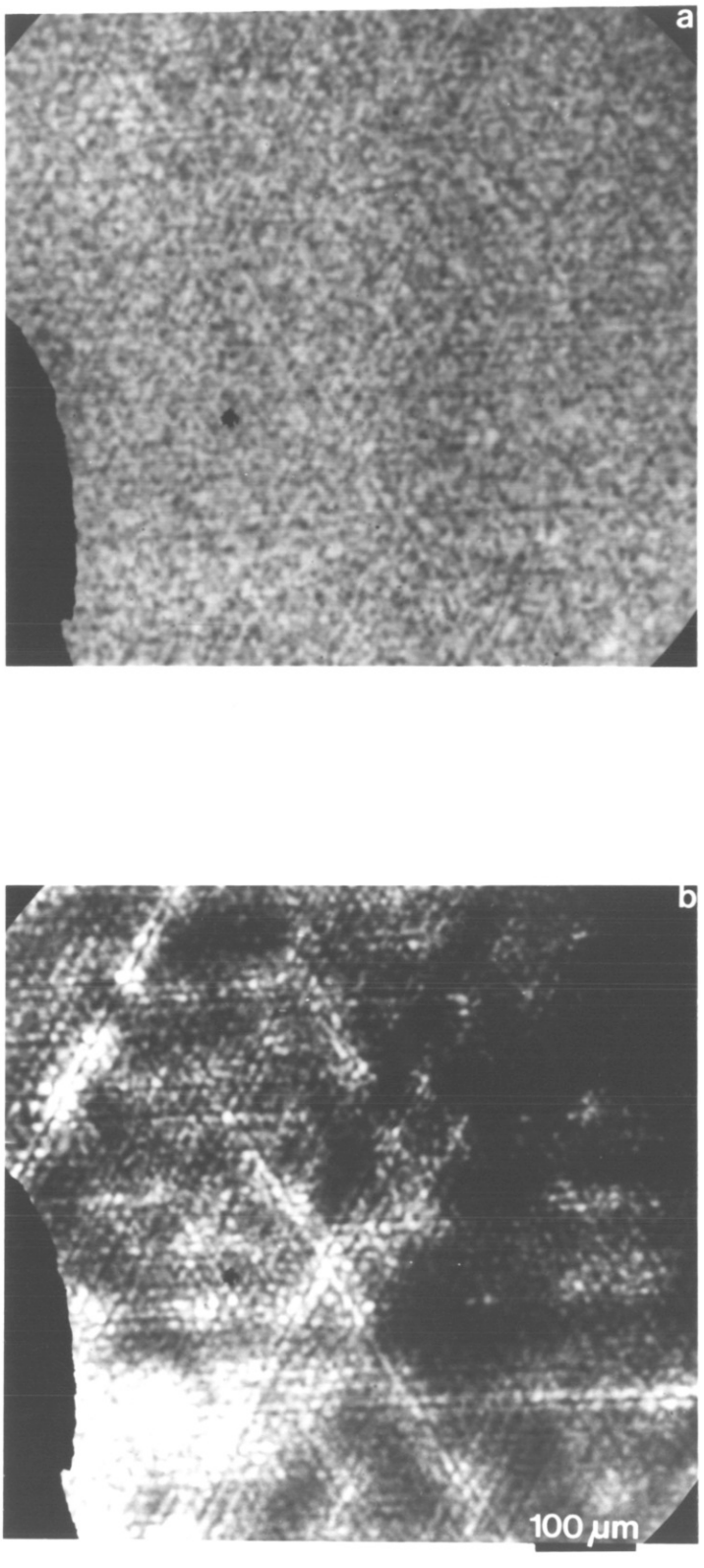


Fig. 42 - SEM CC micrographs of a device with high density of line defects at biases (a) and OV and (b) 400. (Diode D2)

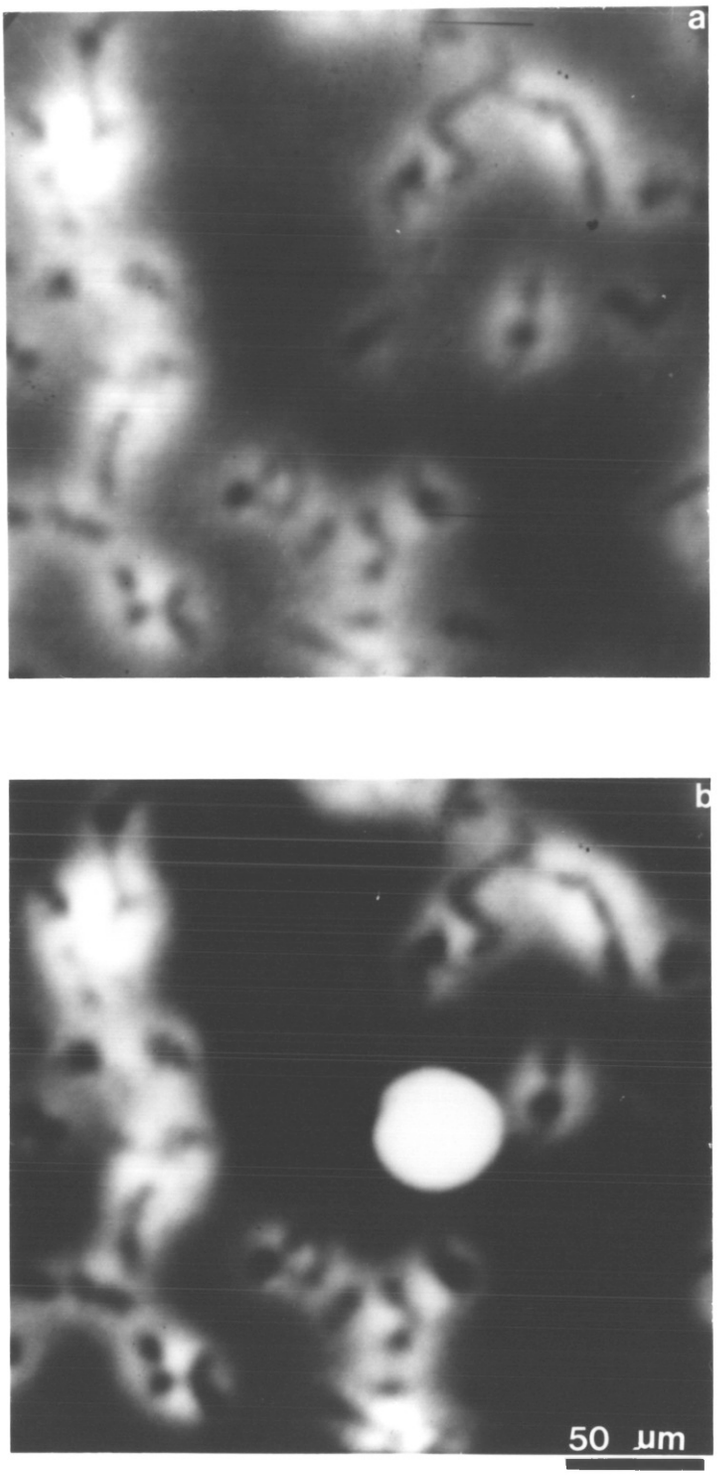


Fig. 43 - SEM CC micrographs of a device with a low density of "deep going" dislocations, at biases (a) 50V and (b) 110V. The round white spot is presumably a region of reduced junction depth (diffusion void) due to the presence of an oxide cap on the surface during diffusion. (Diode D3)

avalanche breakdown "knee". Fig. 46 presents EBIC micrographs of the active area of the same device as recorded at different electron beam energies and bias voltages. When observed under an 18 keV electron beam, the first "active" microplasma appeared as a bright spot marked M1. Further increase in the bias voltage revealed another channel located at the perimeter of the n^+ region (see M3). The CC micrographs in Fig. 46 were collected from the device cooled down to liquid nitrogen temperature. The SEM CC mode "cold" stage described in section 3.2. was used for this purpose. The CC studies of microplasma sites carried out at low temperatures were advantageous as compared to those at room temperature in terms of improved signal to noise ratio and the possibility of using a lower range, and more stable power supply for d.c. biasing. Cooling of the sample allowed the breakdown voltage V_{br} to be brought down to more easily achievable voltage levels. The RTAPD breakdown level is defined as the minimum voltage necessary for the microplasma to start switching the junction current. The reduction in breakdown voltage with temperature when monitored for M1 was found to follow an exponential form as shown in Fig. 45.

The CC micrograph of Fig. 46(b), was taken with the device biased just below the breakdown voltage i.e., 98 V at 77 K. The micrograph in Fig. 46(c), was recorded at 104 V bias i.e., 3 V above the breakdown level of the secondary microplasma. In the last example, the overvoltage applied

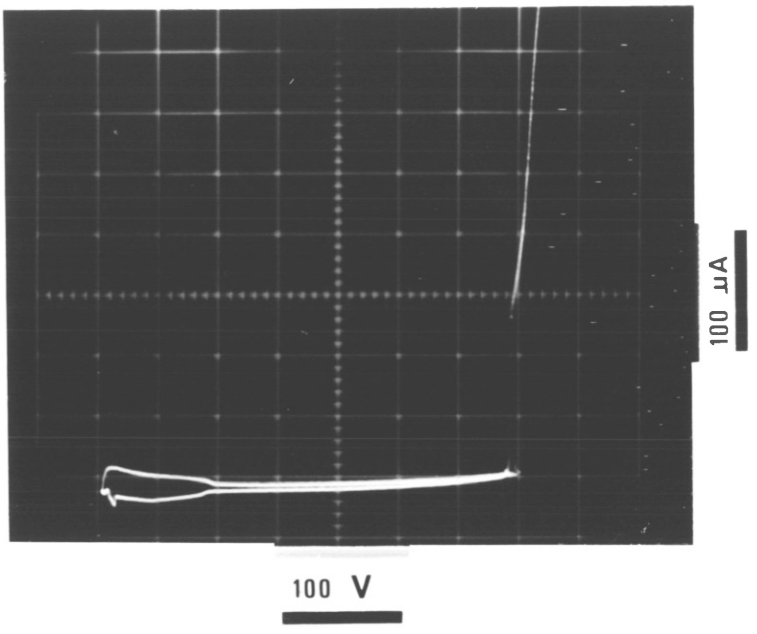


Fig. 44 - "Soft" I-V characteristic exhibiting microplasma (M1) switching noise at the breakdown "Knee".

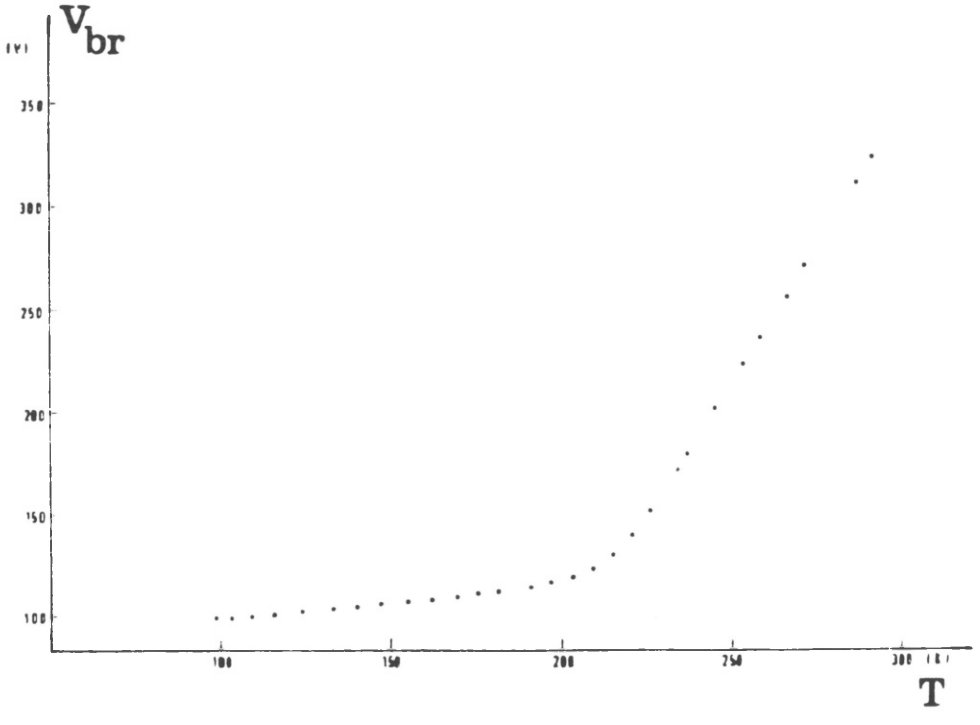


Fig. 45 - Breakdown voltage V_{br} vs temperature relation recorded for the device represented in Fig. 44 and 45.

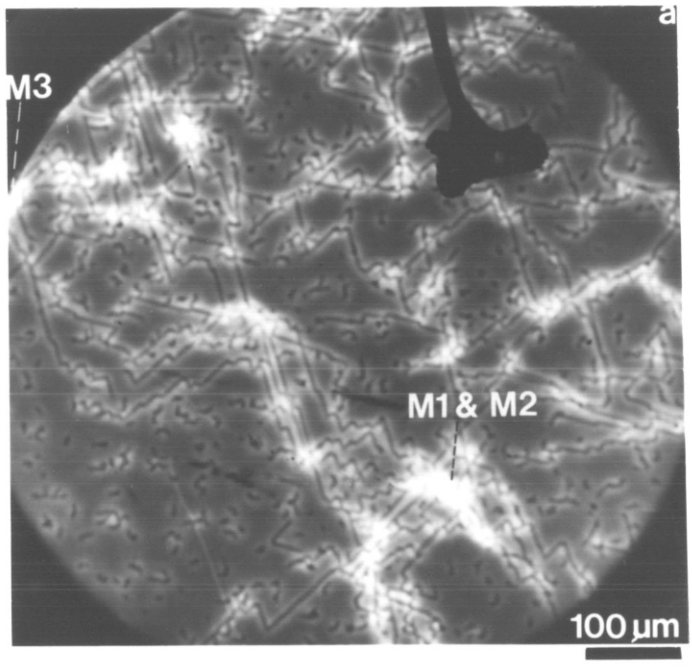


Fig. 46

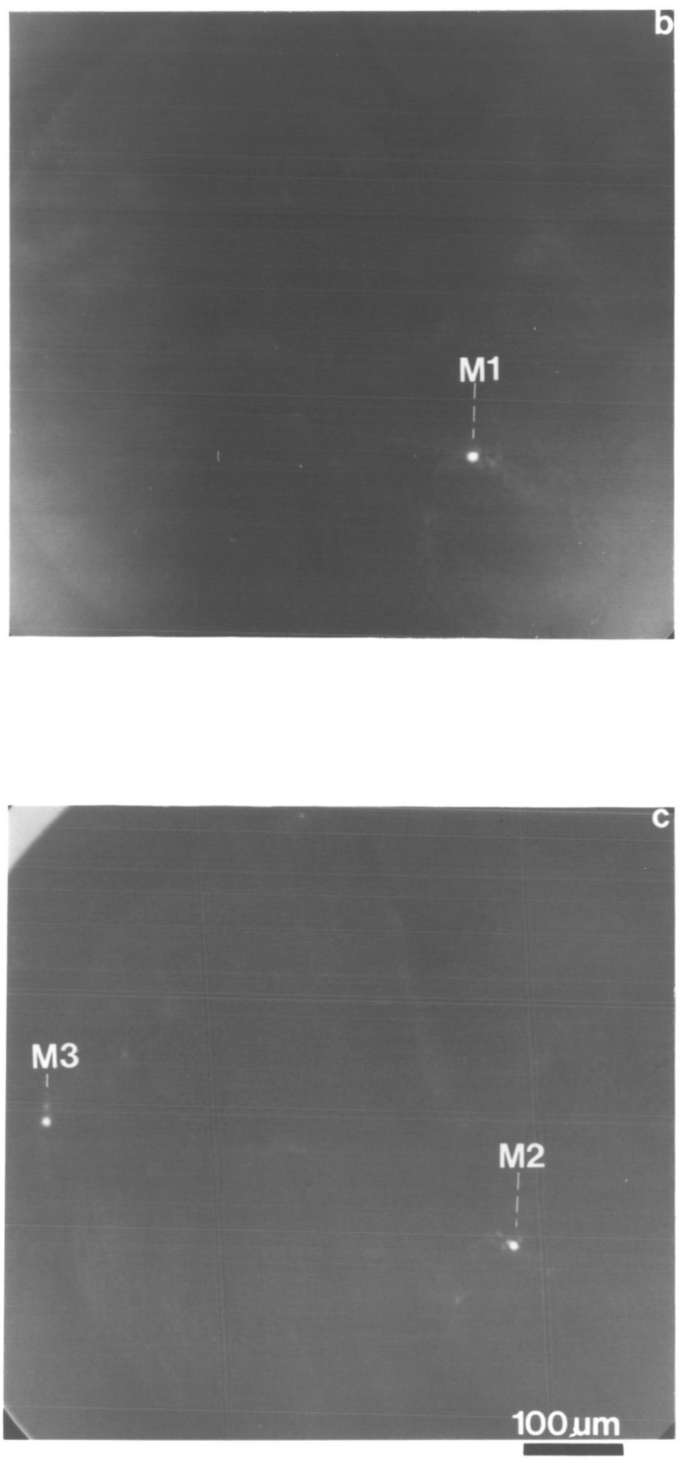


Fig. 46 - Influence of bias voltage and energy of primary electrons on the EBIC contrast. Strong contrast (a) V_{br} = 98V (breakdown level), E_b = 25 KeV; weak contrast (b) and (c), E_b = 17 KeV, V_{br} = 98 V and 104 V respectively. T = 77 K.

was high enough so that both microplasma sites were essentially "quiet" (above the instability region on the I-V curve). The separation voltage of the two instability regions corresponding to the switching action of primary (M1) and secondary channels, was 2.8 V at 77 K and 35 V at room temperature.

Direct evidence linking bright spot microplasmas to soft characteristics and noise was provided by BEVE I_{sc} line scan studies as shown in Fig. 47 and 48. This presents a number of records of the CC current for scans along a line passing through the microplasma spot. The microplasma appears as the peak M1 in Fig. 47(a). The bias voltage was set at the value for M1 to turn on, i.e., to commence steady avalanche current generation and contribute a step to the reverse I-V characteristic of the device. Irregular noise was then generated by the microplasma site defect at M1, except when the electron beam was incident on M1 directly. Similar microplasma noise appears in the micrograph of Fig. 52(b) in the form of the speckled background.

The set of CC line scans of Fig. 48, demonstrates the effect of bias voltage on the electrical activity of the microplasma channels M1 and M2.

Microplasma M1 is identified in Fig. 48(a) as the point of the highest current enhancement factor. Fig. 48(b)

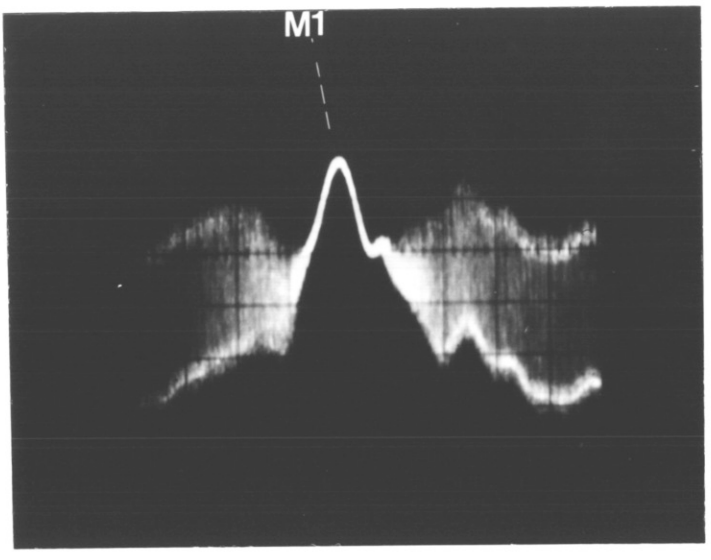


Fig. 47 - EBIC Line scan, at a temperature of 77K. The microplasma M1, at the smooth peak position, switched between two current levels except when the electron beam was incident on the microplasma itself, i.e., when it was continuously "on".

reflects the situation when the overvoltage has been applied. The electron beam now converts the noise from the "half on" characteristic to the "fully on" type as it scans across the spot M1. It is evident from Fig. 47 and 48(a), (b), that a single microplasma (M1) is responsible for the appearance of noise observed at the "knee" of the I-V characteristics of Fig. 44. It can also be seen (Fig. 48(c)that at higher bias voltage values, microplasma M1 becomes "quiet" and that the surrounding CC current peaks P1, P2, P3 become more pronounced. At still higher overvoltages (V_{br} = 101 V) peak M1 disappears (Fig. 48(d)) and the area adjacent to M1 is activated to work as a secondary microplasma M2 simultaneously with another channel M3 of Fig. 46(c).

In the next part of the experiment a single pulse overvoltage was superimposed onto the d.c. bias voltage and applied to the diode. The pulse technique was used in order to provide a synchronisation between the microplasma switching sequence and the oscilloscope sweeping rate. The experimental set up used was described in section 3.3. The sample was initially d.c. biased. The bias voltage was set at 0.05 V below the breakdown voltage of the first microplasma (see Fig. 21(b)). The channel M1 could be set at any working condition by means of the pulse overvoltage. The overvoltage was initially 0.7 V, so that the microplasma did not reach its "half on" stage. The pulse width was adjusted to be 100 μs. The microplasma

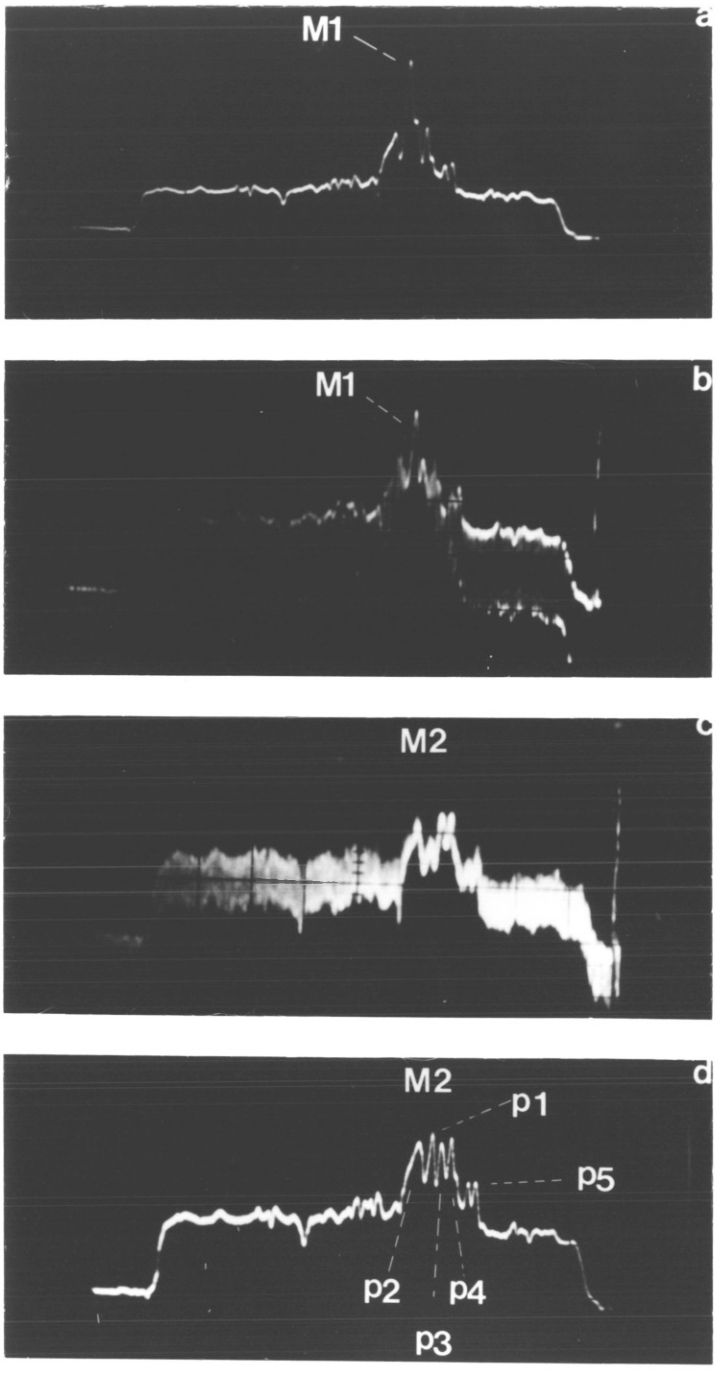


Fig. 48 - CC current line scan traces recorded across two microplasma sites M1 and M2 at reverse biases of (a) 97.5V, (b) 98V, (c) 100V and (d) 101V. Regions where the trace is sharp produced steady CC currents when electron beam bombarded. The jagged regions arise when the noise generated at a microplasma site elsewhere and superimposed on the CC current generated by the beam incident on that point is relatively large. Peaks P1, P2, P3, P4, P5 indicate the secondary microplasma sites marked collectively as M2.

noise appeared as a square waveform when observed on the oscilloscope. The noise pulses were of different width. The micrograph in Fig. 49(a) reveals such a microplasma noise burst containing three single pulses. The noise current pulses were of 4.1 μA amplitude (at 77 K) which was independent of the biasing pulse overvoltage. When the overvoltage was increased up to 1 V so the microplasma was set at its "half on" characteristic, the width of the pulses increased considerably and the switching rate gave the well known impression (Kikuchi and Tachikawa 1960) of the appearance of "negative" pulses. One of these pulses is shown in Fig. 49(b). Further increase in overvoltage caused the gradual reduction in the width of the "negative pulses" and eventually their complete disappearance. The latter situation corresponds to the condition that the microplasma remains "on" indefinitely (becomes quiet).

Further observations were based on the measurements of the delay time which occurred between the application of the overvoltage pulse and the actual start of the avalanche discharge. Small amplitude voltage pulses were superimposed onto the large d.c. - bias level. The pulse overvoltage was set at 1.2 V so that the microplasma M1 could reach its "on" state. The biasing module of the CMDS provided the facility for the accurate adjustment of the d.c. bias voltage. The d.c. bias level was held all the

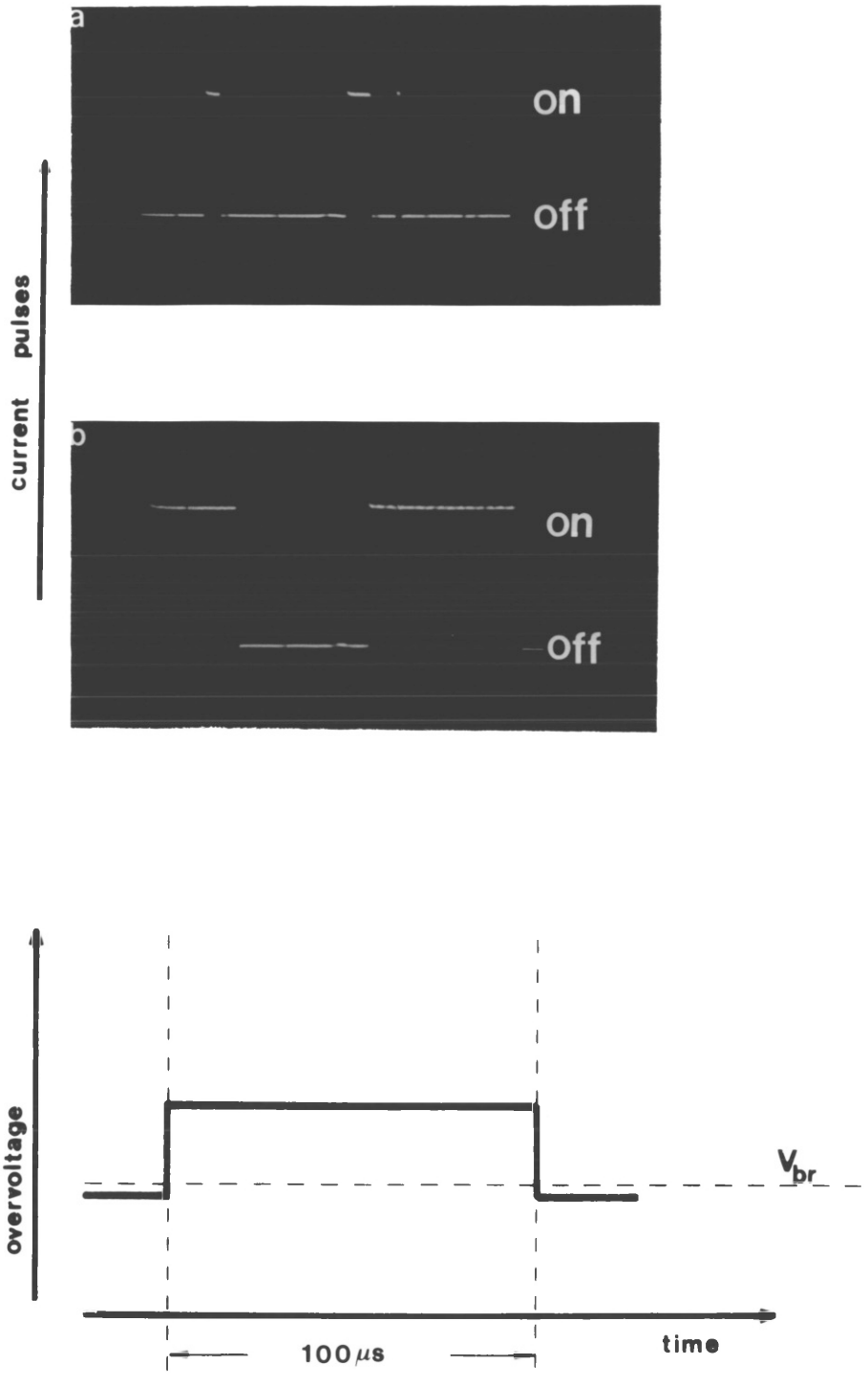


Fig. 49 - Microplasma noise pulses at different overvoltage levels (a) 0.7V and (b) 1V.

time at 0.05 V below the breakdown level. The number of voltage pulses which resulted in the avalanche breakdown was determined by counting the avalanche current discharges using a digital counter. The overvoltage pulse length was varied. For each selected pulse length an equal number of 500 pulses was applied with a rest period of 1 sec, between successive pulses. This was sufficient to secure that the effects of previous avalanches decayed. The results are presented in Fig. 50. The proportion of applied pulses during which breakdown did not occur (N_x), was observed to decrease exponentially with pulse duration (Fig. 50). The mean delay time t_d was then calculated using (after Nield and Leck, 1966):

$$(26) \qquad N_x/N_o = \exp(-t_1/t_d)$$

where N_x is the number of applied voltage pulses that do not initate breakdown; N_o is the number of pulses applied and t_o is the pulse duration. The delay time measured was 26.8 ms at 83 K and 20.9 ms at 101 K for the same overvoltage level.

In the following experiment a train of single pulses was replaced with cycles of double overvoltage pulses of the same level. The first pulse was used to precondition the channel and the second for recording breakdown time delays. This way the influence of previous avalanches

on the delay time to avalanche, could be evaluated. The delay times of the breakdown on application of the second pulse, were measured as a function of time interval t_s between the two pulses. Observations were made at 77 K.As previously, the double pulse trains were triggered automatically, one second being allowed between pairs of pulses so as to ensure no interaction. A typical set of results is shown in Fig. 51. Values of t_t represent the time constant characteristic for the re-emergence of the carriers due to traps emptying. As they emerge from traps the carriers reinforce the trigger particles already present. Following Nield and Leck (1967) t_r was calculated using equation:-

$$(27) \qquad t^{-1} + t_t^{-1} = t_d^{-1}$$

t - represents the observed delay time on application of the second pulse; t_d - refers to the single pulse case at the same overvoltage.

Discussion

The zig-zag lines in the SEM CC micrographs taken with reverse bias applied, were seen as dark lines lying within bright stripes. The dark line contrast was bias independent. The bright stripe contrast appeared after applying bias voltage to the diode.

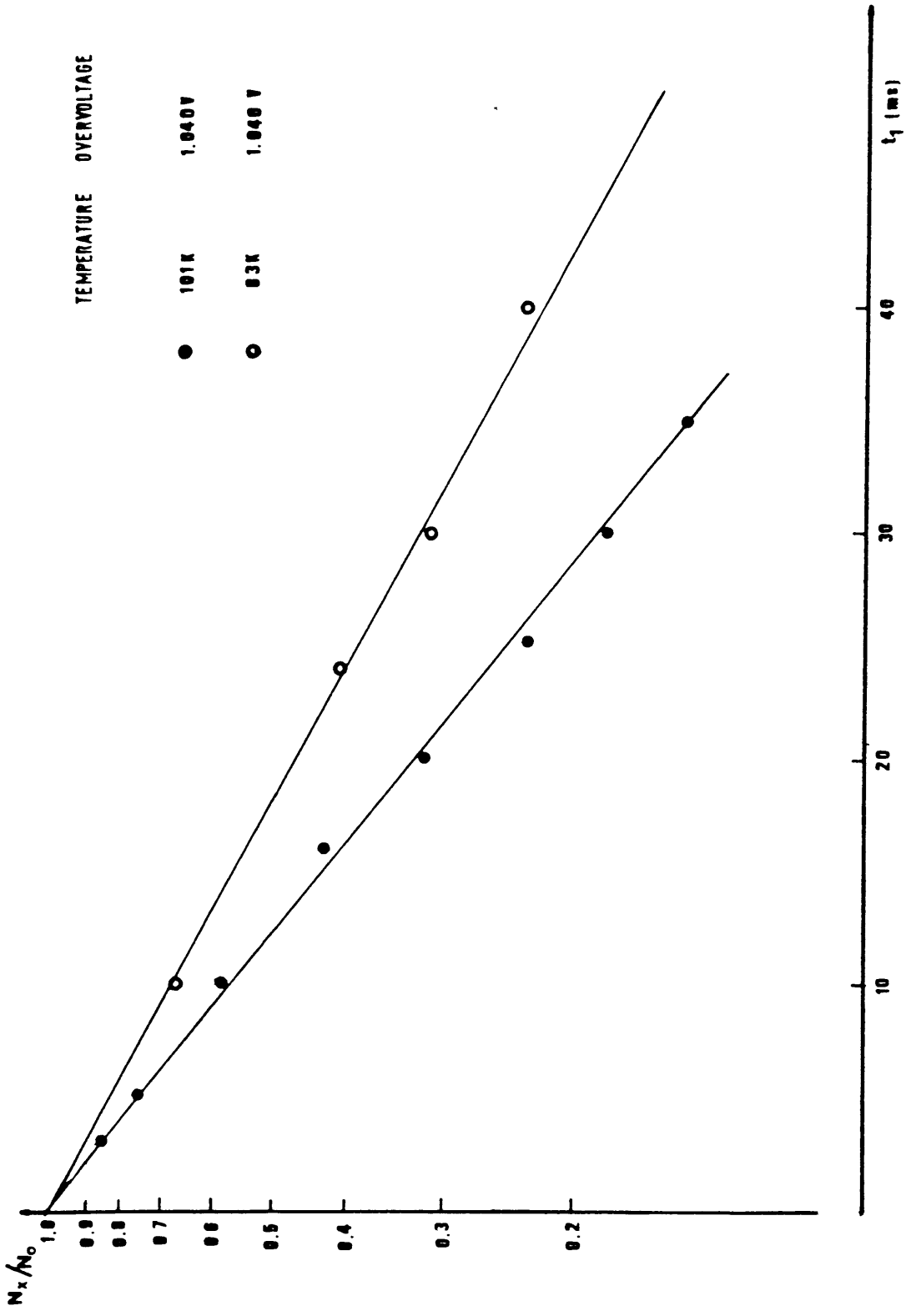


Fig. 50 - The fraction of the applied pulses not leading to breakdown N_x/N_o, shown as a function of time interval t_1 from the instant of application of the overvoltage pulse. The operating temperatures are marked on the lines.

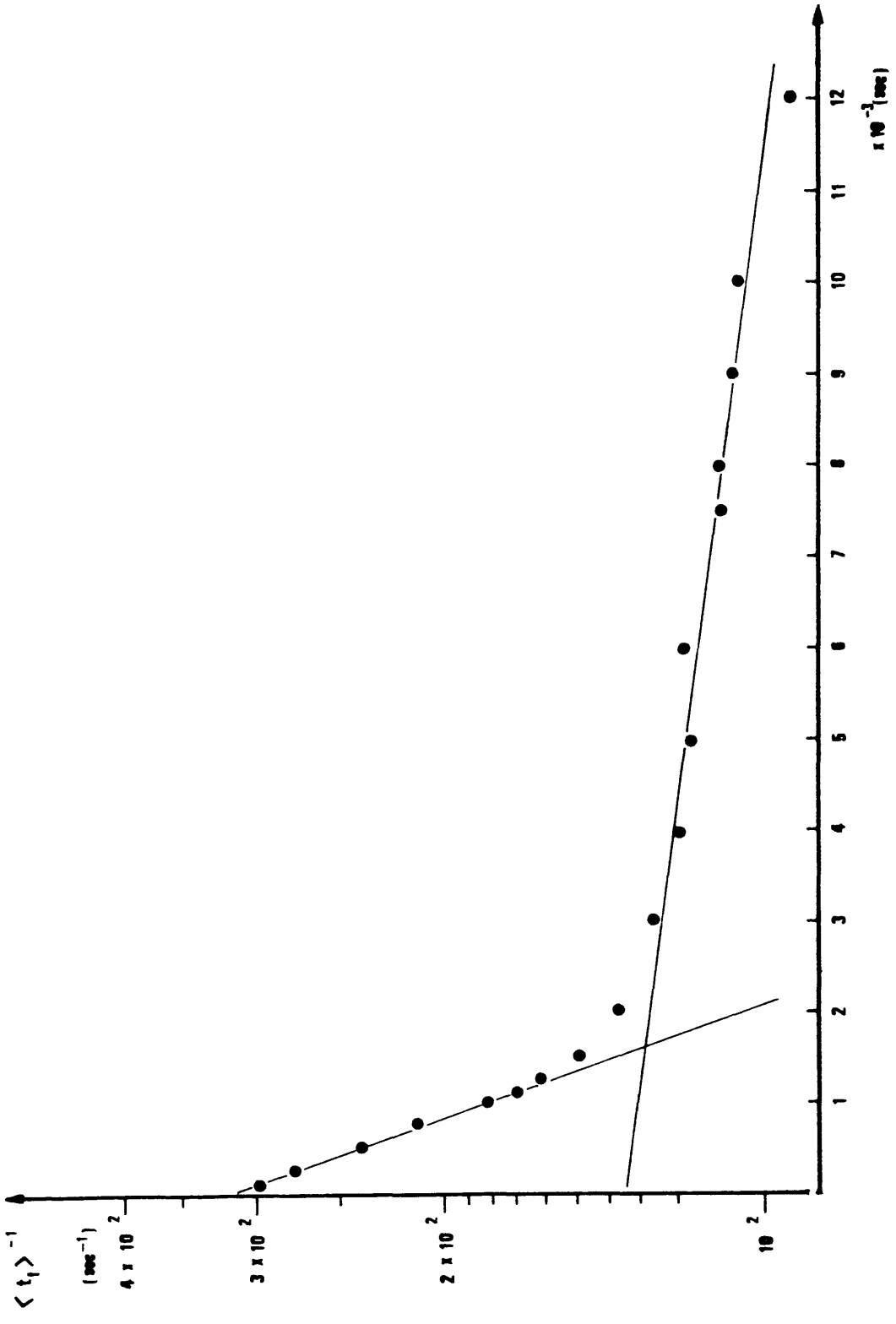


Fig. 51 - Decay of the contribution to the breakdown rate due to trap relaxation.

The bright stripes observed in the EBIC mode indicate junction current enhancement sites. The microplasma channels were identified as parts of the bright stripes with the strongest current enhancement effects (as observed at elevated bias voltages). Such channels were irregular in shape and were most frequently seen at nodal points where several dark line defects cross each other.

In isolated cases a different type of circular microplasmas were observed. These could not be visibly related to any dark line defects (Fig. 43). Varker (1971) reported similar microplasmas, found in silicon Zener diodes. The circular junction channels were shown to arise due to diffusion voids caused by residual oxide caps on the diode surface. Antecendent breakdown in such voids was suggested to occur as a result of the small radius of curvature in the junction surrounding the void. Analogy in the EBIC appearance and other electrical effects (i.e., microplasma noise and very soft I-V characteristic) may suggest that the circular defects in the RTAPDs originated from the same reason.

The individual microplasmas were found to switch on and off in an irregular manner, the current through them occurring in rectangular pulses all of the same height but following no regular pattern. With progressively increasing bias voltage the current pulses become longer and the off-period

shorter, until a stable condition was reached with a steady current flowing along the microplasma channel.

Direct evidence linking bright spot microplasmas to soft characteristics and noise was provided by EBIC line scan studies as shown in Fig. 48. In the examined diode basically three efficient channels were detected. Two of them were activated at the same bias voltage. It is found that the initially activated microplasma M1 was surrounded by secondary sites marked collectively as M2. Both M2 and M3 were observed to switch the junction current at the same time although above the voltage level where M1 becomes "quiet". The presence of several secondary microplasmas resulted consequently in the increase of the microplasma noise frequency and reduction in the noise amplitude since the total current has been distributed over several discrete regions as compared to M1 working in isolation. The characteristic features and differences between I-V characteristics observed for D1 and D2, can also be interpreted in terms of numbers of the microplasma sites being active at the same time. SEM EBIC examination of D2, revealed numerous small size current channels within the n^+ region. In consequence the microplasma noise amplitude observed for D2 was relatively small (at the breakdown onset), since the avalanche current was distributed over many simultaneously switching channels. In contrast, the isolated microplasma (marked M in Fig. 40) active at the

breakdown "knee" in D1, was associated with large amplitude microplasma noise, observed in Fig. 39(b) as the extensive discontinuity in the I-V characteristic.

It was typical to observe that the number of the active junction channels consistently increased with the overvoltage for all the defective diodes examined. In D1, with fewer effective microplasmas, the transitions between primary and secondary microplasmas could be easily observed. In D2 on the other hand the channels activated at different overvoltages, exhibited considerable overlap so that an impression of a continuous and correct I-V curve appeared (Fig. 39(a)).

The pulse technique applied for the evaluation of the breakdown characteristics in RTAPDs was similar to that used by Nield and Leck (1966) for the study of an avalanche discharge in silicon. However, the experimental arrangement used for the purpose of the present work was different. Essential advantages of the experimental set up described in paragraph 3.3. are as follows:-

- Small amplitude a.c. bias pulses and corresponding avalanche breakdown current can be monitored simultaneously as two separate waveforms.

- Sample under examination can be placed within the SEM specimen chamber allowing also EBIC observations to be performed and the results immediately correlated.

In the part of the experiment where single pulses were used only, the statistical nature of the breakdown mechanism was firstly verified. The difference in t_p corresponding to different temperatures confirmed that the time delays become shorter if the temperature of the junction is increased. This is to be expected since the increase in temperature increases the number of charge carriers present in the channel, therefore, increasing the chance of avalanche formation in any given time interval. Fig. 51 represents the situation when double voltage pulses were applied to the junction. It was evident that previous history of the channel influences the time delays. The time delays were substantially shortened as a consequence of the recent avalanche discharge. Such an effect was observed for pulse separation times t_s, smaller than 50 ms. Nield and Leck (1966) and Nuttal and Nield (1975) have attributed similar effects to the presence of charge carrier traps located at microplasma sites. They have postulated that the traps become filled during the previous avalanche. Then the subsequent time delays appear shortened due to the delayed re-emergence of trapped carriers, which as they emerge from traps, reinforce the trigger particles already present. Through the application of the pulse technique Nuttal and Nield were able to gain

quantitative information about trap recovery and its activation energy. The observed reduction in the delay time was an order of magnitude when recorded at 83 K. Shortening of the delay time has not, however, been observed at room temperature.

In conclusion it has been shown that the microplasma sites discovered in RTAPDs are of the conventional type in terms of their electrical properties. The results suggest that some of these microplasma sites may be associated with the presence of trapping centres.

The observations based on the application of the pulse technique as described above have been performed so far without an electron beam being applied. The introduction of a controlled amount of charge carriers at the microplasma site by the use of the electron probe may provide a convenient means of varying the experimental conditions. Such a technique may supplement the well known SEM SDLTS method and appears to be worth further exploration.

4.2.3. The SEM Contrast Mechanisms of Line Defects

Charge Collection Contrast

Observations of the visibility of dark lines as a function of beam voltage and thus penetration depth, were carried out. The results of such observations are represented in Fig. 46(a) and (b) for a reverse biased diode. The first micrograph (Fig. 46(a)) was recorded when a 25 KeV (R_e = 4.8 um) electron beam was used. The bias voltage applied was set just below the diode breakdown level. The EBIC contrast observed was the usual linear white-black-white pattern. The effect of the reduction in the electron beam energy (penetration depth) can be noticed from the micrograph shown in Fig. 10(b). This was recorded when applying the same reverse bias voltage as previously (Fig. 10(a)) across the diode. The electron beam power was maintained constant but the energy of the electrons was reduced to 17 KeV. It could be seen that the familiar line pattern contrast now faded away. The only contrast feature still prominent on the image was a single bright spot indicating the most efficient microplasma site. Micrograph (b) was taken using higher (an order of magnitude) sensitivity range set at the head amplifier. An attempt to restore the original contrast by applying a considerably higher electron beam current, did not prove successful. At this stage it was strongly suspected that the characteristic line patterns originated from the planar

network of diffusion induced misfit dislocations, located at a certain depth between the sample surface and the n^+p junction. Hence, an electron beam of relevant energy was required in order to penetrate down to the depth of dislocations, so some contrast could be obtained.

Another type of SEM RTAPD specimen was prepared in an attempt to define the precise location of the dark line defects within the n^+ layer. Several RTAPD samples were gradually thinned down from the top (n^+ surface), as shown in Fig. 52. A "test" RTAPD was used to establish initially that the plane of the defects was located within the range from 2 to 2.8. μm below the surface. When re-examined in the SEM the sample (having removed 2 um of the top layer) still revealed a network of dark lines. When thinned again down to 2.8. μm below the surface, it was partially cleared of the dark line contrast within the central region. The next sample was first thinned down to approximately 2 μm below the original surface. During the next stage the sample was re-examined in the SEM after each 0.1 μm thick layer was removed from the surface. This way, it was established that the planar network of defects was located at the depth of 2.5 μm. At this depth the dark line contrast started to vanish at the very centre of the specimen. Two additional experiments have confirmed this result within the same tolerance. The samples were selected from the same device wafer.

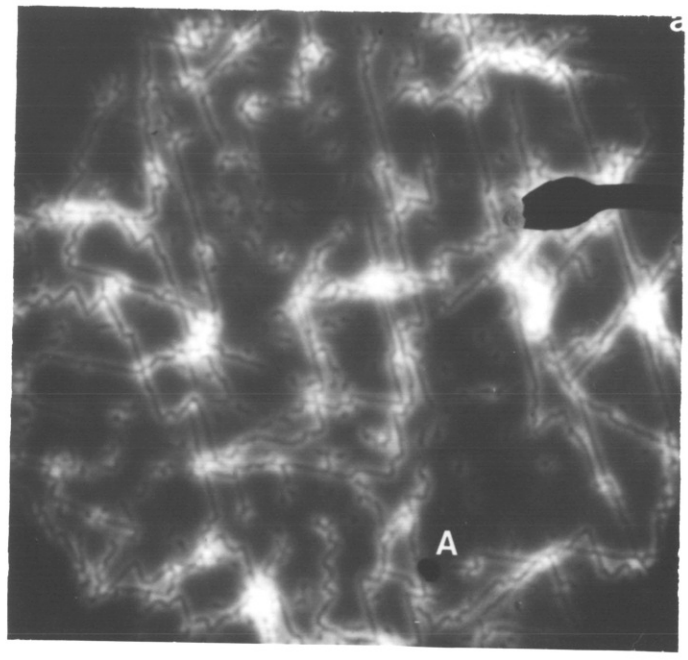
Control of the thinning process relied on precision timing. The speed of the ion beam polishing was measured beforehand using the same type of sample. This was 1.9 μm/h, referring to the following settings applied at the (ION-TECH) ion beam thinner:-

ion beam current - 1.2 μA
ion beam voltage - 6.1 KV
working angle - 12°

The thickness of the removed layer of silicon was evaluated in each case by the use of the profile testing instrument (TAYLOR-HOBSON talystep).

Fig. 52 and 53, summarise the results obtained in the experiment.

Fig. 52(a) is the SEM CC micrograph of a RTAPD before the removal of the top surface layer at a bias of 380 V. Fig. 52(c) was taken after the removal of a layer 3.8 μm deep. In the second case, the sample was unbiased. Fig. 53 presents a set of Talystep profile scans from the same specimen. The first one (Fig. 53(a)) corresponds to the initial situation before removal of the top layer. The next profile reflects the situation when the EBIC dark line contrast started to disappear at the very centre of the



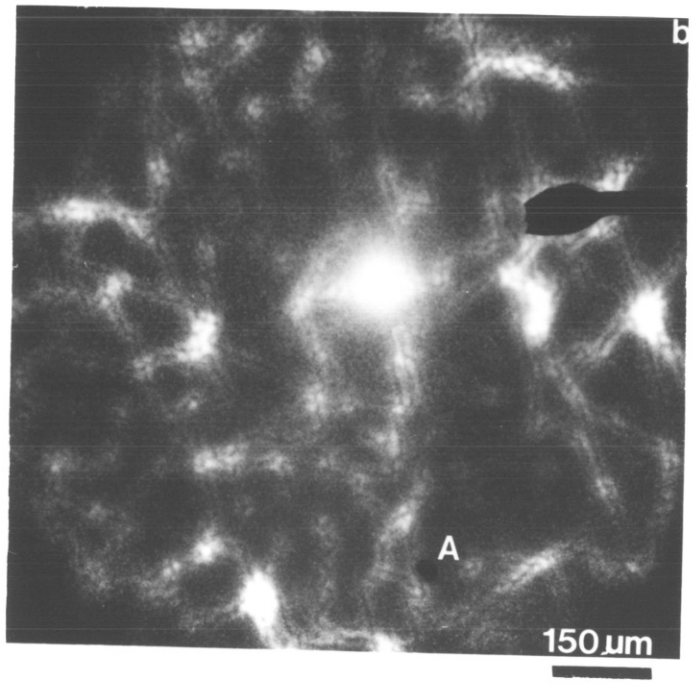


Fig. 52

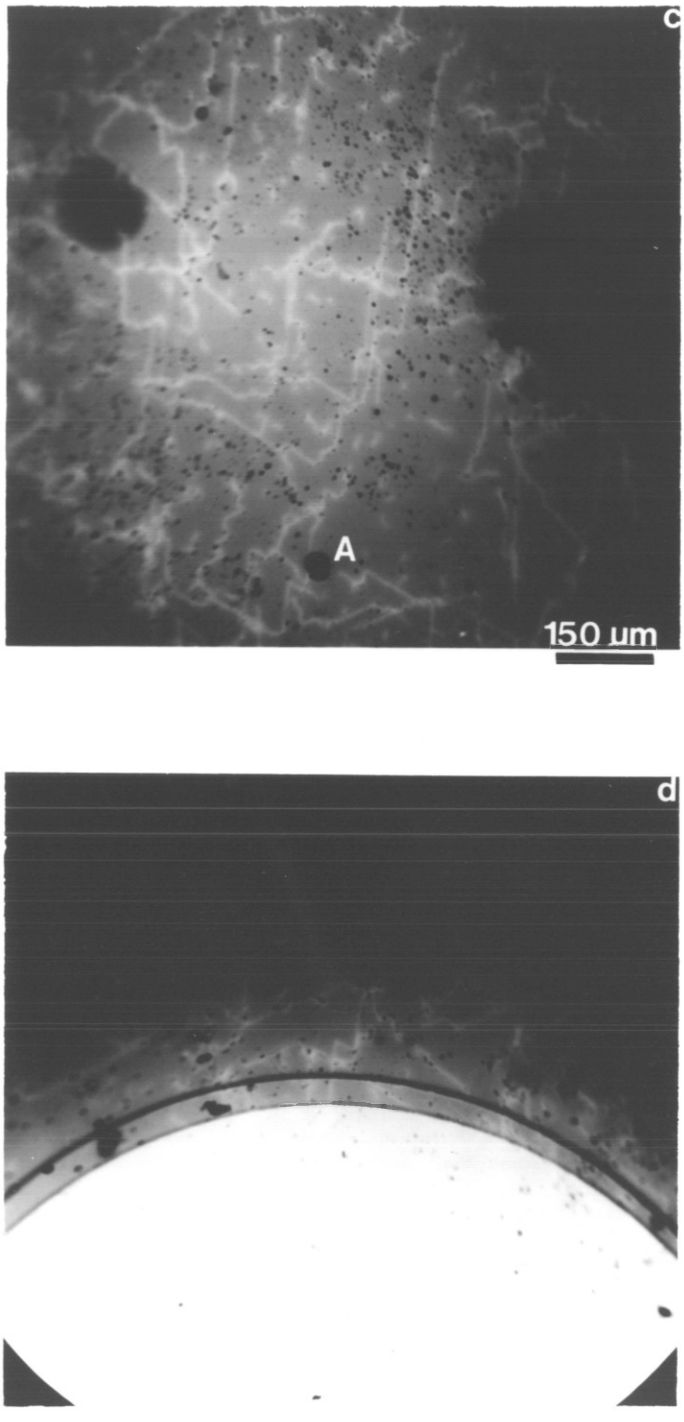


Fig. 52 - SEM CC micrographs of an RTAPD before removal of the top surface layer at a bias of (a) 380V and (b) 381 (breakdown level), and after removal of a layer more than 2.4 µm deep as in Fig. 53(b) showing (c) the central n^+p area and (d) a part of the diffused n^+ region outside the implanted p region.

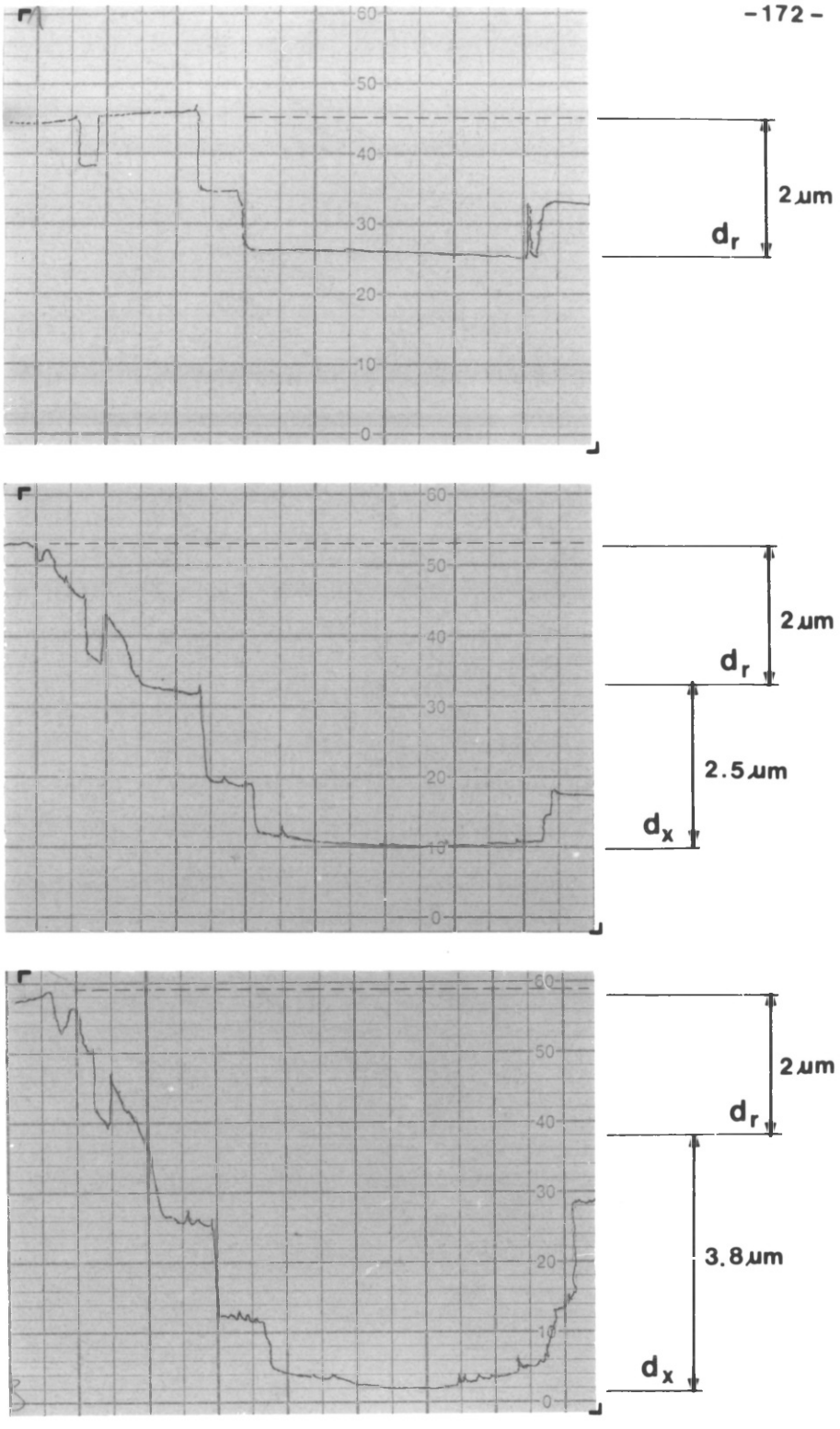
device. This is after removal of a 2.5 μm thick top layer. The last profile has been recorded after prolonged thinning, down 3.8 μm. Each of these profiles was taken with the testing probe scanning across the centre of the device and following approximately the same track.

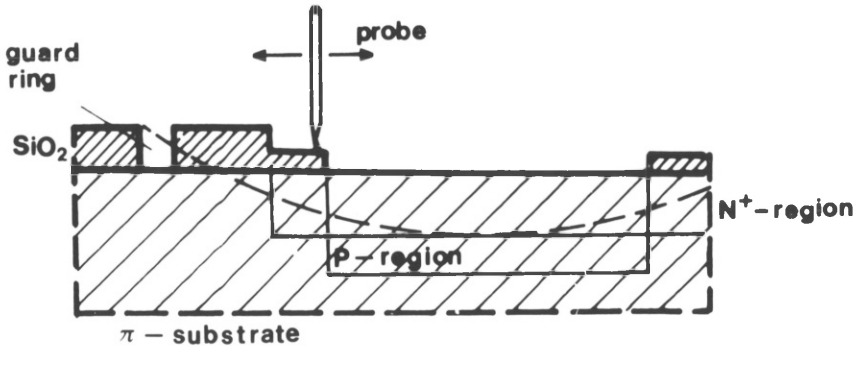
Discussion

It can be seen by comparing the micrographs shown in Fig. 12(a) and (b) that after thinning down more than 2.5 μm from the top, the pattern of lines is still present but only the bright stripe contrast remains, following the same geometry. The bright stripe contrast is ascribed to the charge collecting n^+p junction being "less deep" below the lines of the dislocation network due to "dislocation retarded diffusion". The reduced depth increases the number of the injected carriers reaching the junction and contributing to the brightness of the picture at such points. Under high reverse biases this effect is seen even in specimens not thinned as in Fig. 52(a), because under reverse bias the depletion region widens, reaching significantly nearer to the surface along these shallow junction lines.

The dark line contrast, seen even in the absence of specimen bias, was presumed to be due to recombination at the dislocations of the diffusion induced misfit network.

Faster recombination would eliminate more of the electron beam injected carriers before they could be collected by the n^+p junction and so reduce locally the signal and the picture brightness. The linear white-black-white contrast observed, is then due to two separate mechanisms.





d_r – reference level

d_x – effective crater depth

Fig. 53 - Talystep profiles taken with the testing probe (d) scanning across the centre of the device and following approximately the same track. Each of the profiles (a), (b), and (c) represents different amounts of material being removed from the top n^+ layer i.e., 0, 2.5 and 3.8 μm respectively.

4.2.4. The Nature of the Dark Line Defects and Microplasma Sites

In order to investigate the nature of the anomalous EBIC contrast observed in faulty RTAPDs, a more comprehensive study of the diffused n^+ region was carried out using high a voltage (1 MeV) TEM.

Specimens were prepared for the TEM examination by first photoelectropolishing from the bottom side ($p^+ \pi$) and next ion beam thinning from the top (n^+ - side). A diagram of the processed sample is shown in Fig. 54.

Fig. 55 shows a transmission electron micrograph of the n^+ region of the diode D2 exhibiting a dense network of dislocations. It can be seen that within the n^+ material a dislocation network is present. The spreading of the network and the length of the component dislocations indicate that the dislocations lie in the plane of observation i.e., in the (111) plane, which is also the most active glide plane. In cases where dislocations leave the (111) plane to terminate at the specimen surface, an abrupt change in direction takes place revealed by the wavy appearance of the dislocation (explained by the dynamical theory of diffraction contrast (Hirsch et al. 1965)). The observed array of dislocations is unstructured i.e., no stringent regularity occurs. Most of the dislocations were pure edge in character with Burgers vector a/2 ⟨110⟩, lying in the ⟨211⟩ directions. These are exactly the same as

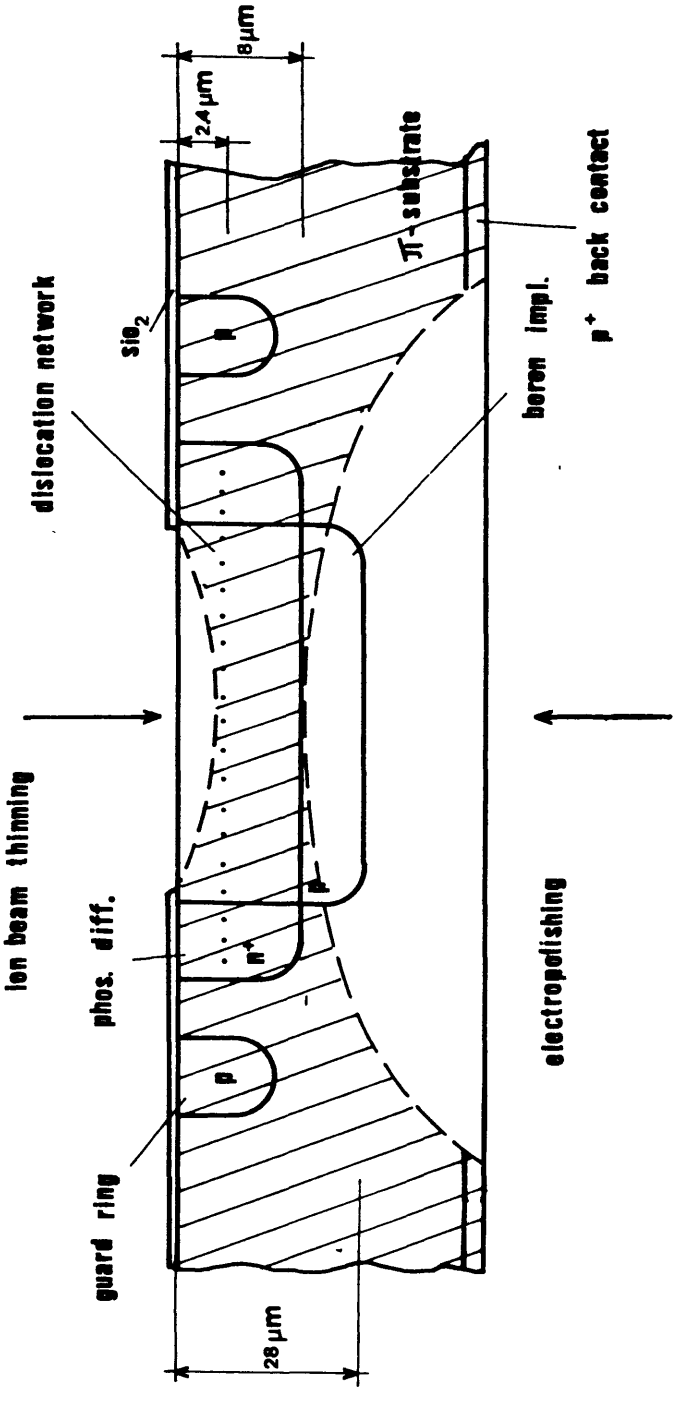


Fig. 54 - Schematic diagram of the double thinning of an APD for TEM observations on the misfit dislocation network. Deep electropolishing from below was followed by shallow ion-beam thinning from the top.

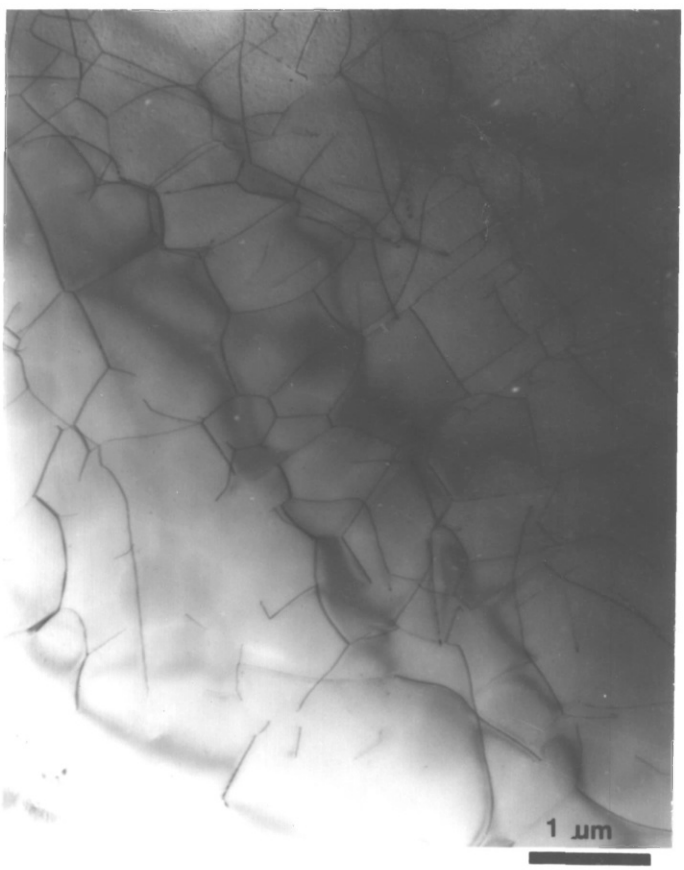


Fig. 55 - TEM micrographs of the area of misfit dislocations network.

those reported by Joshi and Wilhelm (1965) who concluded that the dislocation networks are the result of the relief of the stress gradient introduced by a diffused-phosphorus impurity gradient. The nature of the dislocations was determined by observing the visibility of the dislocations when using (220) and (311) beams to produce the image. This is the standard technique and further details can be found in Edington (1975).

Another sample examined in TEM has been selected from the group of diodes characterised by the lowest possible densities of EBIC dark lines within the n^+ region. An SEM EBIC micrograph obtained from the selected diode is shown in Fig. 56. It shows diffraction contrast from a long dislocation discovered within the area marked with a circle on the EBIC micrograph of Fig. 74. The spacing between the dark lines was large enough to provide evidence that the dark EBIC line within the circle corresponds to the single dislocation. The network represented by the dislocations in Fig. 56 was composed of 60^o dislocations being partially screw in character. The Burgers vectors were of the type 1/2 <110> and were parallel to the <110> directions.

Fig. 57 represents samples characterised by dense networks of dark line defects. In this type of sample it was characteristic to observe the presence of networks of dislocations accompanied by a spotty contrast. Large, elongated precipitates and impurity segregation along

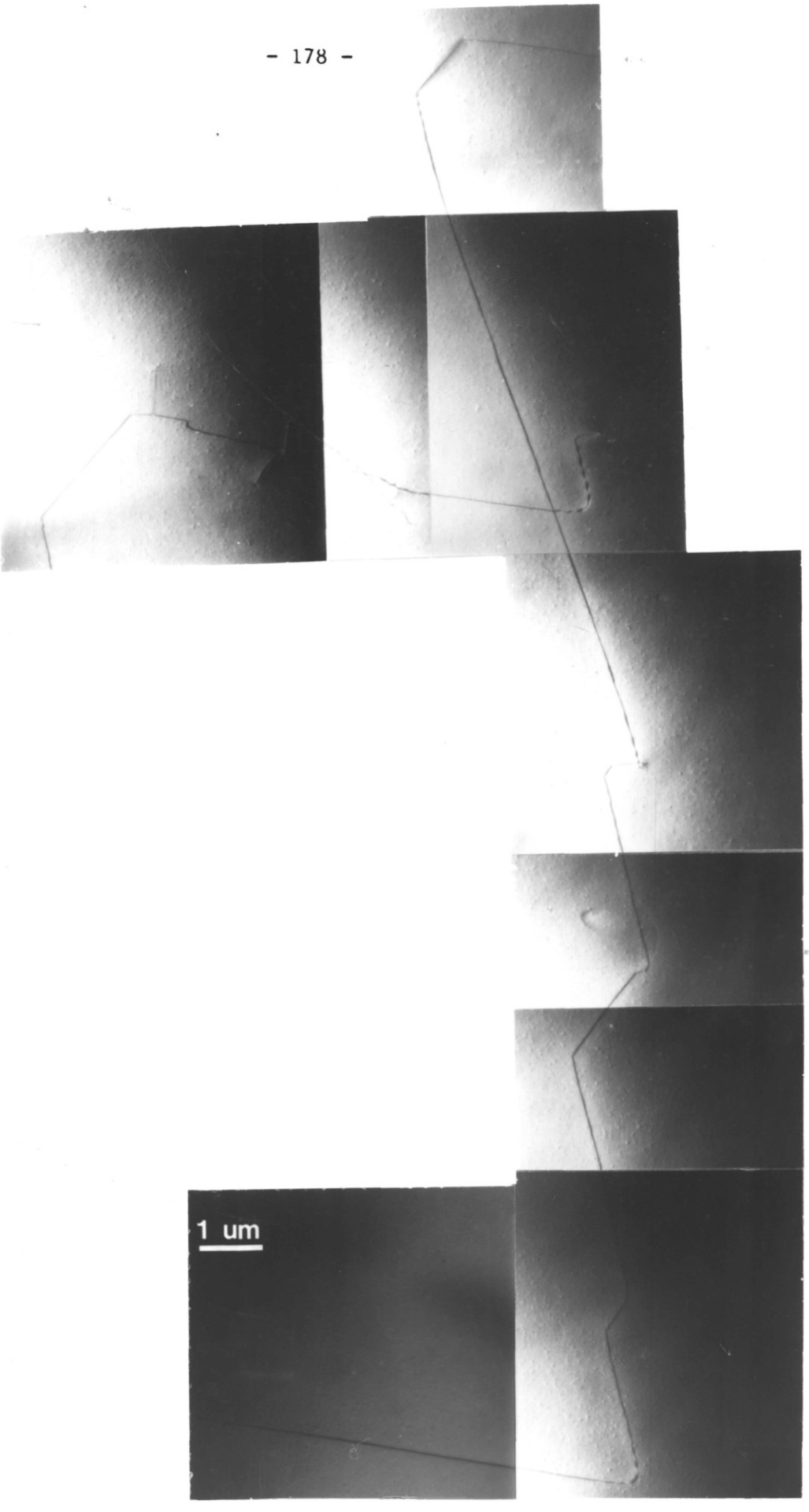


Fig. 56 - TEM micrographs representing a segment of a long misfit dislocation discovered within the circled area in Fig. 75(a).

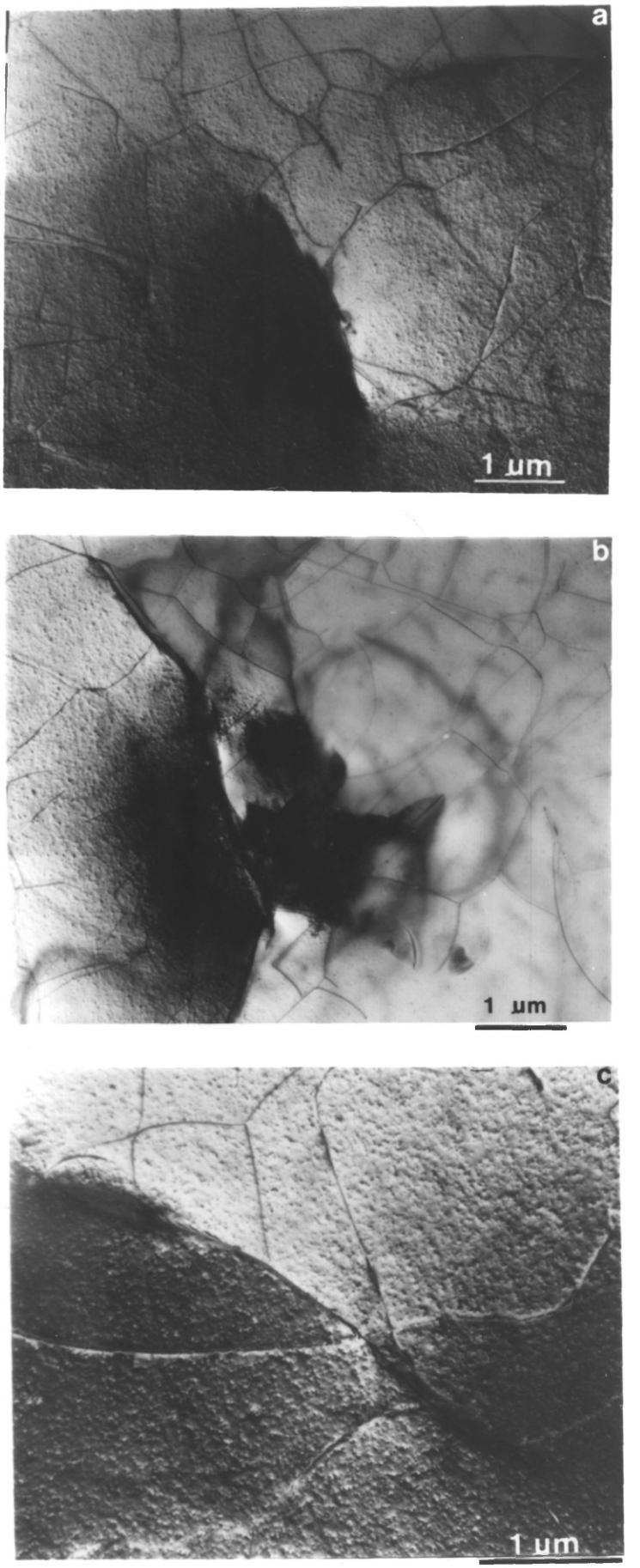


Fig. 57 - TEM micrographs of areas of misfit dislocation networks in RTAPDs (a) and (b) with smaller and larger area precipitates respectively and impurity segregation along some of the dislocations (c).

some of the dislocations were sometimes encountered within the n^+ region (Fig. 57(b), (c)). The spots can be attributed to the general precipitation effect. Spots and precipitates of such size and density however, have not been observed in samples which were characterised by low densities of dislocations (see Fig. 56). Such differences in contrast between the two samples seem to reflect the differences in the phosphorus concentrations involved. The higher P-concentrations correspond to the higher densities of misfit dislocations and precipitates.

Additional evidence for diffusion induced slip and misfit dislocations was obtained in the form of the doping profile of phosphorus in the n^+ material, determined by secondary ion mass spectrometry (SIMS). The phosphorus concentration profile shown in Fig. 57 was taken from a diode having a dense network of dark line defects. It was characterised by a high surface concentration of phosphorus, above 5×10^{21} cm^{-3} and an anomalous tail corresponding to the depth below the network of dislocations (~ 2.4 μm). It resembled the profiles seen in P-diffused silicon, containing misfit dislocation networks (Duffy et al. 1968). The spatial resolution of SIMS is not sufficient for the localised dislocations retardation of the junction, to be directly observed in concentration profile measurements. The same profile suggests the presence of precipitates at the depth corresponding to the dislocation network. A direct indication of the occurrence of precipitation is the

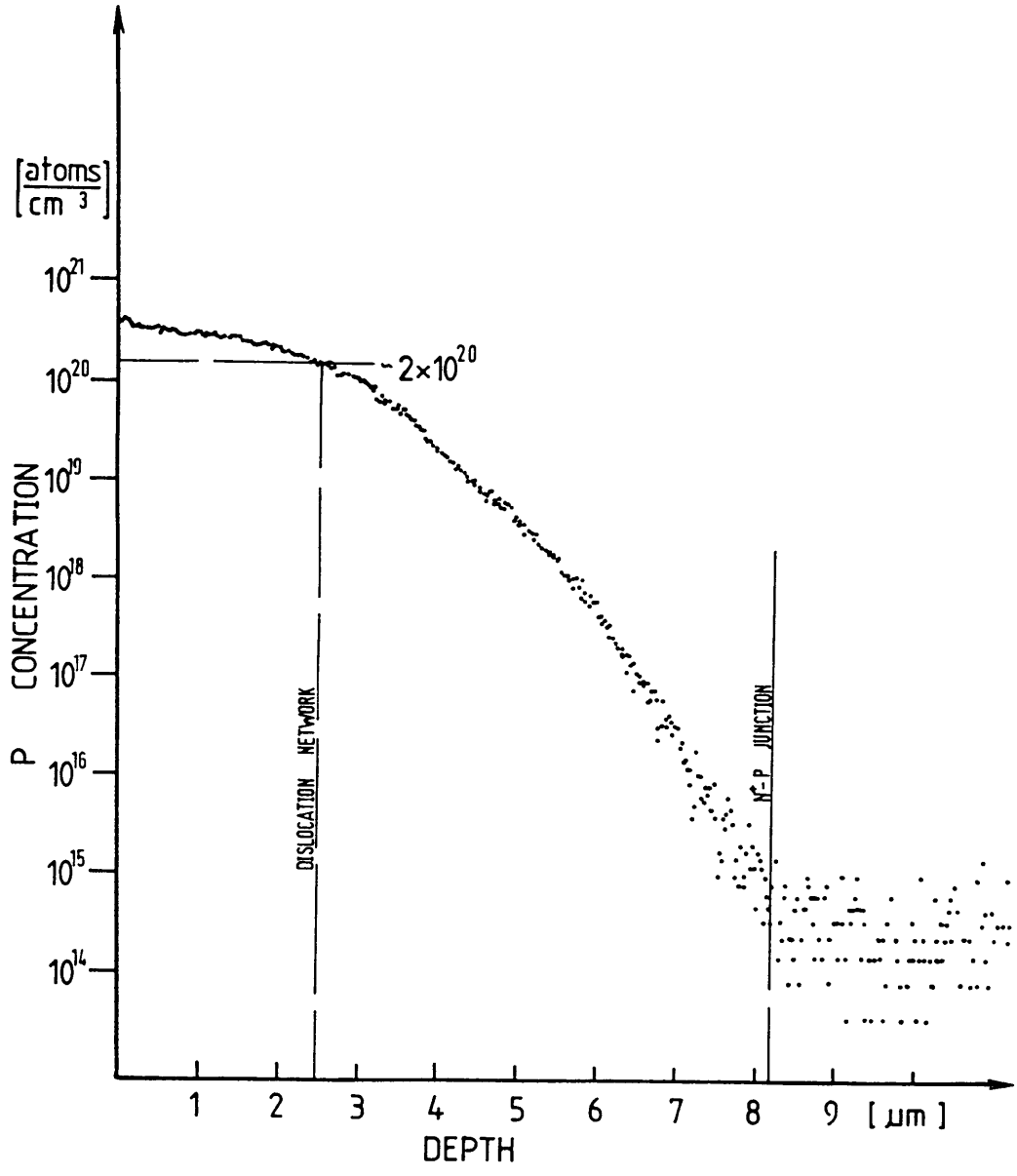


Fig. 58 - The phosphorus concentration profile in the n^+ layer produced by a diffusion in a RTAPD. This was measured by SIMS and is anomalous in form. The position of the planar dislocation network and n^+p junction are represented by two vertical lines.

observation whether the amount of electrically active phosphorus (P - in substitutional sites), is less than the total phosphorus of the diffused layer (Tannenbaum 1961). Tannenbaum's analysis of her diffusion data indicates the existence of a plateau region (saturation) at a P concentration of approximately 2×10^{20} atoms/cm^3 occuring in the electrical profile. At concentrations above this value the excess phosphorus is in the form of a precipitate and is electrically inactive. A comparison of the chemical (SIMS) profile and Tannenbaum's limit of the electrically active phosphorus, indicates (Fig. 58) that precipitation can be expected to a depth around 2.5 μm.

An example of large size precipitates seen in misfit dislocation networks, is shown in Fig. 57. Such extensive precipitates were extremely rare in the TEM samples examined, generally one in an area corresponding to 1/3 of the phosphorus diffused region. In addition, they were discovered only in samples having very dense networks of dislocations. It is unlikely that such rare large precipitates can be responsible for the presence of numerous microplasmas, typical for all the samples examined.

More evidence of precipitation was found in the specimens that were ion beam thinned and examined in the SEM as in Fig. 52(c), where numerous small black dots were revealed in the CC mode of operation. SEM emissive mode micrographs of the surface topography showed these dots to be due

to less-thinned, stump-like protuberances. These are impurities that reduce the sputtering rate during ion bombardment. Closer observation of these nonuniformities indicated that they involve a precipitate exposed at the top of a hump on the silicon surface (see "A" in Fig. 59. The primary impurity that could be responsible for the observed surface non-uniformities is oxygen in the form of precipitated oxides since such protuberances were seen not only in n^+ regions but also in their surroundings i.e., areas subjected repeatedly to the oxidation process.

It was generally observed that the black spots (Fig. 52(c)) indicating the locations of the precipitates did not correspond to the locations of microplasmas. From correlation between Fig. 59, 52(a) and (c), it is evident that the presumed silica precipitates did not produce any electrical effects in the complete device.

Many observations have been made of dislocations caused by the diffusion of phosphorus in silicon (section 2.12.), and it has not been the intention to add any detail to this work. It was important to establish that the dark EBIC lines correspond to the misfit dislocations.

In conclusion it was shown that the phosphorus diffusion in RTAPDs resulted in the formation of planar misfit dislocation arrays. The dislocation arrays were of the

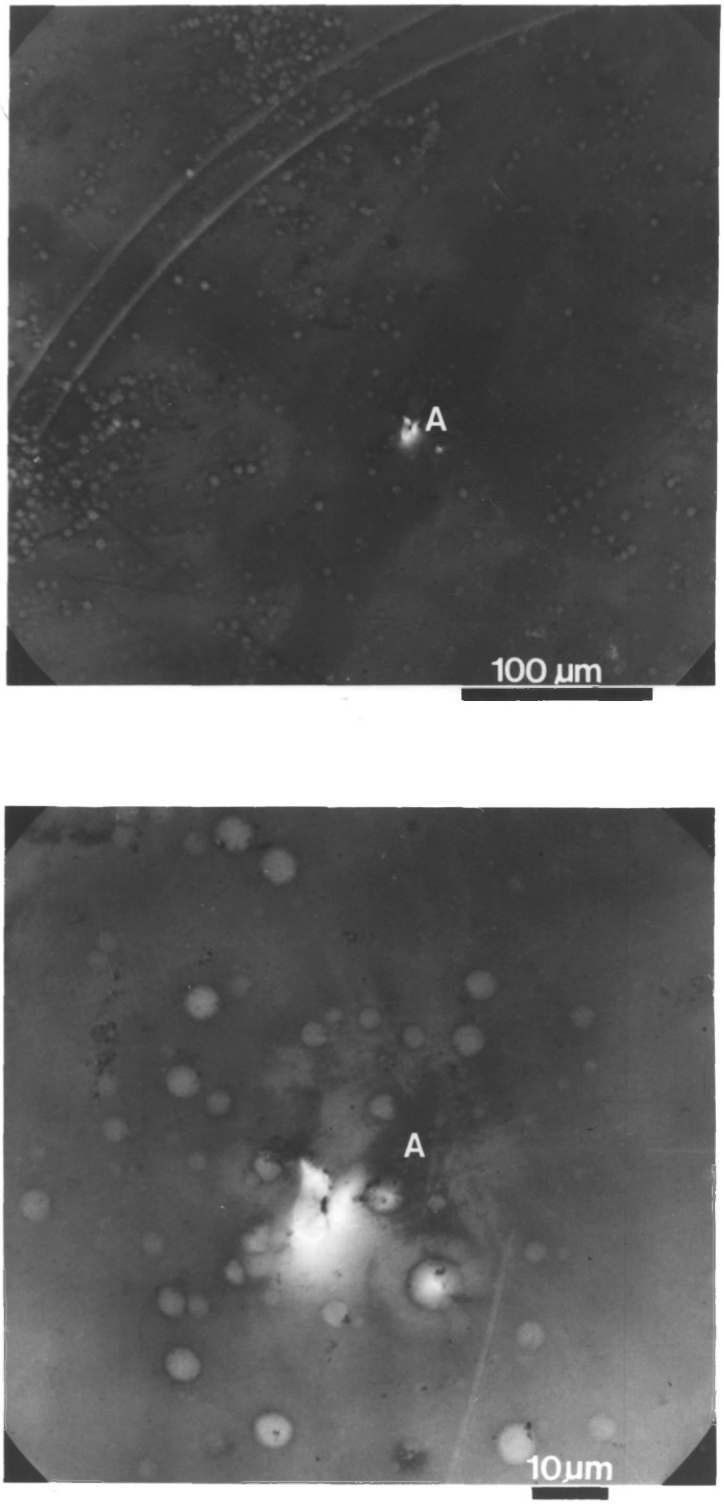


Fig. 59 - SEM SE micrographs showing surface nonuniformities left after ion-beam thinning at different magnifications.

necessary type to relieve misfit strain caused by the diffused phosphorus layer. The densities of the dislocations involved varied considerably from device to device within the same silicon wafer. The broad EBIC dark lines were found to represent individual dislocations. Also, there is evidence that some of the dislocations were associated with impurity cloud and precipitates.

In addition, there is evidence of the presence of a precipitated second phase in the volume of the P-diffused layers. This most probably involved large silica precipitates, at the specimen surface and SiP precipitates within the bulk material.

4.2.5. Measurement of the Depth of the Misfit Dislocations using the EBIC Technique.

a) In paragraph 4.2.3. it was established that the planar networks of dislocations in RTAPDs were located at a depth of approximately 2.5 μm within the n+ film. However, the experimental method employed for the determination of this parameter was troublesome and time consuming. It seemed interesting to examine whether EBIC observations on the dislocations at various beam energies can independently provide information about the location of the dislocations within the n^+ layer. The fact that the E_b variation of image contrast can be used to determine the depth location of defects has been realised theoretically (Donalato 1978) and experimentally (Leamy et al. 1976), for the case of Schottky barriers. As far as is known, this has not been confirmed for deep-lying p-n junction geometry.

The influence of the primary electron energy on the EBIC contrast and resolution of dislocations is demonstrated in Table 6. A series of EBIC scan lines was taken at accelerating voltages of 18, 19, 20, 22, 23, 24, 25, 26, 27, 28, 30, 32 and 33 keV. The line scans representing 20, 28 and 33 keV are shown in Fig. 60. They were collected from a specimen containing a few, well spaced dislocations. The scans

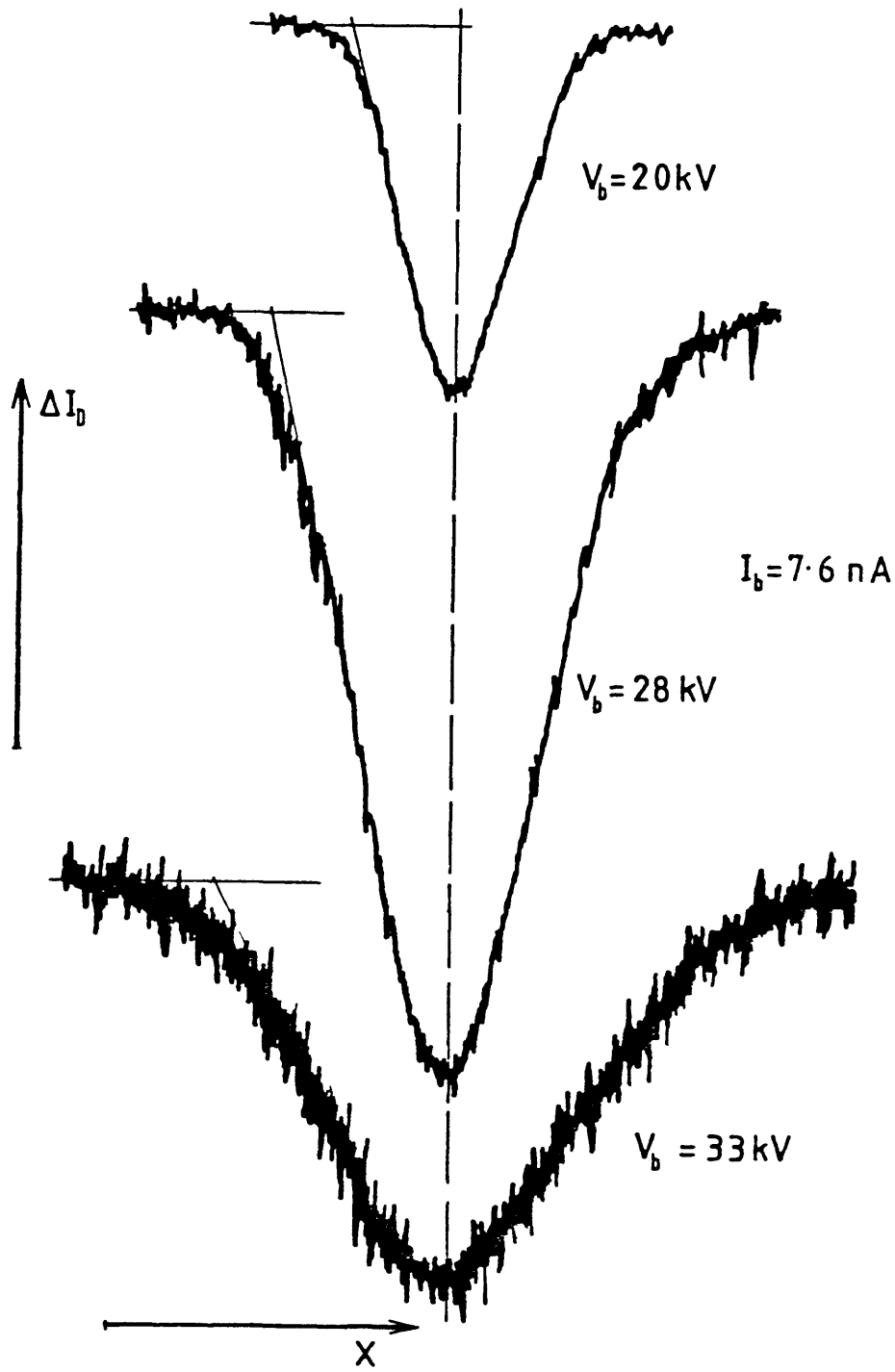


Fig. 60 - Series of EBIC experimental profiles of dislocation taken with different energies of primary electrons: a) 20 keV, b) 28 KeV, c) 33 keV. For values of contrast and resolution see Table 6.

TABLE 6

Values of resolution and contrast of a dislocation in dependence on beam energy, measured with nearly constant beam current ($1_b = 7.6 \times 10^{-9}$A)

Beam Energy [keV]	18	19	20	22	23	24	25	26	27	28	30	32	33
Range of Electrons [µm]	2.7	3.0	3.2	3.8	4.1	4.4	4.8	5.1	5.5	5.8	6.6	7.4	7.8
Image Width * [µm]	5.0	5.4	5.6	6.1	6.9	6.8	7.0	7.5	7.7	8.4	9.3	9.4	10.2
Contrast ** C [%]	9.8	9.6	9.0	6.8	5.7	4.7	3.9	3.4	3.0	2.7	1.7	1.2	0.7
$\Delta I = (I_B - I_D)$ [x 10^{-9}A]	4.63	8.88	137.1	215.2	246.1	274.0	296.0	320.9	333.1	331.0	316.2	300.0	180.9

* Resolution represents half the width of the line profile

** Conbtract is defined as $C = (I_B - I_D)/I_B$

were performed in a direction perpendicular to the dislocation. The dislocation examined was not associated with a microplasma site, but exibited a typical white contrast in its surroundings (this is after applying bias voltage). In this experiment the device was short circuited (no bias applied). The H.A. sensitivity and the electron beam current were kept constant. Only the electron beam energy and current back-off levels were varied. Values of resolution were measured as the half width of the line profiles like those shown in Fig. 60. Corresponding contrast values were calculated according to eq. 21, for the measured values of I_B and ΔI_D. This is given in Table 6. The calculated values of contrast give a significant monotonic decrease in all cases with increasing beam energy (Fig. 61).

On the other hand, the resolution for the imaging of dislocations degraded considerably with increase in E_b. It was interesting to observe that the resolution followed a $E_b^{1.75}$ dependence, as is shown in Fig. 62. Similar scaling of resolution on dislocations with E_b has been reported by Leamy et al. (1976) for the case of Schottky barriers.

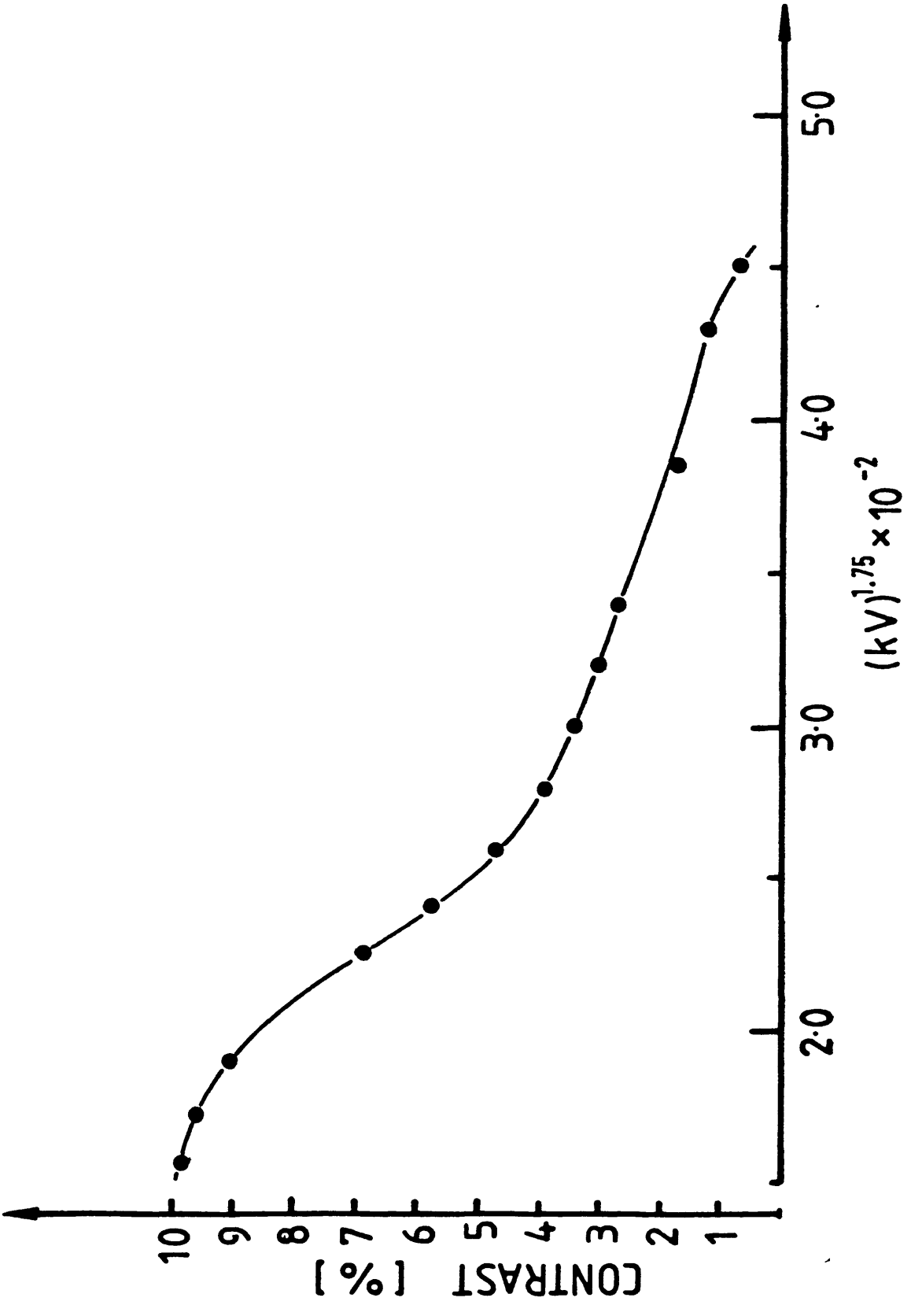


Fig. 61 - Contrast of dislocation vs energy of primary electrons. Contrast is defined as $(I_b - I)/I_b$ where I_b and I are the signal intensities corresponding to the immediately adjacent background and the dislocation respectively.

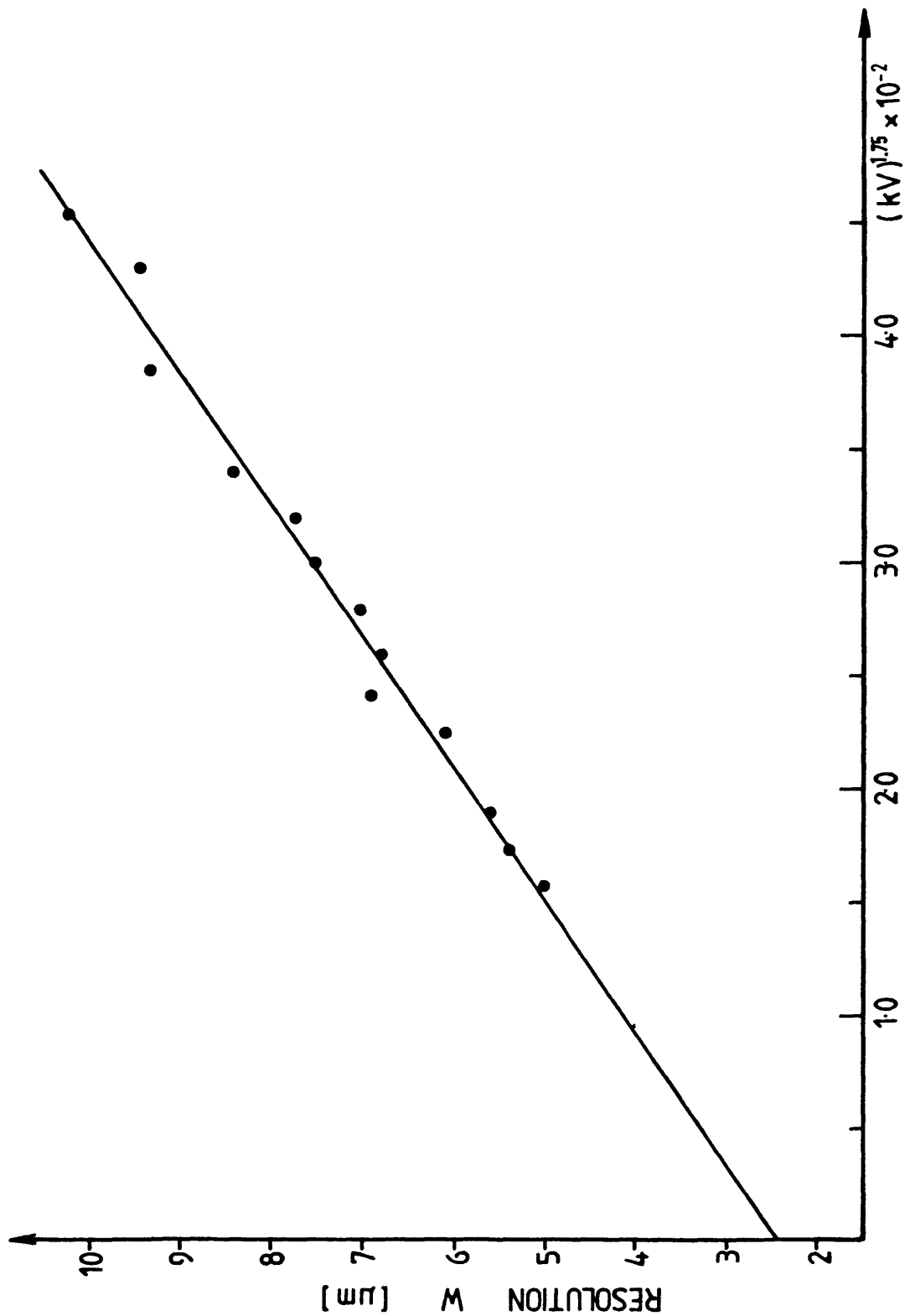


Fig. 62 - Dependence of a dislocation image width on energy of primary electrons.

Discussion

Dislocations representing one dimensional defects are much smaller than R_e in both dimensions normal to the line. The resolution with which they can be imaged therefore depends upon the extent of the energy dissipation volume, hence R_e. For higher beam energies the resolution of the EBIC images of dislocations is more restricted in the way indicated in Fig. 63. It may be expected that the R_e-dependent image width of a dislocation located at certain depth, should reflect an R_e vs E_b relation. This is in agreement with the experimental observations presented above. The resolution of the dislocations located at approximately 2.4 μm beneath the surface followed an $E_b^{1.75}$ dependence.

The misfit dislocations observed in RTAPDs were characterised by two outstanding EBIC features:-

- They exhibited relatively large EBIC image widths, being approximately 5.6 μm at 20 KeV. Blumtritt et al.(1979) and Ourmazd and Booker (1979), studied P-diffusion induced misfit dislocations in shallow p-n junctions. The EBIC spatial resolution they observed was 3.3 μm at the most.

- The dislocations in RTAPDs produced high EBIC contrast, exceeding 10% at 18 KeV. This notably

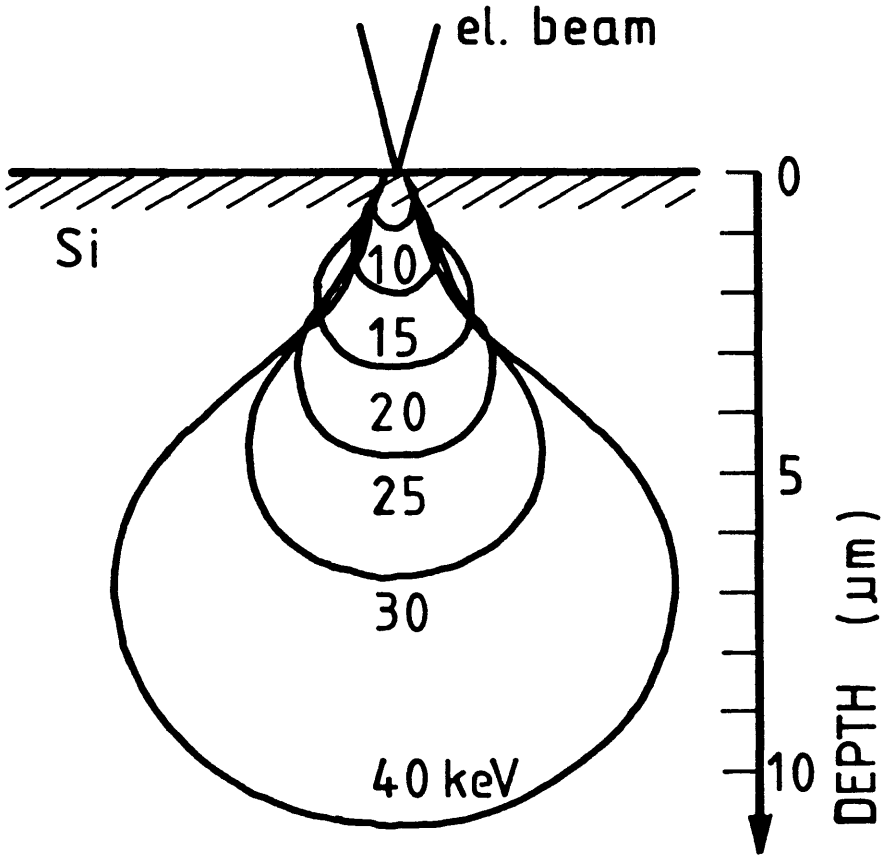


Fig. 63 - Schematic drawing of minority carrier excitation volume in dependence on primary electron energy (vertical extent calculated for Si after Everhart and Hoff 1971).

exceeded the contrast levels reported by other investigations on dislocations considered as being decorated (Ourmazd and Booker 1979; Blumtritt et al. 1979; Heydenreich et al. 1981). Such high contrast levels were observed only by Heydenreich (1979) in Si device-type specimens. Those segments of dislocations decorated with observable impurity particles gave EBIC contrast at 300 K of typically 10 to 20%.

In a series of works, a direct influence of clusters of impurities on the recombination action of dislocations has already been proved (Marcus et al. 1977; Blumtritt et al. 1979; Kawado 1980; Heydenreich et al. 1981). The common result of all this work is that the decorated defect has a much higher EBIC contrast than defects without clusters. Dislocations considered as being "clean" are known to appear in very weak EBIC contrast, much less than 1%, or do not produce any contrast at all. So it can be assumed that the main electrical effects in the present case result from the impurity clusters alone and the dislocations themselves act as gettering centres for the impurity.

The assumption that the misfit dislocations in RTAPDs are decorated is justified in view of the:-

- High phosphorus doping concentration preseent, being in excess of 10^{21} cm^{-3};

- Occurrence of the P-retarded diffusion observed in association with the dislocations;

- TEM observations presented in the paragraph 4.2.3.; where some of the dislocations are shown directly in association with a precipitated second phase.

The electrical activity of dislocations as observed in EBIC images in general can be associated with two effects i.e., EBIC contrast and resolution. The available data is almost entirely concerned with the influence of impurity decoration and core structure of defects on the image contrast. As far as is known there is no data available on the resolution being studied in a similar context.

One of the interesting questions which arose during the course of the experimental work, was whether the unusually broad dislocation image width in RTAPDs can be related to the extensive decoration effects. Only a few investigations have been carried out on the defect resolution which principally may be influenced by the same geometrical and material parameters as

the defect contrast. In particular it has been found that even large minority carrier diffusion lengths have a little effect on resolution (Donalato 1978). The available data suggest the assumption that the defect position is the most limiting factor (Donalato 1979; Leamy 1982).

The experimental values of the resolution on the dislocations given in Table 6, were used to calculate the parameters of the straight line representing the data in Fig. 62. The method of least squares was used for the approximation and the line is given as:-

$$(28) \qquad w = 0.5\ (\underbrace{1.70\ (10^{-2}\ E_b^{1.75})}_{a} + \underbrace{2.44}_{b}) \quad [\mu m]$$

The constant b = 2.44 µm is the limiting value of the resolution in the present case. It corresponds to the intercept of the experimental line and the vertical axis. Such resolution could be approached at the smallest possible E_b values. The other part of the relation "a" refers to the resolution being dependent on the extent of the energy dissipation volume.

The constant b = 2.44 µm defining the limit of resolution in the present case provides a satisfactory match to the value of 2.5 µm for the depth location of

the examined dislocation. Relation (28) can be represented as:

$$(29) \quad w = 0.5\ (0.0170\ E_b^{1.75} + Z_o) = 0.5\ (R_e + Z_o)[\mu m]$$

Where Z_o indicates a defect depth location. Eq. (29) provides an excellent fit to the experimental relation (28).

In conclusion, relation (29) suggests that the spatial resolution of dislocations in RTAPDs does not depend on L_p, nor on the decoration effects or even dislocation core structure, but is entirely related to the geometrical factors R_e and Z_o.

b) Dislocations appear on EBIC micrographs as dark lines, the contrast of the line being a measure of the electrical recombination efficiency of the dislocation. The observed monotonic decrease in the normalised EBIC contrast C on dislocations (see Fig. 61) is in agreement with the intuitive notion that the electrical effect of the defect should be screened by the rapid increase in the amount of carriers being collected by the n^+p junction, following the increase in E_b (see Fig. 63). A similar C vs E_b dependence has been observed by Blumtritt et al. (1979) for a similar device structure. Although the resolution dependence on E_b for the present case revealed a similar variation to that observed in Schottky barriers, no such similarity was observed for the variation in contrast on dislocations. In fact, no simple indication as regards the depth location of the dislocation could be extracted from the measured contrast data (contrary to the analysis presented by Donolato 1978, for the Schottky barriers). For this reason a different approach to the experimental data was considered. The analysis presented below is concerned with the absolute values of the EBIC contrast on a dislocation (i.e, $\Delta I_D = I_B - I_D$), rather than the normalised contrast C. In order to satisfactorily explain the results presented below it is first necessary to describe the mechanism by which changes in E_b may affect changes in ΔI_D.

Everhart and Hoff (1971) have published theoretical curves of electron energy dissipation as a function of penetration distance (see eq. 21). They showed that for a given energy E_b, the number of minority carriers generated as a function of depth rises to a maximum at approximately one third of the electron range R_e and decreases smoothly to zero at a depth equal to the range R_e. From these curves and the range-energy relationship (see eq. 3) it is possible to plot a series of theoretical dose vs depth curves, examples of which are reconstructed in Fig. 64. In addition if the electron beam current and voltage are known then the number of electron-hole pairs generated at a given depth $g(Z_o)$ can be evaluated (see Appendix A) as a function of E_b. The generation rates $g(Z_o)$ representing different E_b values, as monitored at the fixed depth Z_o, are presented in Table 7 and are graphically shown in Fig. 67. The $g(Z_o)$ values were computed assuming the electron beam current was constant ($I_b = 7.6 * 10^{-8}A$). From Fig. 65 it can be seen that each of the $g(Z_o)$ vs E_b relations reveals a maximum. The peak shifts towards higher E_b levels for larger Z_o depths.

Shea et al. (1978) have presented a semiempirical model of the distribution of the electron beam induced minority carriers in planes parallel to the axis of the beam in a semiconductor and have termed this

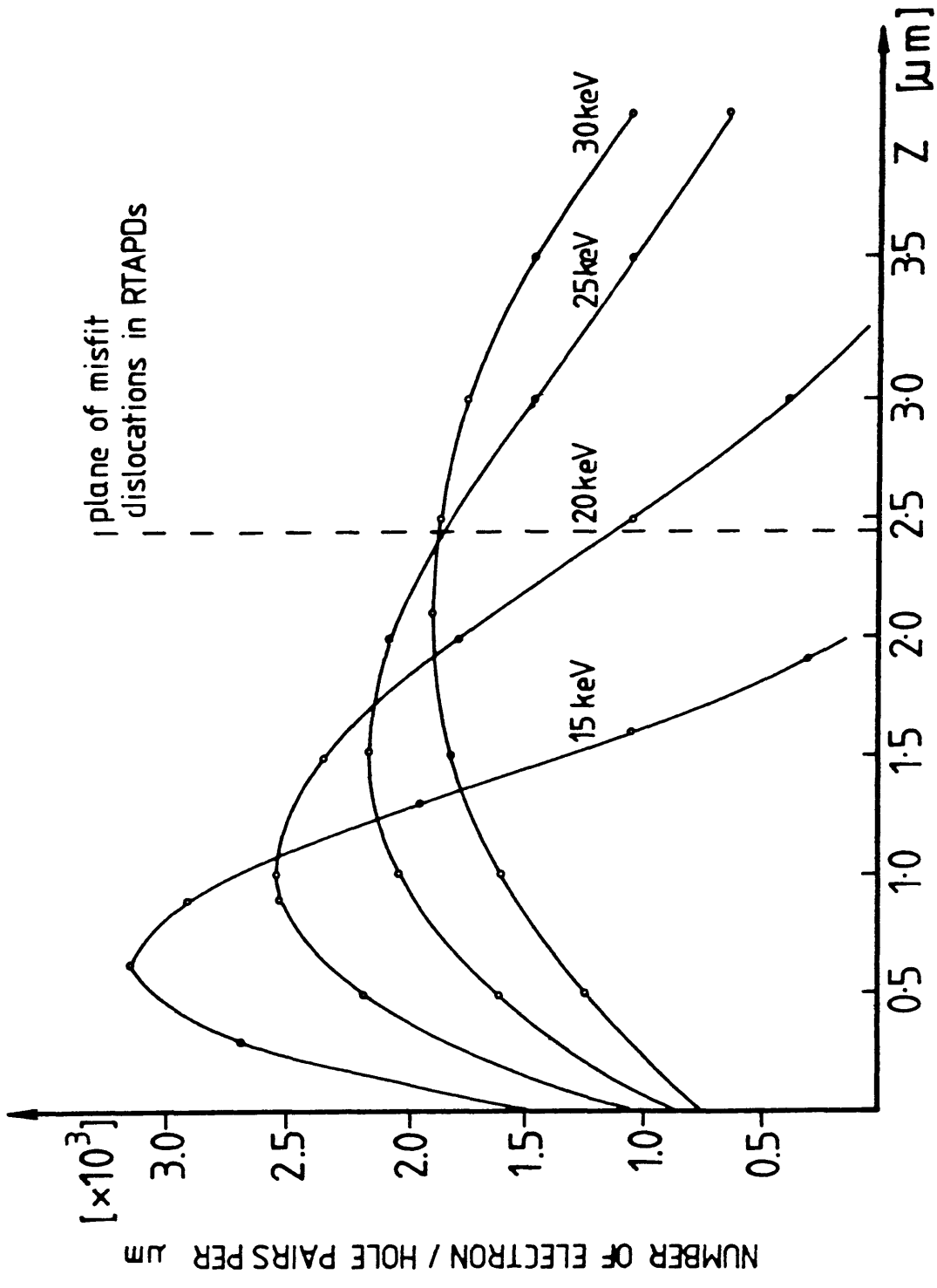


Fig. 64 - Theoretical depth/dose relationships obtained from the work of Everhart and Hoff (1971).

distribution the "lateral-dose" function. Referring to the lateral-dose function, they made two predictions concerning the shape of semi-log plots of the EBIC vs distance data, in an experiment designed to measure minority carrier diffusion lengths L:-

1) For L much smaller than $.25R_e$, it is expected that the EBIC would follow the shape of the lateral does function and thus be independent of the value L, but strongly dependent on E_b.

2) For L much bigger than $.25R_e$ it is expected that the EBIC would exhibit a single, straight line dependence on the source position and that the value of the diffusion length could be determined from the inverse slope of this line (in accordance with eq. 18).

Their experimental results corfirmed these predictions. A useful conclusion from the work of Shea et al., is that the EBIC data can be understood by directly referring to the primary electron deposition function, in situations where the minority carrier diffusion length is short as compared to R_e. The practical advantage of this conclusion has been realised experimentally by Ashburn and Bull (1979). They found that information on the extent of junction ununiformities can be acquired through direct

correlation between the EBIC data and the theoretical depth - dose relations, similar to that shown in Fig. 65.

The case of a straight dislocation parallel to the surface, at a depth Z_o, has been a frequently investigated configuration (see Fig. 2). Donolato (1983) has shown that the maximum dislocation absorbed current can be expressed in such cases as:

$$(30) \quad I_D = \gamma * \varphi(Z_o) * \left[\int_{-\infty}^{\infty} p\ (0,Y,Z_o)dY \right]$$

assuming that the dislocation is parallel to the X axis, γ is a phenomenological parameter representing the line recombination velocity (see eq. 23); $\varphi(Z_o) = \exp(-Z_o/L)$ is the carrier collection probability; $p\ (0,Y,Z_o)$ is an effective hole distribution within the structure (assuming an n-type semiconductor).

In eq. (30), the term in square brackets in a given experiment is a function of Z_o only and represents the effective excitation strength at the dislocation. From this definition, the dislocation can be seen as a form of sensor readily responding to the variations in the excitation strength at the depth Z_o.

In view of the work by Shea et al. (1978) and Everhart and Hoff (1971), the relation ΔI_D vs E_b can be expected to follow a similar dependence to that of the theoretical relationships of Fig. 66, under the assumption of a short minority carrier lifetime within the bulk material. It can be expected that the E_{bmax} energies indicating the peak values of the ΔI_D vs E_b and $g(Z_o)$ vs E_b relations, should be accurately the same, as long as both the experimental and theoretical curves refer to the same depth Z_o. In practical terms, if the ΔI_D vs E_b is given experimentally, then the corresponding $g(Z_o)$ vs E_b relation can be selected from the set of similar theoretical curves representing different depths Z_o, so that both E_{bmax} values are the same. As a result the dislocation depth location Z_o can be acquired.

The aim of the experiments presented below was to test whether the electron beam depth profiling technique, as applied to the RTAPD, can provide any information about the depth location of the misfit dislocations.

The experimental values of ΔI_D as a function of E_b were obtained from the line scans across the dislocation introduced already in part a) of this section. Examples of the line scans examined are presented in Fig. 60. The experimental ΔI_D vs E_b data are given in Table 6 and Fig. 65 (for the

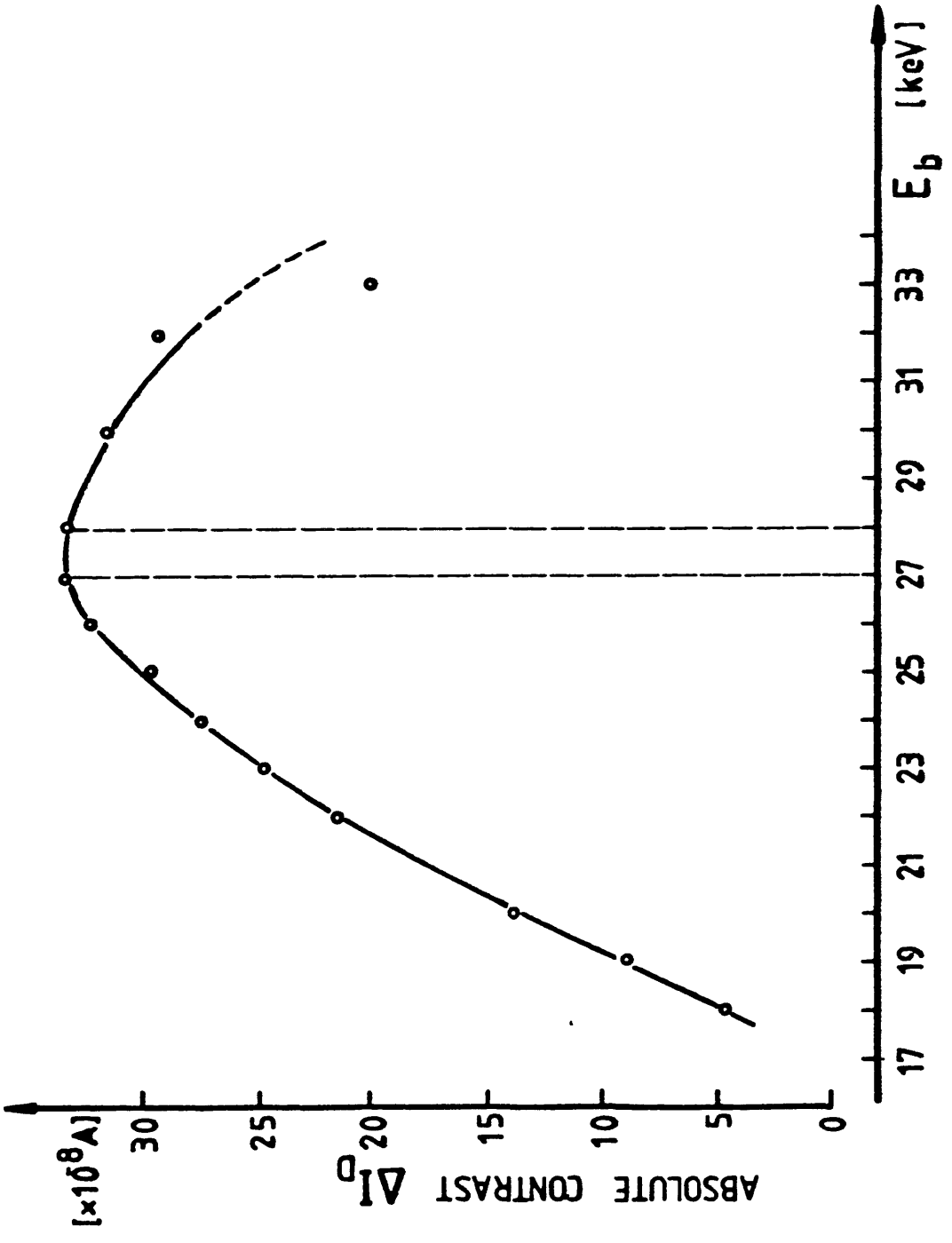


Fig. 65 - Experimental variation of the magnitude of the dark contrast ΔI_D on the dislocation as a function of electron energy.

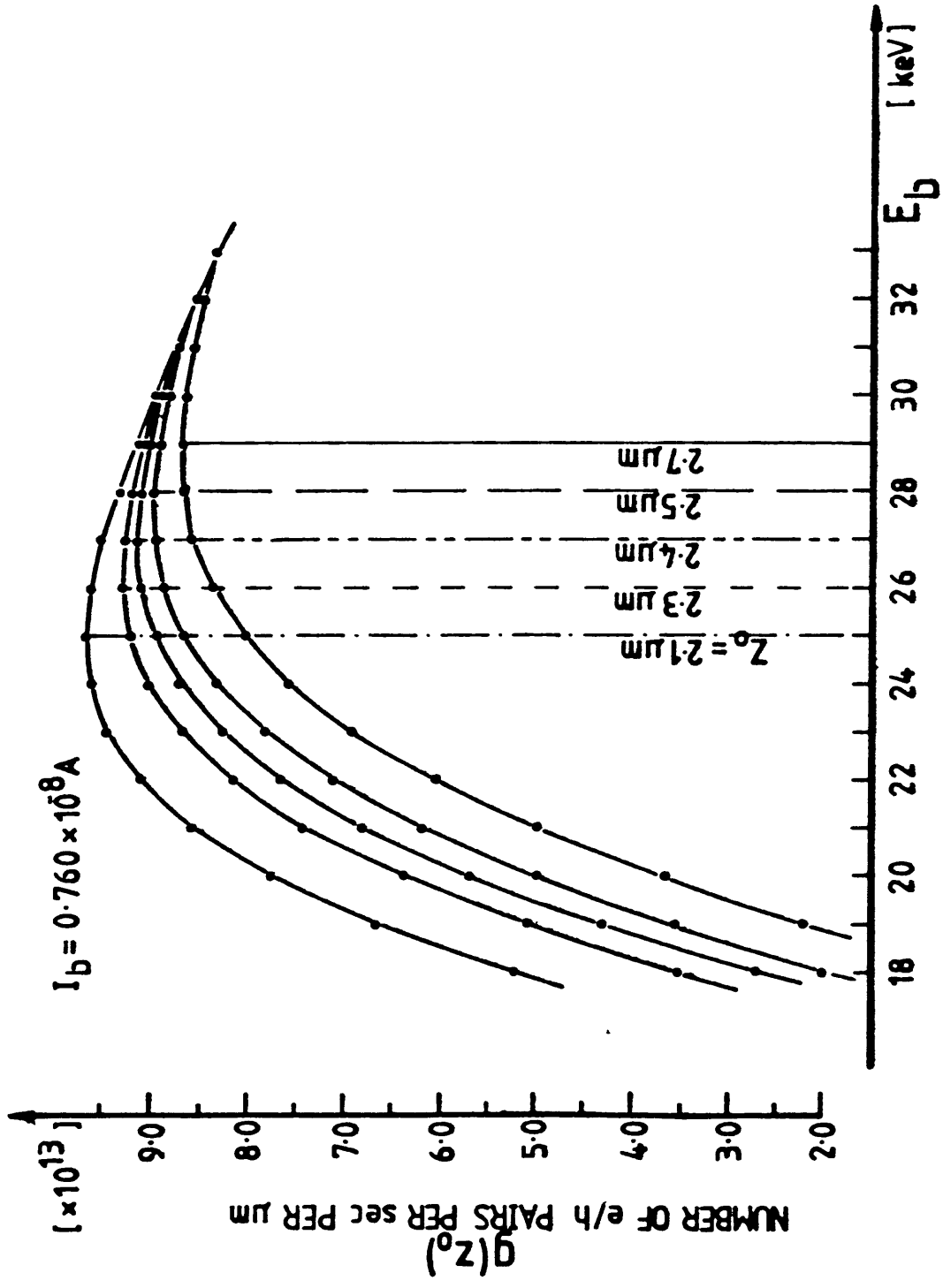


Fig. 66 - Theoretical number of carriers generated at a given depth (2.3, 2.4, 2.5 and 2.7 μm) as a function of electron energy.

constant electron beam current condition). From Fig. 65 it is evident, that ΔI_D depends strongly on the primary electron energy. The well pronounced maximum of the experimental curve corresponds to the E_b being between 27 and 28 keV. Fig. 66 comprises a set of theoretical $g(Z_o)$ vs E_b relations representing different Z_o values i.e., 2.3, 2.4, 2.5 and 2,7 μm. It appears that the maximum of the $g(2.4)$ vs E_b relation occurs at 27 keV and that of the $g(2.5)$ vs E_b corresponds to E_b being 28 keV. In view of the predictions given above the dislocation being examined should be located at the depth Z_o specified as $2.4 \leqslant Z_o \leqslant 2.5$. This is in good agreement with Z_o being 2.45 μm and 2.5 μm, the results of the two previous evaluations (section 4.2.3. and 4.2.5.). Fig. 67 shows both experimental and theoretical results after being normalised to their maximum values respectively. It can be seen that the experimental ΔI_D vs E_b relation reveals a faster fall on both sides of the maximum, than would be expected from the theoretical curve $g(Z_o)$ vs E_b.

Discussion

The experimental results presented in this section indicate that the technique based on the monitoring of the ΔI_D vs E_b data provides a means for the evaluation of the depth location of dislocations in p-n junctions.

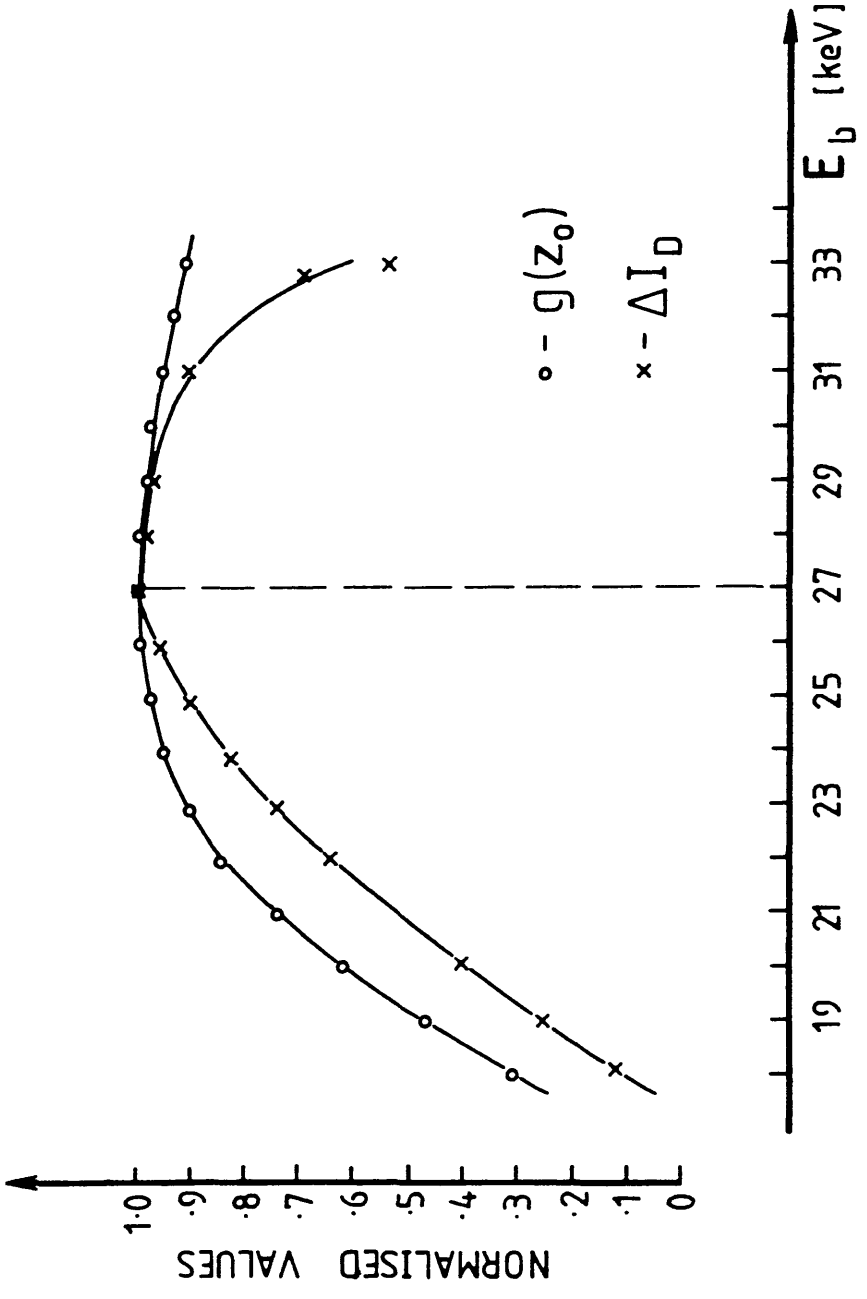


Fig. 67 - Normalised values of the ΔI_D vs E_b and $g(Z_o = 2.4)$ vs E_b.

The dislocation depths assessed in three different ways (see paragraphs 4.2.3., 4.2.5.(a), 4.2.5.(b)) constitute a satisfactory match. The latest method represents also the simplest means of such investigation. The accuracy of the EBIC depth profiling technique was about .1 μm and was determined by the smallest step in E_b that could be applied in the SEM (JEOL-35). The tolerance can be reduced by using smaller E_b steps (less than 1 keV).

One part of the work where theory and experiment may not agree so well, is concerned with the overall shape of the ΔI_D vs E_b and $g(Z_o)$ vs E_b relations (see Fig. 67). The reason which should account for this discrepancy could be found in the difference in the physical representations behind those relations. $g(Z_o)$ represents the total generation rate as monitored on the imaginary plane perpendicular to the axis of the beam and being located at the depth Z_o. Unlike this, ΔI_D reflects the total concentration of generated minority carriers as observed on a straight (dislocation) line within that plane.

In addition, the requirement of the minority hole diffusion length L_p being much smaller than $0.25 * R_e$, might not have been met in the case of the RTAPD being

examined. The measured L_p representing an undefected area was about 1 μm (in the particular device examined), implying the L_p/R_e ratio was about 0.5 for the smallest applied E_b values. This indicates that the experiment can not be fittedstrictly to the two cases distinguished by Shea et al. (1978). On the other hand the L_p/R_e ratio at the dislocation line (acting as a recombination centre for minority holes) can be expected to be considerably smaller than 0.5. This seems to have reflection in Fig. 65 where the contrast on a dislocation ΔI_D exhibits a strong dependence on the E_b value.

However, further experimental and theoretical work would be necessary before a full account of the problem could be given in any detail.

So far, the results collected from the study of dislocations in RTAPDs, suggest that the method based on the correspondence between the experimental ΔI_D vs E_b and well known electron beam depth/dose relations, provides a simple means for the evaluation of the depth location of dislocations, under the condition of short minority carrier diffusion length (as compared to the actual electron range R_e).

4.2.6. SEM EBIC Contrast and Depth Resolution on Misfit Dislocations

The results obtained so far show conclusively that the misfit dislocations induced during phosphorus diffusion are responsible for the impurity retardation effect. The dislocations have therefore been investigated in greater detail using the SEM EBIC technique in the search for further information concerning the mechanism of the retardation process itself.

Fig. 68 shows an EBIC micrograph of the RTAPD taken at an electron energy of 25 keV and the bias voltage reaching the breakdown level (approx 300 V). The micrograph already shows familiar, general features that is:

- Dislocations represented by dark zig-zag lines, present at a relatively low density.

- Junction irregularities appearing in bright contrast and accompanying most of the dislocations.

- Microplasma sites, the most efficient of which (see arrows) correspond to the nodal points, where several dislocations seem to cross each other.

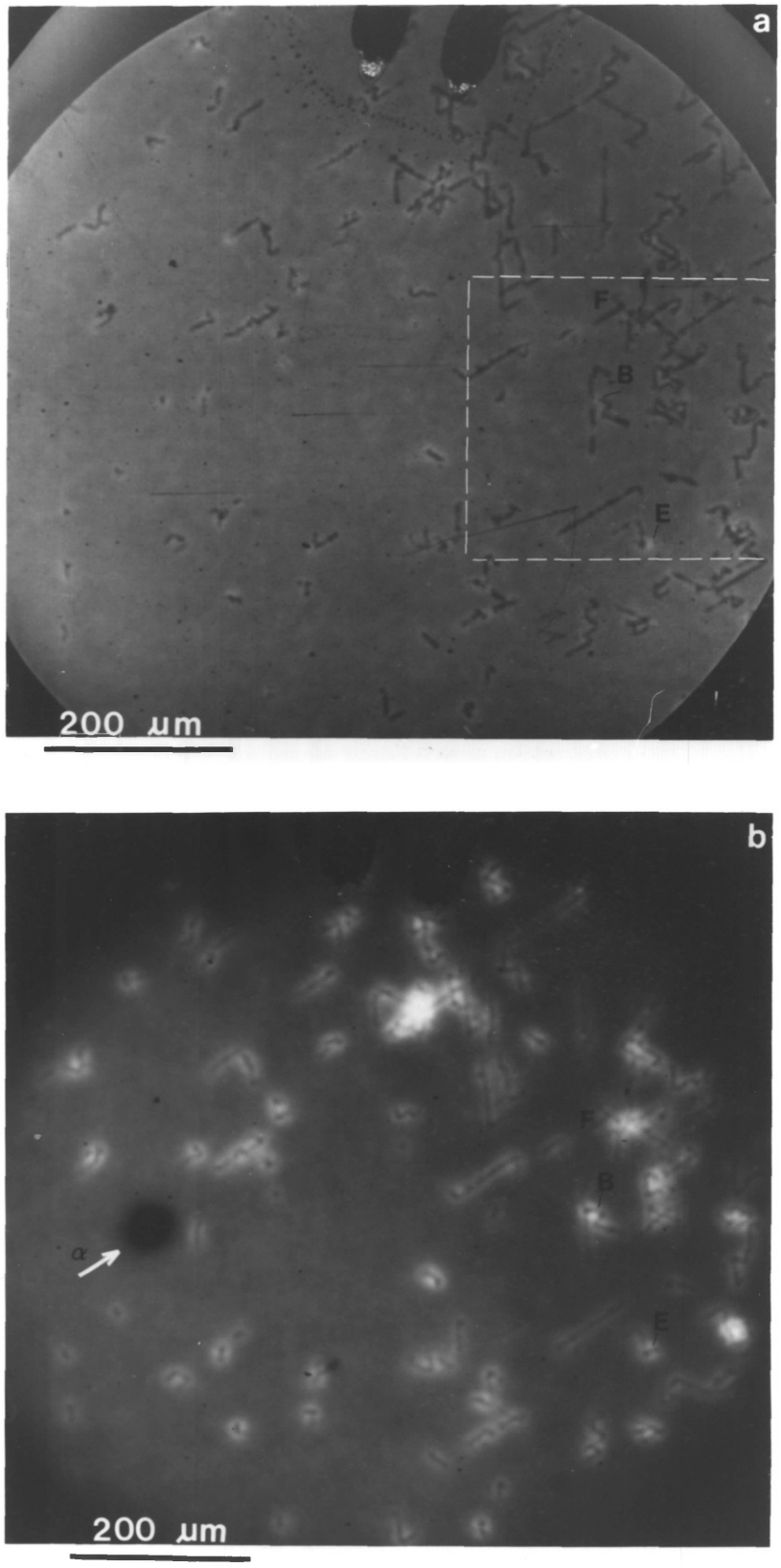
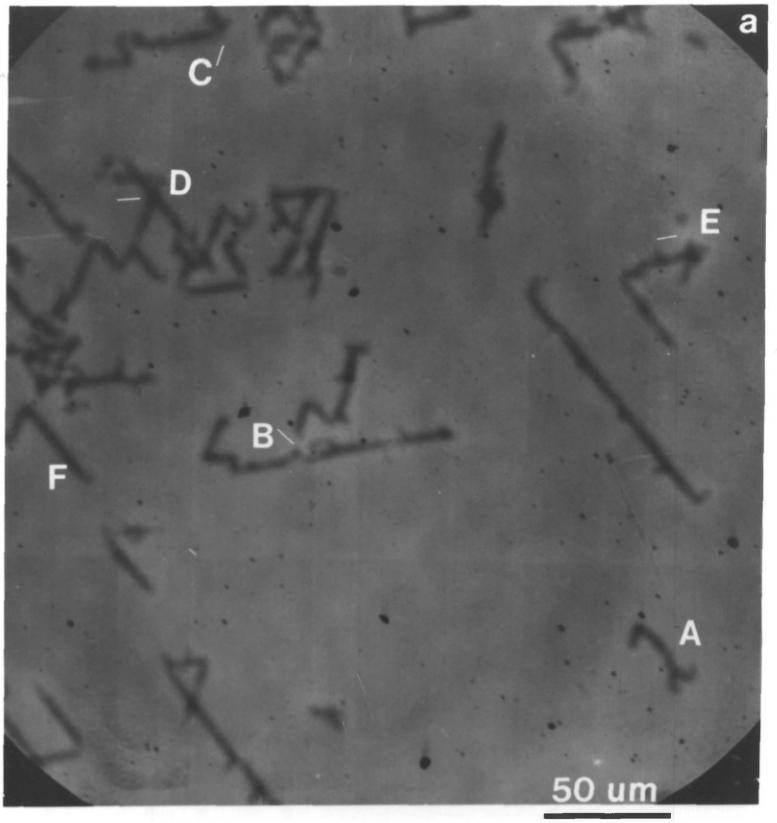


Fig. 68 - CC micrograph of a RTAPD at (a) 0V and (b) 300V biases.

It was interesting, however, to observe that the amount of dark and bright contrast, due to dislocations and junction irregularities respectively, changed considerably for different dislocations and segments of the same dislocation.

The TEM observations revealed that the misfit dislocations in general did not lie precisely on the same (111) plane, parallel to the diode's surface. In addition some of these dislocations were shown to be inclined at various angles to this characteristic plane. It seemed a reasonable suggestion that the dislocations located at different depths or being inclined, may account for the observed variations in EBIC contrast. In order to investigate this possibility an EBIC examination was carried out, based on the recording of any variations in EBIC contrast and resolution in relation to changes in electron beam energy.

Fig. 69 contains EBIC micrographs, all representing the same selected area of the device shown in Fig. 68. The micrographs were recorded using 20, 25 and 35 keV electron beams respectively at constant electron beam current conditions. They demonstrate the influence of the primary electron energy on the EBIC resolution and contrast on dislocations. All three images were taken at OV bias in order to prevent any field effects from affecting images of dislocations.



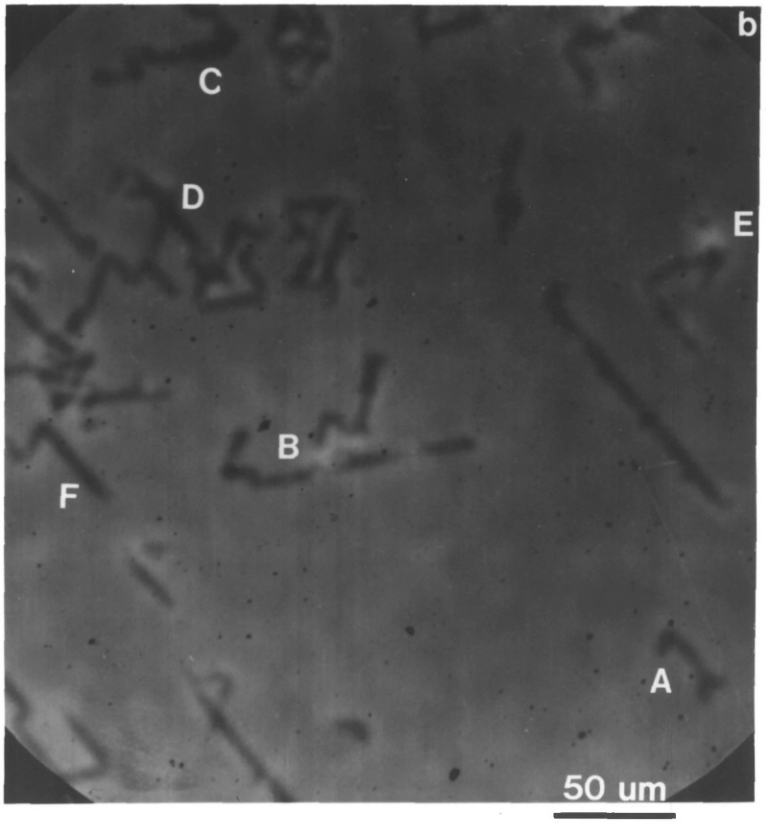


Fig. 69

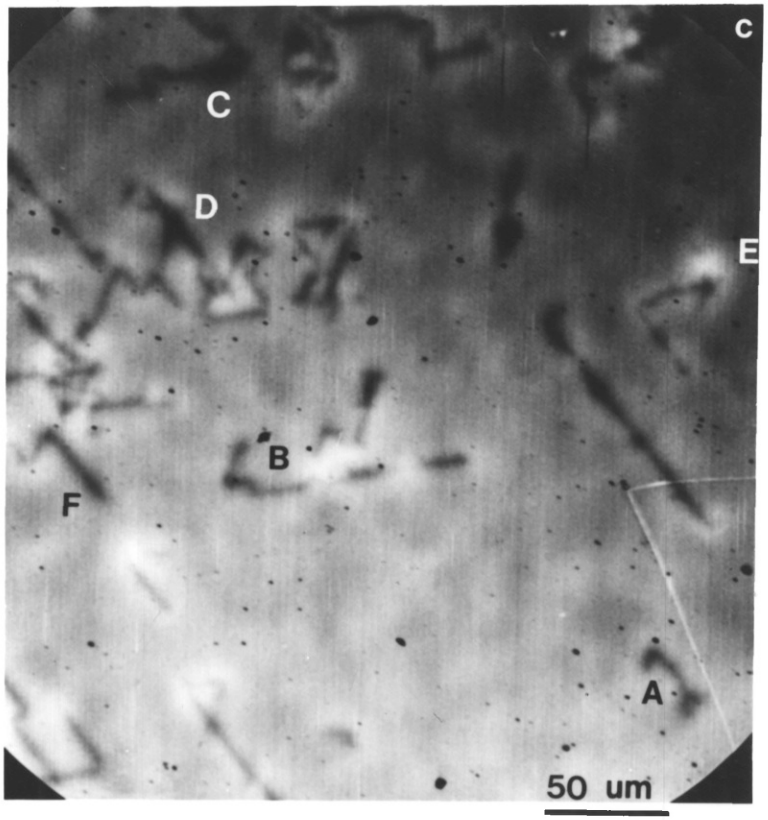


Fig. 69 - Series of EBIC micrographs taken with different energies of primary electrons (selected area from sample in Fig. 68); (a) 20 KeV, (b) 25 KeV, (c) 35 KeV.

The sensitivity of the H.A. and the video amplifier gain were adjusted for each of these images to provide approximately equal contrast levels (i.e., pseudo contrast, as observed on the SEM display unit), so that the images could be compared directly. In practical terms the amount of dark contrast ($I_B - I_D$, equivalent) at the same (for all micrographs), arbitrarily selected dislocation, was maintained approximately identical. A defect which revealed the least EBIC contrast changes was chosen as a reference (dislocation marked A in Fig. 69).

Examination of the micrographs presented in Figures 68 and 69 resulted in the following observations:-

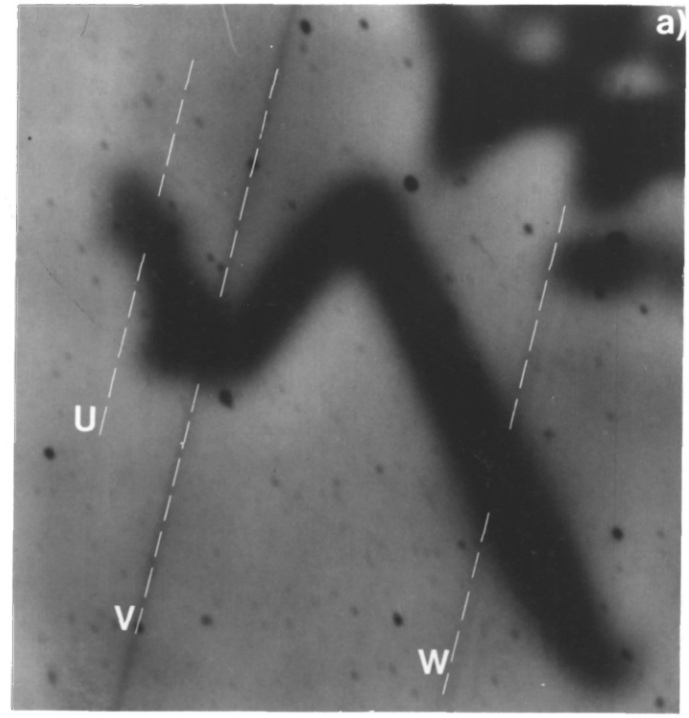
1. EBIC resolution at some of the dislocations degraded with increase in the primary electron energy i.e., the dark lines became broader and more diffuse at higher E_b levels (marked C and D in Fig. 69 (a)).

2. Contrast on dislocations as observed at 20 keV, was not uniform but varied from defect to defect as well as through the length of a single dislocation. Such differences in contrast were found to intensify with increase in E_b. The dislocations which already appeared with weak contrast at 20 keV (0V - bias), were observed to vanish gradually at higher electron beam energies. An example of such a defect was marked as B in Fig. 69(a). On the other hand, there were

several dislocations observed in strong dark contrast at 20 keV. These again appeared in strong contrast at higher E_b levels although images were considerably broadened and diffused (see C and D in Fig. 69).

3. Closer examination of the device at OV bias, revealed the presence of bright contrast areas emerging progressively with increase in R_e. Comparison between micrographs corresponding to the device with and without applied bias (Fig. 68 and Fig. 69(c) respectively), confirmed the existence of the one to one correspondence between areas of bright contrast in both cases.

4. It was interesting to observe that dislocations (or their parts) which appeared in weak contrast at OV bias, emerged in strong contrast after applying a large bias voltage to the device. In addition, the same defects could also be associated with the highest intensities of the bright contrast appearing in their neighbourhood. The defect marked B in Fig. 69 may serve as an example. The extreme cases of such correlation were observed at E, where the corresponding dislocation segment could not be seen at all at OV bias in (Fig. 68(a)), however it was clearly pronounced in Fig. 68(b). Such dislocations were also seen to have the most bright contrast around them.



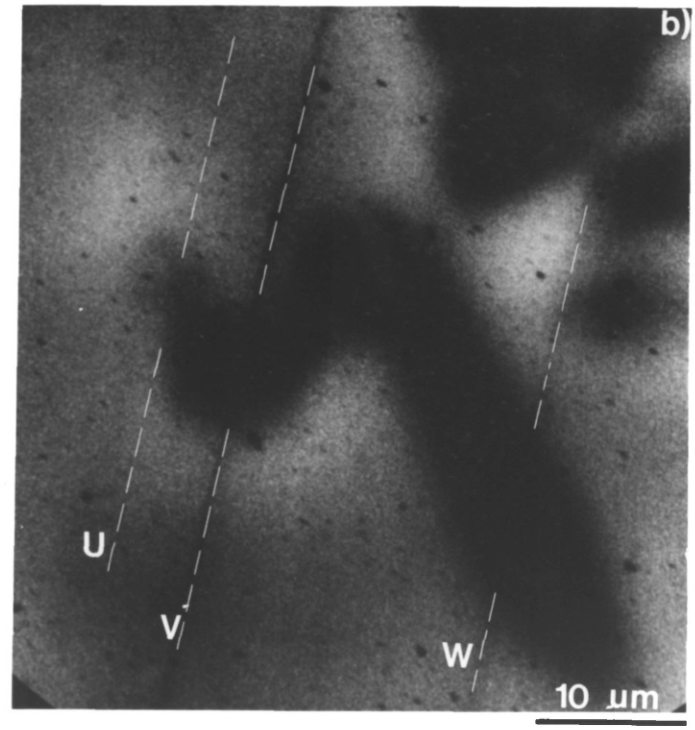


Fig. 70 - Dislocation "F" of Fig. 69(a) shown at large magnification. The EBIC micrographs were taken at (a) 20 KeV and (b) 33 KeV electron beam respectively.

In contrary, the defects marked C and D were observed in strong and broad dark contrast at 0V bias. They appeared in low contrast at high bias voltages and revealed the least bright contrast in their surroundings.

More detailed examination was carried out on the dislocation marked "F" in Fig. 69(a). The dislocation was relatively long and represented the cases described above, where all variations in contrast and resolution were concentrated on a single dislocation line. In the previous section it has been demonstrated that the technique based on the EBIC depth profiling can be successfully used for the determination of the depth location of defects in the RTAPDs. In the following experiment the method has been applied to the dislocation F in order to verify whether the observed changes in contrast and resolution, along the dislocation line, can be related to the changes in the depth location of the particular segments of the dislocation.

Fig. 70 shows the defect F at large magnification. The lettered lines indicate the locations in the dislocation from which the experimental data was collected. At each dislocation segment a series of measurements were carried out. This involved direct measurements of I_D and I_B for every particular E_b applied so that relations $\Delta I_D (= I_B - I_D)$ vs E_b could be determined for each of the three locations. The results are presented in Fig. 71 in a

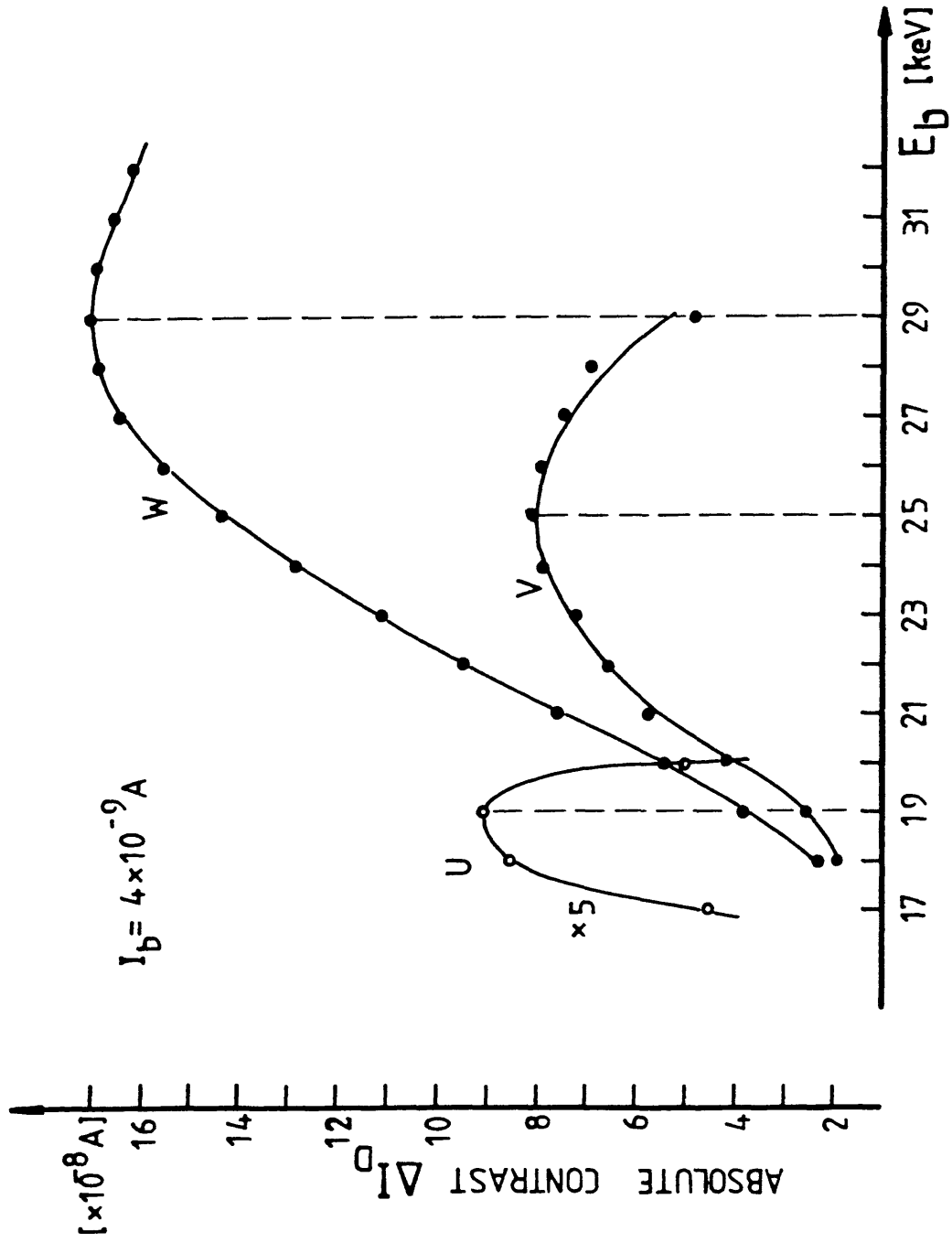


Fig. 71 - Experimental ΔI vs E_b data collected from points U,V,W on dislocation "F" of Fig. 70.

TABLE 7

		Test Point		
	I_b = 4nA = const.	U	V	W
	E_b max [KeV]	19	25	29
Maximum	I_B [A]	4.95×10^{-7}	3.95×10^{-6}	8.16×10^{-6}
Values	I_D [A]	1.8×10^{-8}	8.0×10^{-8}	17.0×10^{-8}
	g (Zo) electron/hole pairs per sec per µm	6.25×10^{13}	5.1×10^{13}	4.5×10^{13}
	Z_o [µm]	1.3	2.3	2.7

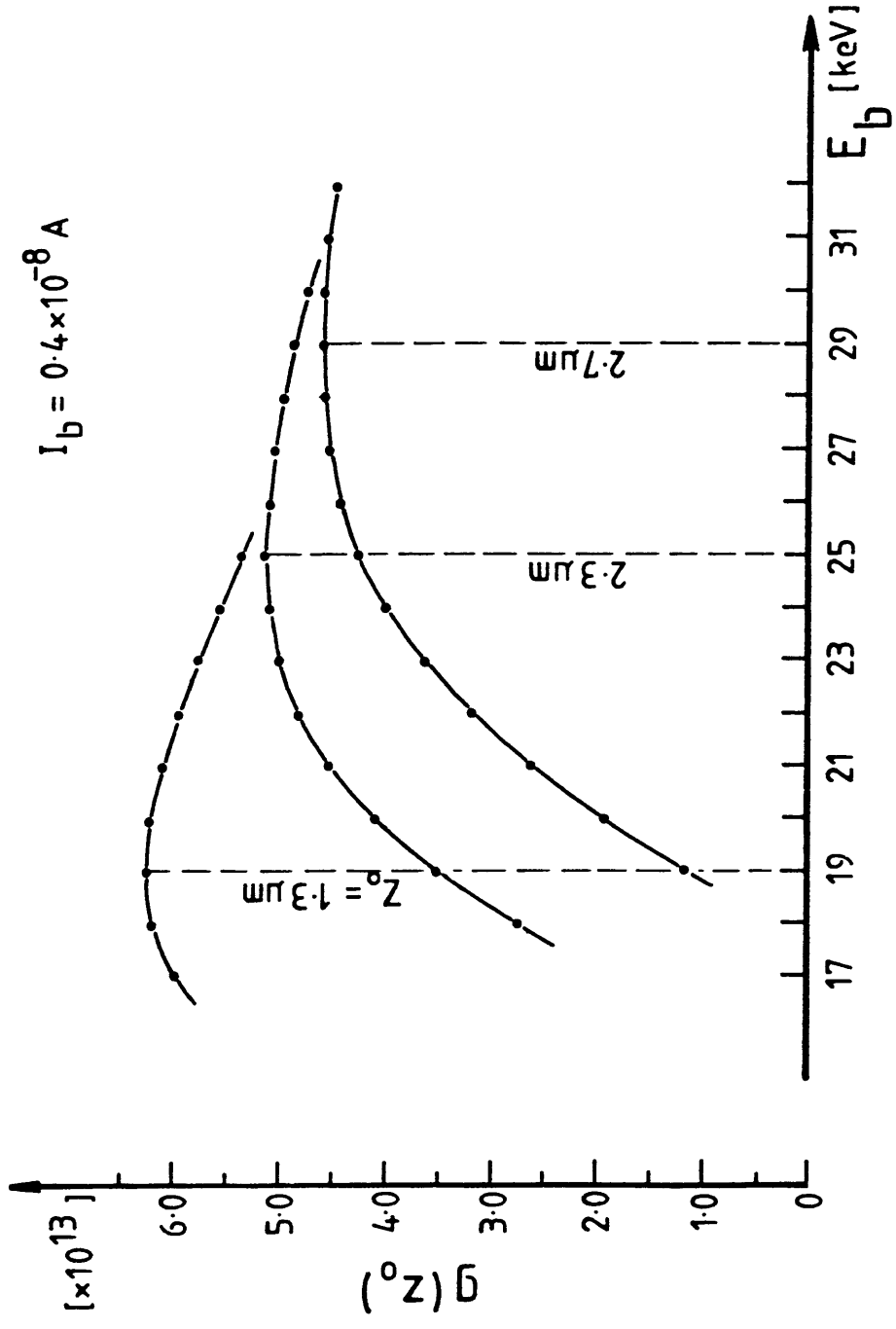


Fig. 72 - Theoretical $g(Z_o)$ vs E_b relations representing three different Z_o values 1.3, 2.3, and 2.7. These relations were matched to the ΔI_D vs E_b curves of Fig. 71.

graphical form. The experimental ΔI_D vs E_b relations in Fig. 71 are marked so they can be identified with a particular location on the dislocation. Theoretical relations g(Zo) vs E_b were selected to match each of the ΔI_D vs E_b relations and they are shown in Fig. 72. The selection was based on the adjusting of the Z_o so that the maximum values of both theoretical and experimental relations respectively, referred to the same E_b max. In result, three different Z_o values were obtained being: 1.3, 2.3 and 2.7 μm. They correspond to the depth locations of the dislocation segments marked U,V and W (Fig. 71), respectively.

Table 7 contains the measured values of ΔI_D and I_B corresponding to the E_b max levels for the three test points U, V and W.

Fig. 73 shows an EBIC micrograph representing another device. The device was biased up to nearly breakdown level and a 25 keV electron beam was used. The micrograph shows a microplasma site clearly related to the nodal point where several dislocations cross each other. It can also be seen that the intensity of the bright contrast, always increases locally in places where two or more dislocations overlap, or where the contrast on the dislocation appears weaker accompanied by a narrow image.

Fig. 74 shows EBIC Y-modulation line scans collected by scanning a single line across two dislocations. They were collected from the same device as in Fig. 73. One of the dislocations examined produced strong and broad images (marked I in Fig. 74). The second one (marked II), taken within a microplasma zone, appeared in weak contrast with a narrow image.

Discussion

Dislocation F in Fig.70 is shown to be composed of segments located at different depths. This was established through the application of the depth profiling method (section 3.5.5.), at three different points spaced along the dislocation line (i.e., U, V and W in Fig. 70). Each of the dislocation segments examined was characterised by a pair of ΔI_D (Z_o) vs E_b and $g(Z_o)$ vs E_b relations (see Fig. 71 and Fig. 72). The most obvious differences between ΔI_D vs E_b relations (representing particular dislocation segments) were manifested in:

- Shifts in the characteristic E_b values (E_b max), each being specified by the maximum value of the corresponding $\Delta I_D(Z_o)$ vs E_b relation.

- Scaling of the $\Delta I_D(Z_o)$ maximum values, the lowest of which was that of the segment nearest to the surface.

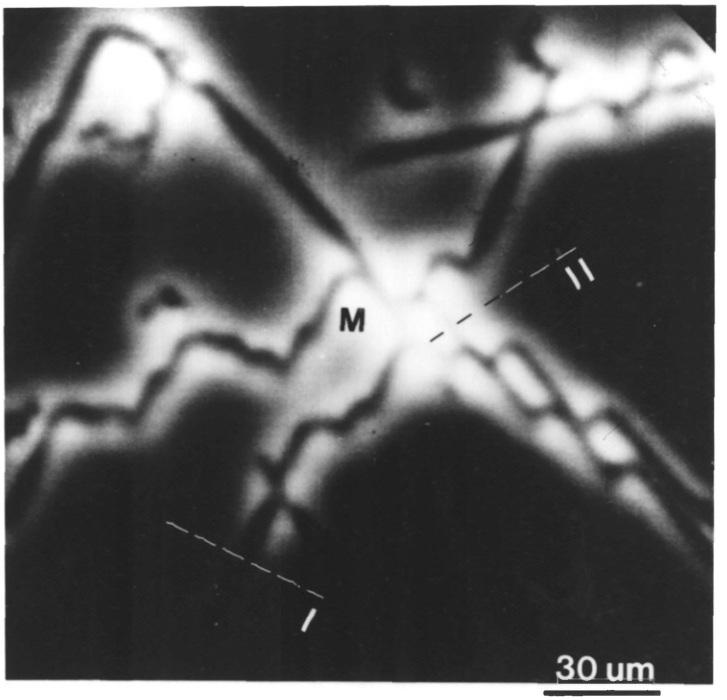


Fig. 73 - A larger magnification CC micrograph showing microplasma site "M" and misfit dislocations.

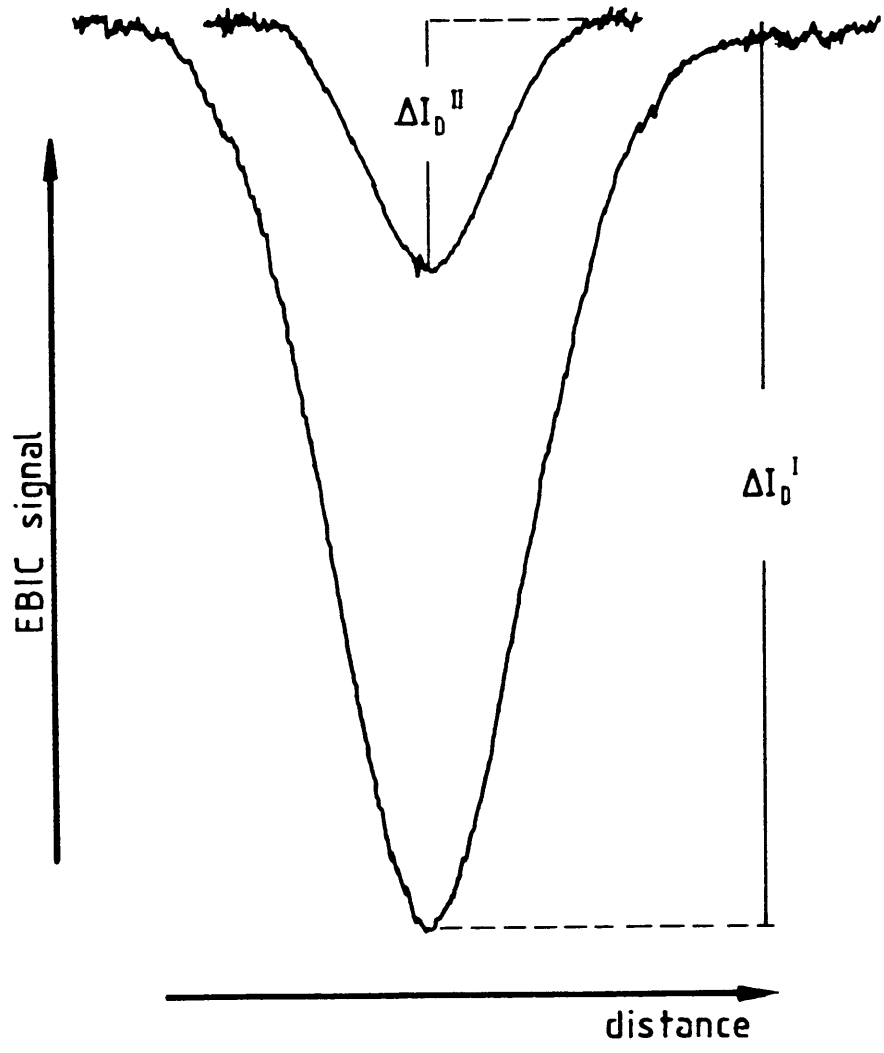


Fig. 74 - The near surface dislocation segments producing comparatively weak EBIC contrast and narrow image width (II) were associated with the strongest retardation effects and the most efficient microplasma sites (refer to Fig. 73). Both profiles I & II refer to OV bias and identical electron beam parameters.

The shifts in the E_b max values were used in combination with $g(Z_o)$ vs E_b relations to establish the differences in the depth location between points U, V and W. As a result of the examination carried out on the dislocation F, several conclusions were secured in reference to Fig. 69 and 71(a).

I For constant electron beam current condition, the visibility of a dislocation (amount of dark contrast - ΔI_D) reaches its maximum at a certain primary electron energy E_b max and degrades for E_b values lower or higher than that.

II A dislocation lying deeper requires a higher primary electron energy to reach E_b max.

III A dislocation located nearer to the surface is less visible (lower ΔI_D - level) for fixed electron beam current and voltage conditions.

IV The amount of bright contrast appears greatest along the dislocation (or its segment), at points nearest to the surface (Fig. 69).

From the conclusions presented above it is evident that the principal variations in the EBIC appearance of the dislocations in Fig. 69(a), (b), (c), arose due to differences in the depth location of these defects or their segments.

Using the examples already familiar from the points 1 - 4 (experimental section above), it can be seen that the dislocation segment B is the nearest to the surface. It appeared in a very faint contrast at 20 keV (Fig. 69(a) and vanished completely at the higher electron beam energies (Fig. 69(b) and (c)). Contrary to this, the deep lying segment C revealed a broad and strong EBIC image increasing in strength and size with E_b. This is justified in view of the remarks I - III and equation 29. In accordance with conclusion IV the dislocation segment B, being located nearer to the surface was associated with a zone of strong bright contrast stronger than the one observable around D (Fig. 69).

Microplasma sites, in principle, were seen in association with nodal points, where several dislocations cross each other. However, the most efficient channels (like that in Fig. 73) could be always found in conjunction with dislocation segments looping locally towards the surface. It can be seen in Fig. 73 that the dislocation segment associated with the central microplasma has a much narrower image width and lower ΔI_D levels as compared to the rest of the dislocations. This observation is supported through the line scans in Fig. 74 taken at OV bias from representative dislocation segments.

So far it has been established that the dislocations or their segments located near to the surface, were the most effective as far as the retardation phenomenon is concerned. Some of the dislocations seen in Fig. 68 were inclined towards the surface at relatively low angles with one end crossing the surface and the other tending towards the junction (dislocation F in Fig. 70). An interesting observation was that the dislocations were only seen within the depths down to approximately 3 μm beneath the surface. This statement can be generalised over all the samples examined since in each case, the inclined dislocations revealed approximately the same EBIC image width at their ends directed towards the n^+p junction. The experimental data suggest (I - II and eq. 29) that the nearer to the junction the dislocation gets the more pronounced it becomes in the sense of stronger absolute EBIC contrast ΔI_D and broader EBIC image. For example, Fig. 69(c) was recorded at 35 keV, that is the electron range R_e value slightly exceeded the junction depth. If electrically active, the dislocation would be expected to reveal a 16 μm wide image at the junction level. There is strong evidence provided by other researchers that the dislocations are electrically active (detectable using the EBIC technique) as long as they are decorated (section 1.7 and 1.11). It is concluded that the dark line defects observed in RTAPDs using the EBIC method represent only the parts of the dislocations that are decorated. These are located within

the surface area of the n^+ layer, where the concentration of phosphorus reached its highest possible levels. It appeared that there was a threshold level of the solute phosphorus concentrations above which the dislocations became detectable.

The dislocation segments located nearer the n^+p junction i.e., within the region characterised by lower phophorus concentrations, stayed undetectable. They continued on either threading the junction or stretching in directions parallel to the junction plane.

The former alternative might be justified in view of the EBIC micrographs like the one in Fig. 43, where many dislocations can be seen to follow the direction perpendicular to the surface plane. In view of several reports showing strong electrical effects (leakage sites) caused by dislocations crossing the junction (Ravi and Varker 1973, 1974; Ravi 1981), it was rather surprising not to see such consequences in the high voltage biased RTAPDs. On the other hand it has been suggested by Heydenreich et al. (1981) that crystallographic defects, as long as they are not decorated by impurities, seem never to generate high field effects. Some evidence of this has been provided through the combined TEM and EBIC observations on stacking faults. This would also be consistent with the fact that the dislocations in RTAPD were "clean" and undetectable by EBIC near to the junction.

In a single case however, contrast like that marked by an arrow (α) in Fig. 68(b) was observed. Such a regular dark contrast circle appeared at higher bias voltages and is consistent with being the junction leakage path possibly due to an intersecting dislocation.

The argument is thus tipped in favour of the dislocations threading the junction, but the possibility that the deep lying segments of the dislocations in RTAPDs, stretch parallel to the junction rather than cross it, cannot be ruled out entirely for now.

4.2.7. Observations of the EBIC Temperature Dependent Contrast on Misfit Dislocations

The electrical properties of defects in semiconductors are temperature sensitive. The transition in the electrical activity of defects occurs at higher temperatures, consistent with the movement of the Fermi level towards the middle of the bandgap. This may be used to advantage in change collection microscopy. As the Fermi level moves through a defect energy level with increasing T, the recombination efficiency of the defect will be altered and the energy level of the defect may be determined (Kimerling et al. 1977).

In the experiment described below it was aimed to provide more evidence on the properties of the misfit dislocations studied through EBIC observations of the effect of specimen temperature.

Two RTAPD samples with a low density of dislocations were selected. Observations of the effect of specimen temperature are presented in Fig. 75, Fig. 76 and 77. Fig. 75(a), (b), and (c) show three charge collection micrographs taken from the first device at -70, 25 and 120°C and 0V bias voltage. They correspond to the same electron beam current and voltage conditions. An 18 keV electron beam was used with I_b being 7.2 nA. The

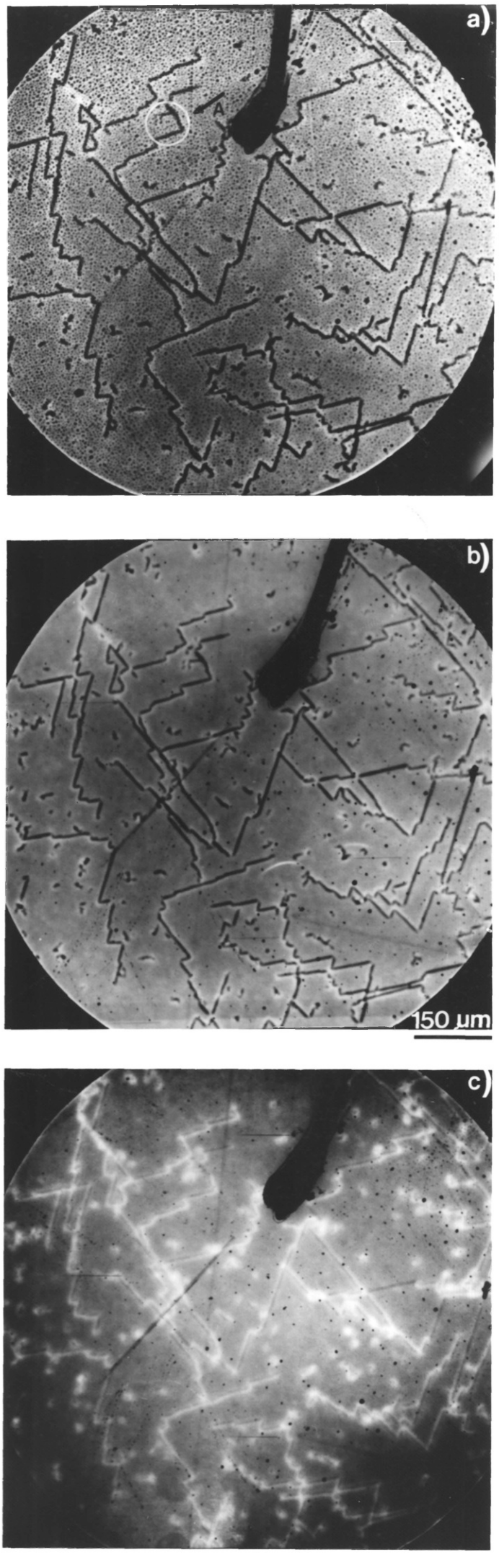
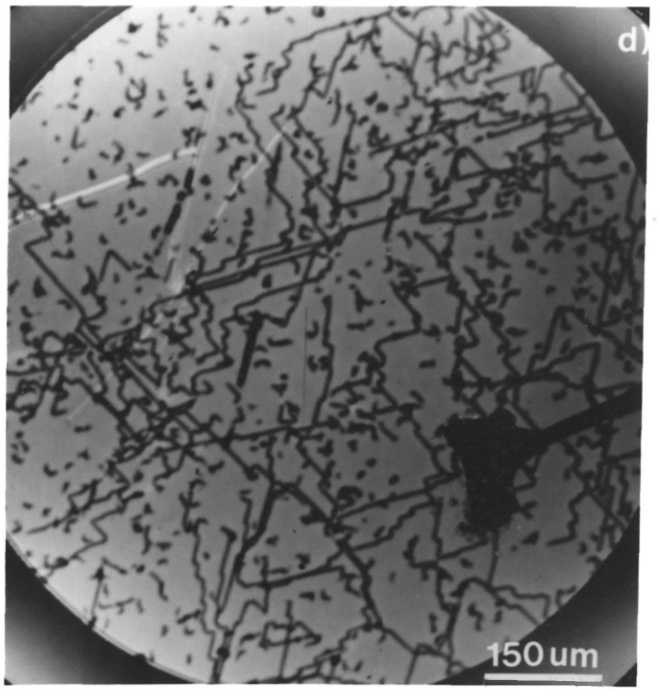


Fig. 75



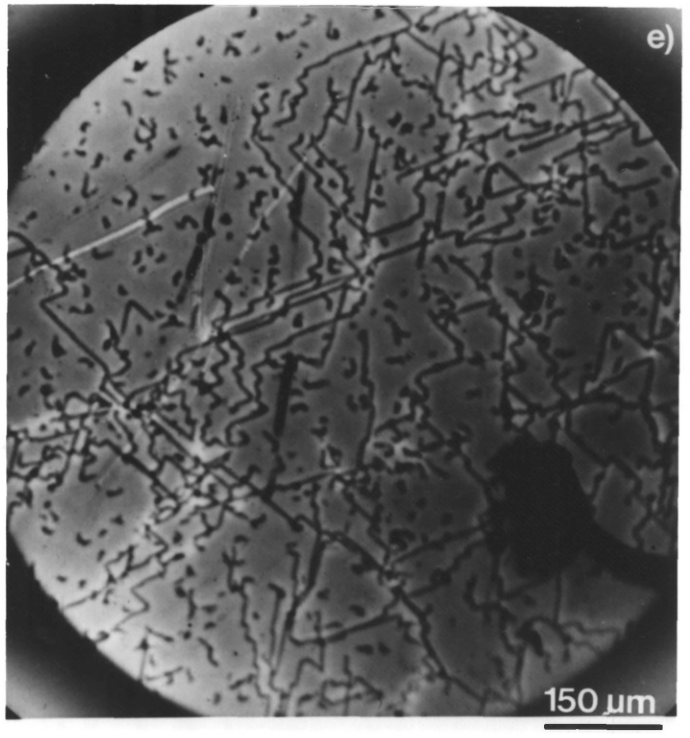


Fig. 75 - The effect of rising specimen temperature on misfit dislocation network dark line contrast in the SEM CC pictures.
Sample 1: (a) - 70°C, (b) 25°C, (c) 120°C
Sample 2: (d) - 173°C, (e) - 25°C

sensitivity of the H.A. and the gain of the video amplifier were maintained the same for all the micrographs. D.c. back off offset was also at the same level. The hot specimen stage used, is described in section 3.2.

Occasional control of I_b involved shifting of the specimen stage so that the electron beam could be aligned with a Faraday cage mounted on the side of the specimen holder. The specimen holder was subsequently repositioned so that another line scan could be collected from the same defect following approximately the same scanning track. The sample temperature in the microscope was controlled by a Cu block on one end attached to the TO-5 header and on the other to a Cu braid connected to a liquid nitrogen Dewar through a metal-glass feedthrough at the microscope port. The specimen temperature was recorded using a thermocouple attached to the TO-5 header. The cooling rate was extremely low, less than 1 deg/min so that collection of scan lines and measurement of I_B occurred at the same temperature. Recording of line scans and measurements of I_b and I_B were done with the application of identical electron beam parameters.

The effect of rising specimen temperature resulted in a marked reduction of EBIC contrast on dislocations (Fig. 75(b) and (c)). Simultaneously bright contrast junction irregularities distinctly appeared. Fig. 76 shows the

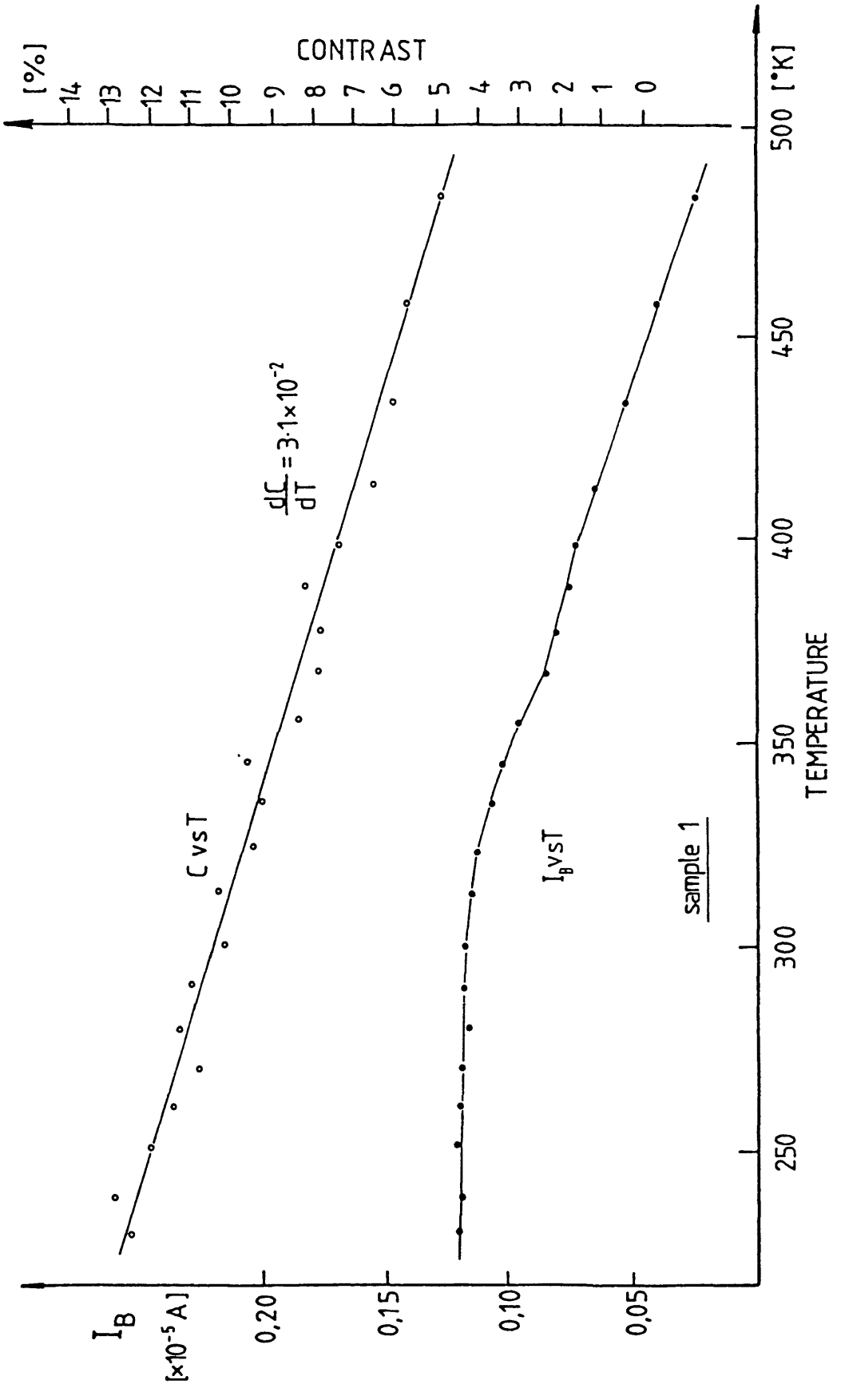


Fig. 76 - Temperature dependence of EBIC contrast due to dislocation d_1 Electron beam parameters: V_b = 18 KV; I_b = 7.2 nA.

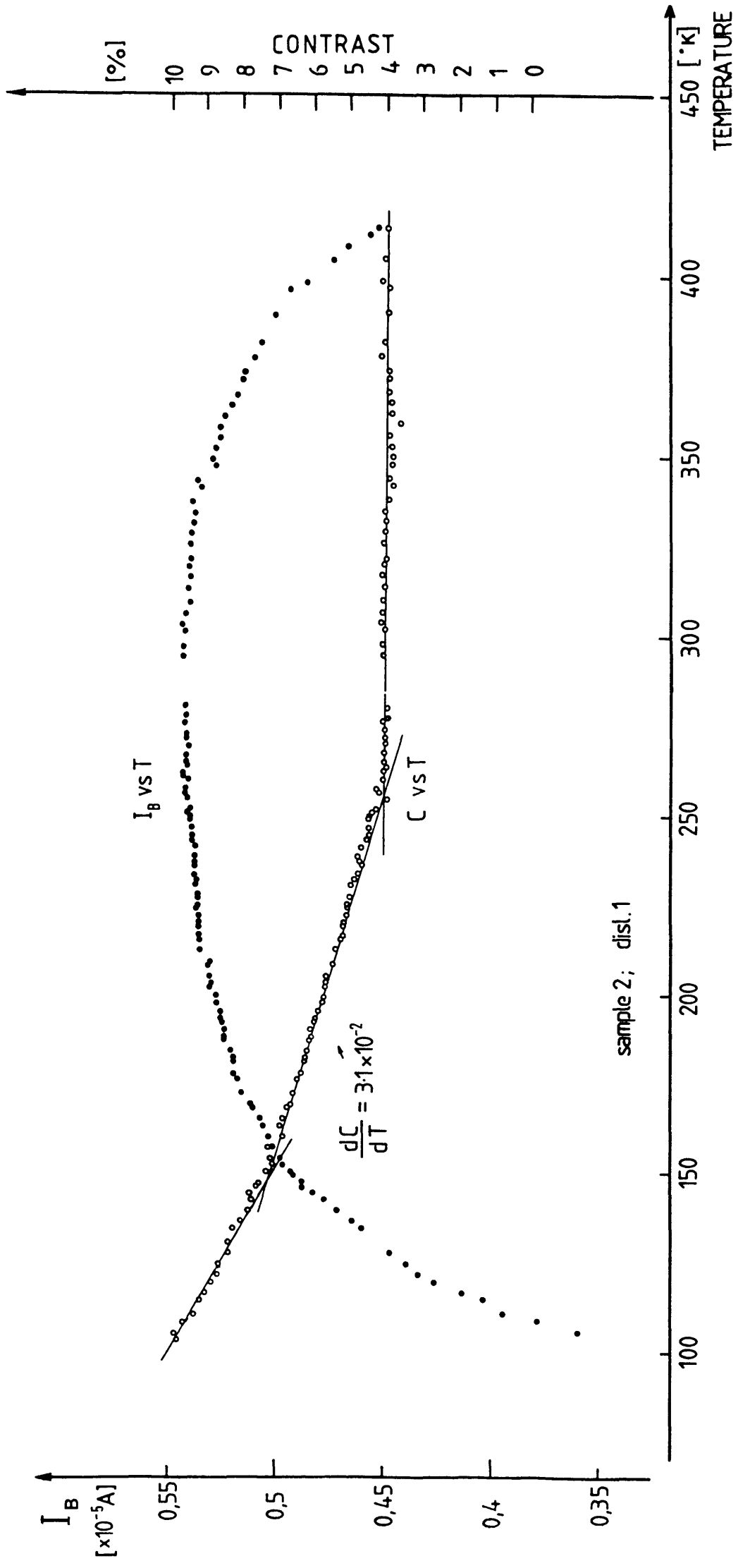

CONTRAST
[%]
10
9
8
7
6
5
4
3
2
1
0
TEMPERATURE
450 [°K]
400
350
300
250
200
150
100
I_B vs T
C vs T
$\frac{dC}{dT} = 3{\cdot}1\times10^{-2}$
sample 2; dist.1
I_B
[$\times10^{-5}$A]
0,55
0,5
0,45
0,4
0,35

Fig. 77a

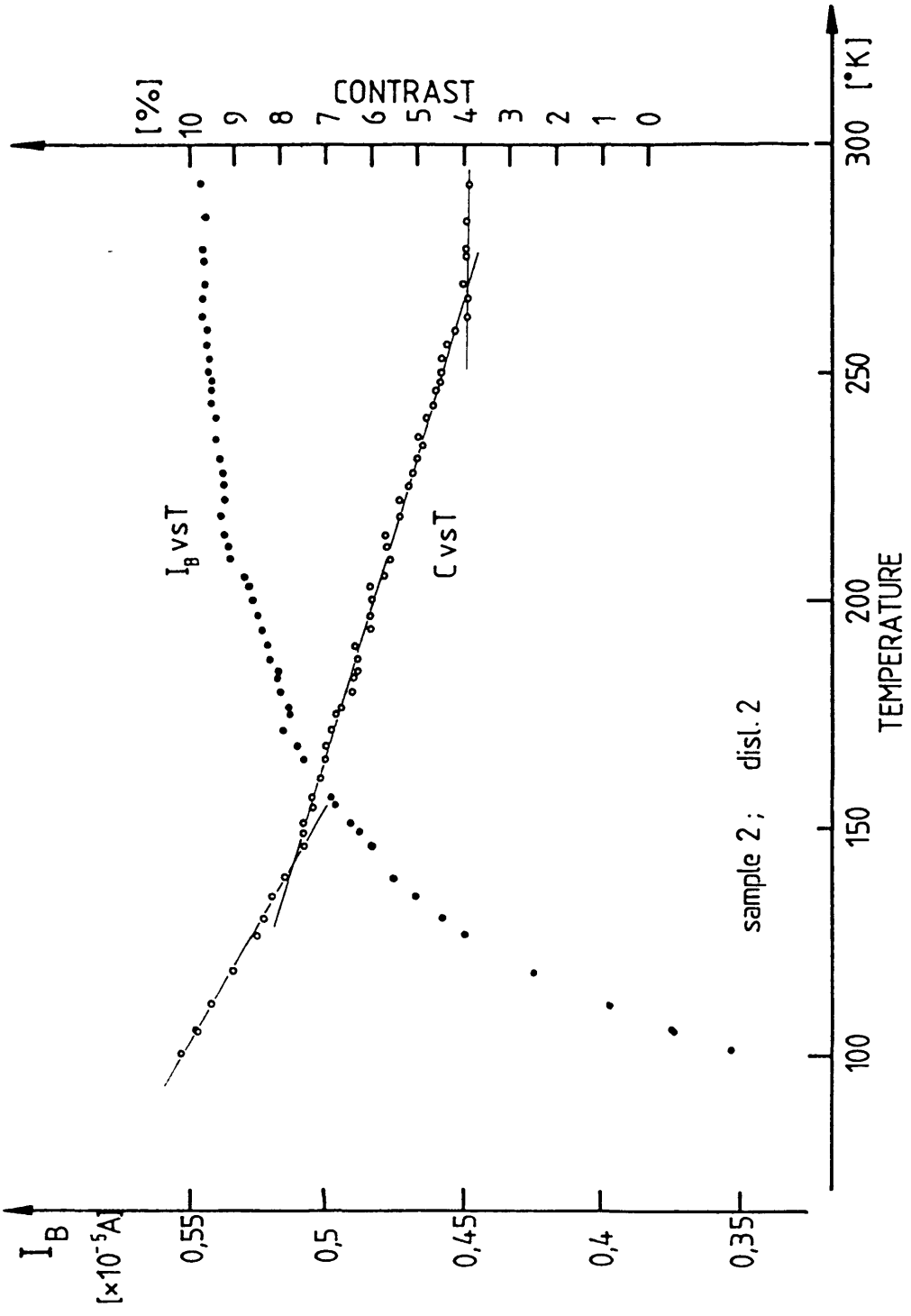


Fig. 77 - Temperature dependence of contrast at the dislocation (a) d_{21} and (b) d_{22}. Electron beam parameters: V_b = 25 KV; I_b = 7 nA.

variation in dislocation normalised contrast with temperature. The dislocation examined was parallel to the surface. Fig. 75(a) shows a charge collection micrograph of the device taken at 70°C. The transition in the electrical activity of the dislocation as observed in Fig. 75(a) and 76, suggests a linear dependence of the contrast on the temperature within the range from 70 to 120°C. The contrast on the dislocation was observed to decrease with increasing temperature. Since there was no thermal shield provided, the specimen was gradually covered with condensation, evident from Fig. 75(a) at low temperatures.

A similar experiment was carried out using another specimen. This time however, a specially designed "cold" specimen stage was used (described in section 2.3.) for measurements at low temperatures. The electron beam current was measured using a small graphite coated Cu wire attached to the spare pin on the TO-5 header (see section 2.1.6.). This eliminated the problem of shifting and repositioning of the specimen stage after each measurement of I_b. Experimental measurements were based on the same principles as previously, however, different electron beam parameters were used i.e., I_b was 7 nA and E_b was set at 25 keV. Measurements were carried out at a stable electron beam and temperature, both were controlled continuously during the experiment.

Fig. 77 shows the temperature dependence of charge collection of two separate dislocations d_{21} and d_{22} marked in Fig. 75(d). Fig. 75(d) and (e) present two EBIC micrographs recorded at near room and liquid nitrogen temperatures respectively. Similarily to the previous case, they indicate that CC contrast at the dislocations, increased considerably at low temperatures. The C vs T relations corresponding to d_{21} and d_{22} are shown in Fig. 77(a) and (b), respectively. They are very similar although different from the C vs T response recorded for d_1. It was interesting to observe that when tested at 18 keV and the same beam current of 7 nA, all three dislocations d_1, d_2 and d_{22} produced the same contrast level of 10.2% at room temperature.

Discussion

The transition in electrical activity at the dislocation shown in Fig. 76, suggests a change in the defect state occupation as the Fermi level moves with temperature. Increase in temperature corresponds to the Fermi level moving down (n-type material) towards the middle of the energy band gap. When the Fermi level "scans" through the defect energy levels, their occupation changes from full to empty. This apparently reduces their effectiveness as recombination centres. This interpretation found reflection in the observed decrease in the dark line

contrast. The width of the observed transition is extensive, stretching over the entire experimental temperature range. Such a wide transition range of temperatures is consistent with the presence of impurities associated with the dislocations that result in a "smeared out" distribution of states. From the results presented in the previous chapters, it also appeared that the observed electrical activity is to be associated with a surrounding impurity atmosphere rather than the dislocation itself. The C vs T relations representing the dislocations examined within the second sample (d_{21} and d_{22}), were significantly different. There was no change observed at temperatures above 260 K. However, the recombination efficiency of both dislocations revealed a linear increase with decreasing temperature below 260 K. The rate of increase in the EBIC contrast was in fact the same as in the previous case but occurred at lower temperatures. A slight inflection in the data was observed at about 140 K in both dislocations. This suggests that a second, shallow state may be present.

Such remarkable differences in the C vs T relations may be understood in terms of differences in the concentrations of impurity associated with dislocations in the two samples. However, there is another possible explanation which seems to be more important. This is concerned with the differences in the electron beam power applied to the diodes during the tests. The electron beam

power was larger by nearly a factor of two in the case of the second sample (Fig. 77). In addition, the primary electron energy used was 25 keV, so that the maximum of the electron energy dissipation occurred at the depth where the misfit dislocations were usually observed (see section 3.4.3.). If the temperature increases from the liquid nitrogen level upwards, as the local density of the electron beam injected minority holes changes from low to high densities, the quasi-Fermi level moves further down the energy band gap, leaving more of the dislocation states emptied. Since the effects of T and those of the carrier injection level on the recombination efficiency of the defect are additive, for each temperature an adequate concentration of extra holes may leave all the states emptied. The dislocation then is not able any longer to act as a recombination centre for holes. Above that temperature, the C vs T relation would remain unaltered. This is represented schematically in Fig. 78. The effect due to electron beam energy and power on the dislocations studied has been explained tentatively. However, there is some evidence supporting this interpretation. Firstly, when examined under similar electron beam excitation conditions the dislocations present in both diodes (d_1 and d_{21}), produced similar contrast levels. Secondly, extensive portions of the C vs T relations were parallel i.e., the dC/dT ratio was the same. This may indicate that the dislocations were of the same character (Ourmazd et al. 1983). Additionally, an effect that is similar in

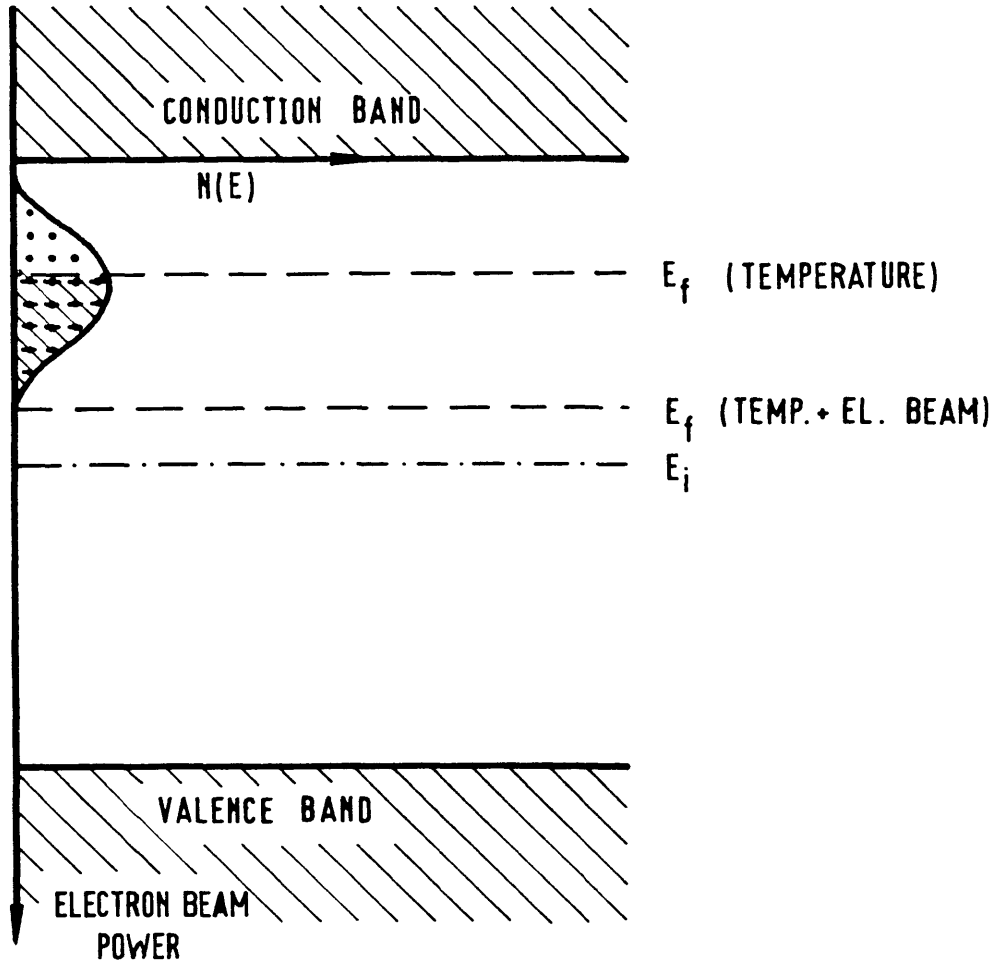


Fig. 78 - Energy level diagram of the dislocation in the band gap of a RTAPD being subjected to heating. The appropriate position of the quasi-Fermi level of holes for different electron beam excitation levels is indicated.

principle was demonstrated by Ravi (1981). The recombination activity of defects in solar cells, as observed in the SEM CC mode, was reduced considerably after the application of additional illumination.

4.2.8. Discussion

Having discussed the correlation between the depth location of the misfit dislocations and the extent of the associated dislocation retarded phosphorus diffusion (section 4.2.6.), the physical mechanism of the retardation process itself is still not explained.

Despite a significant amount of work on the effects of dislocations on diffusion in semiconductors, no clear concensus exists regarding the exact mechanisms involved. This in particular applies to the dislocation retarded diffusion effect. Duffy et al. (1968) suggested that the dislocation retarded diffusion phenomenon results because the misfit dislocations reduce strain-enhanced diffusion and that precipitates of dislocations may also have an effect. No direct evidence however has been secured behind this suggestion.

The experiments described earlier in this section have been designed to look at this problem and a few definite remarks can be made. In order to satisfactorily explain the contrast effects described in section 4.2.3. and 4.2.6., a model schematically illustrated in Fig. 79 has to be considered. The figure illustrates a situation in which the phosphorus n^+ layer diffusion has been locally retarded at the points where the dislocations occur. EBIC contrast arises from the electron/hole pairs generated within the

bulk of the n^+ layer, above the junction level. At the diffusion voids the junction stretches nearer towards the free surface and hence the electron beam generation zone. This promotes locally increased charge collection (refer to eq. 18). Thereby, the junction irregularities appeared on EBIC micrographs in bright contrast, superimposed upon the background signal. Furthermore, the magnitude of the bright contrast reflects the extent of the junction irregularities i.e., the distance by which the diffusion voids stretch above the plane of the junction.

From the foregoing observations it appears that the ragged junction area could only be correlated with the dislocations or their segments being also electrically active i.e., detectable in EBIC mode. On the other hand the electrical activity of these dislocations was shown to be essentially dominated by the impurity atmospheres stretching along the dislocation lines. In addition, the dislocations located nearer to the free surface appeared to result in stronger impurity retardation effects, manifested in more pronounced EBIC bright contrast zones (dislocation marked "F" in Fig. 70).

From the EBIC micrographs it appears that the impurity segregation along dislocations and the formation of the junction irregularities, (in the form of diffusion voids) are directly competing processes. This also indicates that the impurity atmospheres associated with the misfit

dislocation must be composed mainly of phosphorus atoms. The impurity segregation along dislocation lines could be due to both the Cottrell atmosphere (involving a reduction in elastic energy) and the negative charge of dislocation lines (in an n-type semiconductor), having a Coulombic attraction for the positively charged impurities (donors) present.

The presence of solute phosphorus can promote the formation of both mentioned types of atmospheres. However, in view of the extensive effects (ragged junctions) left as a result of phosphorus accumulation on dislocations, the Cottrell atmosphere formation seems to be favourable. The role of the space charge cylinder around the dislocation seems to be insignificant since even in pure semiconductors there are enough impurity atoms to saturate the dislocations present. There is another argument promoting the Cottrell atmosphere mechanism in association with the misfit dislocations. This is concerned with the observation that the dislocations located nearer to the surface, thereby surrounded by higher solute phophorus concentrations, resulted in a stronger retardation effect. This is most probably because more phosphorus atoms, otherwise available for diffusion, were accummulated within the atmosphere. Such an observation appears to be predicted in eq. (20), in which the concentration of phosphorus atoms built into the Cottrell atmosphere is proportional to the solute phosphorus concentrations within the matrix.

TEM observations presented in section 4.2.3. indicate that the formation of precipitates and dislocations can be considered as a possible contributory mechanism for dislocation retarded diffusion. Some of the dislocations seen in diffraction contrast were surrounded by impurity clouds and large precipitates. The diffusion induced dislocations and precipitates may thus act to reduce the effective mobility of the diffusing phosphorus atoms, by providing precipitation sites for some of these atoms or simply through mechanical masking (in the case of the larger precipitates).

In conclusion, the microplasma channels, having a ruinous effect on the performance of the RTAPDs can be attributed to the junction nonuniformities caused by the diffusion induced dislocations. The microplasma sites were most frequently encountered at the nodal points where several dislocations crossed each other. This is justified in view of the presented model. At the nodal points the diffusion retardation effect should be magnified due to the combined action of several dislocations. The extent of the resulting diffusion voids should be adequately larger, promoting a stronger high field effect in the complete device.

So far, the discussion has not commented on the observation that only some of the misfit dislocations or their segments were electrically active. The dislocations which were

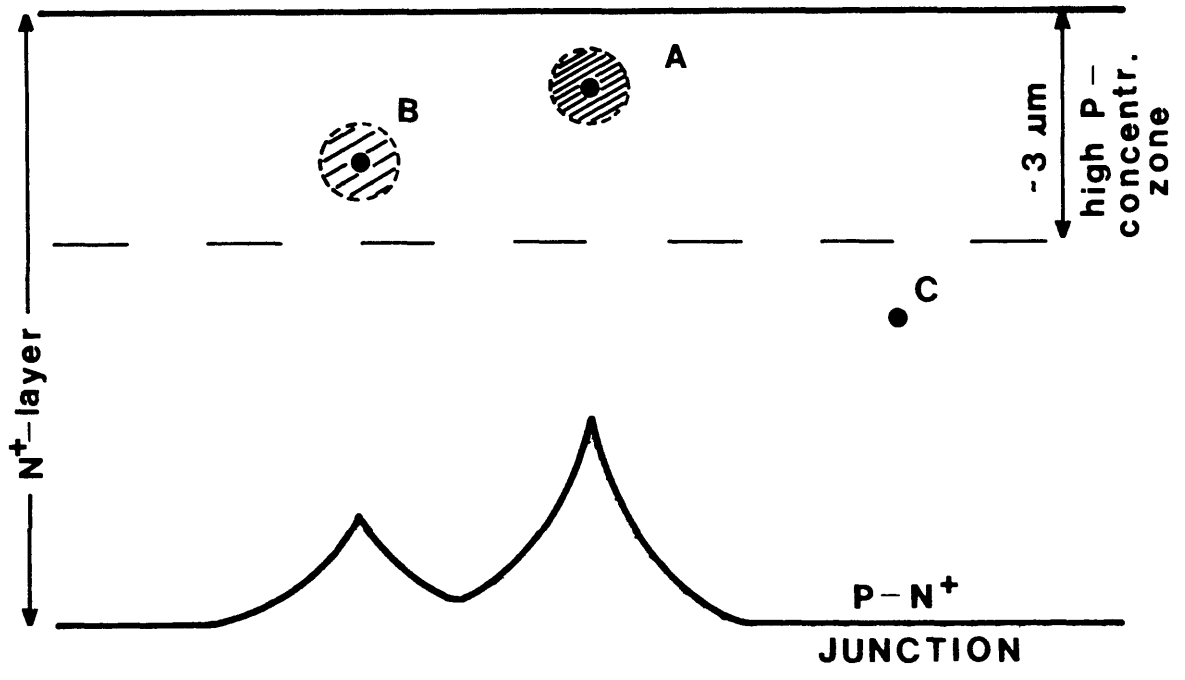


Fig. 79 - Schematic illustration of the dislocation network and the junction irregularities. Dislocations A and B are surrounded by Cottrell atmospheres composed of phosphorus atoms. Both A and B promote the formation of the junction nonuniformities. The electrical activity of A and B is entirely ruled out by their impurity atmospheres. Dislocation A, located nearer to the surface (being accompanied by a higher solute phosphorus concentration) results in a stronger retardation effect. Dislocation C stays within the low P-concentration zone of the n^+ layer. It does not develop a Cottrell atmosphere and therefore does not disturb the P-diffusion process, although it is rendered electrically inactive by the impurity ions saturating its core.

detectable using the EBIC mode were found within the near surface zone about 3 μm deep. This portion of the n^+ layer was also characterised by the highest possible concentrations of the solute phosphorus. The electrical activity of the dislocations within that surface zone appeared to be entirely dominated by the impurity atmospheres. The evidence was provided through systematic EBIC contrast and image width measurements and temperature dependent contrast analysis. The dislocation segments that were located nearer the n^+p junction (where the phosphorus concentration was much lower), have not exhibited any electrical activity i.e., stayed undetected. As mentioned above, only these detectable dislocations could be visibly related to the diffusion retardation process.

One of the possible explanations would refer to the undetectable dislocations as being "clean" - impurity free and therefore electrically inactive. There is some discussion on this matter in section 2.7., since it is generally assumed that the clean dislocations should be electrically active, although a few experimental observations seem to support the opposite view.

In the most basic approach, the electrical activity of dislocations can be understood in terms of dangling bonds making up the dislocation core. With reference to the fore mentioned EBIC observation, the most likely explanation therefore involves the dangling bonds which produce the

acceptor states being rendered electrically inactive by impurities (phosphorus ions). So the undetectable segments of dislocations may represent such saturated defects. This interpretation is also consistent with the measurements of EBIC image width of the misfit dislocation (in the detectable segments). The spatial resolution obtainable was determined exclusively by the instrumental and geometrical factors (R_e and Z_o, see section 4.2.5.). No visible contribution from the dislocation core was observed.

5. Discussion and Conclusions

The aim of this work was to design and accomplish a flexible, modular detection system capable of working with the different types of SEM conductive mode signals. This proved successful. The potential of the developed detection system was tested mainly through a study of the electrically active defects in silicon optoelectronic devices. SEM analysis of defects in general requires high spatial resolution and therefore operation in the low excitation regime and high sensitivity range of the detection system (CMDS). Temperature control, production of accurate data and easy operation must all be secured for the measurements to be performed efficiently. The Mark II CMDS facilities with the low noise head amplifier mounted inside of the specimen chamber, the battery based floating power supply, "on-line" signal processing functions and hot-cold stage, all performed satisfactorily and were found necessary in quantitative as well as micrographical work.

It is important that the CMDS can detect low levels of current so the long-range charge collection can be measured. In this case it made possible the determination of L_e in the π material (section 4.2.1.).

One of the advantages of the floating power supply was demonstrated in the experiments, where small amplitude a.c. bias waveforms had to be superimposed onto high d.c. bias levels in order to enable the observations of the microplasma noise and trapping effects in reach through avalanche photodiodes (RTAPDs) to be carried out.

The results presented in section 4 were selected to illustrate the performance of the Mark II CMDS and also to demonstrate the EBIC technique from the angle of its advantages and possible applications. This can be summarised as follows:-

(i) Combined SEM X-ray and EBIC analysis revealed that the soft I-V characteristics and large junction leakage currents in Si photodiode arrays resulted from diffusion pipes consisting of high phosphorus concentrations. The defects arose from process problems resulting in the poor quality of the masking oxide.

(ii) EBIC results obtained from both Si polycrystalline solar cell and polycrystalline GaP samples have been described. The role of impurities in the electrical properties of grain boundaries cannot be fully answered yet, but some evidence has been presented which indicates that impurities may prevent recombination at grain boundaries, acting either as the n^+n type or back to back Schottky barriers.

(iii) The EBIC examination of the RTAPDs revealed the dark lines and microplasma sites occurring throughout the n^+ diffused regions.

Tranmission electron microscope observations showed classical diffusion induced misfit dislocation networks to be present. In some cases the misfit dislocation segments

were traced to particular dark lines seen on a much larger scale in the scanning electron microscope, confirming that the dark EBIC lines represented single dislocations. TEM and SEM observations showed precipitates of different sizes to be present in the networks. These precipitates were shown not to produce any major electrical effects in the complete device. Premature breakdown voltage steps in the reverse I-V characteristics of the RTAPDs were traced to particular microplasmas. The onset of noise and then microplasma turn-on at these voltages was observed directly in short circuit current line scan traces as well as in the micrographs.

Combined SEM and TEM studies showed that a second bright stripe contrast mechanism operated to make the location of diffusion induced dislocations still visible after the layer containing the dislocations was ion-beam etched away. This is ascribed to "dislocation retardation of diffusion" resulting in the n^+p junctions being non-flat. Thus, the evidence is overwhelming that the noise and soft reverse characteristics of these RTAPDs, were due, not to diffusion induced misfit dislocations, but to related defects, that is ragged junctions due to dislocation retarded diffusion. These all were caused by in-diffusion with too high a surface density of the dopant.

(iv) A model explaining the retardation or ragged junction phenomenon has been presented. This refers to the gettering effect of the dislocations generated at high concentrations of phosphorus, so that in their neighbourhood, zones denuded of impurity atoms are formed. Therefore, the diffusion front became retarded below these dislocations.

(v) The experimental data suggests that there are two physical mechanisms governing the electrical properties of the diffusion induced misfit dislocations in RTAPDs. Firstly, the dislocations were being saturated with positively charged impurity ions and rendered electrically inactive. Relatively low phosphorus concentrations would be required to result in the dislocations being saturated. In addition the dislocations being "anchored" within the high phosphorus concentration (surface) zone, developed Cottrell-type atmospheres and promoted diffusion retardation effects.

(vi) From studies reported recently by other investigators, it appeared that by monitoring the EBIC contrast as a function of temperature and dopant concentration, the position of the defect energy can be determined. Clearly this has been demonstrated through the systematic measurements presented in this work. The C vs T transitions observed, imply that the electrical activity of dislocations present in RTAPDs, is determined by the impurity atmosphere associated with the defects. The results described here show that the

interpretation of the EBIC temperature dependent contrast on dislocations must also involve the effect of the electron beam excitation level. In addition, it appears that the combination of the temperature and the injection level as experimental variables promises to provide an interesting method for the study of defects.

(vii) The detailed SEM study of the individual misfit dislocations, has provided evidence that the EBIC spatial resolution depends exclusively on instrumental and geometrical factors i.e., the electron range R_e and depth location Z_o of the defect. Contrary to the intuitive notion, no visible evidence of the dependence of resolution on the monority carrier diffusion length or the extent of decoration, has been discovered. In consequence, the resolution vs primary electron energy data provide a means for the evaluation of the depth location of the dislocation.

(viii) It also follows that the method based on correlating the experimental ΔI_D vs E_b data and the electron beam depth/dose relations, provides the simplest means for the evaluation of the depth location of dislocations under conditions of short minority carrier diffusion length.

A good deal of literature on the quantitative interpretation of BEVE I_{sc}, i.e., true EBIC data is available (Bresse 1982; Leamy 1982; Davidson et al. 1981; Marten and Hildebrand 1983). Detection

systems like that reported here, in some cases with the use of a cold stage, make it readily possible to test and apply these theoretical treatments. It will also make it relatively easy to explore the utility of the largely neglected bulk EVE EBIC and EBIV and the β-conductivity information obtainable from a wide range of materials with forbidden energy gaps.

6. APPENDIX: CALCULATION OF g(Z)

The nomalised electron energy-loss parameter and range/energy relation were obtained from work by Everhart and Hoff (1971). This is represented by equations (4) and (3), respectively. From the same work the theoretical number of electron-hole pairs generated at a given depth can be expressed as:-

$$N(Z) = (E_b\ (1-\chi)/e_i\ R_e)\ \lambda\ (f) \tag{31}$$

where $f = Z/R_e$, Z is a distance below the irradiated surface, R_e the electron range, $\lambda(f)$ is the nomalised electron energy deposition parameter, E_b is the electron beam energy, e_i is the mean formation energy for electron hole pairs and the amount of energy carried away by back scattered electrons is represented by χ .

Using eq. (31), the total number of electron hole pairs created per second per unit length at depth Z can be expressed as:

$$g(Z) = (I_b/e)\ \ N(Z) \tag{32}$$

where I_b is the electron beam current and e is the electronic charge.

Eq. (32) represents the distribution of the electron hole generation rate within the electron energy dissipation volume for particular values of the electron beam energy and current level.

Eq. (32) can also be used to estimate the number of electron/hole pairs created at a given point below the surface for various levels of the electron beam power. Table 8 lists the calculated values of $g(Z_o)$ for the selected distances Z_o below the silicon surface. This involves different electron beam energy levels and a constant beam current of 0.760×10^{-8}A.

TABLE 8

E_b	I_b	R_e	Z_o = 2.3 µm g(2.3)	Z_o = 2.4 µm g(2.4)	Z_o = 2.5 µm g(2.5)	Z_o = 2.7 µm g(2.7)
[KeV]	[A]	[µm]	Number of electron/hole pairs per sec. per µm			
18		2.69	3.49×10^{13}	2.71×10^{13}	1.99×10^{13}	0.82×10^{13}
19		2.96	5.06	4.29	3.55	2.20
20		3.23	6.38	5.68	4.96	3.65
21	I_b =	3.52	7.39	6.79	6.18	4.95
22	const.	3.82	8.14	7.64	7.11	6.03
23	= 0.760 x	4.13	8.66	8.25	7.81	6.89
24	10^{-8}	4.45	9.00	8.67	8.31	7.54
25		4.78	9.19	8.93	8.64	8.01
26		5.12	max 9.27	9.07	8.84	8.33
27		5.47	9.26	max 9.11	8.94	8.53
28		5.83	9.18	9.07	max 8.95	8.63
29		6.20	9.05	8.98	8.89	max 8.66
30		6.58	8.89	8.85	8.79	8.62
31		6.96	8.71	8.70	8.66	8.55
32		7.36	8.51	8.51	8.54	8.43
33		7.77	8.29	8.31	8.31	8.29

7. BIBLIOGRAPHY

Arita, Y. and Sunohara, Y. (1977), "Formation and Properties of Porous Silicon Films", J. Electro-Chem. Soc. : Solid-State Science and Technology, 124, p. 285.

Ashburn, P. Bull, C., Nicholas, K.H. and Booker, G.R. (1977), "Effects of Dislocations in Silicon Transistors with Implanted Bases", Solid-State Electronics, 20, p. 731.

Ashburn, P. and Bull, C.J. (1979), "Observation of Dislocations and Junction Irregularities in Bipolar Transistors using the EBIC Mode of the Scanning Electron Microscope", Solid State Electronics, 22, p. 105.

Augustus, P.D. Knights, J. and Kennedy, L.W. (1980), "A Correlation between the Electrical Breakdown of Silicon Bipolar Transistors and Impurity Precipitates", J. Microscopy, 118, p. 315.

Balk, L.J. Kubalek, E. and Menzel, E. (1975), "Time-Resolved and Temperature Dependent Measurements of Electron Beam Induced Current (EBIC), Voltage (EBIV) and Cathodoluminescence in the SEM", Scanning Electron Microscopy I, (IIR Research Institute, Chicago, ILL 606616), p. 447.

Batdorf, R.L. Chynoweth, A.G., Dacey, G.C. and Foy, P.W. (1960), "Uniform Silicon p-n Junctions. I. Broad Area Breakdown", J. Appl. Phys., 31, p. 1153.

Berz, F. and Kuiken, H.K. (1976), "Theory of Lifetime Measurements with the Scanning Electron Microscope: Steady State", Solid State Electron. 19, p. 437.

Bishop, M.E. (1965), "A Monte Carlo Calculation on the Scattering of Electrons in Copper", Proc. Phys. Soc. 85, p. 855.

Blumtritt, M. and Gleichmann, R. (1977), "A Direct Comparison between SEM (EBIC) and HVEM Images of Crystal Defects in Semiconductors", Ultramicroscopy, 2, p. 405.

Blumtritt, H. Gleichmann, R., Heydenreich, J., and Johansen, H. (1979), "Combined Scanning (EBIC) and Transmission Electron Microscopic Investigations of Dislocations in Semiconductors", Phys. Status-Solidi, (a) 55, p. 611.

Booker, G.R., and Stickler, R. (1962), "Method of Preparing Si and Ge Specimens for Examination by Transmission Electron Microscopy",Brit. J. Appl. Phys., 13, p.466.

Breitenstein, O. (1982), "A Capacitance Meter of High Absolute Sensitivity Suitable for Scanning DLTS Application", Phys. Stat. Sol., (a) 71, p. 159.

Breitenstein, O. and Heydenreich, J. (1983), "Combined Electron Microscopical and DLTS Investigations in Semiconductors", J. De Physique Colloque C4 pp. C4/207-C4/215.

Bresse, J.F. and Lafeuille, D. (1971), "SEM Beam Induced Current in Planar p-n Junctions Diffusion Length and Generation Factor Measurements", in Proceedings of the 25th Anniversary Meeting of E.M.A.G., (Institute of Physics, London), p. 220.

Bresse, J.F. (1977), "Quantitative Use of the Electron Beam Induced Current(EBIC) for the Characterisation of Semiconductor Devices", in Scanning Electron Microscopy I (IIT Research Institute, Chicago, ILL 606616), p. 683.

Bresse, J.F. (1982) "Quantitative Investigations in Semiconductor Devices by Electron Beam Induced Current Mode", in Scanning Electron Microscopy IV, (IIT Research Institute, Chicago, ILL 60666), p. 1487.

Chaplin, K.S. (1959), "Microplasma Fluctuations in Silicon", J. Appl. Phys, 30, No.7, p. 1039.

Chi, J.Y. and Gatos, M.C. (1977), "Nondestcructive Determination of the Depth of Planar p-n Junctions by Scanning Electron Microscopy", IEEE Trans. Electron Devices ED-24, p. 1366.

Chynoweth, A.G. and Pearson, G.L. (1958), "Effect of Dislocations on Breakdown in Silicon P-N Junctions", J. Appl. Phys., 29, p. 1103.

Chynoweth, A.G. and McKay, K.G. (1957), "Internal Field Emission in Silicon P-N Junctions", Phys. Rev., 106, p. 418.

Ciszewski, B. (1972), "Defekty Struktury Krystalicznej", Fizyka Krysztalow, Cz.5, Warszawa 1972, WAT.

Cornu, J. Sitting, R. and Zimmermann, W. (1974), "Analysis and Measurement of Carrier Lifetimes in the Various Operating Modes of Power Devices", Solid State Electronics, 17, p. 1099.

Cullis, A.G. and Katz, L.E. (1974), "Electron Microscope Study of Electrically Active Impurity Precipitate Defects in Silicon", Phil. Mag., 30, p. 1419.

Czaja, W. and Wheatley, G.H. (1964), "Simultaneous Observation of Diffusion Induced Dislocation Slip Patterns in Silicon with Electron Beam Scanning and Optical Means", J. Appl. Phys., 35, p. 2782.

Czaja, W. and Patel, J.R. (1965), "Observations of Individual Dislocations and Oxygen Precipitates in Silicon with a Scanning Electron Beam Method", J. Appl. Phys., 36, p. 1476.

Czaja, W. (1966), "Conditions for the Generation of Slip by Diffusion of Phosphorus into Silicon", J. Appl. Phys, 37, p. 3441.

Czaja, W. (1966(a)), "Detection of Partial Dislocations in Silicon with the Scanning Electron Beam Technique", J. Appl. Phys., 37, p. 918.

Davidson, S.M. (1977), "Semiconductor Material Assessment by Scanning Electron Microscopy", J. Microscopy, 110, p. 177.

Davidson, S.M. and Dimitriadis, C.A. (1980), "Advances in the Electrical Assessment of Semiconductors using the Scanning Electron Microscope", J. Microscopy 118, p. 275.

Das, G. and O'Neil, N.A. (1974), "Preparation of Large-area Electron Transparent Samples from Silicon Devices", I.B.M. J. Res. Develop., 18, p. 76.

Davidson, S.M. Innes, R.M. and Lindsey, S.M. (1981), "Injection and Doping Dependence of SEM and Scanning Light Spot Diffusion Length Measurements in Silicon Power Rectifiers", Solid State Electronics, 25, p. 261.

De Kock, A.J.R. Ferris, S.D., Kimerling, L.C. and Leamy, H.J. (1975), "Investigation of Defects and Striations in As Grown Si Crystals by SEM Using Schottky Diodes", Appl. Phys. Lett., 27, p. 313.

Dushman, J.M. Haszko, S.E., Marcus, R.B., Murarka, S.P. and Sheng, T.T. (1979), "Electrically Active Stacking Faults in CMOS Integrated Circuits", J. Appl. Phys., 50, p. 2689.

Donalato, C. Merli, P.G. and Vecchi, J. (1977), "Characterisation of Microplasma Sites in Silicon n^+p Junctions", J. Electrochem. Soc., 124, p. 473.

Donalato, C. (1978), "On the Theory of SEM Charge-Collection Imaging of Localised Defects in Semiconductors", Optica, 52, p. 19.

Donalato, C. (1979a), "Contrast and Resolution of SEM Charge-Collection Images of Dislocations", Appl. Phys. Lett., 34, p. 80.

Donalato, C. (1979b), "Contrast Formation in SEM Charge-Collection Images of Semiconductor Defects", Scanning Electron Microsc., I. (IIR Research Institute, Chicago, ILL 606616), p. 257.

Donalato, C. (1979c), "Spatial Resolution of SEM-EBIC Images". Sol. State. Electron., 22, p. 797.

Donalato, C. (1980a), "Quantitative Properties of SEM-EBIC Images of Stacking Faults in Silicon", Japan. J. Appl. Phys., 19, p. L771.

Donalato, C. and Klann, H. (1980b), "Computer Simulation of SEM Electron Beam Induced Current Images of Dislocations and Stacking Faults", J. Appl. Phys., 51, p. 1624.

Donalato, C. (1981), "EBIC Image Profiles of Dislocations in the STEM", Microscopy of Semiconducting Materials 1981. Conf. Series. No. 60 (A.G. Cullis and d.c. Joy, ed.) Inst. Phys. Bristol and London, p. 215.

Donalato, C. (1983), "Quantitative Evaluation of the EBIC Contrast of Dislocations", J. de Physique Colloque C4, p. C4/269.

Duffy, M.C. Barson, F., Fairchild, J.M. and Schwutte, G.H. (1968), "Effects of High Phosphorus Concentration on Diffusion into Silicon", J. Electrochem. Soc., 115, p. 84.

Dumke, W.P. (1970), "Effect of Minority Carrier Trapping on the Low-Temperature Characteristics of Si Transistors", IEEE Trans. Electron Devices, ED-17, 388.

Edington, J.W. (1975), "Electron Diffraction in the Electron Microscope", Philips Technical Library, Monograph in Practical Electron Microscopy in Materials Science, N.V. Philips Gloeilampen Fabrieken, Eindhoven, 1975.

Ehrenberg, W. Lang, C.S. and West, R. (1951). "The electron voltaic effect", Proc. Phys. Soc. London, Sect. A64, p. 424.

Everhart, T.E. Wells, O.C. and Matta, R.K. (1964a), "A Novel Method of Semiconductor Device Measurements", Proc. IEE, 52, p. 1642.

Everhart, T.E. Wells, O.C. and Matta, R.K. (1964b), "Evaluation of Passivated Integrated Circuits Using the Scanning Electron Microscope", J. Electrochem. Soc, 111, p. 926.

Everhart, T.E. and Hoff, P.M. (1971), "Determination of Kilovolt Electron Energy Dissipation versus Penetration Distance in Solid Materials", J. Appl. Phys., 42, p. 5837.

Fathy, D. Sparrow, T.G. and Valdre, V. (1980), "Observation of Dislocations and Microplasma Sites in Semiconductors by Direct Correlations of STEBIC, STEM and EELS", J. Microscopy (London), 118, pp. 263-273.

Galloway, K.F. Leedy, K.O., and Keery, W.J. (1976), "Electron-Beam Induced Currents in Simple Device Structures, " IEEE Trans. Parts, Hybrids, Packag., PHP-12, p. 231.

Garret, I. (1982), "Receivers for Optical Fibre Communication", Wireless World, April 1982, p. 62.

Gaylord, J.W. (1966), "Microplasma Observations in Silicon Junctions Using a Scanning Electron Beam", J. Electrochem. Soc., 113, p. 753.

Ghezzi, C. and Servidori, J. (1974), "X-Ray Study of Heterogenous Nucleation of Dislocations in P-Diffused Silicon", J. Mat. Sci., 9, p. 1797.

Goetzberger, A. and Schockley, W. (1960), "Metal Precipitates in Silicon p-n Junctions", J. Appl. Phys., 31, p. 1821.

Goetzberger, A. and Stephens, C. (1961), "Voltage Dependence of Microplasma Density in p-n Junctions in Silicon", J. Appl. Phys., 32, p. 2646.

Gopinath, A. (1970), "On Scanning Electron Microscope Conduction Mode Signals in Bulk Semiconductor Devices: Linear Geometry", J. Phys. D. Appl. Phys., 3, p. 467.

Gopinath, A. and De Monts De Savasse, T. (1971), "On Scanning Electron Microscope Conductive Mode Signals in Bulk Semiconductor Devices: Annular Geometry", J. Phys. D. Appl. Phys., 4, p. 2031.

Henisch, H.K. (1962), "Electroluminescence", Pergamon Press, New York.

Heydenreich, J. Blumtritt, H., Gleichmann, R. and Johansen, H. (1979), "High Voltage Electron Microscopy and Scanning Electron Microscopy (EBIC Mode) of the same Dislocation", J. Phys. (Paris), 40, C6-23.

Heydenreich, J. Blumtritt, H., Gleichmann, R. and Johansen, H. (1981), "Electron Microscopic Investigations of the Recombination Activity of Dislocations in Silicon", Cryst. Res. Technol., 16, p. 133.

Hirsch, P.B., Howie, A., Nicolson, R.B., Pashley, D.W., Whelan, M.J. (1865), "Electron Microscopy of Thin Crystals", Butterworth & Co., (Publishers) Ltd., London.

Holt, D.B. (1974), Chapter 8, "Quantitative Conductive Mode Scanning Electron Microscopy", Academic Press: London p. 335.

Holt, D.B. Ogden, R. (1976), "Observation of Dislocations in a Silicon Phototransistor by Scanning Electron Microscopy Using the Barrier Electron Voltaic Effect", Solid State Electron., 19, p. 37.

Holt, D.B. (1981), "Recent developments in SEM Detection Systems for the Cathodoluminescence and Conductive Modes", in Microscopy of Semiconducting Materials, 1981. Conf. Series. No. 60 (A.G. Cullis and D.C. Joy. Editors), Inst. Phys., Bristol and London, p. 165.

Holt, D.B. Lesniak, M.P. and Luther, P. (1983), "Image Processing of SEM Micrographs of Integrated Circuits for Defect Location", J. Mat. Sci. Letters, 2, p. 565.

Hovel, W. (1975), Semiconductors and Semimetals, 11, Academic Press, New York (1975).

Huang, H. Aliotta, C.F., and Ho, P.S. (1982), "Schottky Barrier Height Measurement by Electron Beam Induced Voltage", Appl. Phys. Lett.,41, p. 54.

Jaccodine, R. (1964), "Diffusion-Induced Dislocation Network in Si", Appl. Phys. Lett., 4, p. 114.

Joshi, M.L. and Wilhelm, F. (1965), "Observation of Diffusion-Induced Dislocation Lines in Silicon through Optical Microscopy", J. Appl. Phys., 36, p. 2593.

Joshi, M.L. (1965), "Effect of Fast Cooling on Diffusion-Induced Imperfections in Silicon", J. Electrochem. Soc., 112, p. 912.

Joy, D.C. (1974), "SEM Parameter and their Measurements", Proc. 7th Ann. SEM Symposium (IITRI, Chicago), p. 332.

Kaiser, W. Keck, D.H., Lange, C.F. (1956), "Infrared Absorption and Oxygen Content in Silicon and Germanium", Phys. Rev., 101, p. 1264.

Kaneda, T., Matsumoto, H., Yamaoka, T. (1976), "A Model for Reach-Through Avalanche Photodiodes (RAPD's)", J. Appl. Phys., 47, p. 3135.

Kawado, S. Hayafuji, Y. and Adachi, T. (1975), "Observation of Lattice Defects in Silicon by Scanning Electron Microscopy Utilising Beam Induced Current Generated in Schottky Barriers", Japan. J. Appl. Phys., 14, p. 407.

Kawado, S. (1980), "Scanning Electron Microscopic Observation of Oxidation Induced Stacking Faults in Silicon", Jap. J. Appl. Phys., 19, p. 1591.

Kikuchi, M. and Tachikawa, K. (1960), "Visible Light Emission and Microplasma Phenomena in Silicon p-n Junction", J. Phys. Soc. Japan, 15, p. 835.

Kilbesen, B.O. Mayer, K.R., Schuh, G.E. (1975), "A New Preparation Method for Large Area Electron Transparent Silicon Samples", J. Phys. E. Sci. Instrum., 8, p. 197.

Kimerling, L.C. Leamy, H.J. and Patel, J.R. (1977), "The Electrical Properties of Stacking Faults and Precipitates in Heat Treated Dislocation Free Czochralski Silicon", Appl.Phys. Lett., 30, p. 217.

Kimerling, L.C. Leamy, H.J., Benton, J.L., Ferris, S.D., Freeland, P.E. and Rubin, J.J. (1977b), "Analysis of Impurity Distributions and Defect Structures in Semiconductors by SEM Charge Collection Microscopy" in Semiconductor Silicon 1977, edited by H.R. Huff and E. Sirlt (Electrochemical Society, Princeton, NJ), p. 468.

Kittler, M. and Seifert, W. (1981), "On the Sensitivity of the EBIC Technique as Applied to Defect Investigations in Silicon", Phys. Stat. Sol., (a) 66, p. 573.

Kressel, H. (1967), "A Review of the Effect of Imperfections on the Electrical Breakdown of P-N Junctions", RCA Rev., 28, p. 175.

Kurtz, A.D. Kulin, S.A., Averbach, B.L., (1956), "Effect of Dislocations on the Minority Carrier Lifetime in Semiconductors", Phys. Rev., 101, p. 1285.

Lander, J.J. Schreiber, H., Buck, T.M. and Matthews, J.R. (1963), "Microscopy of Internal Crystal Imperfections in Si p-n Junction Diodes by Use of Electron Beams", Appl. Phys. Lett., 3, p. 206.

Lang, D.V. (1974), "Deep-Level Transient Spectroscopy: A new Method to Characterise Traps in Semiconductors", J. Appl. Phys., 45, p. 3023.

Leamy, H.J.. Kimerling, L.C., and Ferris, S.D. (1976), "Silicon Single Crystal Characterisation by SEM", in Scanning Electron Microscopy I (IIT Research Institute, Chicago, ILL 606616), p. 529.

Leamy. H.J. (1982) "Charge Collection Scanning Electron Microscopy", J. Appl. Phys., 53, p. R51.

Lesniak, M.P. and Holt, D.B. (1983), "Eletrically Active Defects in Si Photodetector Devices", in Microscopy of Semiconducting Materials 1983, Conf. Series No. 67 (A.G. Cullis, S.M. Davidson and G.R. Booker, ed), Inst. Phys., Bristol and London, p. 439.

Lesniak, M. Unvala, B.A. and Holt, D.B. (1984), "An Improved Detection System for Electrical Microcharacterisation in a Scanning Electron Microscope", J. Microscopy, 135, p. 255.

Levine, E. Washburn, J. and Thomas, G. (1967), "Diffusion Induced Defects in Silicon I and II", J. Appl. Phys., 38, p. 81.

MacDonald, N.C. and Everhart, T.E., (1969), "Direct Measurement of the Depletion Layer Width Variation vs. Applied Bias for a p-n Junction", Appl. Phys. Lett., 7, p. 267.

Marten, H.W. and Hildebrand, O. (1983), "Computer Simulation of EBIC Linescans across PN Junctions", Scanning Electron Microscopy III, (IIR Research Institute, Chicago, ILL 606616), p. 1197.

Marcus, R.B. Robinson, M., Sheng, T.T., Haszko, S.E., Murarka, S.P. and Katz, L.E. (1977), "Electrical Activity of Epitaxial Stacking Faults", J. Electrochem. Soc., 124, p. 425.

Mayes, L.J. (1982), "Computer-Based Characterisation of Detectors for Optical Communication", Electro-Optical System Design, December 1982, p. 28.

McIntyre, R.J. (1961), "Theory of Microplasma Instability in Silicon", J. Appl. Phys., 32, p. 983.

McKay, K.G. (1954), "Avalanche Breakdown in Silicon", Phys. Rev, 94, p. 877.

Meek, R.L. (1971), "Anodic Dissolution of N^+ Silicon", Electrochem Soc. : Solid State Science and Technology, 118, p. 437.

Melchior, H. and Lynch, W.T. (1966), "Signal and Noise Response of High Speed Germanium Avalanche Photodiode", IEEE Trans. Electron Devices, ED - 13, p. 826.

Menniger, H. Raidt, M. and Gleichmann, R. (1980), "On the Interaction between Crystal Defects and Impurities in Silicon Investigated by Electron Microscopic Methods", Phys. Stat. Solidi, (a) 58, p. 173.

Munakata, C. (1966), "On the Voltage Induced by an Electron Beam in a Bulk Semiconductor Cyrstal", Jap. J. Appl. Phys., 5, p. 756.

Munakata, C. (1967 a), "An Electron Beam Method of Measuring Resistivity Distribution in Semiconductors", Jap. J. Appl. Phys., 6, p. 963.

Munakata, C. (1967 b), "Detection of Resistivity Variation in a Semiconductor Pellet with an Electron Beam", Microelectronics and Reliability, 6, p. 27.

Munakata, C. (1968 a), "Voltage Signal due to Electron Beam Induced Conductivity in Semiconductors". Jap. J. Appl. Phys., 7, p. 1051.

Munakata, C. (1968 b), "An Application of Beta Conductivity to Measurement of Resistivity Distribution", J. Phys. E., 1, p. 639.

Munakata, C. (1969), "Scanning Electron Micrograph using Beta-Conductive Signal", J. Phys. E., 2, p. 738.

Nield, M.W. and Leck, J.M. (1967), "A Report on the Delay Time of an Avalanche Discharge in Silicon", Brit. J. Appl. Phys.,18, p.185.

Nuttall, K.I. and Nield, M.W. (1975), "An Investigation into the Behaviour of Trapping Centres in Microplasmas", Solid-State Electron., 18, p. 13.

Oelgart, G. Fiddicke, J. and Reulke, R. (1981), "Investigation of Minority Carrier Diffusion Lengths by means of the Scanning Electron Microscope (SEM)", Phys. Status. Solidi., (a) 66, 283.

Ourmazd, H. and Booker, G.R. (1979), "The Electrical Recombination Efficiency of Individual Edge Dislocations and Stacking Fault Defects in n-type Silicon", Phys. Status Solidi, (a) 55, p. 771.

Ourmazd, A. Weber, E. Gottschalk, G.R. and Alexander, H (1981), "The Electrical Behaviour of Individual Screw and 60° Dislocations in N-type Silicon", in Microscopy of Semiconducting Materials 1981. Conf. Series No.60 (A.G. Cullis and D.C. Joy Editors). Inst. Phys., Bristol and London, p. 63.

Ourmazd, A. Wilshaw, P.R. and Booker, G.R. (1983a), "The Electrical Behaviour of Individual Dislocations, Shockley Partials and Stacking Fault Ribbons in Silicon", Physica, 116B, p. 600.

Ourmazd, A. Wilshaw, P.R. and Booker (1983b), "The Temperature Dependence of EBIC Contrast from Individual Dislocations in Silicon", J. De Physique Colloque, C4 (1983) p. C4/209.

Pankove, J.I. (1962), "The Electrochemistry of Semiconductors", P.J. Holmes, Editor, Academic Press, Inc. New York.

Pasemann, L (1981), "A Contribution to the Theory of the EBIC Contrast of Lattice Defects in Semiconductors". Ultramicroscopy, 6, p. 237.

Pasemann, L. Blumtritt, M. and Gleichmann, R. (1982), "Interpretation of the EBIC Contrast of Dislocations in Silicon", Phys. Stat. Sol., (a) 70, p. 197.

Pettit, H.R., Booker, G.R. (1971), "Tem Studies of Cross-Sections, Prepared by Ion-Beam Thinning, through Epitaxial Silicon Layers", Proc. 25th Anniversary Meeting of EMAG. Inst. Physics, p. 290.

Petroff, P.M. and Lang, D.V. (1977), "A New Spectroscopic Technique for Imaging the Spatial Distribution of Nonradiative Defects in a Scanning Transmission Electron Microscope", Appl. Phys. Lett., 31, p. 60.

Petroff, P.M. Lang, D.V. Strudel, J.L. and Savage, A. (1978), "New STEM Spectroscopic Techniques for Simultaneous Electronic Analysis and Observation of Defects in Semiconductor Materials and Devices", in Electron Microscopy 1978 (ed. J.M. Sturgess), Microscopical Society of Canada, Toronto, Canada, I, p. 130.

Petroff, P.M. Logan, R.A. and Savage, A. (1980), "Nonradiative Recombination of Dislocations in III-V Compound Semiconductors", Phys. Rev. Lett., 44, p. 287.

Possin, G.E. and Kirpatrick, C.G. (1979a), "Electron Beam Depth Profiling in Semiconductors", J. Microscopy, 118, p. 291.

Possin, G.E. and Kirpatrick, C.G. (1979b), "Electron Beam Measurements of Minority Carrier Lifetime Distributions in Ion Beam Damaged Silicon", J. Appl. Phys., 50, pp. 4055-4051.

Prussin, S. (1961), "Generation and Distribution of Dislocations by Solute Diffusion", J. Appl. Phys., 32, p. 1876.

Queisser, H.J. and Goetzberger, A. (1963), "Microplasma Breakdown at Stair-Rod Dislocations in Silicon", Phil. Mag., 8, p. 1063.

Ravi, K.V. Varker, C.J. and Volk, C.E. (1973), "Electrically Active Stacking Faults in Silicon", J. Electrochem. Soc., 120, p. 533.

Ravi, K.V. and Varker, C.J. (1974), "Comments on the Distinction Between Striations and Swirls in Silicon", Appl. Phys. Lett., 25, p.69.

Ravi, K.V. (1981), "Imperfections and Impurities in Semiconductor Silicon", Wiley - Interscience Publication, John Wiley & Sons, New York, 1981.

Read, W.T., Jr, (1954), "Theory of Dislocations in Germanium", Phil. Mag., 45, p. 775.

Rose, D.J. (1957), "Microplasmas in Silicon", Phys. Rev., 105, p. 413.

Rupprecht, H. and Schwutte, G.M. (1966), "Distribution of Boron-Induced Defects in Shallow Diffused Surface Layers of Silicon", J. Appl. Phys., 37, p. 2862.

Russell, G.J., Waite, P. and Woods, J. (1981), "Electrically Active Grain Boundaries in Polycrystalline Zinc Selenide", in Microscopy of Semiconducting Materials 1981 Conf. Series No. 60 (A.G. Cullis and D.C. Joy, eds), Inst. Phys. Bristol and London, p. 371.

Schick, J.D. (1981) "Electron Beam Induced Current Analysis of Integrated Circuits", in Scanning Electron Microscopy I, (IIR Research Institute, Chicago ILL 606616), p.295

Schwutte, G.H. and Queisser, H.J. (1962), "X-Ray Observations of Diffusion Induced Dislocations in Silicon", J. Appl. Phys., 33, p. 1540.

Senitzky, B. and Mill, J.L. (1958), "Breakdown in Silicon", Phys. Rev., 10, p. 612.

Servidori, M. and Armigliato, A. (1975), "Electron Microscopy of Silicon Monophosphide Precipitates in P-Diffused Silicon", J. Mater. Sci., 10, p. 306.

Shea, S.P. Partain, L.D. and Warter, P.J. (1978), "Resolution Limits of the EBIC Technique in the Detection of Diffusion Lengths in Semiconductors", Scanning Electron Microscopy I (IIR Research Institute, Chicago ILL 606616), p. 435.

Shimizu, R. Ikuta, T. Everhart and De Vore, W.J. (1975) "Experimental and Theoretical Study of Energy Dissipation Profiles of keV Electrons in Polymethyl-Methacrylate", J. Appl. Phys, 46, p. 1501.

Shockley, W. (1961), "Problems related to p-n Junctions in Silicon", Solid State Electron, 2, p. 35.

Smith, P.J. Kulkarni, M.V., Troutman, H.A. (1971), 29th EMSA meeting Proc. Elect. Micros. Soc. America, p. 148.

Smith, R.A. (1964), "Semiconductors", Cambridge University Press, p. 254.

Sternglass, E.J. (1954), "Back Scattering of Kilovolt Electrons from Solids", Phys. Rev., 95, p. 345.

Tannenbaum, E. (1961), "Detailed Analysis of Thin Phosphorus Diffused Layers in P-type Silicon",Sol. State. Elect., 2, p. 123.

Thornton, P.R. (1968), "Scanning Electron Microscopy" (London: Chapman and Hall Limited).

Toth, A.L. (1981), "Measurement of EBIC Contrast and Resolution of Dislocations in Silicon", in Microscopy of Semiconducting Materials 1981 Conf. Series No.60 (A.G. Cullis and D.C. Joy, eds), Inst. Phys. Bristol and London, p. 221.

Turner, D.R. (1962), "Electrochemistry of Semiconductors", P.J. Holms - Editor, Academic Press, Inc., New York.

Unvala, B.A. Lesniak, M.P., Regan, B, and Holt, D.B., (1981) "A versatile Quantitative Detection System for Conductive Mode Scanning Electron Microscopy", in Microscopy of Semiconducting Materials, 1981. Conf. Series. No. 60, Inst. Phys, Bristol and London, p. 223.

Van Opdorp, C. (1977), "Methods of Evaluating Diffusion Lengths and Near Junction Luminescence Efficiency from SEM Scans", Philips Res. Rept., 32, p. 192.

Van Roosbroeck, W. (1955), "Injected Current Carrier Transport in a Semi-Infinite Semiconductor and the determination of Surface Recombination Velocities", J. Appl Phys., 26, p. 380.

Von Staszewski, G.M. (1978), "Thinning Method for Electron Microscopy Transparent Silicon and Germanium Foils", Micron., 9, p. 207.

Varker, C.J. (1971), "An Investigation of Microplasma Noise in Zener Diodes with the SEM". Proc. 9th Annual Conf. Reliability Physics (IEEE: New York), p. 155.

Varker, C.J. and Ravi, K.V. (1974), "Oxidation - Induced Stacking Faults in Silicon II Electrical Effects in pn Diodes", J. Appl. Phys., 45, p. 272.

Washburn, J. Thomas, G. and Queisser, J. (1964), "Diffusion-Induced Dislocations in Silicon", J. Appl. Phys., 35, p. 1909.

Watanabe, M. Actor, G. and Gatos, H.C. (1977), "Determintion of Minority Carrier Lifetime and Surface Recombination Velocity with High Spatial Resolution", IEE Trans. Electron Devices, ED-24, p. 1172.

Wilshaw, P.R. Ourmazd, A. and Booker, G.R. (1983), "Some aspects of Electrical Effects of Dislocations in Silicon using a Computerised EBIC System", J. de Phys. Colloque, C - 4, p. C4-445.

Wittry, D.B. and Kyser, D.F. (1965), "Cathodoluminescence at p-n junctions in GaAs", J. Appl. Phys., 36, p. 1387.

Wu, C.J. and Wittry, D.B. (1978), "Investigation of Minority Carrier Diffusion Lengths by Electron Bombardment of Schottky Barriers", J. Appl. Phys., 49, 2827.

Yoshida, M. and Kamamori, S. (1970), "Retardation of Diffusion by Diffusion Induced Dislocations in Silicon", J. Appl. Phys., 9, p. 338.

Zimmermann, W. (1972), "Measurement of Spatial Variations of the Carrier Lifetime in Silicon Power Devices", Phys. Status Solidi, (a) 12, p. 671.

General Background Sources

Shockley, N. and Read, W.T. (1952), "Statistics of the Recombination of Holes and Electrons", Phys. Rev., 87, p. 835.

Sze, S.M. (1969), "Physics of Semiconductor Devices". (Wiley, New York).

ACKNOWLEDGEMENTS

The Author wishes to express his gratitude to Dr. D.B. Holt for his constant guidance and encouragement throughout this work and to Dr. B.A. Unvala for his invaluable help and advice.

The Author is greatly indebted to Mr. J. Bujakowski and Mr. R. Luzar for their sponsorship and support without which this work would not have been possible.

Finally, the Author would like to thank his wife for her patience and the many hours of spare time she devoted to typing this thesis.

.....oooo000oooo.....